DYNAMICS AND PARTITIONING OF SINGLE *CLB2* mRNA AND ITS ROLE IN CELL CYCLE PROGRESSION

Insights from using light microscope prototypes

DISSERTATION

zur Erlangung des akademischen Grades

DOCTOR RERUM NATURALIUM

(Dr. rer. nat.)

im Fach

Biophysik

eingereicht an der
Lebenswissenschaftlichen Fakultät
der Humboldt-Universität zu Berlin

von M.Sc. Severin Ehret

Präsidentin der Humboldt-Universität zu Berlin
Prof. Dr.-Ing. Dr. Sabine Kunst

Dekan der Lebenswissenschaftlichen Fakultät
Prof. Dr. Dr. Christian Ulrichs

Gutachter/innen:

1. Prof. Dr. Dr. h.c. Edda Klipp
2. Prof. Dr. Andreas Herrmann
3. Dr. Carlas Smith

Tag der Disputation: 09.06.2021

Severin Ehret: *Dynamics and partitioning of single CLB2 mRNA and its role in cell cycle progression,* Insights from using light microscope prototypes, 02.03.2021

ABSTRACT

The eukaryotic cell cycle is regulated on all levels of gene expression. Genetic screens and functional studies of the involved proteins have shaped our understanding of this fundamental process. In this thesis I use single cell and single molecule light microscopy methods to investigate spatial aspects of post-transcriptional cell cycle regulation. I investigated the subcellular localization of *CLB2* mRNA, a central regulator of mitosis in the eukaryotic model organism *Saccharomyces cerevisiae* (baker's yeast). Previous studies have shown that that this messenger RNA is enriched in the emerging daughter cell, the bud, during vegetative growth. Using pre-commercial fluorescence microscopes I characterized the dynamics and partitioning of single *CLB2* mRNA on time scales from milliseconds to the generation time of this yeast. I demonstrate that using aberration corrected multifocus microscopy, optimized fluorescent markers, and here developed objective analysis methods, the translocation of single mRNA molecules between mother and bud can be observed. In addition, I report a method to make these trajectories available for the mathematical approaches of Systems Biology. Further, the observation of single *CLB2* mRNA partitioning throughout the cell cycle with the use of lattice light sheet microscopy suggested a previously unknown localization behavior of the transcript. The methods developed here enable a quantitative analysis of spatial aspects of post-transcriptional cell cycle regulation.

ZUSAMMENFASSUNG

Der eukaryotische Zellzyklus ist auf allen Ebenen der Genexpression reguliert. Sowohl breit angelegte genetische Screens als auch funktionale Studien zu den beteiligten Proteinen haben unser Verständnis dieses fundamentalen Prozesses geprägt. In dieser Arbeit behandle ich räumliche Aspekte der post-transkriptionalen Regulation des Zellzyklus, die mit lichtmikroskopischen Einzelzell- und Einzelmolekülmethoden experimentell zugänglich werden. Insbesondere untersuchte ich die subzelluläre Lokalisierung der messenger RNA von *CLB2*, einem zentralen Regulator der Mitose im eukaryotischen Modellorganismus *Saccharomyces cerevisiae* (Bierhefe). Frühere Studien zeigten, dass diese RNA sich im Laufe des vegetativen Zellwachstums in der entstehenden Tochterzelle, der Knospe, anreichert. Mithilfe modernster Fluoreszenzmikroskopie charakterisierte ich die Bewegung und Verteilung einzelner *CLB2* messenger RNA-Moleküle auf Zeitskalen von Millisekunden bis hin zur Generationszeit dieser Hefen. Ich zeigte, dass sich mit Hilfe von Multifokusmikroskopie unter Verwendung optimierter Fluoreszenzmarker und der Entwicklung objektiver Analysemethoden die Bewegung einzelner RNA-Moleküle zwischen Mutterzelle und Knospe nachvollziehen lässt. Dazu präsentiere ich eine Methode um die beobachteten Trajektorien der messenger RNA mathematischen Analysen der Systembiologie zugänglich zu machen. Weiterhin gab die Beobachtung der Verteilung einzelner *CLB2* messenger RNA Moleküle über den Zellzyklus hinweg mittels einer neuartigen Lichtblattmikroskopie (Lattice Light Sheet Microscopy) Hinweise auf eine bisher unbekannte Dynamik in der Lokalisierung dieser messenger RNA. Die hier entwickelten Methoden ermöglichen eine quantitative Untersuchung räumlicher Aspekte der posttranskriptionalen Zellzyklusregulation.

CONTENTS

LIST OF FIGURES

LIST OF TABLES

ABBREVIATIONS AND SELECTED GENE NAMES

4TU	4-thio-uracil
ABC-MDR	ATP-binding cassette multidrug resistance
acMFM	aberration corrected multifocus microcscopy
AIC	Akaike Information Criterion
APC	anaphase promoting complex

ASH1	Asymmetric Synthesis of HO
CCD	charge coupled device
CCG	chromatic correction grating
CDC	cell division cycle
CDK	cyclin dependent kinase
CKI	Cdk inhibitor
Cdk1	cyclin dependent kinase 1
CRLB	Cramér-Rao lower bound
ddH_2O	distilled, deionized water
DH-PSF	double helix point spread function
DoG	difference of Gaussian
EMCCD	electron multiplying charge coupled device
FBM	fractional Brownian motion
fps	frames per second
GST	general systems theory
G_1	gap1 phase
G_2	gap2 phase
HILO	highly inclined and laminated optical sheet
HO	homothallic switching endonuclease
LAP	linear assignment problem
LLSM	lattice light sheet microcscopy
LoG	Laplacian of a Gaussian
M	mitosis
MBF	Mlu1 cell cycle box binding factor
MBS	MS2 binding site
MCP	MS2 coat protein
MFG	multifocus grating
MIP	maximum intensity projection
MSD	mean square displacement

MSL	MS2-stem loop sequence
MUM	multifocal plane microscopy
NA	numerical aperture
NCT	nascent chain tracking
NES	nuclear export signal
NLS	nuclear localization signal
ORF	open reading frame
PBS	phosphate buffered saline
PCR	polymerase chain reaction
PDF	probability density function
PSF	point spread function
QE	quantum efficiency
RBP	RNA binding protein
RNP	ribonucleoprotein particle
rpm	rotations per minute
S	synthesis phase
SBF	Swi4–Swi6 cell cycle box binding factor
sCMOS	scientific complementary metal-oxide-semiconductor
SD	synthetic definedwere
SDCM	spinning disk confocal microscopy
SFF	SWI five factor
She	Swi5p-dependent HO expression
SINAPS	single-molecule imaging of nascent peptides
smFISH	single molecule fluorescence *in situ* hybridization
SNR	signal to noise ratio
SPIM	selective plane illumination microscopy
SPT	single particle tracking
STD	standard deviation
TCA	trichloroacetic acid

TF	transcription factor
TFN	transcription factor network
TIRF	total internal reflection fluorescence
TRICK	translating RNA imaging by coat protein knock-off
$t_{1/2}$	half-life time
UTR	untranslated region
VRC	vanadyl ribonucleoside complexes
YPD	yeast extract peptone dextrose
$t_{1/2}$	half-life time

1 INTRODUCTION

> The whole is greater than the sum of the parts
>
> *Aristotle*
> did not really say that

Aristotle has often been called as a patron when it comes to the striking, seemingly inexplicable features of living systems; mostly with a misquotation. Setting his famous quote straight[1] does, however, not make for a less motivating aphorism for the study of living systems:

> 'In the case of all things which have several parts and in which the totality is not, as it were, a mere heap, but *the whole is something beside the parts*, there is a cause; for even in bodies contact is the cause of unity in some cases, and in others viscosity or some other such quality.' *Aristotle* translated by Ross, 1924, emphasis added)

To me, this is to encourage the use of the quantitative methods of physics to investigate the parts of living systems, *besides* adopting a systems perspective. This perspective, of course, should harness the power of mathematics through different methods; like the general systems theory (GST) of Bertalanffy, 1949 that ascribes the apparent finality of a system to inherent properties of the differential equations describing it instead of incurring vitalistic or metaphysical explanations. The field of systems biology, which draws on the concepts of systems theory and cybernetics (Bertalanffy, 1949; Rapoport, 1986; Wiener, 1948), has since developed to study properties that emerge from the interaction of many biomolecules and to formalize this understanding in the language of mathematics (Cvijovic et al., 2014; Kitano, 2002; Klipp et al., 2005). With the analysis of the movement of single molecules of *CLB2* messenger RNA at the core of this thesis, the main points of interest lie (i) in the integration of advanced microscopical and mathematical methods for the analysis of a biological system, a budding yeast cell, and (ii) the provision of quantitative data on intracellular molecular movement that can serve to improve mathematical models of biological processes.

1 Inspired by a blog on Systems Theory: SE-scholar, 2019

1.1 BUDDING YEAST

Unfortunately Jacques Monod worked with bacteria, not yeast. His utterance

> 'Tout ce qui est vrai pour le Colibacille est vrai pour l'éléphant.' (Monod, 1995)

which translates to 'everything that is true for the coli bacterium is true for the elephant', would have been equally great for baker's yeast. The unicellular eukaryotic fungus *Saccharomyces cerevisiae* (Baker's yeast / budding yeast) is separated from humans by a billion years of divergence from a common ancestor (Douzery et al., 2004). Notwithstanding, more than one third of the genome has clearly identifiable orthologues, i.e., homologues related by speciation, in the human genome (Kachroo et al., 2015; O'Brien et al., 2005). Core functions seem to be even more conserved, as for the about 1100 essential genes (Giaever et al., 2002; Winzeler et al., 1999) in *S. cerevisiae* a human ortholog exists in more than two thirds of the cases (Laurent et al., 2016). As posited by the ortholog-function conjecture (Gabaldón and Koonin, 2013) and implicit in the concept of biological models orthologous genes retain a similar or identical function in diverged species. As proof of the usefulness of budding yeast to elucidate central functions of human cells, and human disease, the Nobel Prize for Physiology or Medicine has been awarded 2001, 2009, 2013 and 2016 for work involving yeast; with a Nobel Prize in Chemistry (2006) making it five in the current century alone. The reasons why yeast (which I use as a shorthand for budding yeast) is a preferred model organism, in particular with regards to cell cycle research, are manifold. Yeast has been used for millennia in the production of beer, bread and wine; cultivation is accordingly straightforward. Compared to other microorganisms, yeast is mostly beneficial to human health and usually not pathogenic. While the first genetic experiments have been performed on peas by the monk Gregor Mendel in the 1850's (Mendel, 1866), yeast started to play a major role in genetic research almost a century later thanks to Øjvind Winge at Carlsberg Laboratories (Barnett, 2007; Winge and Laustsen, 1937, 1938, 1939). A further important impulse came from Lee Hartwell in the 1960's who wanted to study the cell cycle of human cells, but picked up on the suggestion to use a 'more simple' model and described dozens of cell division cycle (CDC) mutants in budding yeast (Hartwell et al., 1970, 1973). Together with cyclins (Evans et al., 1983), originally described by Tim Hunt's group in sea urchins and cyclin dependent kinases (CDKs), described by Paul Nurse et al., 1976 in fission yeast (*Schizosaccharomyces pombe*), this description of CDC mutants is the basis of our understanding of eukaryotic cell cycle regulation. This CDK-centered view has been complemented by a transcription factor network in more recent studies, as will be discussed in section 1.2. The fact that CDC genes

have the same phenotype in haploid and diploid cells (Hartwell et al., 1970) and the more direct genotype-phenotype relationship in haploid organisms further explains the popularity of haploid yeast cells for cell cycle research. Finally, yeast was the first eukaryote with a fully sequenced genome (Goffeau et al., 1996), which clearly helped in brewing up more yeast research (Williams, 1996). It has been suggested that yeast biology, as quantified by the discovery of genetic interactions and protein-protein interactions, has been growing exponentially for decades (He and Zhang, 2009) due to the aforementioned factors. Despite the conservation of parts of cell cycle regulation architecture from yeast to humans it has to be said that other non-mammalian organisms are more similar to humans in some respect, e.g., fission yeast and plants (Harashima et al., 2013). By way of example, while the genome of *S. pombe* is smaller than the one of *S. cerevisiae* (5100 vs 5800 protein coding genes, Hoffman et al., 2015), *S. cerevisiae* has lost more than 300 genes that are conserved from *S. pombe* to vertebrates, while less than 200 genes lost between *S. pombe* and vertebrates are present in *S. cerevisiae* (Aravind et al., 2000; Wood, 2006). As Paul Nurse suggested, this should rather encourage the use of both, fission and budding yeast, as genes, or cell cycle control elements, shared between these disparate yeasts are likely to be important in humans as well, and not discourage the use of *S. cerevisiae* (Lee and Nurse, 1987). There are, nonetheless, further findings that challenge the status of yeast as 'universal' model organism for all eukaryotes (Herskowitz, 1985) alluded to at the beginning of this section. While universality seemed compatible with phylogeny some decades ago, it is now assumed that the clades of Opisthokonta (containing yeasts and animals) and Viridiplantae (plants and green algae) diverged first, whereas yeasts and animals diverged from each other at a later time point (Cross and Umen, 2015; Rogozin et al., 2009). This phylogeny implies that findings from yeast might be less useful for understanding plant cell cycle regulation, but does little to challenge its model status for humans and other animals. A challenge for the current phylogenetic model, and interesting for the position of yeasts as model organisms are a number of genes conserved in plants and animals, but not in yeasts. An example is the cell cycle regulator Rb (Retinoblastoma protein), slowing down cell cycle progression in most eukaryotes, but not yeast (Cross and Umen, 2015). Of particular interest for this study is a difference regarding classes of Cyclins: While cyclin D and cyclin A are core regulators in plants and animals, they are absent from yeasts, where rounds of genome duplications and ensuing divergence are presumed to lie behind the dominance of B-type cyclins (Archambault et al., 2005, see also section 1.2.1). Although this makes other organisms such as *Chlamydomonas* - that share more cell cycle regulators with animals and plants (Cross and Umen, 2015) - more attractive as models, yeast has an edge regarding previous knowledge and established techniques

for its investigation. Thus, even if one cannot hope to understand all human (or elephantine) genes based on yeast experiments, systems features like the cell cycle regulatory circuitry (Cross et al., 2011; Haase and Wittenberg, 2014), enzymatic cascades or biochemical networks (Klipp, 2007) are often conserved and can be studied rigorously and cheaply in yeast.

1.2 CELL DIVISION CYCLE

What is life? The question has been answered in numerous, partly contradictory, ways (Koshland, 2002; Schrödinger, 1944; Tsokolov, 2009) and has been brought into disrepute on the stage of science as the definition of life is arbitrary (Tessera, 2011). An autonomous, orderly program allowing an entity to coordinate its growth and proliferation, to replicate its building plan and to pass it on to a new entity can, irrespective of fuzzy borders regarding, e.g., the status of viruses, still safely be regarded as a central hallmark of living systems. While prokaryotic cells cycle in their own way (Margolin and Bernander, 2004; Taheri-Araghi et al., 2015), there are many similarities in eukaryotic cell cycle control, both regarding sequence conservation (Lee and Nurse, 1987; Léopold and O'farrell, 1991) and topology of the regulatory networks (Cross et al., 2011). How well certain cell cycle regulatory proteins are conserved, even across domains of life, has been demonstrated by complementation experiments, where deletions could be rescued with proteins from another species (Koff et al., 1991; Lew et al., 1991). While a specific gene of the cell cycle control machinery may be conserved, it could, however, play different roles in different species (Cross et al., 2011). An example are the kinases Chk1 and Cds1 that are involved in one specific cell cycle checkpoint each in yeast, while their roles are swapped in metazoans (Rhind and Russell, 2000). In the following subsections I will, thus, focus on yeast and outline CDC in yeast, along with the relation between cell cycle and cell size homeostasis, which is peculiar in asymmetrically dividing yeast.

1.2.1 Yeast cell division cycle

Yeast cells can replicate through budding; a vegetative growth process leading to genetically identical daughter cells (figure 1). This cell cycle can be divided into three to four phases which are discernible through morphological changes and molecular events. A cell grows as an individual in G_1 before duplicating its genome in S. The onset of S roughly coincides with the emergence of a bud that will develop into a daughter cell. The canonical description also contains a G_2 prior to M (reviewed in Nurse, 2000), although many authors negate the

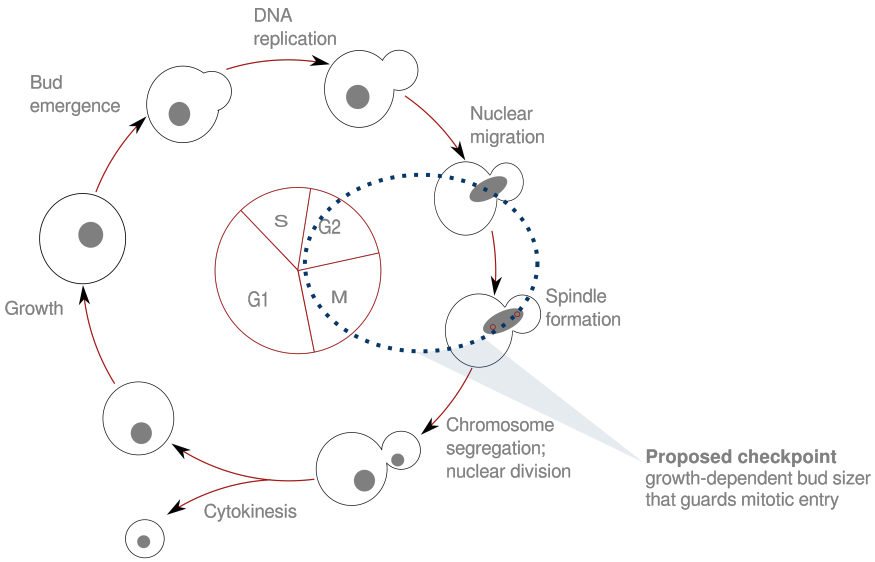

Figure 1: Vegetative cell cycle of haploid yeast. This cell cycle is an important model for mitosis, particularly as the diploid vegetative cell cycle proceeds the same way. Progression through the cell cycle is regulated by the conserved master kinase Cdc28/Cdk1 with its cell phase specific cofactors, cyclins, and a network of transcription factors that is independent, to some degree, of the CDK/cyclin system. While there is a well described checkpoint at the G_1 /S transition ('START'), this work is related to a checkpoint guarding mitotic entry (G_2 /M transition). Alternative cell cycles that budding yeast can undergo, including mating of haploid cells, sporulation of diploid cells, or diploid vegetative growth are not shown.

presence of a second gap phase in budding yeast as they commence mitosis during S phase (Forsburg and Nurse, 1991; Lovrics et al., 2006; Nasmyth, 1996). A recent publication challenging the concept of a G_2 phase in budding yeast came from the groups of Manuel Mendoza and Lucas B. Carey. They demonstrated that the segregation of sister chromatids in budding yeast starts before DNA replication is complete in 20 - 40 % cells under 'normal' laboratory conditions (Ivanova et al., 2020). The authors went so far as to suggest S_1 and S_2 phases that both would overlap with M. Undisputedly, though, the cell cycle culminates in the division of nucleus and cytoplasm, i.e., mitosis and cytokinesis. This sequence is repeated until mother cells senesce, limited by their replicative life span of 30-50 divisions (Kaeberlein et al., 2005; Mortimer and Johnston, 1959; Powell et al., 2003). It is worth mentioning that this does not reflect the behavior of wild yeast. In most laboratory yeast strains, homothallic switching endonuclease (HO) (Jensen et al., 1983; Kostriken et al., 1983) has been deleted; which locks a cell's offspring in the current mating type, a or α. In yeast cells with intact HO, mating type switching occurs after budding and cells of opposite mating type can grow a mating projection (a process called shmooing)

towards a potential partner. Upon fusion of the cytoplasm of compatible haploid cells a zygote, and eventually a diploid cell (of mating type a /α) forms (mating reviewed in Haber, 2012). As opposed to fission yeast, this diploid state is the dominant form of budding yeast outside the laboratory. A total of four haploid spores, contained in an ascus, forms only if cells are deprived of a sufficient source of carbon or nitrogen. These spores leave the ascus and resume their, now haploid, life cycle once conditions are more favorable (sporulation reviewed in Neiman, 2011). To discuss molecular mechanisms I want to introduce a few naming conventions for yeast: Gene names are capitalized and in italics (e.g., *CLB2*), RNA names are denoted by an additional m before the respective name (*mCLB2*) and proteins are denoted with a lowercase p (Clb2p) that can be omitted, e.g., when protein complexes are described (Cdc28/Clb2) and confusion with genes or RNAs seems unlikely. The sequence of molecular events that steer the progression of the CDC in yeast revolve mainly around Cdc28, or Cdk1, the master kinase of the cell cycle. Cdc28 activity is subject to activation by binding of cyclins and phosphorylation, as well as inhibition by Cdk inhibitors (CKIs) in a phase specific manner, imparting directionality to the cell cycle (Enserink and Kolodner, 2010; Mendenhall and Hodge, 1998; Murray, 2004; Nasmyth, 1996; Surana et al., 1991). The cyclins Cln1-3 and Clb1-6 can be grouped into clusters that refer to the phases or transitions they are involved in: G_1, S, G_2/M and M/G_1. The group of Steven I. Reed has shown, however, that cell cycle specific gene expression was partly maintained in the absence of entire cyclin clusters (Orlando et al., 2008); as had been suggested much earlier by Haase and Reed, 1999. The significance of a transcription factor network (TFN) that maintains CDK-independent oscillations in cell cycle specific transcription is a matter of active discussion, with many publications detailing a synthesis between the CDK/cyclin and TFN systems (Cho et al., 2019; Linke et al., 2017; Simmons Kovacs et al., 2008, 2012), while others perceive the CDK/cyclin system as dominating (Landry et al., 2014; Lu and Cross, 2010; Rahi et al., 2016). In addition, metabolic oscillations have also been shown to coordinate cell cycle progression (Ewald, 2018; Özsezen et al., 2019; Papagiannakis et al., 2017). The first checkpoint in the cell cycle described in yeast is called 'START' (Hartwell and Weinert, 1989). It designates the transition from G_1 to S, when the cell commits to completing a cell division cycle through Swi4–Swi6 cell cycle box binding factor (SBF)- and Mlu1 cell cycle box binding factor (MBF)-mediated transcription of an S specific cluster of more than 200 genes (Spellman et al., 1998). START is activated by Cdk1 in its Cln3-bound state, with Cln1p/2p further increasing Cdk1 activity up to the threshold required for effective phosphorylation of Whi5p (Cross and Tinkelenberg, 1991; Enserink and Kolodner, 2010; Skotheim et al., 2008). In response, the transcriptional repressor Whi5p dissociates from SBF/MBF complexes, leading to derepression of S specifc

genes (Bloom and Cross, 2007). Although sequence conservation in functionally similar key proteins (e.g Cln3 vs. Cyclin D) is low, the network topology of START and the 'restriction point', guarding G_1/S transition in mammalian cells (Pardee, 1974) are very similar (Johnson and Skotheim, 2013). The regulatory mechanism of START is therefore an important model for the principles of cellular decisions, apart from serving as a model for cell cycle misregulation, causing, e.g., cancer, diabetes and neurodegenerative diseases in humans (Boehm and Nabel, 2003; Currais et al., 2009; Zhivotovsky and Orrenius, 2010).

1.2.2 Size homeostasis and cell cycle

The volume of eukaryotic cells can vary by a factor of a quadrillion (10^{15}) between organisms and cell types (Jun and Taheri-Araghi, 2015; Palenik et al., 2007); each cell type has, however, a well defined size. From a thermodynamic perspective, the size and budded shape of yeast cells have been suggested to rely on the balance between osmolyte homeostasis and region-specific extensibilities of the cell wall (Altenburg et al., 2019). With regards to genetic control, cell cycle and cell size are closely related. This is illustrated by the fact that growth rates vary more than cell sizes between different growth conditions, suggesting that cell cycle events be delayed or hastened so that cell size upon division is within the typical range (Rupeš, 2002). Clearly, a cell's size is fundamental as differences in, e.g., surface to volume ratio, the relative size of organelles, or the importance of diffusive processes affect a cells physiology (Chan and Marshall, 2010; Schmoller et al., 2015). Cell size homeostasis arises from the balance of cellular growth and division. This raises the question whether cell size might be controlled by the molecular mechanisms of cell cycle control; or alternatively trigger cell cycle progression (Jun and Taheri-Araghi, 2015; Schmoller et al., 2015; Spiesser et al., 2012); or if cell size simply arises from the correlation of both. There have been many efforts to find and characterize feedback mechanisms between cell size and the cell cycle control circuitry, as this is the main feature setting the aforementioned models apart (Coelho and Leevers, 2000; Neufeld and Edgar, 1998; Polymenis and Schmidt, 1999). Mechanisms regulating the homeostasis of cell size in a cell population have been classified as 'timer' or 'sizer' that would trigger cell division after a certain period of growth, or by sensing a critical size (Rupeš, 2002). By way of example, Schaechter et al., 1962 observed in different bacteria that interdivision times varied within 20 % approx., whereas cell size was more stable (coefficient of variation 10 % approx.), which may speak in favor of a sizer mechanism. For yeast, the search for a sizer took an interesting turn, when Spiesser et al., 2012 suggested that the reliance of metabolism on the surface to volume suffices to explain cell size regulation in the G_1 network guarding START. While the former study

derived size homeostasis from a simplified model with a single, unregulated cyclin, Schmoller et al., 2015 showed that different scaling laws in the synthesis of cell cycle regulatory proteins can relate cell size to the G_1 network. In particular, they described how the ratio between the roughly size-independent synthesis of the repressor Whi5 and the synthesis of Cln3 that is proportional to the cell size act as sizer. Interestingly, the model by Spiesser et al., 2012 also highlighted that size control is likely not only exerted at START, as this would lead to diverging cell sizes of mother and daughter cells. As yeast is primarily used as *model* for human cells, the aspect of cell size divergence due to asymmetric cell division might be considered irrelevant at first glance. However, as Ginzberg et al., 2015 pointed out focusing on animal cells, an increasing body of evidence suggests that cell growth is in general exponential, which also would lead to divergent cell size if no size control is enforced. For yeast the aforementioned model predicted, in agreement with experimental data (Barford and Hall, 1976; Rivin and Fangman, 1980), that G_2 duration depends on the carbon source, implying that cells can compensate their size by varying how long they grow after START before cell division. It is noteworthy that G_2 duration had long been viewed as insensitive to growth conditions in *S. cerevisiae*; whereas in *S. pombe* G_2 duration is the main setscrew to respond to different growth conditions (Pringle and Hartwell, 1981; Rupeš, 2002; Sveiczer et al., 1996). Although they were not knwon to respond to nutrient availability like START, a number of further checkpoints in the yeast cell cycle has been known for more than 30 years. They delay the cell cycle if problems such as DNA damage, spindle-malformation, or morphological defects occur (Lew and Reed, 1995; Pringle and Hartwell, 1981). The morphogenesis checkpoint, e.g., delays mitotic entry if bud formation is deficient or abolished. Mechanistically, it has been suggested to depend on differential susceptibilty of Cdc28 regarding Swe1-mediated phosphorylation on Y19 in cells growing either isotropically or in a polarized fashion (Sia et al., 1996). While this phosphorylation inhibits Cdc28/Clb2 and thus delays entry into mitosis in non-polarized cells (shown for temperature-sensitive *cdc24* mutants), cells that had previously formed a bud progress into mitosis irrespectively of this phosphorylation. Further experiments by McMillan et al., 1998 demonstrated how the morphogenesis checkpoint can even respond to actin depolymerization. This sensitivity towards the status of the cytoskeleton has later been suggested to depend on the bud-size, as actin depolymerization by latrunculin A only induces a Swe1-mediated delay in the G_2/M transition if buds are below a size threshold but fails to do so when buds are larger (Harvey and Kellogg, 2003). This lead to conjectures regarding the molecular nature of a gauging mechanism that would only be sensitive to bud size but *not* overall cell size. Since cytoplasmic molecules are free to diffuse between mother and bud, while membrane proteins are

confined by septins at the bud neck (Barral et al., 2000; Takizawa and Vale, 2000) the latter were early on considered as possible constituents of such a system (Harvey and Kellogg, 2003). As an alternative, Anastasia et al., 2012 hypothesized that trafficking of membrane vesicles to the bud might be an indicator for sufficient bud growth. The cue for entering mitosis would thus be the degree of polarized membrane growth. A third hypothesis, which constitutes the starting point for the present work stems from the puzzling fact that mRNA of the major mitotic cyclin Clb2p (*mCLB2*) has been reported to be predominantly bud-localized while Clb2p is not (Shepard et al., 2003; Takizawa and Vale, 2000; Trcek et al., 2011). As mRNA localization is mostly thought of as an efficient mechanism for the localization of the encoded protein (Condeelis and Singer, 2005; Du et al., 2007; Eliscovich and Singer, 2017; Lasko, 2012), this raises the questions why *mCLB2* is localized at all. There are, however, a number of other roles that mRNA localization can play (see section 1.4). Spiesser et al., 2015 suggested that in the case of *mCLB2* the subcellular localization could be a means to gauge the *biosynthetic capacity* of an emerging daughter cell. Thus, the concentration of Clb2p, and Cdc28/Clb2 promitotic activity would depend on the bud's capacity to translate proteins. Due to the constant density of ribosomes, which are the key determinant of *biosynthetic capacity*, this would relate bud size to the cell cycle machinery and constitute a bud sizer. This leads to the formulation of overarching questions I addressed in my project: Is bud localization of *mCLB2* reproducibly observed in premitotic yeast cells? Can live cell single molecule methods corroborate the localization observed in fixed cells (Trcek et al., 2011) and in live cell experiments lacking single molecule resolution (Shepard et al., 2003)?

1.3 CYCLIN B2 AND MITOTIC ENTRY

As outlined in the previous sections, there are checkpoints guarding progression of the CDC. During budded phase, successive waves of B-type cyclins - Clb5p/6p, Clb3p/4p and Clb1p/2p - bind the master kinase of the cell cycle, leading to the phosphorylation of target proteins and expression of gene clusters in a phase-specific fashion (reviewed in Mendenhall and Hodge, 1998). The present work aims at improving our understanding of the G_2 to M transition and its regulation by *CLB2*. This cyclin maintains the promitotic activity of the G_2/M (or *CLB2*) cluster of approximately 35 genes by a positive feedback loop (Amon et al., 1993; Spellman et al., 1998; Wittenberg and Reed, 2005). Upstream of this self-reinforcing expression an external 'SWI five factor (SFF)' comes into play. It has been shown to consist of Fkh1 and Fkh2, as deletion of both these genes uncouples the cell cycle from periodic expression of the *CLB2* cluster (Zhu et al., 2000).

Specifically, Cdc28 bound to Clb1p/2p intersects with a transcription factor (TF) complex consisting of Mcm1, Fkh1/2 and Ndd1 to coordinate spindle pole body duplication and mitotic spindle assembly with the expression of early mitotic genes and other events required for mitotic entry (Bähler, 2005; Bloom and Cross, 2007). Clb2/Cdc28 further activates *CLB2* expression by different mechanisms, creating a positive feedback loop (Amon et al., 1993). A study involving kinetic and Boolean modeling as well as experimental assays worked out mechanistic details of this interaction: The forkhead protein Fkh2 in particular has been shown to activate *CLB* genes by a coherent type 1 feed forward loop (Linke et al., 2017). In this motif, Clb5p and CLb3p, cyclins peaking in earlier waves of transcription during S-G_2, activate transcription of *CLB2* in a Fkh2-Ndd1 dependent fashion, with *CLB3* expression under control of the same TF complex. The CDK-dependent regulation of mitotic genes via phosphorylation of a forkhead protein (FoxM1 in mammals) is conserved from yeast to animals (Landry et al., 2014; Major et al., 2004; Reynolds et al., 2003). The promitotic activity of Cdc28 relies overwhelmingly on Clb2p (85 %, Grandin and Reed, 1993), while Clb1p is primarily involved in meiosis (Mendenhall and Hodge, 1998). Apart from the transcriptional regulation detailed above; translation and degradation of *CLB2* are under tight control. *mCLB2* and *mCLB1* peak shortly before mitotic entry (Fitch et al., 1992; Ghiara et al., 1991; Surana et al., 1991). The peak of Clb2p production is, however, further narrowed by translational repression, presumably by RNA binding proteins (RBPs) that are also involved in RNA transport. *mCLB2* has been reported to be transported to the bud in a Swi5p-dependent HO expression (She) mediated actomyosin transport (see section 1.4.2, Shepard et al., 2003). While this publication reported binding of *mCLB2* to Myo4, the other type V myosin in yeast, Myo2, has been found to bind *mCLB2* by immunopurification, while all other types of motor proteins were shown not to interact significantly with *mCLB2* (Casolari et al., 2012). The Myo4/She-dependent transport, most thoroughly characterized for *ASH1* mRNA, entails binding of numerous RBPs (Edelmann, 2017; Heym and Niessing, 2012). In the case of *ASH1* the translation repressors Khd1 (Irie et al., 2002; Paquin et al., 2007) and Puf6 (Deng et al., 2008; Gu et al., 2004) are known to constitute part of the transported ribonucleoprotein particle (RNP). These publications showed that Kdh1 and Puf6 RBPs bind mRNA within the nucleolus (Puf6) and the nucleus (Khd1), respectively, and only dissociate from, and thereby derepress the mRNA once it is anchored to the bud tip at the end of its cytoplasmic journey. Although the exact composition of the transport-competent *mCLB2* RNP is not known, these repressors might well be involved in *mCLB2* transport, too: Microarray based polysome profiles suggest that roughly 2/3 of *mCLB2* in rapidly growing, asynchronous yeast cell cultures is not translated (Arava et al., 2003). It is worth mentioning that this is highly

unusual. According to the ribosome occupancy method applied by Arava et al., 2003, for 99 % (5600 out of 5701) of all detected mRNA species the majority of molecules is bound to a polysome. During mitosis Clb2p is degraded to facilitate mitotic exit (Cai et al., 2002; Gill et al., 2004). This degradation has been suggested to rely solely on the promoter of *CLB2*, which mediates cotranscriptional binding of the mitotic exit network protein Dbf2 to *mCLB2* (Haimovich et al., 2013; Trcek et al., 2011). The anaphase promoting complex (APC) mediated destruction of Clb2p at the end of mitosis is important for mitotic exit (Deshaies, 1997; Schwab et al., 1997; Wäsch and Cross, 2002). Proteolysis depends on the ubiquitin-conjugating enzyme UBC9 which targets B-type cyclins to the proteasome (Seufert et al., 1995) and HCT1 and CDC20 as substrate specific regulators (Schwab et al., 1997). Clb2p has been shown to be primarily nuclear throughout the cell cycle (Bailly et al., 2003; Hood et al., 2001). The authors also reported a bipartite nuclear localization signal (NLS) that mediates nuclear import in an importin α/β dependent mechanism and two potential nuclear export signals (NESs). Overexpression studies, using galactose-inducible promoters, reported additional cellular localizations for Clb2p, including bud neck and spindle, whereas other B-type cyclins where not observed there (Hood et al., 2001). Later bud neck localization was observed also for Clb2p expressed from its native promoter, where Cdc28/Clb2 might play a role in the regulation of cytokinesis (Bailly et al., 2003). Nuclear export and bud neck localization of Clb2p also rely on a hydrophobic patch presumably required for the interaction with Bud3 (Archambault et al., 2004; Bailly et al., 2003). This patch is known to bind the so-called RXL motif in CDK-targets, explaining why disruption of the hydrophobic patch decreases the mitotic function of Clb2p (Cross and Jacobson, 2000). A further role for cytoplasmic Clb2p is the interaction of Clb2/Cdc28 with Cdc42p required for the transition from polarized to isotropic bud growth (Pruyne and Bretscher, 2000). Broadening Cdc42p distribution, from the bud tip to the bud cortex at large, acts as the isotropic switch once the bud is "sufficiently" long (Richman et al., 1999), providing an additional mechanism for the implication of *CLB2* in bud size control (see also section 1.2.2). The dominant function of Clb2-bound Cdc28 is in the nucleus, where it represses SBF in a Swi4-dependent way and triggers further early mitotic events. Genetically, this can be shown by the high fraction of budded cells in asynchronous Δ*clb2* cell culture (Epstein and Cross, 1992; Fitch et al., 1992). Synthetically lethal combinations are Δ*clb3* and - not surprisingly - Δ*clb1*. The single deletions Δ*clb1*, Δ*clb3* and Δ*clb4* have no discernible phenotype; while the triple deletion Δ*clb1* Δ*clb3* Δ*clb4* is similar to Δ*clb2*. Like most other lethal triple deletions of *CLB1-4*, the quadruple deletion cells Δ*clb1-4* grow past START, form a bud, but fail to undergo even one cell division (Amon et al., 1993; Epstein and Cross, 1992). Essentiality - and the 'nonessentiality of

[certain] essential genes' (Chen et al., 2016) attests to that - is of course not the only relevant scale on which to judge *CLB2*. Shifting away from classical yeast biology, in the following sections, I want to discuss the motion of cytoplasmic molecules, mainly mRNPs (section 1.4), and techniques to investigate it (section 1.5). These lay the groundwork for the discussion of spatial aspects of post-transcriptional regulation, which might be of interest for the role of *CLB2* in CDC regulation.

1.4 DYNAMICS OF CYTOPLASMIC mRNA

1.4.1 Diffusion

The central limit theorem can serve as starting point for the investigation of mRNA motion in the cytoplasm. This theorem is based on the observations of Laplace, 1812; Moivre, 1733 on n repetitions of an experiment with two possible outcomes p, e.g., *success* and *failure*, (Bernoulli trial) that lead to a *binomially* distributed *success*-rate. For $n \to \infty$, however, the result becomes well approximated by a normal distribution. For the description of free movement of molecules inside a cell it is helpful that this is true not only for binomial, but for a wide range of underlying distributions (Montgomery and Runger, 2010). It is not obvious which type of process governs the motion of biomolecules inside cells - is it that they are "held by the field of force of the surface atoms [of other molecules]" (Langmuir, 1918) and dissociate, only to adsorb to the next molecule? Is it that they experience collisions and change direction? Regardless which process is dominant; the interactions are many and the central limit theorem likely valid. Lampo et al., 2017, e.g., treats the free motion of intracellular particles as a random walk, with each step determined by random collisions with other molecules in the cytoplasm. Such a process gives rise to Gaussian diffusion and experimentally obeys the equation given by Smoluchowski, 1916 and Perrin, 1909

$$D = \frac{H \cdot T}{N} \cdot \beta \tag{1}$$

with D = diffusion coeffient, H = enthalpy, T = temperature, N = Avogadro's number, $\beta = 1/(k_B \cdot \mathrm{T})$ and k_B = Boltzmann factor. Another prevalent notation is $D = k_B T/\xi$, with ξ being a particle-specific drag coefficient. The assumption of free diffusion is indeed common for the analysis of RNA motion in both nucleus (Grünwald and Singer, 2010; Saroufim et al., 2015; Shav-Tal, 2004) and cytoplasm (Bakshi et al., 2012; English et al., 2011; Park et al., 2014; Persson et al., 2013). Apart from free diffusion of cytoplasmic RNA, further diffusive states have been described, e.g., the corraled diffusion (Fusco et al., 2003) of mRNA that is being translated (Katz et al., 2016) or trapped in the

microfilament-rich perinuclear region (Yamagishi et al., 2009). There is increasing evidence that free diffusion in cells is usually not the Gaussian type of diffusion, with normally distributed displacement probabilities resulting in Brownian motion that is commonly observed in air or water (Einstein, 1906; Perrin, 1909; Smoluchowski, 1916). Often, non-Gaussian and subdiffusive behavior describes the movement of molecules like RNPs inside living cells more accurately (Lampo et al., 2017; Weiss, 2013). This is an important difference to the movement of smaller molecules, such as proteins that conform fairly well with Gaussian diffusion (Elowitz et al., 1999). As with soluble proteins, membrane proteins seem to move as expected for Gaussian diffusion, even where subpopulations with higher and lower diffusivity are detected (Anderluh et al., 2014). mRNPs in bacteria and yeast, however, have been found to move by subdiffusion (Joyner et al., 2016; Stylianidou et al., 2015). This implies a weaker time-dependence of the mean square displacement (MSD) than would be found in Brownian motion, where the MSD linearly depends on the lag time

$$MSD \propto D(\Delta t) \tag{2}$$

Instead, the MSD in subdiffusion is governed by a power law with an exponent α lower than 1

$$MSD \propto K_\alpha (\Delta t)^\alpha \tag{3}$$

with K_α being a generalized diffusion coefficient in $[cm^2(s^\alpha)^{-1}]$ (Metzler et al., 2014). From a physico-chemical perspective, molecular crowding has been shown to afford the cytoplasm viscoelastic properties, which in turn can explain subdiffusive behavior (Hasnain et al., 2014; Saxton and Jacobson, 1997; Weiss, 2013). Crowding in the cytoplasm has similarly been suggested to lead to a much stronger size dependence of the diffusivity than expected from the Sutherland-Stokes-Einstein relation (Sutherland, 1905), relating the diffusivity D at low Reynolds number to a particle's size

$$D = \frac{k_B T}{6\pi\eta r} \tag{4}$$

with k_B = Boltzmann's constant, T= temperature, η = dynamic viscosity and r = hydrodynamic radius of the particle. Accordingly, it has been suggested to introduce a scale dependent viscosity that allows to use the above formula for larger particles (Holyst et al., 2009; Szymański et al., 2006). Subdiffusion emerges in this way as a mere side-effect of a cells architecture, shaped by evolutionary constraints on content and compactness. It might, however, also aid reaction efficiency by keeping reaction partners or constituents of a reaction cascade in close vicinity

(Guigas and Weiss, 2008; Jeon et al., 2011). The analysis of purely diffusive mRNP displacements in yeast and bacteria on time scales from milliseconds to minutes revealed that they follow a Laplacian (also known as doubly exponential) distribution (Lampo et al., 2017). For the 1D case, this can be formalized with the probability density function (PDF) of displacements not following

$$P_{Gauss}(\Delta x;\mu,\sigma) = \frac{1}{\sigma\sqrt{2\pi}} exp[-\frac{(\Delta x-\mu)^2}{2\sigma^2}] \tag{5}$$

but instead a Laplacian PDF

$$P_{Laplace}(\Delta x;\mu,\sigma) = \frac{1}{\sigma\sqrt{2}} exp[-\frac{|\Delta x-\mu|\sqrt{2}}{\sigma}] \tag{6}$$

with Δx = displacements, μ, σ = mean and standard deviation of Δx. In broad terms, the observed Laplacian PDF can result (i) from averaging over multiple trajectories with Gaussian displacement distributions that differ due to the heterogeneous nature of the cytoplasm, (ii) from a non-Gaussian behavior within single trajectories, or both. A related question thus is, whether the time-averaged MSD of single trajectories is equal to the ensemble average at one time-point, i.e., whether the system is ergodic (Jeon et al., 2011; Metzler et al., 2014). For the mRNP diffusion in budding yeast recorded in Thompson et al., 2010 and analyzed in depth by Lampo et al., 2017, it was found that both the ensemble, and single trajectory displacement distributions were non-Gaussian. To see whether non-Gaussian behavior of single trajectories was due to the exposure of the mRNP to temporal or spatial heterogeneities on long time scales only, displacement distributions from different time scales were normalized by their respective σ. The distributions for all time scales were similar, showing no evidence for Gaussian behavior on short time scales. I take this to mean that diffusing RNPs sample a similar scale of heterogeneity at the millisecond range as the entire cytoplasm comprises. This relates to the fact that Lampo et al., 2017 report that the MSD of yeast mRNPs shows a power-law dependence that is equal for time- and ensamble averages, with an exponent α=0.75. Accordingly, the motion of these particles can be described as ergodic, non-Gaussian subdiffusion. Focusing again on the temporal evolution of single trajectories, the authors also found subsequent displacements to be negatively autocorrelated, marking a further deviation from Brownian motion. According to the formulas provided by Jeon and Metzler, 2010 to distinguish types of subdiffusive processes encountered in biological systems, this negative autocorrelation suggests fractional Brownian motion (FBM), rather than fractional Langevin equations or continous time random walks, as the most suitable framework to describe the diffusion found by Lampo et al., 2017. For the present study another prediction by Jeon and

Metzler, 2010 regarding ergodicity is relevant: Both, confinement and increasing dimensionality make FBM processes more ergodic. Thus, as the analysis of 2D displacements by Lampo et al., 2017 did not find ergodicity breaking, diffusion in the 3D data presented here is likely to be even more strictly ergodic.

1.4.2 Superdiffusion and active transport

Diffusion is a useful framework to describe the motion of cytoplasmic mRNA. Proteins can traverse small cells like bacteria and yeast cells within milliseconds to seconds (Elowitz et al., 1997, 1999) by diffusion alone, and while mRNA is larger diffusion remains an important factor for cytoplasmic translocation on length scales of entire yeast cells (Oeffinger and Zenklusen, 2012; Shav-Tal, 2004). Diffusion alone, however, is usually not sufficient for symmetry braking; the enrichment of mRNA in certain cellular regions (there are exceptions, cf. section 4.3.1). The first report on the enrichment of a particular RNA species in subcellular regions showed the β-actin mRNA in chicken myoblaststs using autoradiographic in situ hybridization (Lawrence and Singer, 1986). Earlier it was shown by autoradiography of tritium-labeled uridin and histidin that the entirety of RNA in housefly follicles is distributed asymmetrically (Bier, 1963). Since then it has been shown that many RNA species are distributed asymmetrically: In *Drosophila* ovaries ∼20% of all mRNA species were shown to be localized by smFISH (Jambor et al., 2015), and sequencing of subcellular compartments in neurons showed that hundreds of RNA species are preferentially localized to dendrites (Middleton et al., 2019) and axons (reviewed in Turner-Bridger et al., 2020). In yeast, RNA localization has first been observed for *mASH1* (Long et al., 1997), and with it a mechanism for acto-myosin dependent transport has been discovered (reviewed in Edelmann, 2017; Heym and Niessing, 2012). In principle, there are three different mechanism leading to RNA localization: (i) active cytoskeletal transport, such as the conserved microtubuli-dependent transport found in axons (Hazelrigg, 1998), (ii) anchoring at specific locations, and (iii) local protection from general degradation (Medioni et al., 2012). In neurons, where RNA would need weeks to diffuse from the soma to the synaptic terminals, an active transport process is strictly required. In yeast, on the other hand, anchoring at the bud tip (Beach et al., 1999) would be enough to preferentially localize RNA to the bud. As I investigate how mRNA localization comes about in yeast cells, the previous section on diffusive motion calls for an introduction into active processes. In the following I will shortly outline the structure of the yeast cytoskeleton and the role of actomyosin transport in yeast.

1.4.2.1 *Actin cytoskeleton: The route for transport in yeast*

The actin cytoskeleton of yeast is a tripartite network of F-actin bundles that (i) run in actin cables below the plasma membrane in axial direction, (ii) form cortical actin patches and (iii) form an acto-myosin ring around the bud neck (Adams and Pringle, 1984; Kilmartin and Adams, 1984; Mishra et al., 2014). F-actin, the filamentous form, consists of globular actin monomers (G-actin) that polymerize to form a right-handed double-stranded helix. The balance of polymerization at the barbed end, and de-polymerization at the pointed end is the most basic process underlying cytoskeleton dynamics (Pollard and Borisy, 2003). The organizational structure of the actin cytoskeleton can be described in different terms. Conventionally, hundreds of accessory proteins are classified as activators and inhibitors that govern the architecture of the cytoskeleton (Mishra et al., 2014; Pollard and Cooper, 2009; Pollard et al., 2000). For a detailed description, however, the use of such metalanguage to describe the results of quantitative theoretical models [has been suggested to do] more harm than good (Halatek and Frey, 2018) and this kind of pattern formation might be more appropriately described by mass-conserving reaction-diffusion equations (Mori et al., 2008; Semplice et al., 2012). For the scope of this thesis, I will limit myself to a phenomenological description of the cytoskeleton structure, i.e., simply use the known polarity of the actin cables and the cell cycle dependent 3D structure of the actin cytoskeleton. By way of example, electron microscopy (Mulholland et al., 1994) and an early, elegant example of digital fluorescence microscopy (Amberg, 1998) offer a detailed view of the architecture. Of particular interest for this work are the actin cables, which serve as routes for myosin-mediated intracellular transport. The cortical filaments are highly curved close to the bud neck, as they follow the contour of the cell from base to bud (figure 2).

1.4.2.2 *Actomyosin transport*

The description of active mRNA transport in yeast is rooted in research on HO-dependent mating type switching. After budding, it was observed that mother cells adopt a new mating type (a or α) whereas daughter cells maintain their current mating type (Amon, 1996; Herskowitz, 1988). Jansen et al., 1996 described five genes, *SHE1-5*, that are required to confine mating type switching to the mother. Interestingly, they reported two (and later, more) of the She proteins to be localized in growing buds. She1, which is the unconventional myosin Myo4p, has been shown to act as a transporter for the mRNA of HO repressor Asymmetric Synthesis of HO (ASH1), with She2-5p acting as mediators of the binding of myosin and its cargo (Du et al., 2008; Sil and Herskowitz, 1996). The core cytoplasmic complex of mASH1, the locasome, contains transport factors as well as translational repressors

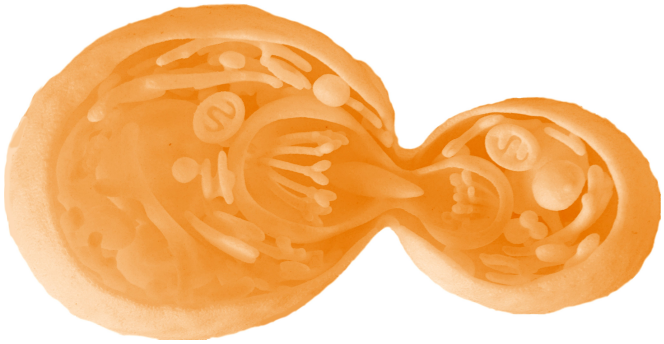

Figure 2: 3D printed yeast cell during mitosis. The constriction between the becoming mother and daughter cell, the bud neck, is of particular interest for the partitioning and transport of RNA, as it constitutes a 'narrow escape' (see section 4.3.1) and causes a kink in the actin filaments serving as 'cargo rails' connecting the poles of a cell. Image modified from Rosser1954 (license CC BY-SA 4.0) https://commons.wikimedia.org/wiki/File:A_budding_model_yeast_cell._Utrastructure_details._3D_printed.jpg, https://creativecommons.org/licenses/by-sa/4.0/deed.en

(Müller et al., 2011). The key features of this transport are reviewed in Heym and Niessing, 2012. Using a microarray-based screen, more than 30 further mRNA species were found to specifically bind She proteins, and to depend on these genes for bud-localization (Oeffinger et al., 2007; Shepard et al., 2003). X-ray crystallography revealed that She2p and She3p jointly bind to localization elements of the transported mRNA to tether it specifically to the Myo4p-containing transport complex once mRNA is in the cytoplasm (Edelmann et al., 2017). *Cis*-acting elements of transported mRNAs are mostly strucural, i.e., not directly related to the coding sequence, and as in *m*ASH1, *mCLB2* contains redundant localization motifs in the untranslated region (UTR) and coding sequences (Shepard et al., 2003). This suggests that molecular details of the transport process investigated for *m*ASH1 may be applicable to *mCLB2*. While *m*ASH1 bud localization entails enrichment of Ash1p in the bud, more than half of the protein species translated from bud-localized mRNA, including Clb2p, is symmetrically distributed between mother and daughter (Gonsalvez et al., 2005), posing the question why mRNA becomes localized in the first place. For *mCLB2* a role in gauging bud *synthetic capacity*, a kind of molecular rheostat, has been suggested to 'motivate' this localization (Kejiou and Palazzo, 2017; Spiesser et al., 2012 see section 1.2.2). Transport competent mRNPs start to form already in the nucleus (section 1.2.1), and are reported to dissociate once mRNA becomes anchored to the bud tip in a translation-dependent manner (Gonzalez et al., 1999; Takizawa et al., 1997). A number of variants of She-mediated RNA transport have been described. Lange et al., 2008 reported cotransport of MS2/λ boxB RNA tagged mRNA species (*IST2* and *ASH1*). Further it was suggested that inheritance of the endoplasmic reticulum is coupled to the transport of certain mRNA species during S/G_2, but not for transcripts later in the

cell cycle (Fundakowski et al., 2012). In this mechanism, of potential relevance for *mCLB2* which peaks in late G_2, mRNAs are hitchhiking on cortical ER tubules, similarly as reported in other organisms (Crofts et al., 2004; Deshler et al., 1997). The active transport mechanisms for *mCLB2* as outlined in this paragraph would not only suggest that this transcript is virtually exclusive to the bud; it would at the same time imply straight or curvilinear mRNP trajectories following the subcortical actin filaments. These directed bouts of transport could, of course, be interspersed with stalling phases or even retrograde transport, as is the case in axonal mRNA transport (Monnier et al., 2015; Park et al., 2014). This behavior is outside the reach of most experiments of mRNA motion in living cells. Although single molecule resolution is often achieved now, most microscopy methods lack optical depth to keep molecules in focus for longer periods or temporal resolution to reliably link detected particles over time (Fundakowski et al., 2012; Saroufim et al., 2015). This leads to another central question which I addressed with single molecule techniques outlined in the subsequent section: Is the observed dynamics of *mCLB2* compatible with the active partitioning mechanism suggested by microarray studies, i.e., *ASH1* type She-dependent actomyosin transport (Shepard et al., 2003)?

1.5 SINGLE PARTICLE TRACKING

Single particle tracking (SPT) is a photon-limited technique. To achieve long trajectories, avoid unnecessary light-stress and achieve a high signal to noise ratio (SNR), it is essential to choose an *appropriate fluorescent label*, *camera* and *microscope*. To motivate my choice of tools, the most prominent live-cell mRNA labeling technique (MS2 system) will be introduced and discussed in comparison to other methods. Further on, I will compare applicable camera types and discuss some aspects of the applied microscope build to complement this rationale.

1.5.1 MS2 live cell mRNA tagging system

The MS2 system, developed by the laboratories of Roy Long and Robert Singer (Bertrand et al., 1998) was the first of an array of systems to visualize mRNA in living cells. In the following years the boxB/λN peptide method (Lange et al., 2008) and the PP7 system (Chao et al., 2008) were published, offering alternatives to the MS2 system and facilitating the observation of more than one mRNA species in living cells. All of these methods rely on high-affinity interactions of a repetitive stem-loop structure inserted into the mRNA of interest with fluorescently labeled complementary protein that is derived from the coat of their eponymous virus. In the U1A method (Brodsky and Silver, 2002), an RNA-binding domain of the human U1 small nuclear

ribonucleoprotein A (U1A) binds specific RNA-hairpins (Allain et al., 1997; Zeng and Hall, 1997). Apart from these protein-aptamers, fluorogenic RNA aptamers that light up when binding their target RNA have gained increased attention. Besides the pioneering showcase of methods by the lab of Samie Jaffrey - Spinach (Paige et al., 2011), Broccoli (Filonov et al., 2014) and Corn (Warner et al., 2017) - that rely on the encapsulation of a hydroxybenzylidene imidazolone-derivative, also other small molecule fluorophores have been used to design RNA mimics of fluorescent proteins (Dolgosheina et al., 2014; Steinmetzger et al., 2019; Wirth et al., 2019). While these RNA aptamers are structurally diverse - as opposed to all fluorescent proteins except for mNeonGreen (Shaner et al., 2013) - most aptamers coordinate their small molecule fluorphore in G-quadruplexes (Warner et al., 2014). Recently, arrays of multiple Mango II RNA aptamers have been shown to achieve single RNA resolution in living cells (Cawte et al., 2020). Since RNA aptamers provide a background-free alternative to the viral coat protein based methods while offering similar brightness, I expect the former techniques to (partly) replace the latter. While the MS2 method in principle can take advantage of small molecule fluorophores, which can be much brighter and more photostable, for RNA visualization in living yeast cells fluorescent proteins are the norm (Hocine et al., 2013; Neurohr et al., 2018; Saroufim et al., 2015). This is mostly due to *S. cerevisiae*'s effective export mechanisms for xenobiotic molecules, namely the three ATP-binding cassette multidrug resistance (ABC-MDR) transporters PDR5, SNQ2, and YOR1 (Ball et al., 2016), and possibly further export proteins (Robert Singer, pers. comm.). While it has been reported that triple deletions of the ABC-MDR transporters can increase labeling with organic fluorophores (O^6-benzylguanine derivatives) four-fold (Chidley et al., 2011) these cells show a severe phenotype (Chidley et al., 2011; Kolaczkowski et al., 1998). At least one study, however, points at the possibility to perform SPT using electroporation on mutants with a single ABC-MDR gene deletion (Δ*pdr5*), which only show a mild phenotype, and yet improved the incorporation of HaloTag ligands by a factor of 20 (Ball et al., 2016).

It has been found that the MS2 system can hinder Xrn1-mediated mRNA decay in yeast, particularly when MS2 coat proteins (MCPs) are bound to the MS2-stem loop sequence (MSL) (Garcia and Parker, 2015, 2016; Tutucci et al., 2018). Previously, defects in MS2-tagged mRNA degradation had been found in *Escherichia coli* (Golding and Cox, 2004). Garcia and Parker, 2015 questioned on these grounds, whether the MS2 system should be used to quantify subcellular RNA localization. While this publication has been criticized for solely relying on northern blots that do not have the potential to address subcellular localization (Haimovich et al., 2016), further studies on possible MS2-related artefacts followed. A study by Heinrich et al., 2017 detailed artefacts caused by the MS2 system finding that local-

ization and metabolism of different mRNA species to be abnormal in MS2-tagged budding yeast strains. However, they found only minor defects in glucose-rich conditions, such as used in the current study. Contrary to the findings by the previously cited studies (Garcia and Parker, 2015, 2016; Tutucci et al., 2018), the defects were found irrespectively of the presence of MCPs. Later on, a detailed study on mammalian β-actin-mRNA metabolism concluded that the MS2 system does not disturb the degradation of MS2-tagged mRNA (Kim et al., 2019). One important factor contributing to these seemingly contradictory findings are differences in mRNA stability. In mammalian cells, transcriptome-wide mRNA half-life times ($t_{1/2}$) in the range of hours have been reported. For mouse embryonic stem cells $t_{1/2}$ = 7.1 h has been found (median, Sharova et al., 2009), whereas for mRNA in human cells $t_{1/2} \approx$ 10 h has been published (Yang et al., 2003). In these studies mRNA metabolism is heavily perturbed by polymerase inhibitor actinomycin D, though. As will be shown in the case of yeast, perturbation-free mRNA stability assays can lead to very different results. In contrast to the data for mammalian cells, transcriptome-wide $t_{1/2}$ of mRNA in yeast has been reported to be 20/23 minutes (mean/median) according to a temperature-shift induced transcription shut-off experiment (Wang et al., 2002). Using a 4-thio-uracil (4TU) metabolic labeling (Miller et al., 2011; Sun et al., 2012), the group of Karsten Weis reported similar values in a perturbation-free experiment (Munchel et al., 2011). A recent 4TU labeling experiment - involving the same group - refined the protocol of the previous publication to improve separation of labeled/unlabeled mRNA and found much shorter $t_{1/2}$ of 4.8/3.6 minutes (mean/median) (Chan et al., 2018). In agreement with the latter metabolic labeling study, investigating the stability of *CLB2* with smFISH data, revealed a $t_{1/2}$ of 3.7 minutes in asynchronous yeast cultures (Trcek et al., 2012). Binning cells by morphological markers into cell cycle phases revealed that during mitosis $t_{1/2}$(*CLB2*) was as low as 1.8 $\pm$ 0.5 min, while *CLB2* mRNA was virtually stable throughout the rest of the cell cycle. In response to the critique aimed at MS2-induced artefacts, a modified version of the MS2 system, exhibiting a decreased affinity between MCPs and MSLs has been published (Tutucci et al., 2018) and, importantly, independent controls, such as smFISH regained attention (Heinrich et al., 2017; Kim et al., 2019; Tutucci et al., 2018). However, even publications that do control for RNA-metabolism effects often fail to control for MS2-induced mislocalization effects. Several publications only observe the localization of the MS2-tagged mRNA, e.g., by smFISH, while omitting the localization of untagged mRNA (Haimovich et al., 2016; Hocine et al., 2013; Kraut-Cohen et al., 2013). While this is useful to check the labeling efficiency of MS2, possible interference with the mRNA life cycle will not be detected in this case.

1.5.2 Camera types for single particle tracking

For SPT, most labs use electron multiplying charge coupled device (EMCCD), charge coupled device (CCD) or scientific complementary metal-oxide-semiconductor (sCMOS) cameras. Camera-related noise, the variation of the measured signal given a constant and uniform illumination, is an important factor for low-light applications like SPT. All scientific cameras are affected by a number of noise sources; the most prominent ones being photon shot noise, thermal noise and read-out noise (Mandracchia et al., 2020; Vliet et al., 1998). The accuracy of single molecule localizations is thus limited by the sum of a Poisson, and Gaussian random variables (Ober et al., 2004), as discussed further down. Ober et al., 2004 provided fundamental limits for the localization accuracy of any object imaged by a lens, as defined by the standard deviation of particle locations estimated from repeated experiments, by recurring to the Fisher information matrix and its inverse, the Cramér-Rao lower bound (CRLB) (Kay, 1993; Rao, 1965; Zacks, 1971). Discretization effects due to the camera pixel size, as well as camera readout noise were also included to allow estimating experimentally achievable accuracy. For experimental conditions, i.e., camera pixel size, fluorophore optical efficiency, acquisition time, wavelength, magnification and photon noise similar to those found in my project, they estimated limits in the range of 10 nm (see also chapter 4). Photon shot noise simply passes the statistical distribution of incoming photons, the Poisson distribution, on to the generation of photoelectrons and is thus a fundamental lower limit for the noise level. Gaussian noise comes from the camera readout process (Janesick, 2001) and thermal noise. The latter can be effectively lowered by cooling (Vliet et al., 1998), which is why modern cameras operate at -40°C to -80°C, some CCD cameras at -100°C. The above camera types rely on the accumulation of charge (photoelectrons) in each pixel that is proportional to the amount of impinging photons. Whereas in sCMOS cameras each pixel consists of an integrated silicon circuit that converts this charge to a voltage-signal, the charge-voltage conversion of the signal takes place outside the camera chip in CCDs. The transfer and external conversion of the signal in CCDs is key to both the slower acquisition speeds and the outstanding sensitivity required for low-light applications (Brouk et al., 2010; Hain et al., 2007; Mandracchia et al., 2020). The serial processing of the signal in EMCCDs is slower than the parallel processing in sCMOS cameras. This design also allows for the distinctive on-chip-multiplication of photoelectrons in EMCCDs, caused by stochastic impact ionization events in the multiplication register that amplifies the signal above the read-noise, at the cost of causing amplification noise (*Andor*). In sCMOS, however, the non-uniform photo-response of different pixels is exacerbated by differences in the downstream-processing units, which also differ slightly between pixels (Mandracchia et al., 2020). It is noteworthy that camera technol-

ogy is developing quickly and that the isolated consideration of their specifications can be misleading. By way of example, the preference for EMCCD cameras for SPT is commonly attributed to their superior quantum efficiency (QE) of up to 95% (i.e., how efficiently photons are converted to photoelectrons) compared to sCMOS (e.g. Diezmann et al., 2017). Camera manufacturers, however, warn against this notion since the amplification noise in EMCCD effectively halves the QE (*Andor*), which shifts the balance in favor of sCMOS as these recently also achieved a QE of 95% (e.g. cameras from Andor or Teledyne Photometrics). To understand the tradeoff between speed and different components of camera-related noise in detail, the reader is referred to reviews (Diezmann et al., 2017; Hain et al., 2007; Joubert and Sharma, 2011) and comparative studies by camera manufacturers (*Andor*; Fullerton et al., 2012). In effect, for this study a back-illuminated EMCCD has been chosen since the low-light sensitivity outweighed the slower acquistion speed; although CCD cameras have been expected to be supplanted by CMOS technology for decades (Fossum, 1993), which finally might happen with recent advances in sCMOS production and image enhancement software (Diezmann et al., 2017; Mandracchia et al., 2020).

1.5.3 Microscopes for tracking single cytoplasmic molecules

Observing dynamics of single, freely moving intracellular molecules, like proteins or mRNA, poses a challenge for microscopy. To achieve high resolution and SNR along with sufficient speed of acquisition to avoid motion blur and the linking of objects from one frame to the next, total internal reflection fluorescence (TIRF) microscopy is a common choice for single particle tracking in living cells (Anderluh et al., 2014; Elf and Barkefors, 2018; Schnyder et al., 2011). However, the evanescent field in TIRF only allows imaging processes at a distance up to $\sim$ 200 nanometers from the cover slip; which limits its use largely to membrane associated molecules - particularly in yeast cells, which possess a cell wall that has been reported to be between 70 nm (Srinorakutara, 1998) and 115 nm (Dupres et al., 2010) thick in cells grown on glucose. This limitation is alleviated in highly inclined and laminated optical sheet (HILO) microscopy (Tokunaga et al., 2008), at the cost of SNR that lies between TIRF microscopy and conventional widefield fluorescence microscopy. This technique relies on an illumination angle that is lower than in TIRF but not parallel to the optical axis as in widefield microscopy to minimize the illumination area and thereby enhancing SNR. It is thus also known as 'dirty TIRF'. Another method for single molecule tracking in living cells that offers particularly high axial resolution is spinning disk confocal microscopy (SDCM). Applications that are of particular interest for this work are the tracking of intranuclear *mCLB2* (Saroufim et al., 2015) and

the simultaneous imaging of single mRNA and the encoded nascent protein (i.e., the visualization of single translation events in living cells, Yan et al., 2016). However, the limited focal depth of SDCM leads to another challenge: If the molecules of interest are not confined to the focal plane as in the two previous examples (the nuclear envelope in Saroufim et al., 2015, a membrane-anchor in Yan et al., 2016) their observation is limited to very short trajectories, as they would simply move away from the focal plane. Similarly to SDCM, light sheet microscopy (Huisken et al., 2004; Keller and Ahrens, 2015; Siedentopf and Zsigmondy, 1903) offers a chance to excite fluorescence in a more restricted axial range, which improves axial resolution. As a narrow sheet of excitation light is coupled into the sample perpendicularly to the detection objective, pinholes that prevent light from out-of-focus planes, but also limit the light efficiency in confocal microscopes, are not required. Light sheet microscopes are therefore an excellent choice, particularly where phototoxicity- and bleaching is limiting, e.g., for developmental biology (reviewed in Wan et al., 2019), where this technique allows imaging of entire embryos at single cell resolution over extended time periods. Most light sheets are, however, simply too thick or too short to benefit single molecule studies μm (Planchon et al., 2011): Assuming the light sheet has a Gaussian intensity distribution, there is a tradeoff between the achievable minimum thickness and the length over which it is approximately uniform, the so called Rayleigh range. In the last decade, a range of light sheet varieties have emerged that pushed this limit. One method that further confines the region where fluorescence is excited, is multiphoton microscopy (Denk et al., 1990), which has been used for light sheet microscopy (Maioli et al., 2020; Truong et al., 2011). Dual-view setups, where two orthogonal excitation light paths are used alternatingly to improve axial resolution have also been presented (Wu et al., 2013). The method I chose for my project is part of a family of methods where the Gaussian intensity profile is replaced by carefully engineered intensity profiles, e.g., Bessel beams (Fahrbach et al., 2010; Gao et al., 2014; Planchon et al., 2011) or Airy beams (Hosny et al., 2020; Vettenburg et al., 2014). The setup I used is based on a lattice light sheet, consisting of an array of parallel, interfering Bessel beams (Chen et al., 2014). In LLSM, an individual light sheet is only about twice as thick (< 600 nm) as the optical depth of the objective (NA 1.1, equation (7)). This makes optical sectioning of yeast cells worthwile, as such a light sheet is - at a high Rayleigh range - much thinner than a yeast cell. This was instrumental for my time lapse imaging throughout the yeast cell cycle, as it limits phtotoxicity. While I did also attempt mRNP tracking with the LLSM, as image acquistion is fast at up to 300 frames per second (fps), volumetric imaging is still sequential and accordingly slows down imaging. The simplest form of fluorescence microscopy, widefield epi-illumination microscopy, is commonly applied for live cell SPT. Like in light sheet

microscopy, there are no elements in the optical path that hamper the light efficiency, such as the pin holes in confocal microscopes. There are a number of publications that rely on widefield microscopy for SPT, including single molecule translation experiments (Pichon et al., 2016; Wang et al., 2016; Wu et al., 2016). This common imaging modality excites fluorescence in a volume ranging from 1 to 100 μm in diameter and the excited fluorescence is detected by a camera (or the eye of an observer), obviating the need to scan that slows down confocal methods. For single mRNA detection in live cells, high numerical aperture (NA) objectives are commonly used, which achieve a high lateral and axial resolution. The resolution can be described by $0.61 \cdot \lambda / NA$ and λ / NA^2 in the lateral and axial direction, respectively, which explains why high NA are preferred for single molecule detection. For the investigation of processes including movement along the optical axis of the microscope, there is, however, a tradeoff, since the NA is inversely proportional to the optical depth (also called depth of field) of the microscope. This property describes the axial distance range from the objective within which an object appears sharp. A common formula for the calculation contains a superposition of a wave optic and a geometrical component according to [2]

$$d_{tot} = \frac{\lambda \cdot n}{NA^2} + \frac{n}{M \cdot NA} e \tag{7}$$

where d_{tot} denotes the optical depth in μm, λ the wavelength of the excitation light source in μm , n the refractive index of the immersion oil (usually 1.515), M the (lateral) magnification of the applied objective and e the smallest resolvable distance of a microscope detector in μm. For green light (λ = 0.55 μm) and using a high (1.4) or intermediate (1.25) NA 100x objective the total optical depth is in the range of 0.5-0.8 μm. There is some controversy around formulas suited for the determination of optical depth in high NA, diffraction limited microscopy and other formulas have been suggested. Young et al., 1993 suggested a different formula that yields an even lower estimate for the optical depth attainable with a given setup [3]:

$$d_{tot} = 2 \cdot \frac{\lambda}{4 \cdot n \cdot (1 - (\sqrt{1 - (\frac{NA}{n})^2}))} \tag{8}$$

2 formula taken from Nikon's dedicated website *Depth of Field and Depth of Focus*

3 To compare these formulas I added a factor 2 to this and the subsequent formula, as the authors treat the maximum distance from the theoretical focal plane that appears in focus, while I use the total optical depth extending symmFetrically from the nominal focal plane.

Here, the optical depth would lie between 0.3 and 0.4 μm given identical parameters as before for NA = 1.4 and 1.25, respectively. A further formula by Born and Wolf, 1999

$$d_{tot} = 2 \cdot \frac{\lambda}{2 \cdot NA^2} \tag{9}$$

yields optical depths of 0.3 and 0.36 μm, respectively. Importantly for this discussion, these values constitute an upper boundary for widefield and all confocal microscopy techniques. Investigating the 3D motion of cytoplasmic mRNA with standard widefield microscopy invariably leads to an underestimation of its movement. Contrasting widefield and 3D microscopy, it has been shown that RNA moving in the axial direction by up to 1.5 μm might be classified as stationary by widefield microscopy (Thompson et al., 2010). Therefore, I will outline strategies to overcome this 'partial blindness'.

1.5.3.1 *Entering the third dimension*

To reconstruct larger three-dimensional volumes, the sequential acquisition of a series of focal planes, widely used in widefield, confocal and light sheet / selective plane illumination microscopy (SPIM), could be used. However, this inevitably leads to a decrease in maximum frame rate (by a factor of $\approx$ number of planes), which renders the linking of freely moving particles from one frame to the next in a crowded intracellular environment virtually impossible (Moerner, 2007). The motion of the tracked particles can furthermore lead to some being counted multiple times in different focal planes, while others might not be detected at all. Since I am analyzing the cytoplasmic motion of freely moving mRNPs I turned to advanced imaging techniques allowing the instantaneous observation of multiple focal planes, i.e., an increased effective optical depth. This allows the extraction of long trajectories that could improve our understanding of spatiotemporal dynamics of cytoplasmic mRNA which so far is mostly shaped by the analysis of short trajectories (Elf and Barkefors, 2018; Persson et al., 2013). Over the last decades, three main families of methods have emerged that transcend (i) the limited optical depth of widefield microscopes; (ii) the weaknesses of sequential imaging of focal planes and (iii) the poor axial resolution of most optical microscopes, ideally all at a time. These methods rely either on the *simultaneous* acquisition of several focal planes; a 'tailored' point spread function (PSF) that encodes the axial position of an emitter in the 2D shape of the signal detected on a single camera, or lastly on methods that are sensitive to the relative position of the emitter to fixed optical components in the light path. I will discuss the two families of methods I deem most accessible [4] for the study of cytoplasmic RNPs below; a timely review

4 While some methods of the last family are simply limited to axial localization close to surfaces (few 100 nm), others, e.g, interferometric methods that use light-phase,

of available methods can be found in Diezmann et al., 2017.

Multifocus methods

The simplest implementation of a microscope capable of simultaneous acquisition of more than one focal plane has been developed in the lab of W. E. Moerner. This instrument, termed multifocal plane microscopy (MUM), relies on precise alignment of 2 detectors that are focused on different planes of the same sample (Prabhat et al., 2004, 2007; Ram et al., 2008). The authors applied epifluorescence and TIRF microscopy simultaneously, which lead to an ≈ 1 μm optical depth within which the axial position of the emitter could be determined with high precision, allowing the extraction of trajectories that contain information of complex 3D dynamics of intracellular molecules. Ram et al., 2012 extended this method to a total of 4 focal planes, i.e., 4 cameras placed at different positions along the tube lens of a microscope, to track the motion of quantum dot tagged single proteins in a 10 μm thick volume. It appears to me that one bottleneck of these techniques consists in the application of 50:50 beamsplitters in the emission light path before and between each detector. This leads to an exponential decay of the light intensity in additional focal planes, requiring a doubling of the excitation light intensity for each additional plane, leading to increased phototoxicity and bleaching of the fluorophore. A further complication of this method, as noted by Abrahamsson et al., 2013, is that spherical aberrations hamper resolution and contrasts if the camera is not in the focal plane. A setup avoiding optical aberrations and circumventing the need for multiple cameras, aberration corrected multifocus microcscopy (acMFM) (Abrahamsson et al., 2013, 2016), is the method I chose for analysis of RNP movement in the yeast cytoplasm. This technique, which I describe in more detail in section 2.2.2, provides an instantaneous stack of nine focal planes on a single camera and primarily relies on a diffractive multifocus grating (MFG) generating focus shifted images (the additional focus planes) and two further optical elements that revert chromatic dispersion introduced by the MFG and distribute the focal planes on the camera chip. Conceptually, the MFG plays a similar role to the phase modulators in PSF engineering methods discussed below. An important difference is, however, that a point shaped emitter produces a diffraction limited spot PSF in 2D in acMFM, whereas PSF engineering methods result in a more complex 2D PSF. When more than one fluorescent particle is present,

rather than -intensity are amenable to the analysis of the cytoplasm. So far these methods, such as iPALM (Shtengel et al., 2009), 4Pi microscopes (Middendorff et al., 2008; Wang et al., 2020) have been mostly angled at super-resolution microscopy and I am not aware of SPT optimized setups. This might in part be due to the more complex setups and need for nanometric alignment for interferometic methods, while PSF engineering and aberration corrected multifocus microcscopy (acMFM) build on conventional widefield microscopes.

the latter techniques can suffer from overlapping PSFs. In acMFM, the lateral field of view is in turn drastically reduced, since the 3x3 array of focal planes is detected on a single camera. On the flipside, for a given SNR, acMFM leads to $\sim$ 10x higher bleaching than single-plane epifluorescence microscopy (Chen et al., 2014). As the acquisition of simultaneous focal planes relies on diffraction, reconstruction of the total volume poses additional challenges: Axial spacing, as well as the lateral deviation of different wavelengths necessitate careful image registration (Smith et al., 2015), and the use of MFGs tailored to specific wavelengths. The setup employed in this work covered a wavelength-dependent optical depth of $\sim$ 4-5 μm by 9 evenly spaced focal planes. Since this is the approximate size of haploid yeast cells, I did not aim for higher focal depth. In principle, acMFM can accommodate more focal planes, thus increasing optical depth. A setup utilizing 25 focal planes (a 5x5 array), in conjunction with polarization microscopy has been built (Abrahamsson et al., 2015). However, this setup further limits the lateral field of view and requires higher excitation light intensity, which is already limiting - particularly when using fluorescent proteins, which are less photostable and less bright than small molecule fluorophores.

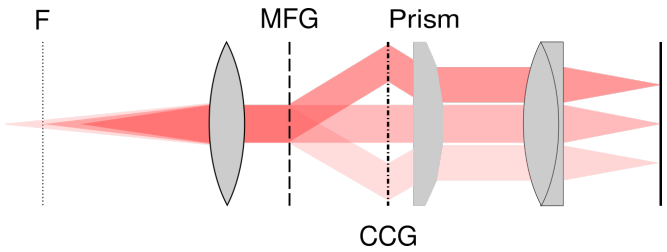

Figure 3: Main optical components and light beams for acMFM. After passing through the primary focus of the microscope (F), light is diffracted and phase shifted at the multifocus grating (MFG). Light from above and below the nominal focal plane is split into 8 first order diffraction beams ($\pm$ 1,1 in x,y; only 2 additional focal planes (encoded by different colors) are shown for simplicity. The chromatic correction grating (CCG) and a prism revert chromatic shifts introduced by the MFG and direct the beams to their respective positions on the camera chip.

PSF engineering methods

The second family of 3D microscopy approaches I want to discuss is PSF engineering. In a straightforward application, a weakly cylindrical lens in the back focal plane introduces astigmatism and encodes the axial position of an emitter in the eccentricity of the 2D PSF (Holtzer et al., 2007; Huang et al., 2008; Kao and Verkman, 1994). This elegant technique exploits that images of a diffraction limited emitter appear

circular when in focus, while their shape changes to an ellipsoid at positions above and below the focal plane. While this technique can even detect whether an emitter is above or below the focal plane - as the orientation of the ellipsoid is different in these cases - it is limited to an optical depth of $\sim 1\mu$m. A whole zoo of methods applying tailored PSFs for increased focal depth and axial resolution has since been devised, including phase-ramp (Baddeley et al., 2011), self-bending (Jia et al., 2013, 2014), double-helix (Casolari et al., 2012; Pavani et al., 2009; Thompson et al., 2010), corkscrew (Lew et al., 2011), and saddle-point PSFs (Shechtman et al., 2014, 2015). They allow simultaneous imaging of optical dephts of up to 3 μm; in the case of saddle-point (or tetrapod) PSFs up to 20 μm and encode axial position in the shape of the 2D PSF on the camera chip (Diezmann et al., 2017; Moerner et al., 2015). For these methods, a phase modulator is placed in the Fourier plane of a microscope to multiply the Fourier transform of an emitter with a transfer function specific for the tailored PSF (Pavani and Piestun, 2008; Pavani et al., 2009). An important tradeoff for PSF engineering methods is the 'footprint' of the 2D structure pertaining to a single imaged particle on the microscope's camera. The tailored PSF with the highest optical depth (20 μm tetrapod) encodes axial position by a complex pattern of up to 8 lobes per imaged particle (Shechtman et al., 2015), limiting its application to sparsely distributed fluorescent particles. A further consideration is the theoretical axial precision that can be achieved with a given PSF as defined by the CRLB[5] tends to be lower for PSFs with higher optical depth (Diezmann et al., 2017). The latter point is, however, not a strict rule, and the double helix point spread function (DH-PSF) has both higher axial resolution (in the range both methods are applicable) and optical depth compared to astigmatism microscopy (Badieirostami et al., 2010). To exemplify some of the aspects of PSF engineering methods, I chose DH-PSF microscopy since (i) it offers high axial resolution and optical depth at a reasonable camera-footprint and (ii) it has been used to investigate cytoplasmic mRNPs diffusion (see section 1.4.1 Lampo et al., 2017; Thompson et al., 2010) and transport (Casolari et al., 2012) in yeast. For this technique, the PSF has been tailored to consist (in 2D) of two lobes symmetrically rotating around a central axis as a function of the axial position of the emitter. A spatial light modulator consisting of a reflective liquid crystal that only affects phase (not amplitude) of the reflected light is loaded with a phase mask resulting in the characteristic rotating intensity distribution (Pavani and Piestun, 2008; Piestun et al., 2000). This setup has proven capable of resolving two photoactivatable emitters that are only $\sim$ 20 nm apart in any direction (Pavani et al., 2009). However, for live

5 More precisely, the CRLB is the inverse of Fisher information and denotes the lower bound of the variance an unbiased estimator can achieve (Kay, 1993). For microscopy it serves, e.g., as a benchmark for localization precision.

cell applications there are some limitations, both regarding efficient use of the photon-budget and overlapping PSF-lobes when more than 1 tagged molecule is observed. More than 3/4 of the emitted light is lost, compared to a widefield fluorescence microscope, as emitted light is reflected from the spatial light modulator (Pavani et al., 2009), while the main bottleneck for light-efficiency in acMFM - the multifocus grating (MFG) - has been optimized to lose only 14% of the diffracted light (Abrahamsson et al., 2016). The race for light efficiency in 3D techniques for *in vivo* SPT might be more even between these techniques now, as more recently the reflective phase modulators were replaced by transmissive dielectric phase masks with purportedly superior light efficiency (Gustavsson et al., 2018). As for overlapping PSFs, which is undeniably more of an issue for DH-PSF microscopy than techniques with widefield PSF due to the higher camera-footprint, an effect seems to be that published SPT experiments focus on molecules present in very low numbers per cell. While Thompson et al., 2010 and Casolari et al., 2012 report 0-3 molecules of interest per cell, (Lampo et al., 2017) focused mainly on cells with a single molecule per cell.

1.6 AIMS

I wanted to use single molecule live cell techniques to study spatial aspects of post-transcriptional regulation on different time scales. On the sub-second to second time scale my aim was to characterize the motion of cytoplasmic *mCLB2*. In particular: Is the observed dynamics of *mCLB2* compatible with the active partitioning mechanism suggested by microarray studies, i.e., *ASH1* type She-dependent actomyosin transport (Shepard et al., 2003) and live cell imaging for other localized mRNA species in yeast (Bertrand et al., 1998; Fundakowski et al., 2012; Thompson et al., 2010)? To this end, I observed single cytoplasmic mRNA using acMFM and contrasted the dynamics of *mSIC1*, which is not expected to be actively transported with *mCLB2*, for which a transport mechanism is assumed to be known. I tested if acMFM, differently from the methods used so far, can reliably track single mRNA in yeast cytoplasm in presence of many virtually undistinguishable tagged molecules. On time scales of minutes to hours, I investigated the localization of *mCLB2* throughout the cell cycle. By LLSM I addressed the question whether the localization of *mCLB2* in living cells is related to cell cycle progression. Specifically: Is bud localization of *mCLB2* reproducibly observed in premitotic yeast cells? Can live cell single molecule methods corroborate the localization observed in fixed cells (Trcek et al., 2011) and in live cell experiments lacking single molecule resolution (Shepard et al., 2003)?

2 MATERIAL AND METHODS

2.1 MATERIAL

2.1.1 Yeast strains

For all experiments haploid strains of the eukaryotic model organism budding yeast (*Saccharomyces cerevisiae*) were used. The strains used in this project are derived from the common laboratory strain BY4741, which is isogenic to the reference strain S288C (Winston et al., 1995). As the genome of BY4741 has been largely stripped of homologies to common marker genes it retains vectors more readily than other strains (Baker Brachmann et al., 1998).

2.1.2 Strains for live cell imaging

For live cell imaging, strains with MS2-labeled *CLB2* or *SIC1* mRNA (24 MS2 binding site (MBS)) and fluorescent fusion proteins marking nuclei and bud necks as cell cycle markers (*CLB2*-tagged cells only). For both species of mRNA (*CLB2* or *SIC1*) fluorescently tagged MCPs expressed from the genomic HO-locus was used. The fluorescent tags consisted of either 4xmGFP or 2xmNeonGreen (Shaner et al., 2013). All strains are listed in table 1. The first strain in the list carries all genetic modifications of the strain used for *mCLB2* live cell imaging except for MBS and has been used as control.

2.1.3 Single molecule fluorescence *in situ* hybridization (smFISH)

Genetically similar strains were used for smFISH and live cell imaging of *mCLB2*, to allow for comparison of mRNA localization table 2. To reduce the risk of spectral overlap, fluorescent cell cycle markers were omitted.

2.1.4 Reagents, buffers and media

Suppliers
Standard chemicals were purchased from Merck KgaA (Darmstadt, Germany), including their subsidiary Sigma-Aldrich (St. Louis, USA, now MilliporeSigma), Thermo Fisher Scientific (Waltham, USA) or Carl Roth GmbH & Co. KG (Karlsruhe, Germany). All other reagents and biomolecules are listed in table 5. Corporate details: BD is Becton, Dickinson and Company, Franklin Lakes, USA; NEB is New Eng-

Table 1: Yeast strains for live cell imaging: All strains were derived from BY4741. Primers for the construction of previously unpublished strains are listed in table 4. 'MCPΔ_{68-80}' is a version of MCP where amino acids 68 - 80 were deleted for improved solubility. All strains were designed for this project.

STRAIN	GENOTYPE
Bud neck + nucleus + MCP	MATa his3Δ1 leu2Δ0 met15Δ0 ura3Δ0 (Hhf2-mTurqoise::loxP) (Cdc10-TagRFP::loxP) HOΔ0::pMet-MCPΔ_{68-80}-2xmNeonGreen
CLB2-MS2 + bud neck + nucleus	MATa his3Δ1 leu2Δ0 met15Δ0 ura3Δ0 (Hhf2-mTurqoise::loxP) (Cdc10-TagRFP::loxP) (Clb2::Clb2-24xMBS-loxP)
CLB2-MS2 + bud neck + nucleus + MCP	MATa his3Δ1 leu2Δ0 met15Δ0 ura3Δ0 (Hhf2-mTurqoise::loxP) (Cdc10-TagRFP::loxP) (Clb2::Clb2-24xMBS-loxP) HOΔ0::pMet-MCPΔ_{68-80}-2xmNeonGreen
SIC1-MS2 + MCP	MATa his3Δ1 leu2Δ0 met15Δ0 ura3Δ0(Spc42-mTurquoise::loxP)(Sic1::Sic1-24xMBS-loxP) HOΔ0::pMet-MCPΔ_{68-80}-2xmNeonGreen

Table 2: Yeast strains for smFISH: All strains were derived from BY4741. The strain 'CC markers' was constructed for (Amoussouvi et al., 2018). The strain clb2Δ is part of the Saccharomyces Genome Deletion Collection at Stanford University.

STRAIN	GENOTYPE
CLB2-MS2 + MCP	MATa his3Δ1 leu2Δ0 met15Δ0 (Spc42::Spc42-mTurquoise KanMX4) Clb2 3'UTR::24xMBS HOΔ0::pMet-MCPΔ_{68-80}-2xmNeon
CC markers	MATa his3Δ1 leu2Δ0 met15Δ0 (Whi5-Tag GFP::loxP) (Spc42::Spc42-mTurquoise KanMX4))
clb2Δ	MATa his3Δ1 leu2Δ0 met15Δ0 ura3Δ0 (clb2Δ::KanMX4)

Table 3: Yeast strains for western blots: One strain is based on a strain used for live cell imaging of *CLB2*; the other one possesses the same genetic background but lacks the MS2 system. Both were tagged with 3xFLAG-tags on the amino terminus of Clb2.

STRAIN	GENOTYPE
3x FLAGTag-Clb2, *CLB2*-MS2 + bud neck + nucleus	MATa his3Δ1 leu2Δ0 met15Δ0 ura3Δ0 (Hhf2-mTurqoise::loxP) (Cdc10-TagRFP::loxP) (Clb2::Clb2-24xMBS-loxP) HOΔ0::pMet-MCPΔ_{68-80}-2xmNeonGreen (CrispR 3xFLAG-Clb2 n term)
3x FLAGTag-Clb2 + bud neck + nucleus	MATa his3Δ1 leu2Δ0 met15Δ0 ura3Δ0 (Hhf2-mTurqoise::loxP) (Cdc10-TagRFP::loxP)(CrispR 3xFLAG-Clb2 - term)

land Biolabs, Ipswich, USA; Biosearch are Biosearch Technologies in Middlesex, UK, OMS is Omni Lifescience, Bremen, Germany and EMS is Electron Microscopy Sciences in Hatfield, USA.

2.1.4.1 *Growth media*

Cells were cultured in synthetic defined (SD) or yeast extract peptone dextrose (YPD) media.
Composition of SD medium: 0,17 % (w/v) yeast nitrogen base, 5‰(w/v) ammonium sulfate, 2% (w/v) D-glucose and amino acid and nucleobases (see table 7) in ddH_2O, pH 7. For plates, 20 g/L agar were added to the liquid medium after autoclaving. Once the medium cooled down to 60°C the pH was adjusted with NaOH to 6.5-7.5 D-glucose and amino acids are added.
Composition of YPD medium: 1% (w/v) yeast extract, 2% (w/v) peptone, 2% (w/v) D-glucose in ddH_2O, pH 7. For plates, 20 g/L agar were added to the liquid medium before autoclaving; once the medium cooled down to 60°C, the pH was adjusted with NaOH to 6.5-7.5 and D-glucose was added.

2.1.5 Equipment

The setup of the precommercial microscopes used in this work is described in detail below. Further equipment is listed in table 9.

Aberration corrected multifocus microscope (acMFM) at the Advanced Imaging Center, Janelia Research Campus, Ashburn, USA (called Janelia from now on). The setup is based on the description in Abrahams-

Table 4: Primers used for construction of yeast strains and plasmids.

N°	NAME	SEQUENCE (5′-3′)
1	fw_Clb2_SalI	GTCGACGATATCTAGAAGATTTATGAAAGC TTCTATAATTTCCGTCCAATGGGCTT-TAAAGG
2	rev_Clb2_SalI	GTCGACTCATTCATGCAAGGTCATTATATC ATAGCCGTTTTTTCTAACCTTTAAAGCC-CAT TG
3	fw_Clb2_SacII	CCGCGGGAAGAGGGGCAGATGCTTAAAATA TCTAAAACGATAATCG
4	rev_Clb2_SacII	CCGCGGCGCCATACATTTTATATGGACATT TATCGATTATCGTTTTAG
5	Clb2_DetF	GAGATATCATTGGTAGATTTC
6	Clb2_DetR	CAGCCATACATTTTATATGGAC
7	BspEI_HO-fw-linker	CCGGATACGTATGCTTTCTGAAAACACGAC TATTCTGATGGCTAACGGTGAAT
8	BspEI_HO-rev-linker	CCGGATTCACCGTTAGCCATCAGAATAGTC GTGTTTTCAGAAAGCATACGTAT
9	EagI_HO-fw-linker	GGCCGCCTCATAAGAGTTGTGGTAACAACG CAGGTGCGCGCATCTGCTACGTAC
10	EagI_HO-rev-linker	GGCCGTACGTAGCAGATGCGCGCACCTGCG TTGTTACCACAACTCTTATGAGGC
11	fw_Clb2_N-term_3xFLAG	cagtACTTGCTATTTCCTTCCAAGAAGCC TTTTATTGATTACCCC-CTCTCTCTCTTCATTGATCTTATA-GATGGGAGACTAC
12	rev_Clb2_N-term_3xFLAG	cagtACTAGTATTCTGTGAGTTTTCTGTGT TTTCTATTGGGTTACTCATTCCTG-CACCAGCTTTAT CGTCGTC
13	fw_Clb2_N-term_ctr	AAAGCTGGTGCAGGAATG
14	rev_Clb2_N-term_ctr	CGCTGAGGAGGATTCTTG
15	fw_TagRFP_PstI	CGCTGCAGGAATGGTGTCTAAG
16	rev_TagRFP_PstI	GACCTGCAGTTAATTAAGTTTGTG
17	fw_Cdc10_Kate2_integ	GCGAATAGTCGTTCCTCAGCTCATATGTCT AGCAACGCCATTCAACGTGCTTCG-TACGCTGCAGGAA TG
18	rev_Cdc10_Kate2_integ	GAGAATTCTTAATAACATAAGATATATAAT CACCACCATTCTTATGAGATGCATAGGC-CACTAGTGG ATCTG
19	fw_TagBFP2/mTurq_PstI	GCTGCAGGAGGAGCAGGTGCTG
20	rev_TagBFP2_PstI	GACCTGCAGTTAATTAAGCTTG
21	fw_Hhf2_GAG_integ	GTTTATGCTTTGAAGAGACAAGGTAGAACC TTATATGGTTTCGGTGGTGCTTCGTACGCT-GCAGGA GGAGCAGGTGCTGGTGCTGGTG
22	rev_HHF2_integ	GGCATGAAAATAATTTCAAACACCGATTGT TTAACCACCGATTGTCATAGGCCAC-TAGTGGATCTG

Table 5: List of chemicals and reagents purchased for this work. As lyticase concentrations are critical, for each batch the enzyme content was measured. Complete company details in section 2.1.4.

ITEM	PROD.	SOURCE
β-mercaptoethanol	M6250	Sigma-Aldrich
Bovine serum albumin (BSA)	A9418	Sigma-Aldrich
CasyTon	5651808	OLS
Dextran sulfate (MW= 10000u)	D4911	Sigma-Aldrich
Concanavalin A	234567	Sigma-Aldrich
FISH probes (Stellaris)	custom	Biosearch
Formaldehyde (32% (w/v)	15680	EMS
Formamide (Deinoized, 99%)	10052370	Thermo Fisher
Lyticase	L5263	Sigma-Aldrich
Peptone (Bacto™)	211677	BD
Vanadyl ribonucleoside complexes (VRC)	S1402S	NEB
Salmon sperm, sheared	10249194	Thermo Fisher
SSC 20x, RNAse free	AM9770	Thermo Fisher
TE buffer	12090015	Thermo Fisher
Triton X-100	HFH10	Thermo Fisher
Yeast nitrogen base (Invitrogen)	Q30007	Thermo Fisher
Yeast extract (Bacto™)	211677	Thermo Fisher

Table 6: Most buffers were prepared and stored for up to 6 months at 4°C, hybridization buffer at -20°C; spheroplasting buffer and hybridization washing solutions were prepared directly before the experiments.

BUFFER	COMPOSITION
Buffer B	1.2 M sorbitol,100 mM potassium phosphate in distilled, deionized water (ddH_2O), pH = 7.5
Hybridization buffer	10% formamide, 5 mM sodium phosphate pH 7,5, 2x SSC, 0.02% BSA, 10 mM VRC, 1 mg/ml DNA competitor mix (1:1 *E. coli* tRNA : salmon sperm DNA, sheared), 0.1 g/ml dextran sulfate
Hybridization washing solution	10% formamide, 1x SSC, ddH_2O
Lyticase storage buffer	100 mM potassium phosphate, pH 7,5, 100 mM NaCl, 50% glycerol in ddH_2O
Spheroplasting buffer	Buffer B, 0.2 % β-mercaptoethanol, 4 mM vanadyl ribonucleoside complexes (VRC), 100 u/mL lyticase
Protein extraction buffer	100 mM Tris-HCl pH 6.8, 20% (w/v) Glycerol, 1.5 M DTT, 10% (w/v) SDS, 10 mMNaF, 100 µM Na_3VO_4, protease inhibtor, 0.14% (w/v) β-mercaptoethanol
TBST for western blotting	1X Tris-buffered saline, 0.1% Tween® 20 detergent

Table 7: Amino acids for SD medium. One or two of the italicized items were omitted when selective media (SD-His, SD-Ura or SD-Leu) were required for the retention of plasmids. Amino acids and D-glucose added after autoclaving.

AMINO ACID OR NUCLEOBASE	CONCENTRATION [‰(W/V)]
L-Arginine	2
L-Aspartic acid	2
L-Lysine	4
L-Phenylalanine	6
L- Threonine	5
L-Tyrosine	5.5
L-isoleucine	6
Adenine sulfate	5.5
L-Histidine	1
L-Leucine	6
L-Methionine	1
L-Tryptophan	4
Uracil	5.5

Table 8: Antibodies used for western blots. Primary antibodies were purchased from Sigma-Aldrich, secondary antibodies from LI-COR Biosciences (Lincoln, USA).

ANTIBODY	PROD.
Monoclonal ANTI-FLAG® M2 antibody (mouse)	F3165
Anti-Glucose-6-Phosphate Dehydrogenase (G-6-PDH)	A9521
IRDye 680RD Donkey anti-Mouse IgG Sec. Antibody	925-68072
IRDye 800CW Goat anti-Rabbit IgG Sec. Antibody	925-32211

son et al., 2013. Several specifications were altered from the original publication:

- Microscope frame: Eclipse Ti Inverted Microscope, Nikon (Chiyoda, Tokyo, Japan)
- Cameras: iXon3-DU897E X-8977 EM-CCD camera, 512x512 px, pixel size 16x16 μm, QE $\sim$ 95 % at 500 nm, Andor Technology (Belfast, UK)
- Objective Plan Apo λ 100x Oil NA 1.45, Working distance 0.13 mm, cover glass thickness 0.17, Nikon (Chiyoda, Tokyo, Japan)
- Excitation lasers:
  - 405 nm, Stradus 405-100, Vortran (Sacramento, USA)
  - 488 nm, 488 Sapphire, Coherent (Santa Clara, USA)
  - 561 nm, MPB Lasertech (Edmonton, Canada)
- Dichroic mirror: Di01-R405/488/561/635 (Semrock, IDEX Corporation, Lake Forest, USA)
- High Efficiency Multifocal Gratings (3x3), Custom design
  - Design wavelength: 515 nm, z-spacing $\sim$ 400 nm emission peak mNeonGreen: 517 nm; GFP: 509 nm
  - Design wavelength: 600 nm, z-spacing $\sim$ 400 nm
- Humidity and temperature control, Okolab (Pozzuoli, Italy)

The lattice light sheet microcscopy (LLSM) setup at Janelia was used. The setup is based on the description in Chen et al., 2014. Several specifications were altered from the original publication. The excitation and detection pathway in this instrument are orthogonal to each other (as usual in light sheet microscopes), but they are skewed in relation to the sample axis (figure 4). Detection occurs at an angle of 31.8° leading to a skewed image. Custom deskewing algorithms have been developed at Janelia, and are routinely applied before data is further processed and analyzed. Samples are mounted on circular, 5 mm diameter glass coverslips (1 thickness, Warner Instruments, Cat.64-0700 (CS-5R) that are cleaned with 1M KOH before sample mounting. The sample is submerged in SD medium during the experiment, attached on a custom-made sample holder. For optical sectioning the sample is moved horizontally through the light sheet.

- Objectives
  - Excitation: 0.65 NA, 3.74 mm working distance, water dipping lens, Special Optics, (Denville, USA)

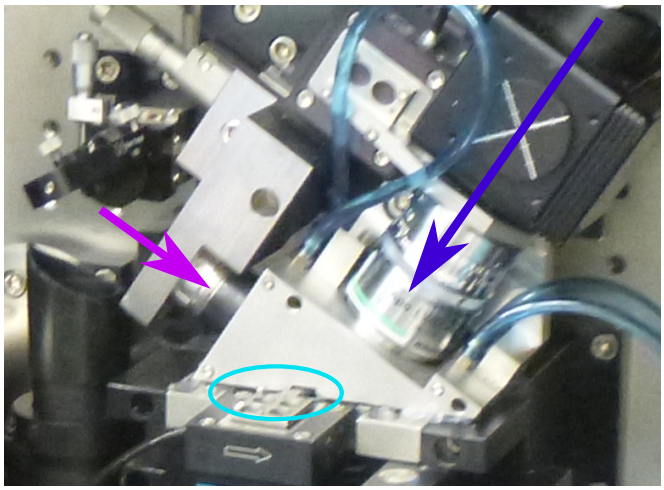

Figure 4: The LLSM light path is skewed relative to the sample position and samples need to be mounted in a particular way due to restrictions imposed by the excitation objective. The sample is mounted on a 5 mm cover slip on a custom sample holder (cyan oval), excitation light is coupled into the sample via a water dipping objective (magenta arrow) and emitted light is detected via the objective marked with a blue arrow. Photograph kindly provided by Dr. Gabriele Schreiber.

  - Detection: CFI Apo LWD 25x water dipping, 63x magnification, 1.1 NA, 3 mm working distance, Nikon (Tokyo, Japan)

- excitation lasers:
  - 405 nm, diode laser, Oxxius (Lannion, France)
  - 488 nm, fiber laser, MPB Lasertech (Edmonton, Canada)
  - 560 nm, fiber laser, MPB Lasertech (Edmonton, Canada)
- Cameras: Orca Flash 4.0 v2 sCMOS, Hamamatsu (Hamamatsu, Japan)
- Humidity and temperature control, Okolab (Pozzuoli, Italy)
- Software control, LABview, National Instruments, (Austin, USA)

2.1.6 Software

Numerous FIJI plugins were used, citeable plugins are listed separately in table 10. Code for image analysis in FIJI (in Jython) was written with input from forum.image.sc.

Table 9: Major lab equipment; parts of the LLSM and acMFM prototypes at Janelia are listed separately.

EQUIPMENT	MANUFACTURER
IX83 inverted microscope	Olympus, Tokyo, Japan
Incubator	Heraeus, Berlin, Germany
CASY® Cell Counter	OLS OMNI Life Science, Bremen, Germany
Bioruptor sonicator	Diagenode, Liège, Belgium
Spark plate reader	Tecan, Männerdorf, Switzerland

Table 10: Software and scripts used in this work.

SOFTWARE	COMPANY /SOURCE
Matlab 2019b Matlab 2017b for Linux Matlab 2016a for Windows	MathWorks, Natick, USA
FIJI / ImageJ	Rueden et al., 2017; Schindelin et al., 2012 Schneider et al., 2012
TrackMate	Tinevez et al., 2017
ImgLib2	Pietzsch et al., 2012
@msdanalyzer	Tarantino et al., 2014
Custom Matlab code	Jesse Aaron, Janelia
Custom Python code	Jorin Diemer, HU Berlin
HMM-bayes	Monnier et al., 2015
Jupyter Notebooks	Project Jupyter, jupyter.org
R	R Core Team, r-project.org
RStudio	RStudio, Boston, USA
NIS Elements	Nikon, Tokyo, Japan
CellSens	Olympus, Tokyo, Japan
Kile	kile.sourceforge.net
GIMP	The GIMP team, gimp.org
Mendeley Desktop	Elsevier, Amsterdam, Netherlands

2.2 METHODS

Experimental contributions:

- acMFM and LLSM: Dr. Gabriele Schreiber and I performed imaging with help from Jesse Aaron and John Heddleston (Advanced imaging center, Janelia Research Campus, USA)
- Western blots were performed by Dr. Gabriele Schreiber and Christiane Müller
- Molecular cloning was performed by Dr. Gabriele Schreiber, Lisa Mallis, Christiane Müller and myself
- Elutriation synchronization was performed by Dr. Gabriele Schreiber, Lisa Mallis, Christiane Müller and myself
- Growth curves were recorded by Lisa Mallis and Christiane Müller
- smFISH was performed by Dr. Gabriele Schreiber and myself
- Code which serves as basis for persistence analysis was provided by Jorin Dimer

I designed the experiments presented here and analyzed data. Affiliation of contributors: All Theoretical Biophysics group (Humboldt-Universität zu Berlin), except where indicated.

2.2.1 Construction of yeast strains

Integration of 24xMBS in CLB-3'UTR The 24x MBS sequence was cut from Addgene plasmid 31865 (Bertrand et al., 1998) with BamHI and BglII. After treatment with mung bean nuclease the MBS array was ligated in pLOXHIS5MS2L (Haim-Vilmovsky and Gerst, 2009) resulting in pLOXHIS5 24xMBS. Since amplification of the MBS array and the selection marker with loxP sites is difficult, we inserted homologous sequences for the 3' end of the *CLB2* open reading frame (ORF) and its 3' UTR in SalI and SacII site of the resulting vector. Primers bearing the homologous sequences are 1/2 and 3/4. From resulting vector the 24xMBS tagging cassette was cut with SfoI and used for transformation in yeast. Positive clones were selected in SD-His and confirmed by colony polymerase chain reaction (PCR) with primers 5 and 6. The loxP flanked selection marker was removed by Cre recombinase.

Integration of MCPΔ_{68-80}-pMet17-2x mNeonGreen in HO-locus The native viral coat protein encoded by pMS2-MCP-3xGFP Haim et al., 2007 was exchanged for the deleted version MCPΔ_{68-80} from pG14 MS2-GFP (Bertrand et al., 1998). 3xGFP was replaced by 2x mNeonGreen

(Shaner et al., 2013) by homologous recombination due to the lack of restriction sites, resulting in MCPΔ_{68-80}-2xmNeonGreen. A yeast codon optimized version of mNeonGreen was derived from pUC57 mNeonGreen (Mathuranyanon et al., 2015). For genomic integration in the HO-locus, hybridized primer pairs bearing homologous sequences for the target were ligated in BspEI and EagI sites of pMet17-MCPΔ_{68-80}-2xmNeonGreen (primers 7/8 and 9/10). The integration cassette was cut out of the vector using SnaBI. Yeast strains were transformed with the integration cassette using the CrispR Cas9 yeast vector pML107 (Addgene plasmid 67639) Laughery et al., 2015 with the gRNA sequence: 5'-GTTTATTCATCCATTATGGACGG-3'. Yeast strains were transformed with the integration cassette and the CrispR-Cas9 Plasmid and clones were selected in SD-Ura or SD-Leu. Positive clones were confirmed by microscopy.

N-terminal 3xFLAG tagging of Clb2p 3xFLAG sequence from vector template was PCR amplified with primer pair 11/12. The PCR product with homologous sequences to the *CLB2* N-terminus was ligated into pJet1.2 (Thermo Fisher Scientific) and cut from vector preparation with ScaI. Yeast strains were transformed with the restriction fragment, again using the CrispR Cas9 yeast vector pML107, with the gRNA sequence: 5'- TTCTGTGTTTTCTATTGGGTTGG-3'. Clones were selected in SD-Ura or SD-Leu. Positive clones were confirmed by colony-PCR with primers 13/14.

Cdc10-TagRFP TagRFP was PCR amplified with primers 15/16 and integrated in the PstI site of pUG72 (Euroscarf, Gueldener et al., 2002). The Integration cassette with TagRFP and loxP-KlUra3-loxP selection was amplified with primer pair 17/18 and used to transform yeast. Clones were selected in SD-Ura and confirmed by microscopy. The loxP flanked selection marker was removed by Cre recombinase.

Hhf2-mTurquoise The construction of Hhf2-mTurquoise was analogous to construction of Cdc10-TagRFP. For amplification of mTurquoise, primers 19/20 were used, while primers 21/22 were used to amplify the integration cassette. Again clones were selected in SD-Ura and confirmed by microscopy; the selection marker was removed by Cre recombinase.

The endogenous markers for spindle pole bodies (Spc42-mTurquoise) and Whi5-GFP were integrated for Amoussouvi et al., 2018.

2.2.2 Aberration corrected multifocus microscopy (acMFM)

To track mRNA in live cells, acMFM was used. acMFM makes use of light stemming from an additional 8 planes, spaced at regular, wavelength-

dependent intervals above and below the nominal focus plane. The light path is outlined in figure 3, and detailed specifications of this system are given in earlier publications (Abrahamsson et al., 2013; Smith et al., 2015). This setup allows for the acquisition of instant focal series of 9 planes on a single camera by appending three optical elements to the light path of a conventional epi-fluorescence microscope. The major element, a binary multifocus grating (MFG), modulates incoming light in two concerted ways. Here, light is diffracted by passing through a grating function designed to create a 3 x 3 array of diffractive orders (orders 0, ±1 in x- and y-direction), which are the base of the resulting 9 image planes. To reverse the spherical aberrations present in all but the 0-th order (the nominal focal plane), the MFG is geometrically distorted, inducing a different phase shift for each diffractive order. Thus, in each diffractive order, the spherical aberration pertaining to one specific distance from the nominal focus plane is reversed; i.e light originating from this plane is now in focus. Furthermore a chromatic correction grating (CCG) attenuates the chromatic dispersion introduced by the MFG, and finally, a prism deflects the individual diffractive orders to their position on the camera chip. The red channel was diverted onto a second camera by a dichroic mirror. 405 nm (mTurquoise), 488 nm (GFP/mNG) and 561 nm (TagRFP) lasers were used for excitation. For imaging, yeast cells were grown overnight on an orbital shaker at 30°C in SD medium and diluted prior to imaging to $OD_{600} = 0.1 - 0.2$. For each day of measurements, a z-stack of 50 planes (mechanical translation of the microscope stage) of Tetraspeck™ beads with Δz = 100 nm was aquired to calibrate the multifocus optics. Cells were left to sediment on an eight-well chambered coverglass (Nunc™ Lab-Tek™ Thermo Fisher, Waltham, MA, USA) at 30°C and medium was exchanged prior to imaging. Chambers were pre-incubated with Concanavalin A (1mg/mL for 5 min, rinsed 2x with ddH_2O, dried over night) to restrict cell movement (Bar-Shavit and Goldman, 1976). Only few, well separated positions per well were imaged to avoid phototoxicity and fluorophore bleaching associated with imaging in areas adjacent to the imaged cells. Acquisition settings: 16-bit tiff time series (.nd2) were recorded with a 488 nm laser, exposure=40 ms, resulting in frame rate of 23.81 fps due to camera readout times. Afterwards, a single volume was recorded with a 560 nm laser, exposure = 100 ms, and with a 405 nm laser, exposure = 100 ms, to image bud necks and nuclei.

2.2.2.1 *Image reconstruction, correction and deconvolution*

Images were saved with nine focal planes in a 3x3 array ('raw data'). Reconstruction of the 3D was performed using custom made Matlab scripts including a GUI by Jesse Aaron, Janelia Research Campus, in Matlab 2016a - 2019b. The two major steps are (i) calibration of the multifocus system using microbeads and (ii) alignment of the focal planes,

along with image deconvolution. Relevant parts of the documentation of the image reconstruction, written by Jesse Aaron is included in appendix B, as it is not publicly available. The author kindly granted permission to include the material here. The parameters used are listed here; for details on technical requirements and the exact workflow the microscope documentation is included in appendix B. In the calibration procedure, relative intensities of the 9 diffractive orders are calculated, and equalized during image reconstruction. Further, background was subtracted with a rolling ball method (radius = 10 pixels) and 6 iterations of a Richardson-Lucy deconvolution were applied to refine the signal by using the measured PSF. A range of background removal, bleaching correction and deconvolution methods were tested. *Deconvolution*: An iterative Richardson-Lucy algorithm (Lucy, 1974; Richardson, 1972), which uses the measured shape of the PSF of a point light source (characterized for each day of measurements) was used to restore the 'true' image from a recorded image. Since at higher iterations the algorithm tends to attempt to deconvolve inhomogeneities and noise, only 6-8 iterations were applied. *Background removal*: As the exact intensity of the RNP spots was not analyzed a simple 'rolling ball' background subtraction with radii of 5-10 pixels, i.e., 800-1600 nm, was used. This is much larger than the image of a diffraction limited light source, the Airy disk (the 2D PSF for a point light source in widefield optics). For the employed objective with NA = 1.45 and green light with λ= 515 nm the radius of the Airy disk is given by

$$r_0 = \frac{0.61\lambda}{NA} \tag{10}$$

as r_0= 217 nm (formula taken from Sheppard, 2004), corresponding to a diameter of $\sim$ 3 pixels in the used setup. *Bleaching correction*: Two bleach correction methods implemented in FIJI. Exponential fit and histogram matching were tested. The 'simple ratio' method was disregarded since it is overly reliant on an estimate of the background (Miura, 2020). The exponential fit method is a simplification, since it fits the average intensity decay with a single exponent, whereas fluorophores often show a double exponential decay (Füreder-Kitzmüller et al., 2005). If the fit to a monoexponential decay is good its use for segmentation of particles (not quantification of brightness!) may be admissible (Miura, 2020). The last method aims at matching the shape of the intensity-histogram in all frames of an image sequence to the first frame (Gopinath et al., 2008), which is a robust method when the distribution of fluorescence is stable. However, increasing detection of spots over time with this method was observed (not expected during 13 s experiments). A last method, combining background subtraction and a certain extent of bleaching correction is the subtraction of a highly blurred image series (Gaussian blur, radius 8 pixels) from the original image series. While this is clearly not appropriate for the

quantification of intensities, this approach was used for particle segmentation. This should lead to a more robust particle detection across experiments because differences in brightness between individual cells (e.g, due to differential expression of the mNeonGreeen-MCP fusion protein) were attenuated before particle detection. Quantitative measurements were made after the following image reconstruction and processing steps:

1. Horizontal and lateral image alignment, based on calibration of the microscope with TetraSpeck™ microbeads, using custom Matlab scripts, performing
   - correction for uneven light intensity in the 9 sub-images (focal planes)
   - rolling ball background removal (radius/σ = 10 pixels)
   - Richardson-Lucy deconvolution (6 iterations)
2. Subtraction of a highly blurred version of the time series (in FIJI -> Process -> Filters -> Gaussian blur with radius 8 pixels) from the original time series (in FIJI -> Process -> Image Calculator)
3. Exclusion of image border effects by cropping images manually

2.2.3 Lattice light sheet microscopy

For a detailed technical description of the generation of non-diffractive light beams and light lattices the reader is referred to publications by the group of Eric Betzig (Chen et al., 2014; Planchon et al., 2011) and Alexander Rohrbach (Fahrbach et al., 2010). In short, Bessel beams are a class of self-reconstructing beams created by either a lens with a conical surface (axicon), or by the projection of an annulus to the rear pupil of a an excitation objective (Lit and Tremblay, 1973; Welford, 1960). Additonally, light beams produced this way can be much thinner over long distances than beams with Gaussian intensity profiles. Fast scanning of such Bessel beams is used to create a (virtual) light sheet (Fahrbach et al., 2010). However, a large fraction of a Bessel beam is in side-lobes around the central maximum, adding to a light sheet's effective thickness. Lattice light sheet microscopy replaces the light annulus on the rear pupil plane by forming a discrete pattern of illuminated points on this annular outline with a spatial light modulator (Chen et al., 2014). This pattern can be designed to result in optical lattices - periodic light interference patterns - with properties tailored to the application. For this project the instrument was used in a 'dithering mode'; i.e., fast scanning of the light lattice, to obtain a homogeneous illumination within the light sheet. For LLSM, cells were inoculated in SD medium in the evening and grown overnight at 300 rotations per minute (rpm), 30°C. 5 mm coverslips were used

for imaging. Since the samples are (i) submerged in medium during imaging and (ii) the stage is mounted on a Piezo-element for z-stack acquisition, cells needed to be immobilized. Cover slips were pre-incubated with concanavalin A (1mg/mL for 5 min, rinsed 2x with ddH_2O, dried over night) to restrict cell movement. Cells were left to sediment for 10 minutes prior to mounting of the cover slips in preheated SD (30°C) on the microscope. For each experiment 5-12 positions on a coverslip were visually selected, which took 10-20 minutes approx., since translation of the sample holder in x and y is coupled to translation in z due to the skewed optical axes, requiring manual re-focusing. *Acquisition settings*: 50 planes were recorded per time point and channel with effective z-spacing (after deskewing) = 93.7 nm. Exposure was 50 ms per plane and laser power per channel was: 560 nm at 50 mW, 488 nm at 30 mW and 445 nm at 31 mW. The selected positions were imaged sequentially, resulting in one stack every 50-100 s, approx. The acquisition was interrupted after max. 3 hours.

2.2.3.1 *LLSM data analysis*

Images were stored in hdf5 format (.h5) containing 50 focal planes and 3 color images (bud necks, nuclei and mRNA signal) per time point. Differently from particle detection for acMFM data anylsis, a Laplacian of a Gaussian (LoG) filter in Trackmate was used. Particle size was estimated to be 600 nm based on equation (10), with $NA_{detectionobjective}$=1.1, corresponding to $\approx$ 6 pixels (pixel size was 104 x 104 x 94 nm). Particle detection was done on image stacks, as numbers of detected particles were not as reliable when detection was performed on maximum intensity projections (MIPs), particularly when multiple spots were close to each other. Time series of control cells were imaged and analyzed with the same parameters. Particle detection threshold was 180.0. A panel showing a time series of MIPs of the control strains is in figure 29. Spots pertaining to a yeasts base and bud were counted separately. To this end, the spots detected in Trackmate were counted manually. This data was compared to counts by Dr. Gabriele Schreiber (for 2 time series using FISH-quant (Mueller et al., 2013)) to check robustness of the method.

2.2.4 Single mRNA tracking

For SPT TrackMate (Tinevez et al., 2017) was used, since this tool offers ample space for customization, and its potential and limitations are under constant scrutiny by an active community (forum.image.sc). The main functions provided by TrackMate are the detection of (i) spots, or rather blobs in the 3D case, and (ii) particle displacements and trajectories. Estimation theory shows that the filter providing maximum SNR in the presence of Gaussian white noise is a whitened matched filter

(Forney, 1972). For the purpose of SPT such an optimal detector can be approximated well with a LoG (Sage et al., 2005). This method applies a Gaussian filter with tunable kernel size to an image to smooth the image, and subsequently applies the Laplace operator to sum up second order partial derivatives to identify local maxima. The difference of Gaussian (DoG) method, which approximates the more common LoG scheme well for small particles, was used. For particle diameters below 5 pixel, the DoG method, has been shown to be faster and more effective, as reported in the TrackMate manual (Tinevez, 2016). The DoG method relies on convolving an image with two Gaussian kernels that possess related standard deviations $\sigma_1 = 1/(1+\sqrt{2})d$ and $\sigma_2 = \sqrt{2}\sigma_1$, with d being the approximate feature size. Images convolved with σ_2 are subtracted from images convolved with σ_1, which similarly to the LoG method identifies local maxima. Image stacks were used for particle detection, not MIPs. Although signals were often found to look brighter in these projections, they were not used for two reasons: If there are 2 or more spots in close proximity in x or y, while they are well separated in z, these points will be suppressed in MIP. Given the heterogeneous cellular background signal, this method can mask spots that are clearly detectable in one focal plane with noise/background stemming from other focal planes. A quadratic fitting scheme by Stephan Saalfeld and Stephan Preibisch, based on Lowe, 1999, 2004 was used for sub-pixel localization. For particle linking the TrackMate linear assignment problem (LAP) tracker, which is based on u-track (Jaqaman et al., 2008), was used. In brief, two consecutive cost matrices are constructed that put a price tag on linking and not linking particles (first matrix) or track segments (second matrix) with elements in previous and subsequent frames. No modifications were applied to the first cost matrix, such that only the sum of squared distances determines particle linking. The second cost matrix was modified to allow gap-closing, i.e., the joining of track segments over a single frame where the track is not detected. Both for particle linking and gap-closing, a maximum displacement needs to be defined to exclude nonsensical trajectories. Finding the maximum displacement is, however, not unambiguous. It would be desirable to know, how far a diffusing particle can move during a given delay time. A common approach is to use a particles' instantaneous velocity (Chenouard et al., 2014; Tinevez, 2016). This relates to *measuring* a particles' instantaneous velocity, which, according to Albert Einstein, 1907 is "impossible - at least for ultramicroscopic particles". He has been disproven (Li et al., 2010). It is complex, however, to measure due to the extremely short time during which a diffusing particle undergoes directed ('ballistic') motion, for which a velocity can be defined. This very fact makes the instantaneous velocity of a diffusing particle also irrelevant for SPT: For a 1 μm silica sphere in water, e.g., this time window, the momentum relaxation time, has been calculated to be 0.1 μs whereas

the behavior on the ms to minutes scales is relevant for current live cell microscopy. Thus, the 'instantaneous velocity' implied in SPT experiments is rather related to the MSD for a specific delay than what is commonly called velocity. The limit for particle linking was based on displacement distributions of *ARG3* mRNPs in budding yeast (Lampo et al., 2017; Thompson et al., 2010). *ARG3* is very lowly expressed (0-3 *mARG3* per cell) making erroneous links between particles that could inflate the maximum displacement unlikely. Furthermore the reported displacement distributions of delays between consecutive time steps exhibit clear doubly-exponential distributions; longer displacements Δ do not seem to have been 'shaved off' by overly restrictive limits imposed by Thompson et al., 2010. In these works, diffusing mRNA was observed to displace by up to $\sim$ 300 nm for δ = 15 ms and up to $\sim$ 450 nm for δ = 150 ms. These values are displacements in x and y combined, whereas also motion in z is included here. If Δ in the three dimensions are independent, and maximum Δ in z is as large as those in x and y, the correction factor would be $\sqrt{3}/\sqrt{2} \approx 1.2$ [1]. Active transport mediated by myosin V, which is another expected type of motion for mRNPs motion in yeast, does not conceivably cause larger displacements at the given delay time of $\approx$ 42 ms (imaging frame rate), as the maximum reported processive speed of myosin V is 1.2 μm/s (Baker et al., 2004; Clemen et al., 2005; Pierobon et al., 2009). Thus, perhaps unintuitively, diffusion could cause displacements of $\sim$ 500 nm between consecutive frames (42 ms); active transport on the other hand is not expected to account for displacements > 50 nm during th same time. To optimize the automatic detection of trajectories that could be confirmed by visual inspection while suppressing noise, a number of image-processing method, particle detection thresholds and trajectory lengths were screened. The images used for comparing the conditions included cells with MS2-tagged *mCLB2* or *mSIC1*, and negative controls that only contained mNeonGreen-labeled MCP. The tested combinations of pre-processing and analysis of this integrated screen are listed in table 11. Negative controls: 12 cells in budding phase from 6 image series; 2 cells were rejected prior to analysis as they contained large amorphous fluorescent structures. For the different scenarios outlined in table 11, two sets of quality thresholds for particle detection were defined: One for scenarios where a highly blurred image was subtracted for background removal (Sc 1-3) and one for the remaining scenarios. This seems justified, as subtraction of the blurred image drastically affects the prominence of local maxima above the cytoplasmic background. Thresholds were set to yield comparable numbers of detected spots in example time series. The same set of thresholds was applied irrespectively of bleaching corrections,

1 This back-of-the-envelope calculation is based on the Pythagorean theorem in 3D. The reported maximum 1D-displacement would be the hypothenusa of a triangle formed by equal Δ in x and y; Δ in each dimension would thus be $\leq 1/\sqrt{2}$ of the reported 1D maximum displacement; $\Delta_{3D}^2 = \Delta_x^2 + \Delta_y^2 + \Delta_z^2$

Table 11: For the given scenarios, the number of detected particles and trajectories, were evaluated for *mCLB2* and *mSIC1*, and negative controls. Prior to the steps outlined here image stacks were reconstructed while applying a rolling ball background subtraction (radius = 10 px) and deconvolution (Richardson-Lucy, 6 iterations).

	Sc 1	Sc 2	Sc 3	Sc 4	Sc5
Subtraction of blurred duplicate	x	x	x		
Exponential fit bleaching correction	x			x	
Histogram matching bleaching correction		x			
Particle detection quality thresholds (1200, 1700, 2200)	x	x	x		
Particle detection quality thresholds (1500, 2000, 2500)				x	x

as those do not affect the first frames of each series which were used to define threshold candidate values for the screen.

2.2.5 Estimating localization errors

Every particle localization has an attached error. This error is assumed to be independent for each time point and distributed normally (Michalet, 2010). It has been suggested that the localization error can be estimated from the offset in MSD curves of purely diffusive trajectories (Michalet, 2010; Montiel et al., 2006; Savin and Doyle, 2005). The localization error will affect the apparent MSD

$$MSD = \epsilon + \tilde{D}t \tag{11}$$

with ϵ = localization error, $\tilde{D}$ = 'real' diffusion coefficient (i.e., the measured diffusion coefficient D convolved with the localization error) and t = time (Michalet, 2010). To estimate the error, the apparent MSD from 39 trajectories of *mSIC1* molecules, for which no active transport mechanism has been described, was calculated. This subsample contained tracks of the entire observed duration range, i.e., 20-300 time points and included trajectories of particles for which sub-pixel localization failed. The first 25% of each trajectory were included for

the calculation of the MSD fit, as longer delays tend to be affected by the finite volume of the cell (Monnier et al., 2012). The trajectories were selected manually to exclude trajectories possibly containing directed motion and were processed in Matlab2019b with functions of the MSDanalyzer class. The MSD was calculated for each track, and a linear fit with offset was performed: MSD = a × dt + b. The offset b of the curve can be used to approximate the localization error σ by a formula given by Tarantino et al., 2014

$$\sigma = \frac{1}{2\sqrt{b}}. \tag{12}$$

For a further test certain trajectories were excluded: When the sub-pixel localization routine (SubpixelLocalization in ImgLib2) did not converge, mRNA positions for these frames are set to the default position corresponding to the respective pixel. Trajectories for which sub-pixel localization failed for more than 10% of the constituting particles were excluded in this scenario ('only subpixel localization trajectories'). For a third scenario, the effect of dimensionality was investigated. MIP of the same images as above were analyzed with TrackMate, adjusting thresholds of the DoG particle detector (from 2000 for 3D to 1650-1800) to obtain a comparable number of trajectories ('2D trajectories'). Lastly, the effect of sample size was assessed by providing larger sets of unfiltered data for the estimation.

Estimating localization error using scripts of the MSDanalyzer class in Matlab2019b):

- calculate linear fit for individual MSD curves of 39/26/34 trajectories (All trajectories / only subpixel localization trajectories / 2D trajectories)
- exclude fits with $R^2 < 0.8$
- only use intitial 25% of each trajectory for calculations
- calculate mean of all MSD fits meeting the R^2 requirement
- use offset of the mean MSD fit to estimate localization error with equation (12)

Requiring that R^2 of the linear MSD fit be > 0.8 leads to the rejection of $\sim 2/3$ the trajectories used for this estimate (23 out of 39, 17 out 26, 21 out 34, 304 out of 521).

2.2.6 Displacement distribution analysis

To analyze the distribution of single time step displacements, trajectories were manually excluded from analysis as in the scenario ('only

subpixel localization trajectories') in the previous section. Curated trajectories were loaded into Matlab and displacement distributions were analyzed using 'distributionFitter', with Normal and Laplacian fits to determine μ and σ. Additionally, the tolerance level for pixel level localizations was lowered to 0 (cropping affected trajectories at the first-pixel level localization) and fits were performed again.

2.2.7 Trajectory analysis

Persistence analysis
For smoothing, particle particle positions were averaged over the current and k = 5 further positions. Thereby, the trajectory was shortened by k time steps. To estimate the effect of smoothing, the distance (norm) between points on the experimentally measured and the smoothed trajectory was measured. The distance was calculated between point i on the smoothed trajectory and point i + k/2 on the original trajectory. Thus, if the particle moves along a straight line for 6 time steps the distance between smoothed and original positions would be 0 (for smoothing with k = 0). For smoothed and original trajectories, the persistence was calculated as an indicator of directed motion. The persistence is defined here as the cosine of the angle between two consecutive displacements, yielding 1 for a straight line and -1 for a 180° turn. For this project a persistence threshold of 0.5 was used, corresponding to $\arccos(0.5) = \frac{\pi}{3}$ or 60°. Highly persistent sections on the trajectory were identified. The sliding window used to identify these sections was 10 displacements, i.e., 415 ms. This analysis is based on a method by Jorin Diemer, Humboldt-Universität zu Berlin. All calculations are performed in Python 3, including NumPy.

HMM-Bayes
To analyze the cytoplasmic trajectories of *mCLB2* recorded by acMFM a routine based on Monnier et al., 2015 was applied. The main challenge addressed by this method is that transient, subtle features of cytoplasmic mRNA motion are not accessible by common methods for trajectory analysis, like kymographs or mean square displacement analysis (Jaqaman et al., 2011; Monnier et al., 2012; Saxton and Jacobson, 1997, see section 3.1). Shortly, hidden Markov modeling was applied to mRNA trajectories to classify the current mode of motion of a particle with single time-step resolution. To avoid excessive switching between states (up to 3 hidden states of diffusive or directed motion were tested), Bayesian model selection was applied to infer the simplest model that suffices for the description of the analyzed trajectory (Persson et al., 2013).

2.2.8 Single molecule FISH

Reagents required for smFISH are listed in section 2.1.4. The cells indicated in table 2 were used. They consist of a pair of yeast strains sharing a common genetic background and a strain in which the targeted mRNA's coding gene has been deleted. All cells were derived from BY4741. Cells were plated from glycerol stocks at -80°C on YPD-agar plates and after incubation at 30°C for 2-4 days they were stored at 4°C. For experiments, single colonies were picked and inoculated in YPD to grow over night at 30°C and 300 rpm. Cells were grown to an OD_{600} = 0.5 and 50 mL and cell culture was fixed by adding formaldehyde to a final concentration of 4% (w/v). Formaldehyde reacts with water to form methylene glycol, which can rapidly diffuse into cells, and upon retransformation to formaldehyde denatures cellular molecules (Kiernan, 2000). This method is common and assumed to be fast enough to preserve cells in an unstressed state. Cells were kept in formaldehyde for 30 min at room temperature and inverted after 10 and 20 min. Afterwards, cells were pelleted by centrifuging for 3 min at 3000 g and 4°C, resuspended in 1 mL Buffer B and transferred to 2 mL tubes. The remaining steps of the method, required for removal of the cell wall and hybridization are listed below. Importantly, spheroplasting (removal of the cell wall) needs to be strictly timed, and for each batch of lyticase, the appropriate timing was determined by brightfield microscopy. The desired timing was found when removal of the cell wall could be confirmed by lowered contrast, but cells still maintain their shape (15-17 min approx.). Buffers are listed in table 6. For readability the protocol following formaldehyde fixation will be presented with bullet points.

- Add ice cold Buffer B and spin down at 3000 g, 4°C, remove supernatant, 3 times
- Incubate in 1 mL spheroplasting buffer (100 u lyticase) at 30°C, 15-17 min
- Add 1 mL ice cold buffer B and pellet cells at 1500 gfor 4 min at 4°C, remove supernatant
- Add ice cold Buffer B and spin down at 1500 g and 4°C, remove supernatant
- Resuspend in 70% ethanol for 2 h, store (up to 3 months).

For hybridization, pre-mixed probe sets were used, as described in Tsanov et al., 2016. Probes for *mCLB2* were labeled with Atto550 dye. For each hybridization experiment 50 µL of the cells stored in ethanol were used.

- Rehydrate cells in ethanol in 1 mL 2xSSC for 5 min at room temperature, spin down for 4 min at 1500 g, remove supernatant

- Resuspend in 1 mL hybridization washing solution for 5 min at room temperature, spin down for 4 min at 1500 g, remove supernatant
- Resuspend in 50 µL hybridization buffer and add labeled probes to a final concentration of 0.25 µM, incubate for 4 h at 37°C in the dark on an orbital shaker
- Add pre-heated 1 mL (37°C) hybridization washing solution, shake slightly and immediately pellet by spinning down for 4 min at 1500 g, remove supernatant
- Wash 3 times by adding 1 mL pre-heated (37°C) hybridization washing solution and shake for 15 min at 37°C in the dark, spin down for 4 min at 1500 g, remove supernatant
- Wash with 2x SSC + 0.05% Triton X-100 for 5 min, shake at room temperature on an orbital shaker in the dark, spin down for 4 min at 1500 g, remove supernatant
- Wash with 2x SSC + 0.05% Triton X-100 for 5 min, shake at room temperature on an orbital shaker in the dark, spin down for 4 min at 1500 g, remove supernatant.

Cells were left in 100-200 µL SSC and transferred to object slides for imaging. All imaging was done within 2 days after hybridization. Samples were stored at 4°subsec:reagents in the dark before imaging. Imaging was performed on an IX83 inverted microscope (Olympus).

2.2.9 Elutriation synchronization

To obtain a synchronized yeast cell culture without affecting cell cycle progression, counterflow centrifugation elutriation (Sanderson et al., 1976) was used. This technique subjects yeast cells in specialized centrifuge chambers to two opposing forces; the centrifugal force and a centripetal force generated by a pump-driven flow of buffer. Drag, and thus the force exerted by buffer on the yeast cells, is dependent on a cell's surface, whereas the centrifugal force is proportional to the mass (and volume, justifiably assuming constant density). The surface to volume ratio is higher in small cells, which causes cells in the centrifuge chamber to establish a size gradient. The smallest cells, which are newborn daughter cells in G_1, can thus be flushed out of the chamber by slightly changing the balance between the opposing forces (i.e., by changing centrifuge speed, flow rate, or both). This method causes a much longer cell cycle than is observed in asynchronous population, as elutriated cells are all small G_1 cells growing isotropically before budding, whereas larger cells can go back to S within few minutes after cytokinesis. Importantly, this method

does not alter cyclin dynamics and cell cycle progression as pheromone (α-factor) or chemical (e.g., by hydroxyurea) synchronization methods do (Futcher, 1999; Schlichting, 2019) and are therefore preferable for cell cycle studies, despite the increased experimental effort. Cells were inoculated from plates in 100 mL YPD medium in the morning and incubated at 30°C. After 8 hours, this pre-culture was used to start 4 L overnight-cultures with OD_{600} = 0.01 and further incubated at 30°C, resulting in OD_{600} = 0.7 the next morning. Cultures with higher and lower concentrations were prepared in parallel; the culture with the highest concentration that did not show morphological defects (increased contrast, increased vacuoles) was used. Prior to elutriaton, cells were transferred to sterile phosphate buffered saline (PBS) by filtering with a vacuum pump onto a 0.45 μm pore size cellulose filter and resuspending in buffer. The subsequent differences in elutriation parameters are purely heuristic; successful sorting was ensured by cell size and count measurements. Parameters for elutriation were

- Load elutriation chamber with 50 mL/min flow rate at 2100 rpm
- Harvest with flow rate of 60 mL/min at 1950 - 2000 rpm.

Elutriation was repeated several times, fractions were stored on ice and pooled for subsequent growth and sampling of a synchronized culture. $\sim$ 10 fractions were pooled in preheated (30°C) YPD with ampicillin (100 μg/mL) and cultured in a water bath at 30°C. During 250 minutes 2 samples were taken every 10 minutes from the culture and immediately processed. Collected samples were:

- 5 mL in 15 mL plastic tube containing 600 μL trichloroacetic acid (TCA) for western blots
- 150 μL in 2 mL plastic tube for cell number and cell size measurement

The 150 μL sample was vortexed and 2 subsamples of 25 - 50 μL were immediately diluted in 5 mL CasyTon, each, inverted 3 times, and cell sizes and numbers were measured in an CASY® Cell Counter according to the manufacturers instructions.

2.2.9.1 *Western blots*

Buffer compositions are specified in table 6 and antibodies are listed in table 8. After protein extraction, proteins were separated by SDS-polyacrylamide gel electrophoresis (15 µL loading volume) on gels containing 0.5% trichloroethanol. To quantify total protein content gels were activated for 2.5 min with UV light and scanned on a BioRad scanner (Hercules, USA). Primary antibodies were diluted 1:2000 and 1:5000 (Anti-FLag/ Anti-G-6-PDH) in TBST, washed in TBST twice for 5 min and once in TBS for 5m̃in. Secondary antibodies were diluted

$1 : 10^4$ in TBS, washed in TBST twice for 5 min and once in TBS for 5 min.

2.2.9.2 *Growth test*

To quantify possible growth defects introduced by the MS2-system, Cdc10-TagRFP and Hhf2-mTurquoise in the cells used for live cell imaging, growth curves were recorded on a Tecan Spark plate spectrophotometer. Cells were grown at 30°C for 20 h in YPD and absorption at 600 nm was measured every 5 minutes. Each strain was tested at least three times. Data was analyzed with a custom R script based on growthcurver, version 0.3.1 (Sprouffske and Wagner, 2016). Growth curves were fitted with the standard form of the logistic equation, generation time t_{DT} was estimated based on the formula $t_{DT} = \frac{ln2}{r}$, with r = maximum growth rate. BY471 (WT) was compared to cells with the MS2 system and to cells additionally containing the nuclear and bud-neck markers used during live cell imaging. Lastly, the effect of including a FLAG-tag in these backgrounds was investigated, as sensitive Clb2p antibodies are not commercially available. Accordingly, FLAG-tagged strains were used for western blots. Genotypes are found in table 1 (strain 1) and table 3; the 'MS2-only' strain is BY4741 with MBSs in the 3' UTR (Clb2::Clb2-24xMBS-loxP). Fits of the individual growth curves are found in appendix A.7. Generation time estimates presented in the main part are based on these fits. For all growth curves shown the initial value was subtracted from the entire curve to make plots comparable.

3 RESULTS

I will first provide an overview of major findings and in this introductory paragraph I refrain from referencing to figures. Details are reported in the respective sub-sections. By combining novel fluorescent probes and the unique focal depth of the acMFM I could extract long trajectories of cytoplasmic mRNA motion on time scales from ms to s. This approach facilitated insights into the behavior of mRNPs and allowed me to reliably track individual molecules as the high frame rate makes erroneous linking of particles less likely. Using LLSM I additionally quantified *mCLB2* over the budded phase of the cell cycle. For these imaging experiments, I designed yeast strains that contained endogenous markers for nuclei and the bud neck additionally to the MS2 system. Apart from their use as cell cycle markers, the Cdc10 fusion protein marking the bud neck facilitates the joint segmentation of base and bud. Taken together, the approach allowed me to evaluate *mCLB2* translocation in yeast and the mRNA's distribution throughout the cell cycle (S-G_2-M) with higher temporal and spatial resolution than previously reported.

For both LLSM and acMFM particle detection I used control cell strains that were imaged under identical conditions to define robust particle detection thresholds. While this approach often leads to lower numbers of detected particles than setting the thresholds by visual inspection, the behavior of the detected particles is more likely to capture the true mRNP motion since this method relies less on the experimenter's expectations. To minimize variability amongst cells the MS2 tagged strain and the control strains expressed MCP from a single genomic locus and shared, apart from the MBS-array in the *mCLB2* UTR, an identical genome. Given the known issues with the MS2 system (Garcia and Parker, 2015, 2016; Tutucci et al., 2018, described in section 1.5.1) I opted for control smFISH experiments figures 34 to 36, and western blots (figure 42) for the quantification of Clb2p throughout the cell cycle to control for excessive perturbations by the MS2 system. Synchronization of yeast cells for imaging experiments was not necessary, as all methods had single cell, single molecule resolution. For western blots, I used elutriaton synchronized cells (Linke et al., 2017; Nasmyth, 1993) as this method, albeit complex, is far less prone to interfere with the cell cycle control (Futcher, 1999; Schlichting, 2019) I aimed to study. Transcripts of the promitotic cyclin *CLB2* have been reported to be primarily bud localized (Shepard et al., 2003; Trcek et al., 2011) and biochemical assays suggest that Myosin V motor proteins are responsible for this bud enrichment (Casolari et al.,

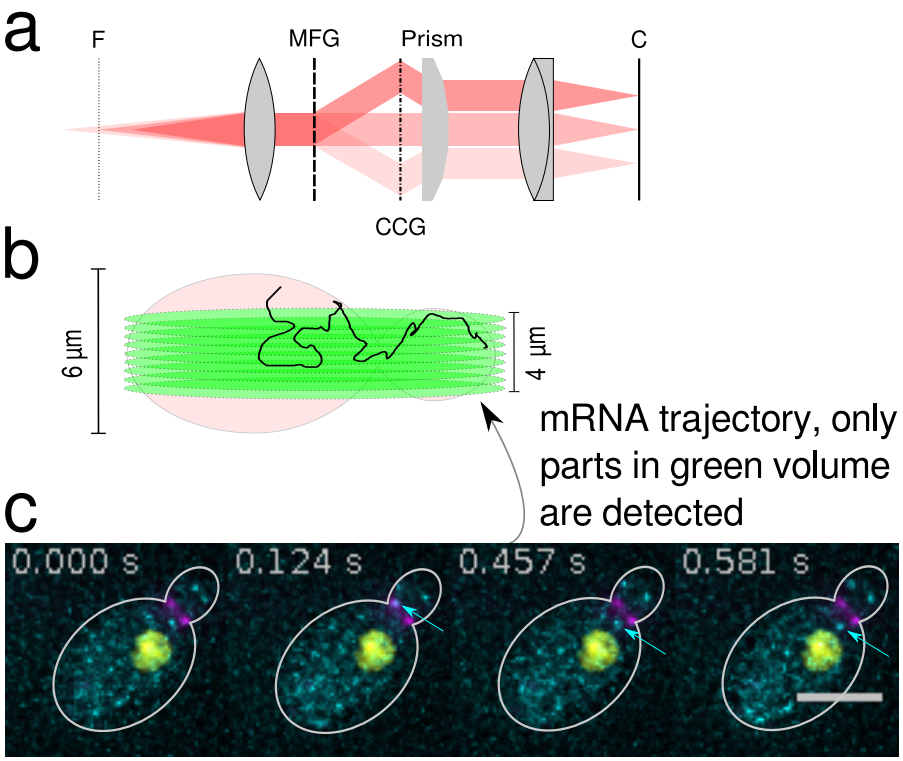

Figure 5: Imaging *CLB2* mRNA in live cells by aberration corrected multifocus microcscopy (acMFM). (a) Main optical components and light beams for acMFM. After passing through the primary focus F of the microscope, emitted light passes through the multifocus grating (MFG), which (i) splits the light to form a 3 x 3 array instead of single image and (ii) induces a phase shift that depends on the diffractive order, thus correcting the spherical aberrations for a series of out-of-focus planes (see also section 2.2.2). Only 3 diffractive orders (x = 0, ± 1) are shown for simplicity, including combinations with y = 0 ± 1, yields 9 orders. The chromatic correction grating (CCG) and a prism revert chromatic shifts introduced by the MFG and direct the beams to their respective positions on the camera chip C. (b) The combined focal depth of these planes is ∼ 4 μm, allowing the recording of long mRNA trajectories (c) Single *CLB2* mRNAs (cyan) in a budding yeast cell. The arrow marks an mRNA moving from the bud through the bud neck (magenta) into the base (nucleus in yellow). Scale bar: 5 µm.

2012; Shepard et al., 2003). In table 12 I present an overview on what the journey of this mRNA is expected to be like, based on dimensions of the yeast cell and literature data on the processes involved in mRNA transport.

Table 12: Approximate time scales of *mCLB2* movement in yeast cells. Maximum processive velocities for Myosin V were between 500 and 1200 nm/s.

STAGE OF MOVEMENT	DURATION	SOURCE
Diffusion to nuclear envelope	1-2 s	Estimate of RNP diffusion coefficient and size of nucleus (Grünwald and Singer, 2010; Oeffinger and Zenklusen, 2012)
Scanning for nuclear pore complexes	10*s*	(Saroufim et al., 2015)
Nucleocytoplasmic translocation	0.2 s	SPT of mRNA in yeast (Oeffinger and Zenklusen, 2012)
Myosin V transport	2-10 s	In vitro / in vivo SPT (Baker et al., 2004; Clemen et al., 2005; Pierobon et al., 2009)

Based on literature data, I hypothesized that any detected *mCLB2* in the cytoplasm would translocate to the bud within 10 seconds. Based on single particle trajectories detected with an objective method and using a defined set of parameters (section 3.1.3 and the distribution of *mCLB2* throughout the cell cycle (section 3.2) my data demonstrates that this is not the case.

3.1 IMAGING mRNA MOTION BY MULTIFOCUS MICROSCOPY

The motion of *mCLB2* was observed in 281 time series of MS2 tagged cells. As a control, 55 time courses of the motion of *mSIC1* were recorded. This transcript is not expected to be transported. 6 time courses of control cells, expressing mNeonGren-MCP, but no MBS were recorded. For all time courses, between 1 and 5 cells were in the field of view. To observe the motion of individual mRNPs I acquired images until photobleaching was complete; limiting timecourses to ≈ 13 seconds (300 frames). Cells with a clearly visible bud were selected

for imaging. Most observed *mCLB2* was stationary or moved without apparent direction. I analyzed images of cells with tagged *mCLB2* for translocation events between mother and bud, and evaluated whether detected trajectories are compatible with actomysoin transport. An example of an mRNA translocating into the bud is shown in figure 6, the reverse direction is shown in figure 7.

3.1.1 Identification of mRNPs

Before describing the motion of cytoplasmic mRNP I want to start by characterizing the RNA detection quality, as this step has the potential to lower the quality of all downstream analysis. Given the low SNR of the MS2 tagged RNP above the background of unbound cytosolic MCP-mNeonGreen I applied a two-tier particle detection approach (figure 9). To avoid biases against fast moving particles I scanned detection thresholds (3 values) for differently pre-processed image series (5 scenarios) to be able to include weaker signals, while limiting the extraction of spurious trajectories. My systematic comparison of these processing methods revealed that particle detection thresholds could be relaxed for longer trajectories. I could thereby reproducibly extract single RNA trajectories from tagged cells, but not from cells lacking MBSs.

To avoid linking of particles over arbitrary distances, the maximum displacement of particles between two frames was constrained by literature data (500 nm per time step, section 2.2.4, Lampo et al., 2017. The approach is remarkably robust considering that in the time series of control cells spot detection was in the same order of magnitude (10^3 spots in a time series of 300 frames) as cells containing MBSs on *mCLB2* or *mSIC1*. Trajectories of more than 20 consecutive spots were almost completely absent in controls (1 exception, stationary bright spot). The comparison is based on 12 control cells; and 27 (*mSIC1*)/ 70 (*mCLB2*) time series of tagged cells, containing 1-3 cells each.

3.1.2 Diffusion of yeast mRNPs

Non-directed, seemingly diffusive motion was observed for most *mCLB2* and *mSIC1* observed by acMFM. I investigated diffusive motion because of two main reasons in this project. Besides the importance of diffusive motion for an estimate of the experimental localization error, a report on non-normally distributed displacement probabilities RNP in yeast cells (Lampo et al., 2017, section 1.4.1) offers an interesting opportunity for cross-validation of acMFM and DH-PSF 3D imaging.

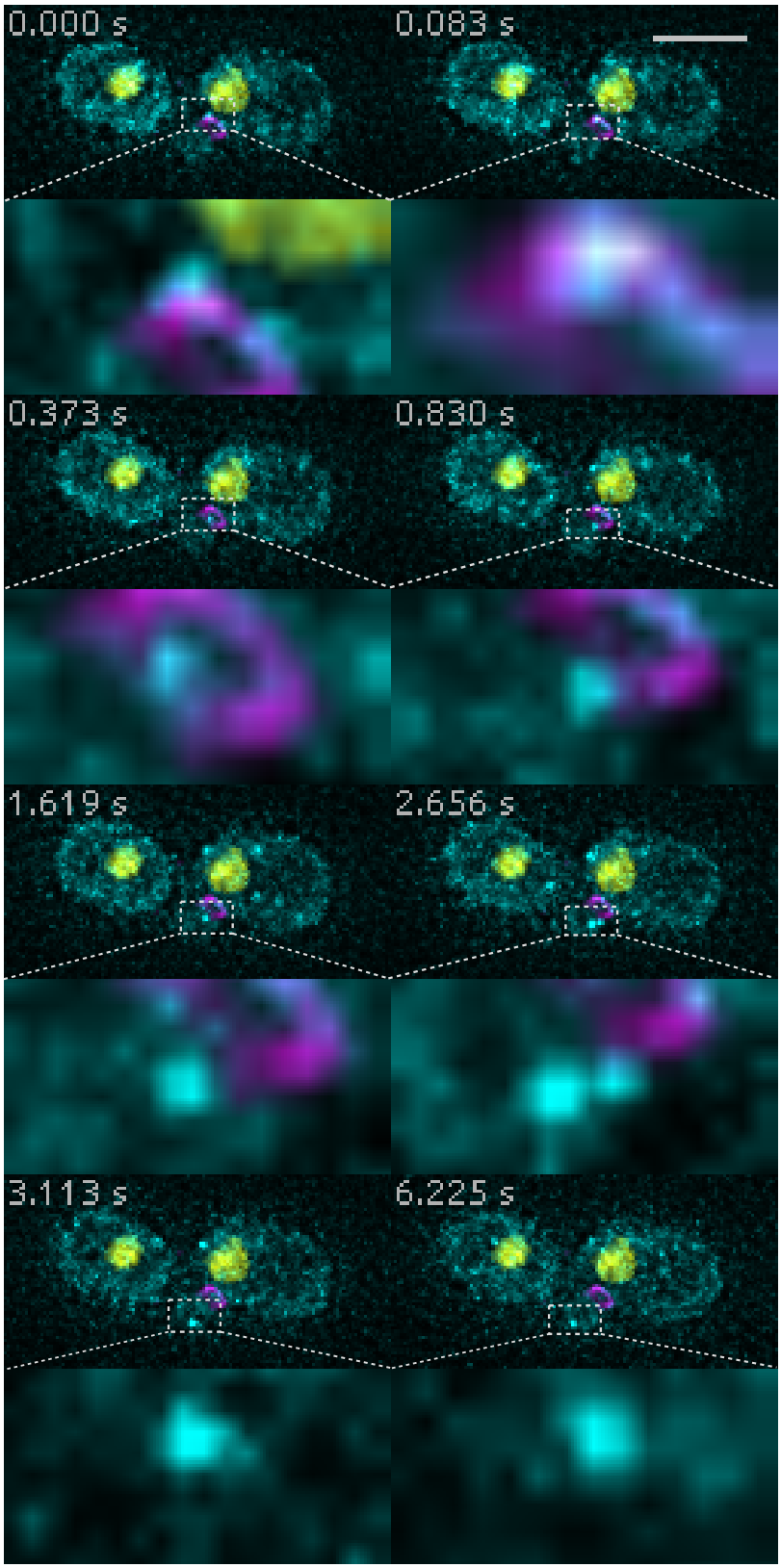

Figure 6: Translocation of *mCLB2* (cyan) from base (becoming mother cell) to bud recorded at 23.8 fps on 9 focal planes covering an optical depth of 4µm (MIPs shown). The zoomed panels give an impression of the variability in single molecule signal. Bud necks (magenta) and nuclei (yellow) are endogenously labeled by Cdc10-TagRFP and Hhf2-mTurqoise, respectively. Videos and 3D projections of the experiments are listed in appendix A.1. Scale bar: 5 µm, zoomed regions are not to scale.

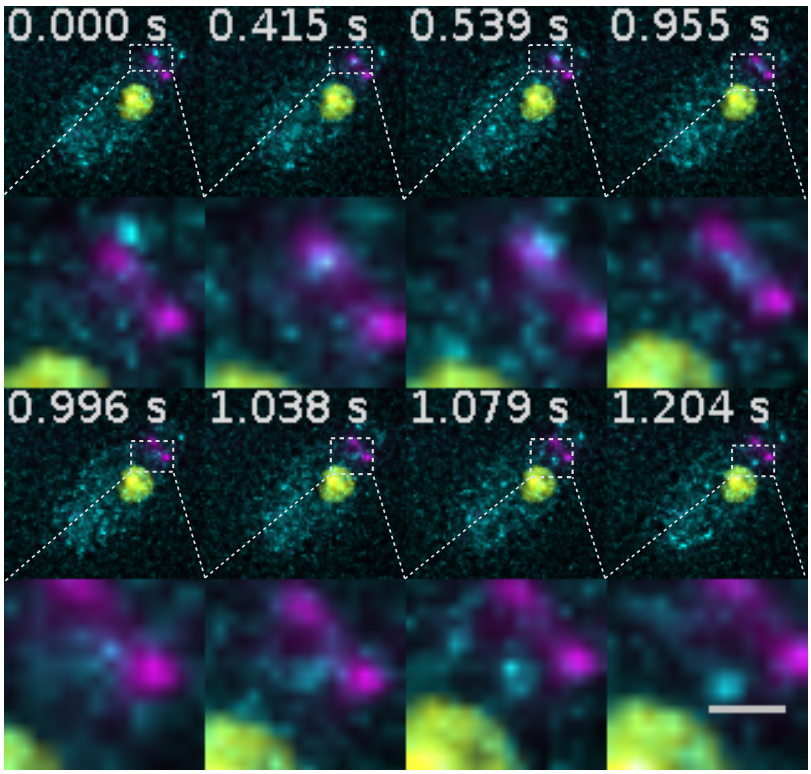

Figure 7: Translocation of *mCLB2* (cyan) from bud (becoming daughter cell) to base (becoming mother cell). This highlights that translocation of *mCLB2* is not strictly unidirectional. Bud necks are shown in magenta and nuclei in yellow. Scale bar: 5 µm, zoomed regions are not to scale.

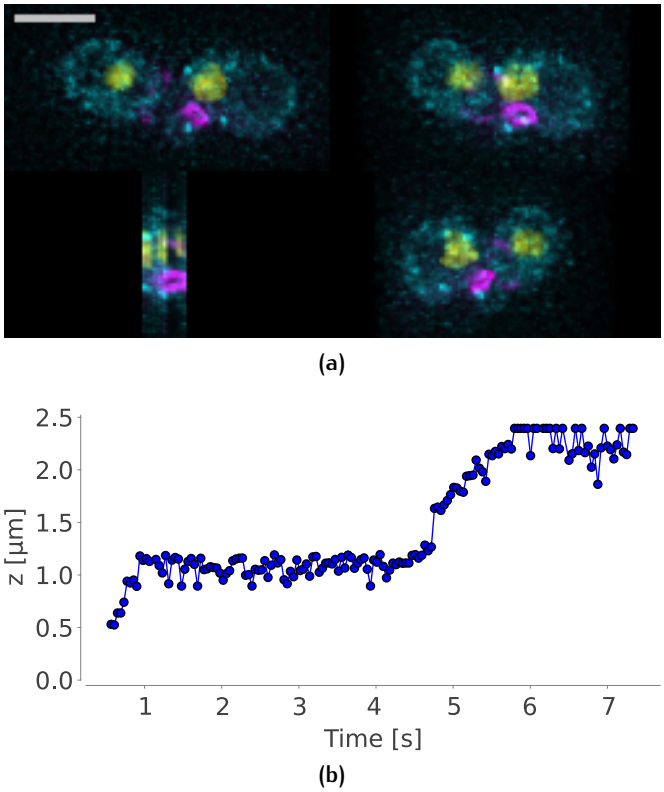

Figure 8: While few events of translocation of *mCLB2* between base and bud were observed, these trajectories typically involved motion in z that is beyond the optical depth of single plane widefield microscopy. Figure 8a is a 3D projection of the focal planes of a single time point of the time series in figure 6. The scale bar (5 µm) only applies to the left panels. In figure 8b the axial dimension of the trajectory in figure 6 is shown. Large jumps in axial direction suggest a limited localization precision in z. A complete rotation of the cell in figure 8a is in appendix A.1.

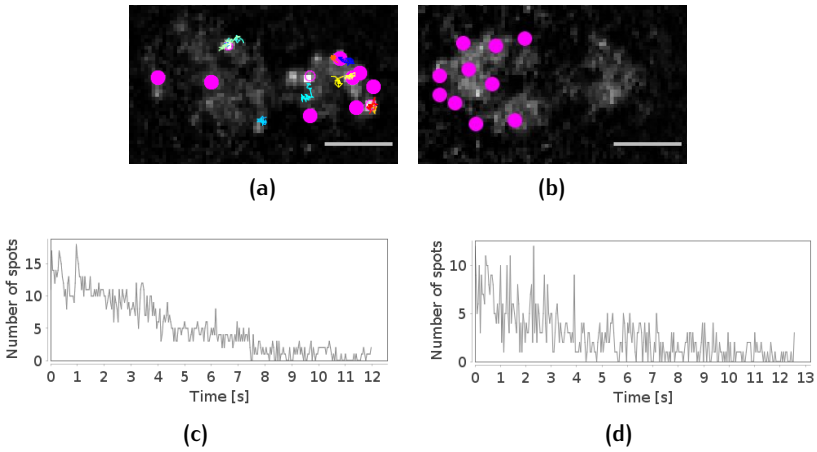

Figure 9: Visualization of the applied mRNA detection method. In these representative examples, particles are detected (pink spots) both in *mCLB2*-MS2 cells (figures 9a and 9c) and the control cells only expressing mNeonGreen-MCP (figures 9b and 9d). Based solely on the number of detected spots, controls and samples are similar. Note, however, that 8 trajectories (colored lines) with a length of 20 or more consecutive detections are found in figure 9a whereas none is found in the control cells (figure 9b). Across 12 control cells a single, stationary spot was detected > 20 frames (appendix A.1).

3.1.2.1 *Estimating the localization error*

Given the small expected mRNP displacements between consecutive images a fine-grained particle localization (sub-pixel localization) and a reasonable estimate for the localization error were desirable to analyze the cytoplasmic trajectories of *mCLB2* recorded by acMFM. The localization error is assumed to be independent for each time point and distributed normally (Michalet, 2010). It has been suggested that the localization error can be estimated from the offset of the mean MSD curve of purely diffusive trajectories (Michalet, 2010; Montiel et al., 2006; Savin and Doyle, 2005). I estimated the localization error for different scenarios. For details on the implementation see section 2.2.5. I evaluated the effect of pixelation artefacts that are commonly found at low SNR. Sample trajectories are shown in figure 32.

The mean error estimates (table 13) are below the size of a pixel (160 nm for my acMFM experiments), which suggests that there is usable information in the calculated subpixel localization. Additionally, the estimates were used to smoothen trajectories of *mCLB2* (figure 14).

The high STD indicates that this data does not strictly meet the requirements for the estimation method by Michalet, 2010. One of its assumptions is infinitely short detection times (40 ms exposure in my experiments), such that any motion blur will affect the estimate in an unforeseeable way. Interestingly, the estimate for localization error in presence of pixelation artefacts (first scenario) become more

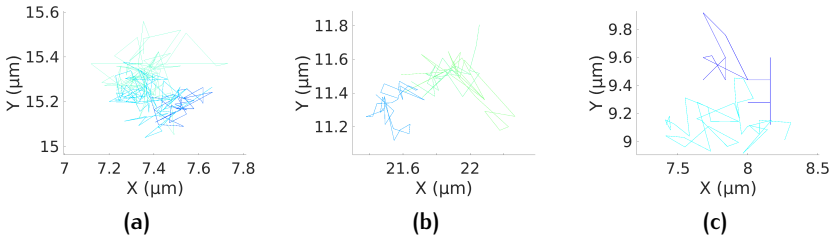

Figure 10: Sample stationary /diffusive tracks used for estimating the localization error. Figures 10a and 10b represent trajectories with sub-pixel localized RNAs, whereas figure 10c contains an example of a trajectory excluded from the MSD-based localization error estimation.

similar to the estimate provided by trajectories not suffering from this effect (i.e. when trajectories with pixel-level localizations were excluded, or in the 2D case) when using larger samples. For the last estimate above, I pooled all *mSIC1* trajectories (N = 521) leading to an estimate of σ=39 nm. Random sampling of intermediate trajectory numbers suggests that there is a slight trend for the estimate based on unfiltered trajectories to converge to the range determined in absence of the tested pixelation artefact. For further calculations, I assumed the error to be in the range of 40-70 nm.

3.1.2.2 *Non-normally distributed single time step displacements*

It became apparent that the observed displacement distributions are affected by pixelation artefacts (table 13). In particular the high central peak in figure 11a clearly is related to the breakdown of subpixel localization for certain positions. I investigated whether deviatons from the normal distribution of displacements persisted even when obvious pixelation issues were excluded, using the same data set as in table 13. To this end, I used the displacement distribution as a probability density and fitted it with a Gaussian as well as a Laplacian distribution to the observed single time step displacements. This resulted in a higher (closer to 0) log likelihood fit for a Laplacian distribution. In general, the goodness of a fit should be analyzed using the Akaike Information Criterion (AIC) (Findley and Parzen, 1995). Since both, the normal distribution and the Laplace (or doubly exponential) distribution require the estimation of k = 2 paramters, the log likelihood provides an equivalent criterion. All 1D displacements are thus rather distributed according to a Laplacian than a Gaussian PDF, as the log likelihood was closer to zero for a Laplacian fit (figure 12). To test wheter remaining pixel-level localizations were responsible for this effect, I removed *all* particle localizations that were not on the subpxiel level manually to confirm the findings. Again the Laplacian distribution was preferred (see figure 33).

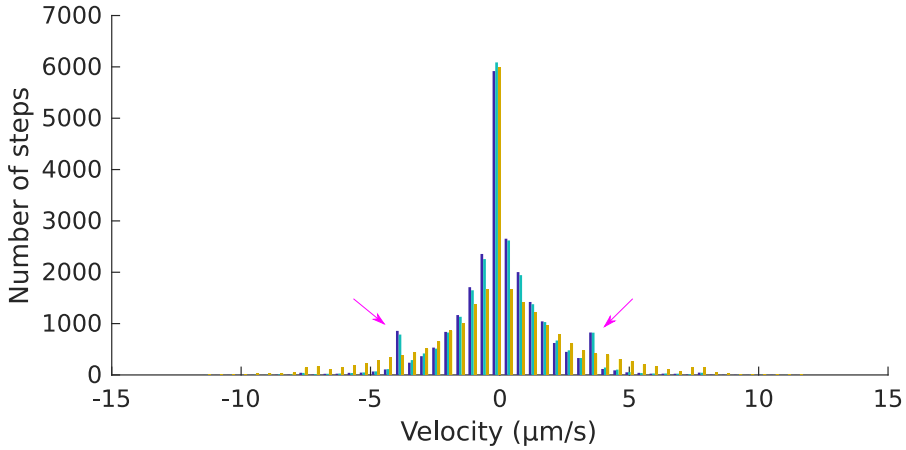

(a)

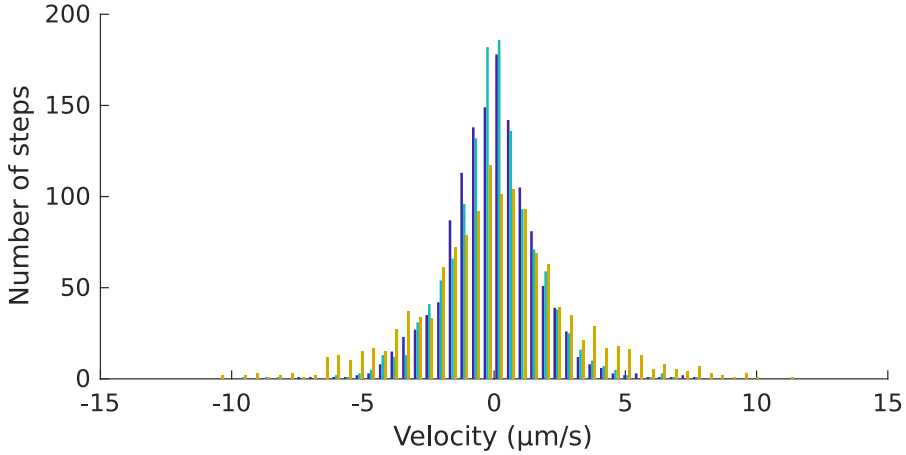

(b)

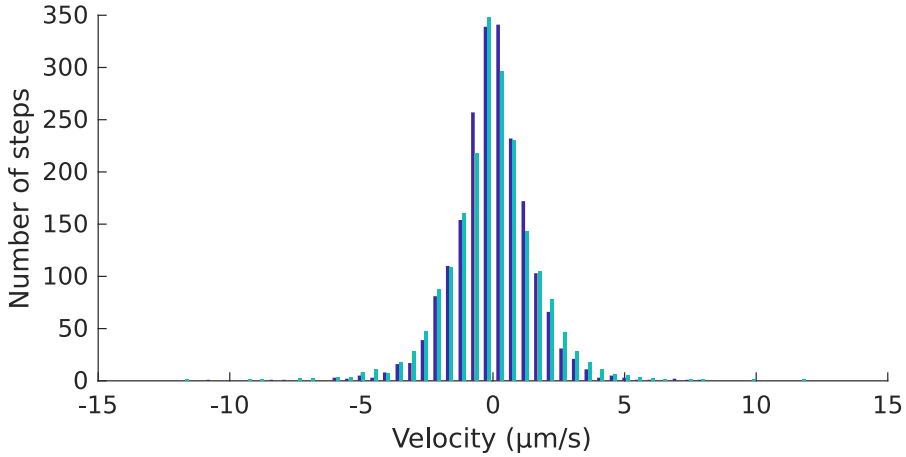

(c)

Figure 11: Single time step displacement histograms of cytoplasmic *mSIC1*. In figure 11a, displacements ('jump sizes') of 200 purely diffusive trajectories are shown for x (blue), y (green) and z (sand) independently. The high central peak as well as a set of lateral peaks (at 160 nm for x,y and $\sim$ 300 nm for z) are due to particle positions for which sub-pixel localization could not be achieved. Removing trajectories that lack sub-pixel localization in > 10% of the constituting positions decreased this bias, as can be seen in figure 11b (based on 26 tracks). Figure 11c: When particle detecion and linking was performed in 2D on maximum intensity projections of the images used in figure 11b no pixel-boundary effects were observed.

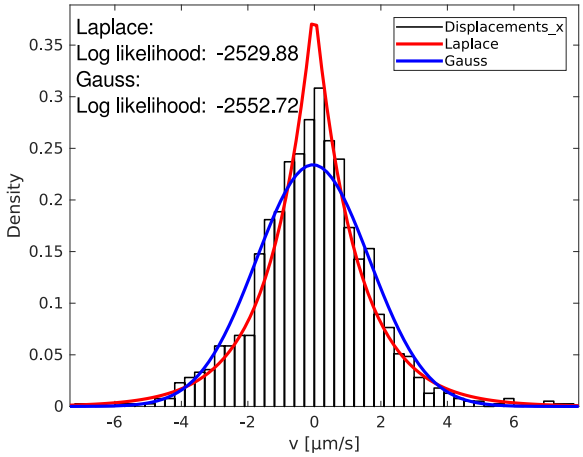

(a)

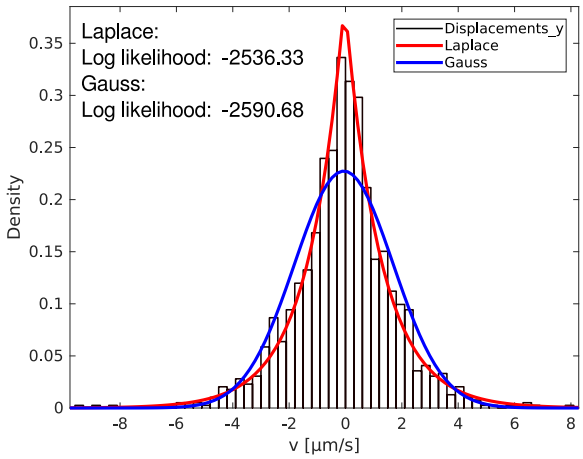

(b)

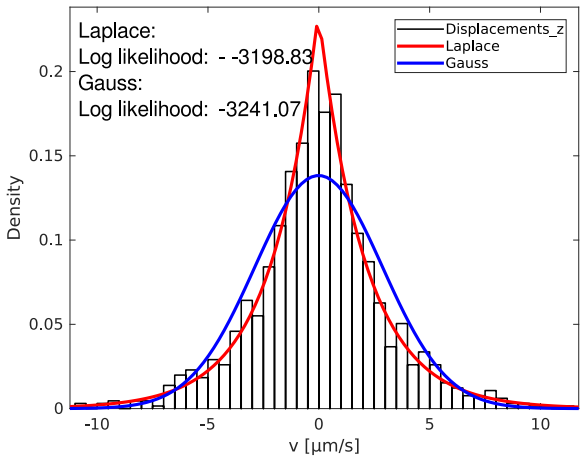

(c)

Figure 12: Probability density functions of one dimensional velocities of cytoplasmic *mSIC1* in x (figure 12a), y (figure 12b) and z (figure 12c). The density is calculated from displacement distributions on trajectories for which subpixel localization was successful (figure 11b).

Table 13: Estimated localization errors based on different sets of trajectories. The approach, based on Tarantino et al., 2014 provides similar estimates (40-65 nm) when exclusively subpixel-localized detections (row 2) or large amounts of tracks are used (last row). 'Stationary' trajectories were selected manually to have virtually no net movement (figure 32), whereas 'diffusing' designates all observed *mSIC1* trajectories.

TRAJECTORIES	ESTIMATED LOCALIZATION ERROR
3D, stationary	σ = 6 nm ± 6.3 µm (mean ± standard deviation (STD), N = 16)
3D, stationary, subpixel only	σ = 65 nm ± 214 nm (mean ± STD, N = 12)
2D, stationary	σ = 40 nm ± 120 nm (mean ± STD, N = 13)
3D, diffusing	σ = 87 nm ± 120 nm (mean ± STD, N = 55)
3D, diffusing	σ = 29 nm ± 1.3 µm (mean ± STD, N = 123)
3D, diffusing	σ = 24 nm ± 1.0 µm (mean ± STD, N = 129)
3D, diffusing	σ = 39 nm ± 913 nm (mean ± STD, N = 217)

3.1.3 Characterization of directed motion

A particular focus of this work lies on a method to detect and analyze long cytoplasmic mRNA trajectories in depth, whereas many SPT studies rely on ensemble averages of many short trajectories to describe the dynamics of single molecules. Often lower limits as short as 3 (Katz et al., 2016; Saroufim et al., 2015) points are applied to define trajectories worth investigating, and trajectories longer than 20 time points are not common in SPT analyses (Elf and Barkefors, 2018; Persson et al., 2013). The observation of transient types of mRNA motion, however, requires longer observations. Using a method by Monnier et al., 2015, I analyzed trajectories by applying a hidden Markov Model with Bayesian model selection to classify trajectories as diffusive, directed or both figure 13. Candidate trajectories were supplied as 3D trajectories and alternatively as 2D versions, disregarding the z-component. The method takes an estimate for the localization into account (70 nm were chosen) and 2 and 3 hidden states were tested. This results in the comparison of the likelihood of models taking into account 1-2 states of diffusion, and 1-2 states of directed motion. For all tested trajectories, the trajectories were preferentially explained by 1 -2 diffusivities; directed motion regimes were not identified with model probabilities < 10% figures 37 and 38, except for one example that was not interspersed with diffusive motion figure 39. However, even in the case of this last image, longer stretches of directed motion were not obtained.

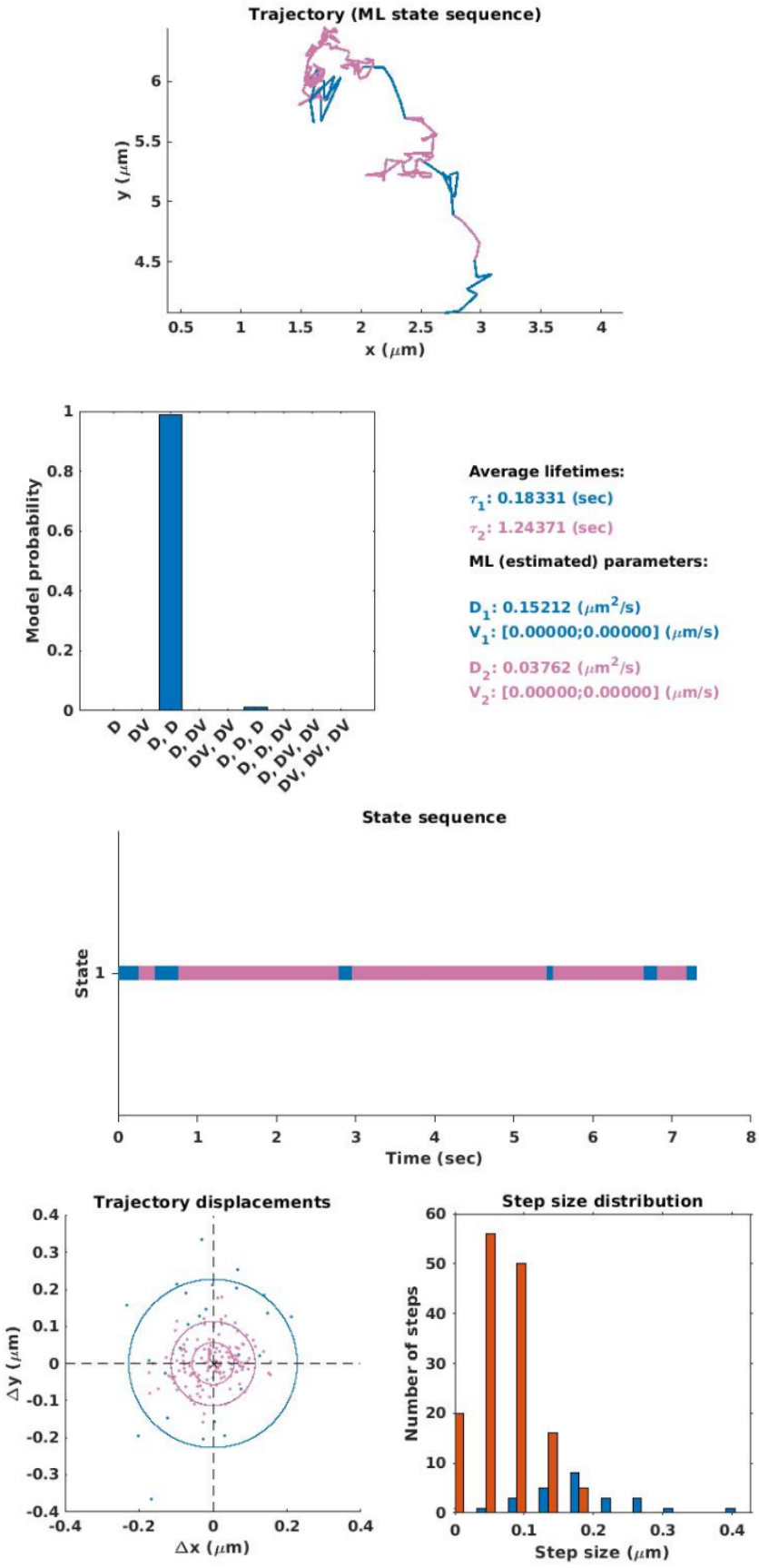

Figure 13: Representative example of a trajectory analyzed with HMM-Bayes. Here, the trajectory was used in 3D and up to 3 states of motion (hidden model states) were included. The estimated localization error was set to 70 nm. The cellular context of the trajectory is shown in figure 6.

Thus, I applied a method based on determining the persistence of a trajectory (figure 14). The persistence, defined as the cosine of two consecutive vectors, is 1 for movement along a straight line and -1 for a change in direction of 180°. On the experimentally measured trajectories, no regions of elevated persistence were identified due to the frequent changes in direction (figure 15). However, not all these changes in direction necessarily reflect the behavior of *mCLB2*. Taking into account the localization error estimate provided in section 3.1.2.1 I identified a smoothing parameter that made trajectories amenable to persistence analysis while retaining the characterstic shape of trajectories. Using a sample trajectory (figure 14a) which, according to visual inspection, contains sections of directed motion, I quantified the effects of smoothing. The mean distance between points on the smoothed trajectory and the original trajectory was 90 nm, which is in agreement with mean localization error estimates. Increasing the smoothing factors k (section 2.2.7) lead to increased distances and was therefore disregarded. The distance between smoothed and original trajectories was dominated by the z-direction (figure 14c). This can be explained by the large jumps due to pixel-level localizations. This effect causes larger (erroneous) jumps in z, as the axial voxel size was $\sim$ twice as large as the lateral pixel size, and since axial resolution is lower than lateral in widefield microscopes (see also figure 9). Of note, the step size along smoothed trajectories is drastically reduced compared to original trajectories (figure 14d). Average step sizes on smoothed trajectories were $\sim$50 nm (zero-displacements were excluded). This corresponds to motion with $v \approx 1$ µm/s in the present data, where time steps are determined by the imaging speed of 23.8 fps. With this approach, I have adjusted a method for analysis of sperm motility to generate improvements of trajectory analysis of intracellular single mRNA molecule translocation.

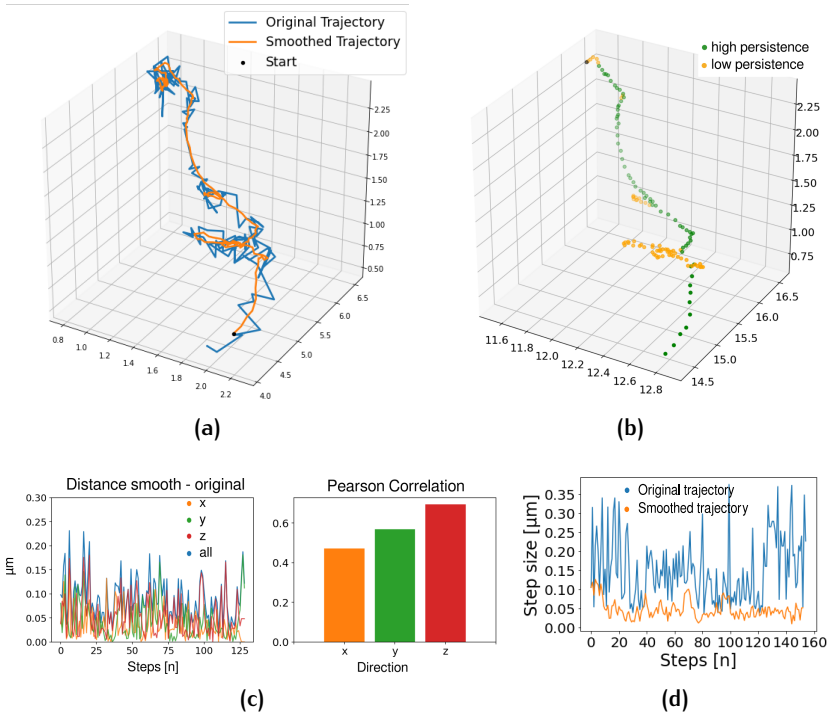

Figure 14: The smoothed trajectory (figure 14a) does not only recapitulate the behavior that is found 'by eye' but importantly the distances between the smoothed and the original trajectory are evaluated figure 14c to tune the deviations introduced by smoothing to the estimated localization error. An important consequence of this approach is that displacement distributions (figure 14d) become compatible with actomyosin transport (40 nm displacements correspond to speeds of 1 µm/s). The smoothed trajectory shows regions of highly persistent movement (figure 14b).

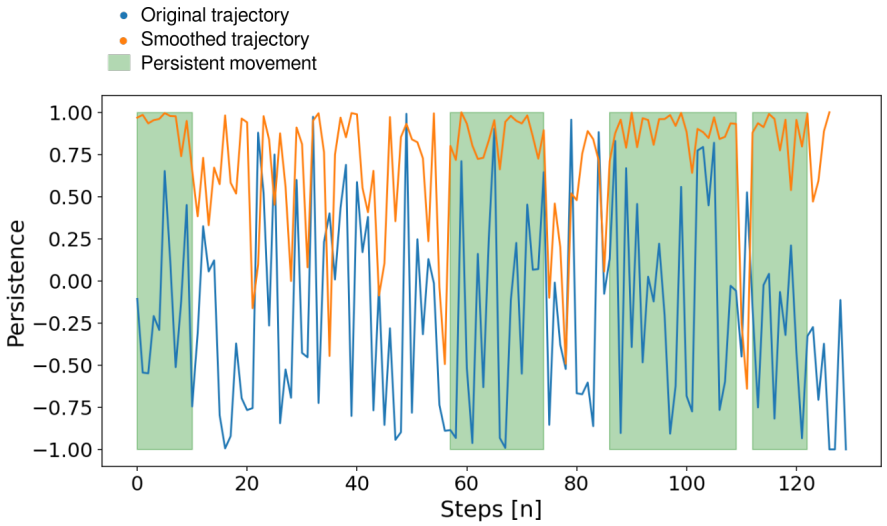

Figure 15: Balancing the experimental localization error and smoothing of particle trajectories makes trajectories usable for quantitative analysis while preserving key features of the observed motion.

3.2 *mCLB2* DISTRIBUTION THROUGHOUT THE CELL CYCLE

3.2.1 Cell cycle segmentation using endogenous fluorescent markers

To characterize the distribution of *mCLB2* on longer time scales I rely on data recorded by LLSM. The data presented here is based on cells that were observed throughout the budded phase. Relying on endogenous markers for structures that change with cell cycle progression all data could be mapped onto a relative cell cycle time scale (figure 16). To robustly determine the onset of budded phase I relied on tagged Cdc10p, which is part of the septin ring of the bud neck. After cell polarity is established around START (G_1/S) transition, the septin ring is formed within 2-10 minutes (Chen et al., 2011). This event is, like cell cycle progression in general, highly sensitive to light stress (Carlton et al., 2010; Chen et al., 2011). Importantly, the method used here minimizes photostress by selective plane illumination and its light beam geometry (Chen et al., 2014). The septin ring is irregular and faint at first, but becomes more pronounced when all required septins are recruited to the site of bud emergence (see appendix A.2, Chen et al., 2011). Cdc10p has been shown to be a reliable indicator of this septin ring formation (Kukhtevich et al., 2020; Okada et al., 2013). I used the first time point when a strong signal from the Cdc10/TagRFP ring observed (figure 16) as an indicator of the transformation of the septin ring into an hourglass shaped septin collar. This shape change has been shown to coincide with bud emergence (Haarer and Pringle, 1987; Kukhtevich et al., 2020) and is designated t_{START} for my experiments. The bud itself is initially not well visible in my experiments, given that brightfield acquisition was not possible with LLSM, and a dedicated fluorescent marker would have increased the risk of spectral overlap and a metabolic burden for the cells. To determine the time of M, I used fluorescently labeled histon proteins (Hhf2/mTurqoise). With this marker, the shape of the nucleus which changes over the course of the budded phase from a near-spherical to a variety of shapes, including elongated, hourglass, sausage and constricted appearances (Wang et al., 2016; Yeh et al., 1995) was monitored. The most clearly visible change occurring in all observed nuclei was the separation of one long hourglass-shaped nucleus spanning through the bud neck into two spherical nuclei. This morphology corresponds to the last phase of the closed M of yeast cells, telophase. Accordingly, I used this time as endpoint of mitosis; $t_{telophase}$. Lastly, decay of the septin collar of the bud neck collar into two separate rings was clearly visible in the observed cells. This process, abscission, marks the end of cytokinesis, as the septum which ties together cytoplasm of mother and daughter is severed at this time point, $t_{abscisssion}$ (Bhavsar-Jog and Bi, 2017; Onishi et al., 2013). Thus, I defined three well visible cell cycle

events that are directly linked to cell cycle progression. The time from bud emergence to telophase in cells that were used for quantification of *mRNA* localization was between 45 and 85 minutes. Including 17 cells for which I determined t_{START} and $t_{telophase}$ that were not used for *mCLB2* quantification, as either (i) the visible fraction of the cytoplasm was too small (out of focus) or (ii) bud or base were disproportionately out of focus, the total range for t_{START} and $t_{telophase}$ was 48 - 120 minutes (n = 30). Cytokinesis, the time between $t_{telophase}$ and $t_{abscisssion}$ was recorded for 26 of these cells and was 6 - 22 minutes. Histograms of durations are in the appendix figure 30.

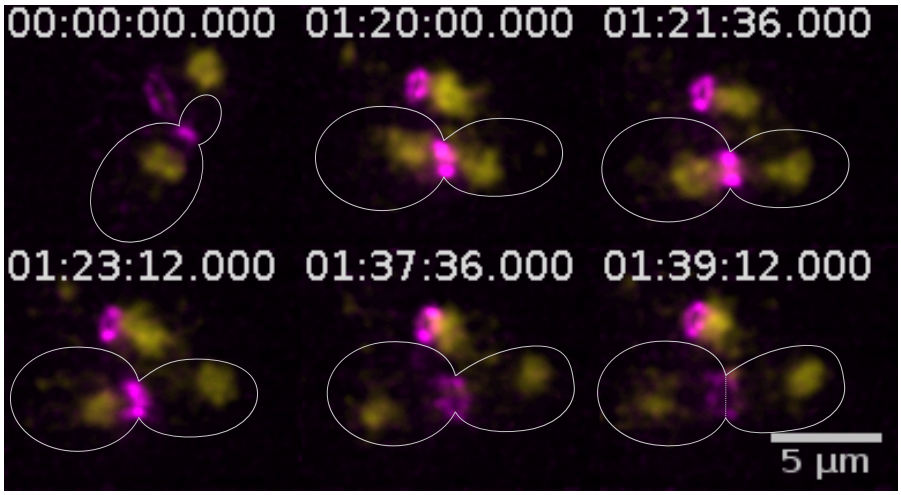

Figure 16: Fluorescent markers on bud necks and nuclei allow direct observation of cell cycle progression during budded phase. Endogenously labeled Cdc10/TagRFP (bud neck, magenta) and Hhf2/mTurqoise (nucleus, yellow) along with MS2-labeled mRNA (see figure 17) were observed at low laser power for several hours at high resolution (50 z-planes, Δ_z = 94 nm ~1 frame per minute) without inducing noticeable stress in the observed cells. Initiation of new budding events was observed throughout the observation times of 2 h. In the time series above the approximate outline of a single cell is marked in grey. The bud neck is observed from t_{START}. During mitosis, the nucleus squeezes through the bud neck adopting the characteristic hourglass shape of closed M (t = 1:20 h). In this time series, $t_{telophase}$ = 1:23 h shows the end of M, when nuclei are completely separated. Cytokinesis is complete at $t_{abscisssion}$ = 1:39 h, when two separate Cdc10/TagRFP rings (magenta) indicate the separation of the cytoplasm. Further time points, showing the formation of a new bud neck adjacent to the current one (axial budding pattern) alongside the complete time series (video) is found in figure 28. Scale bar = 5 µm.

3.2.2 *mCLB2* is enriched in buds at mitosis

Observation of single *mCLB2* throughout the budded phase by LLSM (Chen et al., 2014; Planchon et al., 2011) suggests a slight enrichment of *mCLB2* during late budded phase, in agreement with published data. Interestingly, localization within the bud was not confined to the tip, as suggested by live cell microscopy without single molecule resolution. Rather, oscillating distributions between mother and bud cells suggest that part of the bud localized *mCLB2* is unbound and can move back and forth between a cell's base and bud. An mRNA trajectory recorded by acMFM also suggests this behavior (figure 7). I quantified *mCLB2* throughout the budded phase of the cell cycle in eleven cells (figure 19 and figure 31). The time from bud emergence to telophase in cells that were analyzed was between 48 and 85 minutes. 17 cells for which I determined t_{START} and $t_{telophase}$ were not used for *mCLB2* quantification, as either (i) the visible fraction of the cytoplasm was too small or (ii) bud or base were disproportionately out of focus. Including these cells the total range for t_{START} and $t_{telophase}$ was 48 - 120 minutes (n = 30). The duration of cytokinesis was between 7 and 23 minutes. My interest was the quantification of *mCLB2*, which I found to peak in the bud at later time points during G_2 in agreement with Trcek et al., 2011. A previously not reported peak/peaks in mother cells is suggested in figure 18. All 11 cells underwent mitosis and cells displayed at least one time point with a minimum of four *mCLB2* molecules in the bud simultaneously, prior to mitosis (figure 19).

My single cell data (figure 19) further suggests large variability between cells both with regards to oscillatory behavior and absolute numbers in mothers and buds. The apparent subtle nature of possible *mCLB2* regulation obviously calls for larger screens with the here established methods for more rigorous quantification. However, several observations are generally found in this data set: In only one cell (Cell 6) was the highest detected *mCLB2* count in the bud not observed within few minutes around $t_{telophase}$ (it did occur prior to mitosis). The highest *mCLB2* count for one time point in a mother cell was lower than the highest number in a bud (mother = 9; bud = 14). All cells except one (Cell 7) had the highest *mCLB2* count in the bud, and this occurred early in S. This might be due to MS2-*mCLB2* carried over from a previous budding event. In the cell deviating from this pattern, two (lower count) peaks of *mCLB2* in the bud followed closer to mitosis. These observations are in agreement with the hypothesis that *mCLB2* localization is part of the gauging mechanism for biosynthetic capacity of the bud (Spiesser et al., 2015).

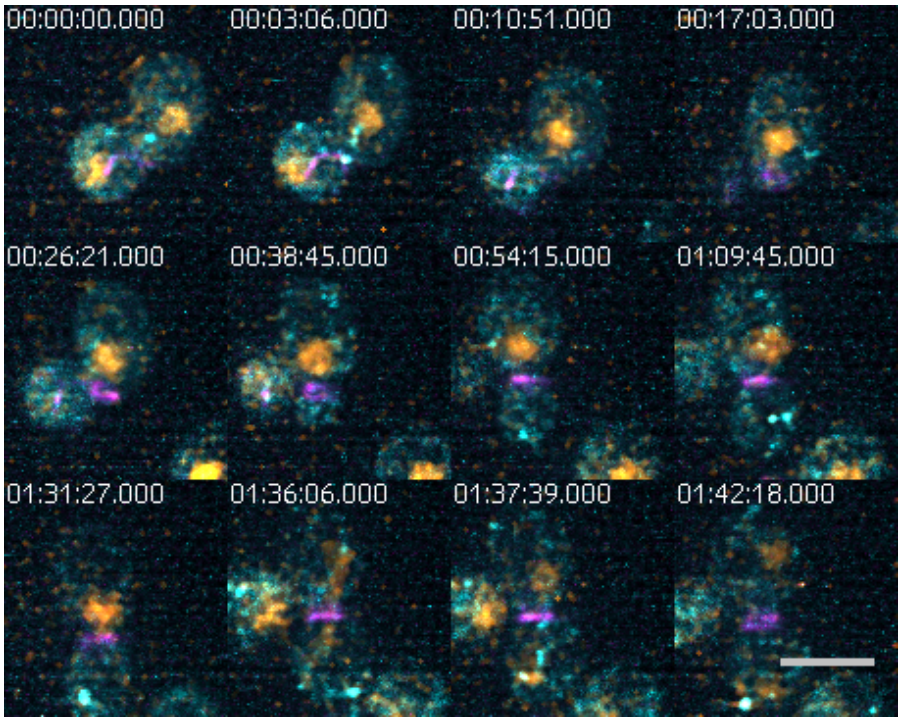

Figure 17: Distribution of *mCLB2* throughout the budded phase of the yeast cell cycle. mRNA distribution as well as the cell cycle phase were observed with a time resolution of 50-90 s by LLSM. End of M ($t_{telophase}$) is at 1:37 h. Cytokinesis is completed between 1:37 and 1:42 h in the example above. In the example *mCLB2* is disappearing during G_1 (time = 0 - 17 min approx.) along with the bud- or birth scar (magenta, adjacent to the site of the previous budding event). During S/G_2 (until 1:30 h approx.) *mCLB2* increase in mother and bud, while *mCLB2* numbers increase in the bud during late G_2 and M in this example. The entire time series as well as 3D projections of the full 50-image z-stacks and a collection of videos is listed in appendix A.2. Scale bar = 5 µm.

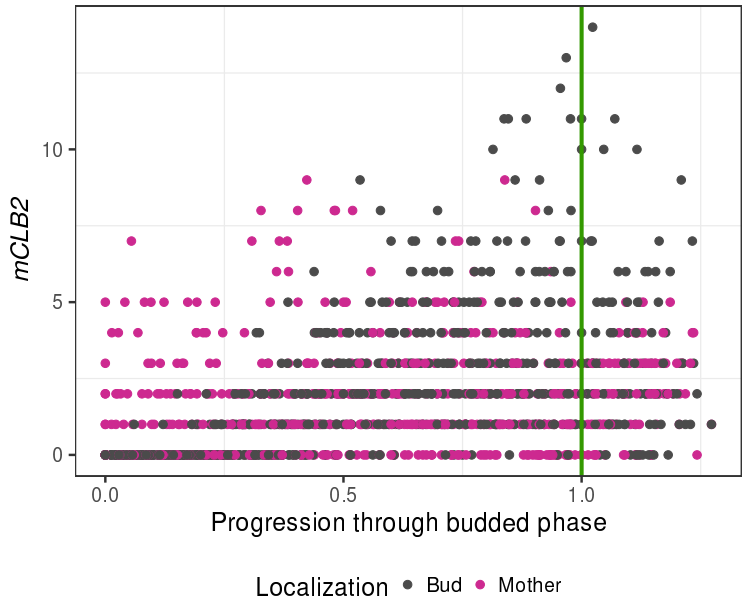

Figure 18: Number of *mCLB2* molecules detected in mothers (pink) and their buds (grey) by LLSM. The distribution of *mCLB2* was quantified for cells which progressed from START to telophase, the last phase of M, in 48 - 85 minutes. The last time point is $t_{abscisssion}$. $t_{telophase}$ (mitosis) is indicated with a green vertical line. Time was normalized to 'progression through budded phase' as detailed in figure 31 to allow pooling of the data. *mCLB2* appears to peak first in mother cells, whereas later in S-G_2-M seemingly more transcripts are found in buds. This plot shows pooled time courses of 11 cells. The same data for individual cells is shown in physical time (minutes) in figure 19. Single time courses (normalized time) are in figure 31.

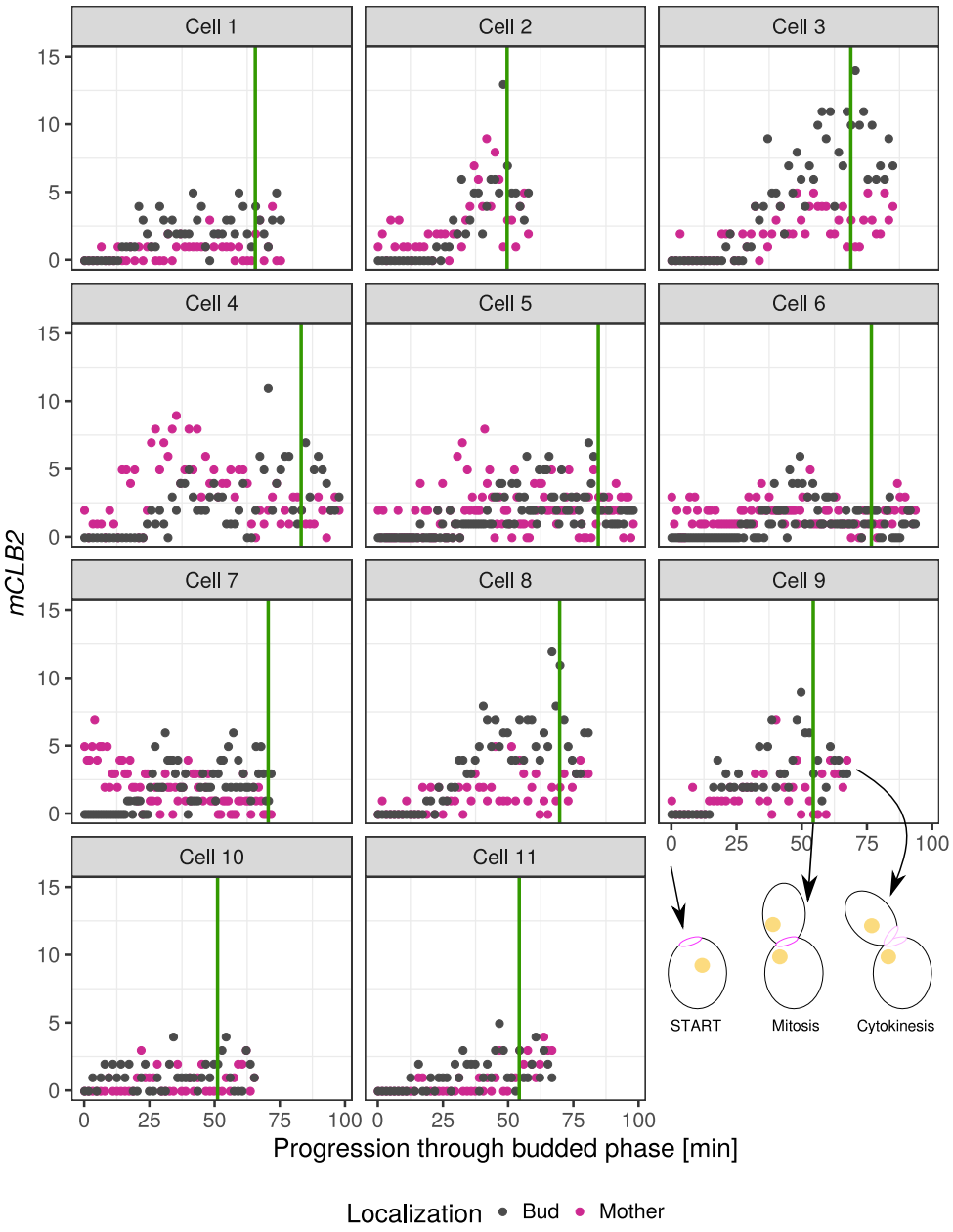

Figure 19: Number of *mCLB2* molecules detected in mothers and their buds. These panels show the distribution in eleven cells that progressed from START to telophase (vertical green line), the last phase of M, in 45 - 85 minutes. For comparability, time courses were cropped at $t_{abscisssion}$. *mCLB2* peaks first in mother cells, whereas later in S-G_2-M more transcripts are found in buds. Interestingly, *mCLB2* numbers decrease during cytokinesis suggesting that the MS2 system does not hinder the phase specific degradation of *mCLB2*. A version of these plots where time is replaced by a normalized 'progression through budded phase' is in figure 31.

4 DISCUSSION

4.1 THE ROLE OF *mCLB2* LOCALIZATION FOR MITOTIC ENTRY

Live cell microscopy by LLSM suggests that *mCLB2* becomes increasingly enriched in the bud of yeast cells in G_2 cells; a finding confirmed by smFISH. The localization is, however, a subtle effect and a considerable amount of *mCLB2* is found in a cell's base (the becoming mother cells) throughout the budded phase. Importantly though, thanks to the high spatial and temporal resolution facilitated by LLSM and improved MS2 tags I discovered unknown dynamical aspects of *mCLB2* localization. By imaging over the entire budded phase, my data suggests a temporal separation of *mCLB2* enrichment in mother (early S/G_2) and bud, respectively, with bud enrichment occurring around mitosis (figure 18). With this high resolution I am also able for the first time to suggest a minimum number of *mCLB2* that become bud localized in fast growing yeast cells prior to mitosis. This aspect is of interest since different lines of evidence suggest that *mCLB2* is translationally repressed while in the mother cell (section 4.4.1). Thus, only bud-localized *mCLB2* would be translation competent. If the suggested lower bound for bud localized *mCLB2* holds, it would also indicate that the exact timing of *mCLB2* bud enrichment is of lesser relevance, since the analyzed cells display significant variation with regards to *mCLB2* number and spatial distribution prior to M. In other words, the time of the peak of bud localized *mCLB2* does not seem to be critical, based on my data. Those differences indicate that further mechanisms are likely to be involved in bud size sensing. My single cell, single molecule data supports previous reports on enrichment of *mCLB2* in buds prior to and during mitosis (Shepard et al., 2003; Trcek et al., 2011). In addition, to my knowledge this is the first report demonstrating a peak or possibly two peaks (e.g. Cells 2 and 3 in figure 19) of *mCLB2* in mothers during early budded phase, as opposed to a steady production and transport to the bud. Such oscillatory behavior could reflect the *CLB2* transcriptional regulation. The key factor determining transcription of the *CLB2* cluster, Fkh2p, activates transcription directly, and indirectly via its interaction with Clb3/Cdk1 and Clb5/Cdk1 in a coherent type I feed forward loop (Linke et al., 2017). It is tempting to speculate that the oscillations of *mCLB2* numbers reflect the direct activation and the delayed, Clb/Cdk-mediated activation of *mCLB2* transcription.

4.2 INVESTIGATING ACTIVE TRANSPORT IN LIVE CELLS

The single *mCLB2* trajectories observed by acMFM rarely seemed directed. However, considering the low number of *mCLB2* per cell and the anticipated duration of translocation into the bud (table 12) this is to be expected: Typically, $\sim$ 10 *mCLB2* are present in a cell (see figures 18 and 34) and this mRNA has been reported to be stable throughout S-G_2-M (Trcek et al., 2011). The assumption that only one *mCLB2* is transported at a time lead to the best case scenario for an observer hoping to detect transport. In this scenario the total duration of transport events would be less than 1 minute. Based on my LLSM experiments, the budded phase (t_{START} until $t_{abscission}$) lasted $\sim$ 80 minutes in a typical cell figure 30. Thus, during 1 in 80 minutes should mRNA translocation be observed. Since I did not select cells with very small buds for acMFM imaging, the success rate for observing directed motion of *mCLB2* could be slightly higher. Essentially, though, one of hundred experiments (of negligible duration, t = 13 s) is expected to contain a translocation event into the bud, if no backward movement occurs. I have scanned 500 cells approx., and detected 1 translocation event from mother to bud, as well as a translocation in opposite direction (figures 6 and 7), along with other suspected translocation events (e.g., figure 38) that could not be confirmed with my thresholding approach. Therefore, I consider the number of detected trajectories to agree with literature data (table 12, (Trcek et al., 2011)). To identify directed motion on short time scales is challenging, since the localization error is often in the range of expected displacements. It is therefore not immediately clear, how trajectories can be processed to (i) retain the true displacements and (ii) limit the influence of the localization error due to limited SNR. The smoothing approach I have applied makes trajectories amenable to persistence analysis. This method has the potential to identify directed motion in yeast, where the expected trajectories due to actomyosin-transport are curvilinear and contain a 'kink' at the bud neck. The smoothing approach resulted in what I deem to be a more realistic trajectory, especially since particle velocity in parts which were found to be persistent (directed) correspond well with myosin dependent actomyosin transport speeds (1 µm/s) after smoothing. Prior to smoothing (i) persistence length was negligible and (ii) the single displacement sizes corresponded to velocities too high to be compatible with myosin V dependent transport (table 12). While directed mRNP motion, interpreted as SHE-dependent actomyosin transport, has been observed in yeast cells more than 20 years ago (Beach et al., 1999; Bertrand et al., 1998; Takizawa and Vale, 2000), it is challenging to approach a visualization that does not suffer from too much noise and is representative of the unstressed, physiological behavior of the tagged molecule. Even

the earliest description by Bertrand et al., 1998 achieved a long-lived clear signal allowing the observation of *mASH1* translocation from a yeast cell's base to its bud. The MS2 system facilitated this, yet the artefacts caused by this method require independent controls and methodological improvements. The particles tracked in Bertrand et al., 1998 are almost certainly composed of all present *mASH1* in a cell, which was overexpressed with a galactose inducible promoter (Long et al., 1995), providing a strong signal. Imaging *single* mRNAs requires increased sensitivity, brighter fluorescent tags, and of course a tag with a lesser tendency to form aggregates. Single mRNPs are also expected to possess a higher mobility as their hydrodynamic radius is smaller. Accordingly they are lost from the focal plane faster and harder to detect as the PSF is more likely to be affected by motion blur. The long-known tendency of MS2 tagged mRNA to form aggregates was mostly neglected in publications until Tutucci et al., 2018 presented a new generation of the MS2 system reported to form fewer aggregates and to not inhibit *Xrn1*-mediated degradation. The novelty of this MS2-generation consists in reverting a single nucleotide mutation that originally was introduced into the wild-type MBS to increase MBS-MCP affinity 10-fold, and modifying the linker-length between the MBS-stem loops. In this work, I took on the challenge of improving the observation of single cytoplasmic mRNP from three different angles: (i) construction of smaller, brighter and more photostable MCP-tags based on mNeonGreen, (ii) use of MCPs optimized in our lab to decrease the formation of aggregates and (iii) the use of acMFM to gain depth of field and 3D resolution. As elaborated in Hansen et al., 2018 and Song et al., 2018 (particle trajectory analysis) and theoretically treated by Metzler et al., 2014 many particle tracking approaches rely on short trajectories (low focal depth) and often fast moving particles could be missed. In this project, I observed translocation from mother to bud only in few instances. This is to be expected from the low number of *CLB2* transcripts, the fast dynamics of actomyosin transport and the short time window during which cells could be observed before photobleaching was complete, even with my specifically designed mNeonGreen tags. The directed trajectories I extracted are, however, an opportunity to aim for analyses of single RNP trajectories that are not accessible by analysis of ensemble averages. In neurons, trajectories of RNA molecules have been shown to mature over time; e.g., by an ageing Lévy walk (Song et al., 2018). In axonal transport, this behavior arises from alternating motor-protein dependent superdiffusion and stationary tumbling. For yeast, one prerequisite for such analyses is the possibility to quantitatively characterize trajectories long enough to capture this switching, and fast enough resolve short live, transient states of motion. One method that has been used to quantify transient particle dynamics in neurons is HMM-Bayes (Monnier et al., 2015). It applies a hidden Markov model to allow state switching at every

time step of a trajectory and enforces some continuity by penalizing this switch by applying Bayesian model selection. At least for the most sensitive implementation of the algorithm, in order to recognize directed motion, the method expects this transport to always point in one direction. For trajectories of mRNA in yeast the model did not, however, predict directed motion, even in cases where this was the impression 'by eye' (see figure 13).

4.3 RNA PARTITIONING IN YEAST CELLS

> *Nihil est in intellectu quod non sit prius in sensu*
> Nothing is in the intellect that is not first in the senses
>
> *Thomas Aquinas*

Looking at mRNP motion and localization in yeast, I find two very general points interesting. First, an mRNA is an order of magnitude heavier than the protein it encodes. For globular proteins, even the size ratio follows this rule of thumb. Whereas the radius of Clb2p is roughly 2.5 nm (491 amino acicds, size approximated by a sphere) (Erickson, 2009), radii of gyration of $\sim$ 20 nm have been measured for mRNAs of $\sim$ 1500 and $\sim$ 2700 nucleotides (Gopal et al., 2012). This radius, which equals the hydrodynamic radius of RNA molecules (Borodavka et al., 2016), might well be similar for *mCLB2*, which totals a length of 2197 nucleotides (including UTRs, David et al., 2006; Gill et al., 2004). As the cytoplasm is a crowded and highly viscuous environment, this 10-fold difference in size affects diffusivity more drastically than would be observed in water, i.e., according to the Sutherland-Stokes-Einstein formula (equation (4), Szymański et al., 2006; Verkman, 2002). Second, the displacements of diffusing mRNAs can be larger than those of actively transported RNA for delays up to seconds. For mRNP dynamics in yeast cytoplasm, type V myosins are the widely accepted agent of actin dependent transport (Casolari et al., 2012; Shepard et al., 2003). Studies *in vivo* and *in vitro* have shown that these motors move their cargo at processive speeds of up to 1200 nm/s (Baker et al., 2004; Clemen et al., 2005; Pierobon et al., 2009). For diffusing particles, however, only a distribution of velocities (like the Maxwell-Boltzmann distribution) can be determined. Measurements of mRNA diffusion in yeast have found displacements up to $\Delta = 300$ nm for delay times $\delta = 15$ ms, and $\Delta = 450$ nm for $\delta = 150$ ms (Lampo et al., 2017). Only at longer times does the intuitive notion that active transport is 'faster' than diffusion become true, in the sense that it can cover longer linear distances. This has practical implications for the analysis of particles for which both, 'slow 'directed transport and 'fast' diffusion.

4.3.1 Asymmetry in purely diffusive systems

Upon cell division, the budding yeast cytoplasm is divided into two cells of unequal size. Certain components, like DNA, need to partition in an equimolar fashion, whereas for other molecules, like ribosomes, the concentration is roughly identical in both cells. While DNA partitioning is a highly orchestrated process, the distribution of many proteins, RNAs, ribosomes etc. can be parsimoniously explained by diffusion (Politz et al., 2003; Verkman, 2002). There are, however, cases where partitioning is unequal both with regards to concentration and molecule numbers. This phenomenon can be explained by a number of processes, including active transport and localized retention. It might be surprising, though, that purely diffusive processes can suffice for asymmetric partitioning given the shape and size of a yeast cell in budded phase (Kinkhabwala et al., 2014; Schuss et al., 2007). In the cited works, a mathematical framework is established that treats the partitioning of diffusing molecules in enclosed domains with an opening that is small compared to the domain. This framework, the narrow escape problem, can be used to describe macromolecules diffusing in the base (mother cell) of dividing yeast and 'escaping' through the bud neck. The analytical description of this narrow escape problem for partitioning in yeast by Kinkhabwala et al., 2014 established, not surprisingly, that enrichment in the bud cannot be obtained by diffusion with a single diffusion constant D describing the movement of a given molecule class throughout the cytoplasm. Rather, the molecule numbers follow the volumetric ratio between bud and mother just before cytokinesis, which is roughly 1/3 - 2/3 depending on the replicative age of the mother cell (Zadrag-Tecza et al., 2009). This behavior persists even when the bud neck opening is increased, as long as the approximation of a 'narrow escape' holds. Enrichment in the bud can, however, be achieved by different compartmental diffusion constants, i.e., $D_{bud} \neq D_{mother}$. In this context, I contribute a further data set on the characterization of diffusive motion in the yeast cytoplasm. Analyzing single time step (δ_t = 40 ms) displacements of diffusive mRNPs I found a better fit to a Laplacian PDF than a Gaussian PDF (figures 12 and 33) in agreement with fits by Lampo et al., 2017 for shorter and longer δ_t; suggesting that the subdiffusion process outlined in that paper is observed for different mRNA species in the yeast cytoplasm . This could be further analyzed, e.g. with regards to bud localized *mCLB2*, which did not seem to be anchored in many of the observed cells. It is tempting to speculate that the wide range of mRNP diffusivities found in earlier works (Lampo et al., 2017) be instrumental in bud enrichment of certain mRNAs including *mCLB2*.

4.3.2 Single molecule detection

The detection of single molecules is the first challenge in the analysis of single molecule dynamics. While for fixed cells (smFISH) the uncertainty related to the detection - mainly detection efficiency and false positive rate - is manageable, for live cell imaging, particularly in 3D this uncertainty is less well defined (Cai et al., 2014; Juette et al., 2008) and has the potential to invalidate all subsequent analyses. A number of approaches have been developed to improve particle detection, particularly for applications with pronounced photobleaching, high noise and background (Izeddin et al., 2012; Smith et al., 2010), such as live cell single RNA tracking. In information theory, similar challenges are well known and have been formulated by Harry Nyquist more than half a century ago, e.g., in the context of signal transmission in the presence of intersymbol interference and noise (Forney, 1972). In the cited publication, a maximum-likelihood estimator for the decoding of a transmitted sequence in the presence of noise, a detector called whitened matched filter, was proposed. Sage et al., 2005 applied such a filter to the analysis of noisy single molecule live cell images, making use of the striking, fractal nature of noise often found in biological image data (Pentland, 1984). This fractional nature is key for the applicability of a matched filter, which by design takes into account correlations to maximize SNR. Approximating the fractal exponent of the noise distribution of a fluorescence micrograph (s=1.8) which follows its spectral power density by the value of 2 proved to effectively transfer the whitened matched filter into a LoG detector. This filter is commonly used for particle detection (Godinez et al., 2009; Pichon et al., 2016; Tinevez et al., 2017; Tsanov et al., 2016). These detection methods are more powerful in identifying particles in the presence of noise than a simple search for maxima. This is because they determine how salient a feature is above the local background by applying a Laplace operator (i.e., the sum of second order derivatives) to an image blurred with a Gaussian kernel, or by subtracting images that were previously convolved with one of two correlated Gaussian kernels, each. While this approach has proven useful, setting a threshold is a quite subjective process. Particularly when signal strength of individual particles is variable and there are inhomogeneities on different length scales, setting a threshold high enough to prevent false positive detections severely limits the chance to extract non-stationary RNA trajectories. A focus on only the spots with highest quality also biases against the detection of fast moving particles (that might show an interesting behavior) as they could suffer from motion blur and thus not correspond to the expected diffraction limited spot ('blob' in 3D). I used the simpler DoG (Marr and Hildreth, 1980) which approximates the LoG detector well and agreed better with my manual spot segmentation than a LoG. As acquisition times in my experiments were short (33-40 ms per frame) given the expected particle speed

(Baker et al., 2004; Lampo et al., 2017; Pierobon et al., 2009), I did not expect considerable blur or deviations from the symmetric shape of the RNA-blob/spot, which is why I did not pursue approaches that can improve detection in such cases (Kong et al., 2013). While further methods for the detection of single molecules, e.g., relying on local radial symmetry (Loy and Zelinsky, 2003) or the analysis of features on several length scales (Olivo-Marin, 2002), none of the methods mentioned so far can quantify the extent of false positive detections. Probability based methods, however, give the experimenter the choice to limit false positive detections – obviously at the cost of increased false negatives. Smith et al., 2015 used a generalized likelihood ratio test for spot detection that can utilize previous knowledge regarding the camera PSF and the measured noise statistics of the camera to avoid the necessarily subjective step of thresholding. Tang et al., 2016 recurred to Bayesian model selection based on photoelectron counts, explicitly also those from false positive spots. While I did not explicitly address the problem of false positives in this way, I assume that my focus on long trajectories (> 20 time steps) is an effective method to remove spurious detections. This assumption is supported by the fact that my extensive manual and automated thresholding led to parameters that prevented the extraction of trajectories in cells containing fluorescently tagged MCPs, but no binding sites on the mRNA (negative controls). In cells containing the entire MS2 system, I confirmed extracted trajectories by visual inspection. I therefore consider my approach robust and conservative, limiting false positive detections. For particle detection in the acMFM time series, which are heavily affected by photobleaching, a dynamic thresholding approach could have been an attractive approach. One example is an algorithm decreasing the threshold for minimum spot quality as a function of time to deal with decaying signal (Eglinger, 2017). As the spot quality varies considerably between successive detections in visually confirmed trajectories, presumably due to its dependence on the axial position of an emitter, I did not apply such a method for my project.

4.4 OUTLOOK

4.4.1 Translation imaging of localized *mCLB2*

mCLB2 is expected to be under tight translational control (sections 1.3 and 1.4.2). The canonical description of the *ASH1*-type actomyosin transport complex in yeast involves two translational repressors (reviewed in Heym and Niessing, 2012), and *mCLB2* has been shown to possess a high affinity for the adapter proteins involved in *ASH1*-type transport (She 2-4, Shepard et al., 2003). This data suggests both actomyosin dependent transport, and translational repression of *mCLB2*.

Deletion of *SHE* genes was also suggested to abolish *mCLB2* bud-localization in this publication; although the results should be taken with caution due to the lack of single molecule resolution of the applied U1A method. Translational repression of *mCLB2* has also been found irrespectively of the identity of involved proteins by polysome profiling (Arava et al., 2003). Thus, *mCLB2 localization* could be complemented by bud localized *mCLB2 translation* in the control of G_2/M transition and the two may jointly act as a bud sizer. By producing the major promitotic cyclin Clb2p, localized translation would relay the status of the periphery (the bud) back to the central CDK oscillator in the nucleus. The seemingly slight difference between the role of localized mRNA and localized translation has drastic implications on experimental design for hypothesis testing. To directly address the localized translation hypothesis, I attempted to establish the published methods for live cell single molecule translation imaging, techniques referred to as single-molecule imaging of nascent peptides (SINAPS) and nascent chain tracking (NCT) (Morisaki et al., 2016; Wang et al., 2016; Wu et al., 2016; Yan et al., 2016). I will briefly discuss the potential of these methods and mention my own observations (data not shown). These methods rely on the binding of fluorescently labeled antibody mimics to repetitive sequences of short linear epitopes at the N-terminus of a protein of interest; colocalization with tagged mRNA is then interpreted as translation. One of the systems ('Suntag', Tanenbaum et al., 2014) used in three of the pioneering publications of NCT, (Wang et al., 2016; Wu et al., 2016; Yan et al., 2016) unfortunately exploits a yeast epitope. It is part of the dimerization site of the transcriptional activator Gcn4p, and the development of this NCT technique could draw on *cytoplasm-soluble* antibody fragments that have been created against this region (Worn et al., 2000). The Suntag system is thus not orthogonal for yeast, and I did not observe specific spots in yeast cells expressing the system. The alternative approach (Morisaki et al., 2016) replaces the linear epitope array of the Suntag with multiple FLAG- or HA-tag epitopes that are presented on the scaffold of a darkened GFP, a so called spaghetti monster (Viswanathan et al., 2015). This type of mounting epitopes on the characteristic β-barrel of fluorescent proteins has been shown to increase epitope-antibody affinity and, importantly, improve solubility. As GFP is widely used in yeast, I also tested this system for translation imaging. I avoided the use of small molecule fluorophores and exogenous antibody-fragments used in Morisaki et al., 2016, which are expected to be problematic in yeast (see section 1.5.1). Instead, I used endogenous GFP-labeled anti-FLAG hybrid antibodies ('Frankenbodies', Zhao et al., 2018, 2019) but again could not detect a specific signal. Similarly, yeast cells expressing the 'Moontag' translation imaging system (Boersma et al., 2019; Boersma et al., 2018) which relies on an HIV epitope did not yield specific signal in yeast cells. Imaging the first round of translation in yeast

cells by translating RNA imaging by coat protein knock-off (TRICK) (Halstead et al., 2015) is possible (e.g. Neurohr et al., 2018), as it relies on the well established PP7 and MS2 techniques. So far, however, no NCT technique has been published for yeast. Filling this gap in the toolbox of single-molecule live cell techniques will undoubtedly help to clarify whether *CLB2* localization is involved in bud size sensing. My data is in agreement with the hypothesis that *mCLB2* bud localization contributes to cell cycle progression in budding yeast. I agree with Spiesser et al., 2015 that localized *mCLB2* translation could act as a bud sizer, and want to emphasize the importance of a clear distinction of mRNA localization and localized translation for hypothesis testing. Ongoing efforts in other labs (discussed in confidence) focus on using antigen/antibody pairs specifically selected for solubility in yeast to establish NCT in this model organism.

4.4.2 3D single molecule imaging perspectives

I aimed to image fast cytoplasmic mRNA dynamics; requiring advanced microscopy and the concomitant experimental effort. Hardware-based methods for instantaneous volumetric imaging have recently started to face stiff competition from experimentally less demanding software methods. Deep-Z (Wu et al., 2019) exploits axial asymmetry in the wide-field PSF to extend depth of field up to 20-fold. This technique does not require any additional hardware or image acquisition, only a one-time effort to record a sequential scan of a point shaped light source once for each imaging setup - although the authors even show that Deep-Z is useful for refocusing in other modalities than those used for training (e.g widefield vs. confocal imaging). This mechanical axial scan is used to train a neural network (generative adversarial neural network) to digitally refocus on an arbitrary plane within the increased optical depth. This technique avoids the adverse effects on field of view or PSF overlap found in 'hardware' 3D imaging. A preliminary test by Wu et al., 2019 showed that a DH-PSF can be faithfully reconstructed by Deep-Z; suggesting this technique could be able to provide similar optical depth as the PSF engineering technique, without requiring specialized optical components. At the time of writing, applications of Deep-Z were limited to lower magnifications (up to 20 x) that are useful for cell-segmentation, but not single molecules. Current work focuses on faster algorithms for 3D reconstruction and improved fidelity at large distances from the (hardware) optical plane (Ma et al., 2020). Future volumetric imaging could also employ a combination of multiple focus planes and deep-learning approaches to push the limits of optical depth. While the instantaneous acquisition of large axial volumes is hard to beat when fast dynamics in the cytoplasm are observed, sequential imaging techniques are improving. LLSM, which I used in its prototype stage, uses the photon budget

available for live cell imaging more efficiently than widefield methods and is capable of up to 300 fps. As mentioned earlier (section 1.5.3), selective plane illumination methods, like LLSM, are increasingly competitive for single molecule imaging. A major challenge for my data analysis was that data acquired with the custom-built LLSM setup requires deskewing of images (which is computationally expensive) before image volumes can be visually evaluated; MIPs were used to confirm appropriate imaging conditions immediately after experiments. Therefore, I realized that most of the acquired images did not cover the entire cytoplasm (along the vertical sample axis) only towards the end of the available slot for imaging. With the setup I used, I could show that single mRNP imaging with high temporal (∼1 min) and near-isotropic resolution of ∼ 300 nm is possible for extended periods of time (multiple budding events) and does not interrupt cell cycle progression. To achieve this I used my mNeonGreen-based MCPs for increased brightness and photostability compared to GFP (Shaner et al., 2013). As LLSMs with standard sample mounting are, as of December 2020, commercially available (Zeiss Lattice Light Sheet 7) it should be feasible to generate much larger data sets on single RNP distribution over the cell cycle in yeast using my improved tags and endogenously marked yeast strains.

Part I

APPENDIX

A APPENDIX

A.1 MULTIFOCUS MICROSCOPY VIDEOS

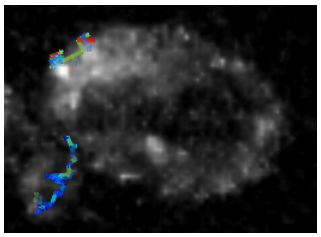

Figure 20: All trajectories of *mCLB2* that were detected for a minimum of 50 consecutive frames. Color of the trajectory indicates the linking cost (see section 2.2.4, blue = low, red = high). Filename: 3D_overlay.avi.

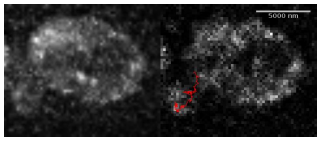

Figure 21: MIP of yeast cell with translocating *mCLB2*. Right: The result of SPT with TrackMate. Left: MIP of the image file used for generation of the trajectory. Filename: Side_by_side.avi.

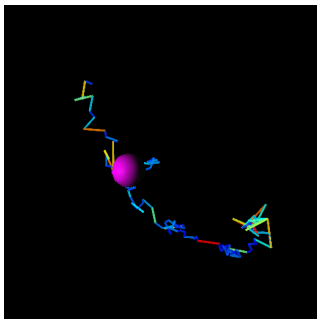

Figure 22: Trajectory of *mCLB2*. The pink ball represents the detected spot moving along the trajectory. The cellular context of the cell is visualized in figure 21 and figure 20. Color of the trajectory indicates the linking cost (blue = low, red = high) Filename: 3D_base2bud.avi.

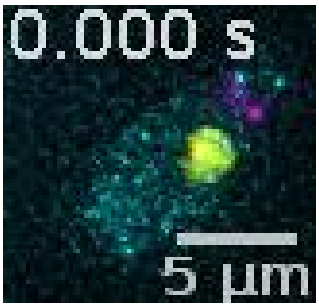

Figure 23: Video of *mCLB2* (cyan) moving from bud to base. Bud neck is magenta, nucleus is yellow. Filename: 3D_bud2base.avi.

A.2 LATTICE LIGHT SHEET MICROSCOPY

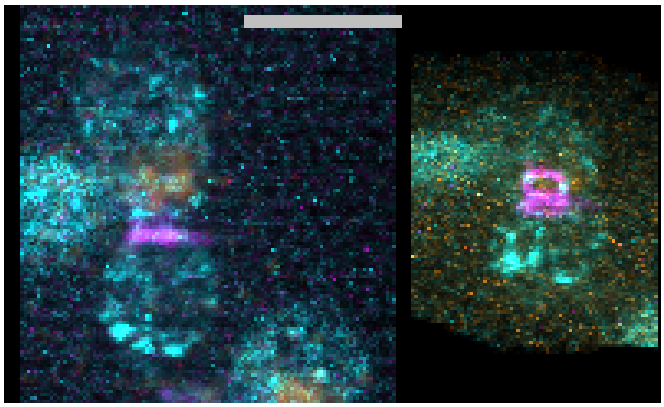

Figure 24: LLSM provided near-isotropic resolution in x,y and z. Single mRNA particles are therefore close to ideal spherical diffraction limited blobs. Voxel dimensions are 104x104x94 nm; 50 z-planes were used to reconstruct entire yeast cells. As can be seen on the right hand side, the acquired volumes are not cubic but have a rhomboid cross section. LLSM records images at an angle; images need to be de-skewed, leading to the observed geometry. Scale bar = 5 µm, Filename: LLSM_3D.avi.

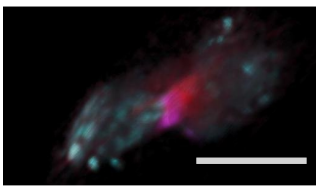

Figure 25: Rotation of a cell around M. Depicted are *mCLB2* (cyan), the dividing nucleus (red) and the bud neck (magenta). The rotation illustrates the near-isotropic reolution of the images; and highlights the fact that cells are not entirely in the field of view in all LLSM time series. Here, small parts of both bud and base are sliced off. Scale bar = 5µm, Filename : LLSM_rotation.avi.

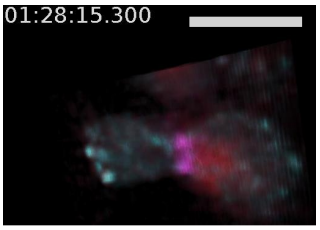

Figure 26: Cell visualized during the budded phase and mitosis. Depicted are *mCLB2* (cyan), the dividing nucleus (red) and the bud neck (magenta). Scale bar = 5µm, Filename : LLSM_3Dtimelapse.avi.

Figure 27: Montage of timelapse LLSM data on *mCLB2* distribution throughout the budded phase. Depicted are *mCLB2* (cyan), the dividing nucleus (orange) and the bud neck (magenta) dissociating into 2 rings shortly after mitosis. The panel omits every other image; all images are included in the enclosed video. Scale bar = 5 µm, Filename: LLSM_3D.avi.

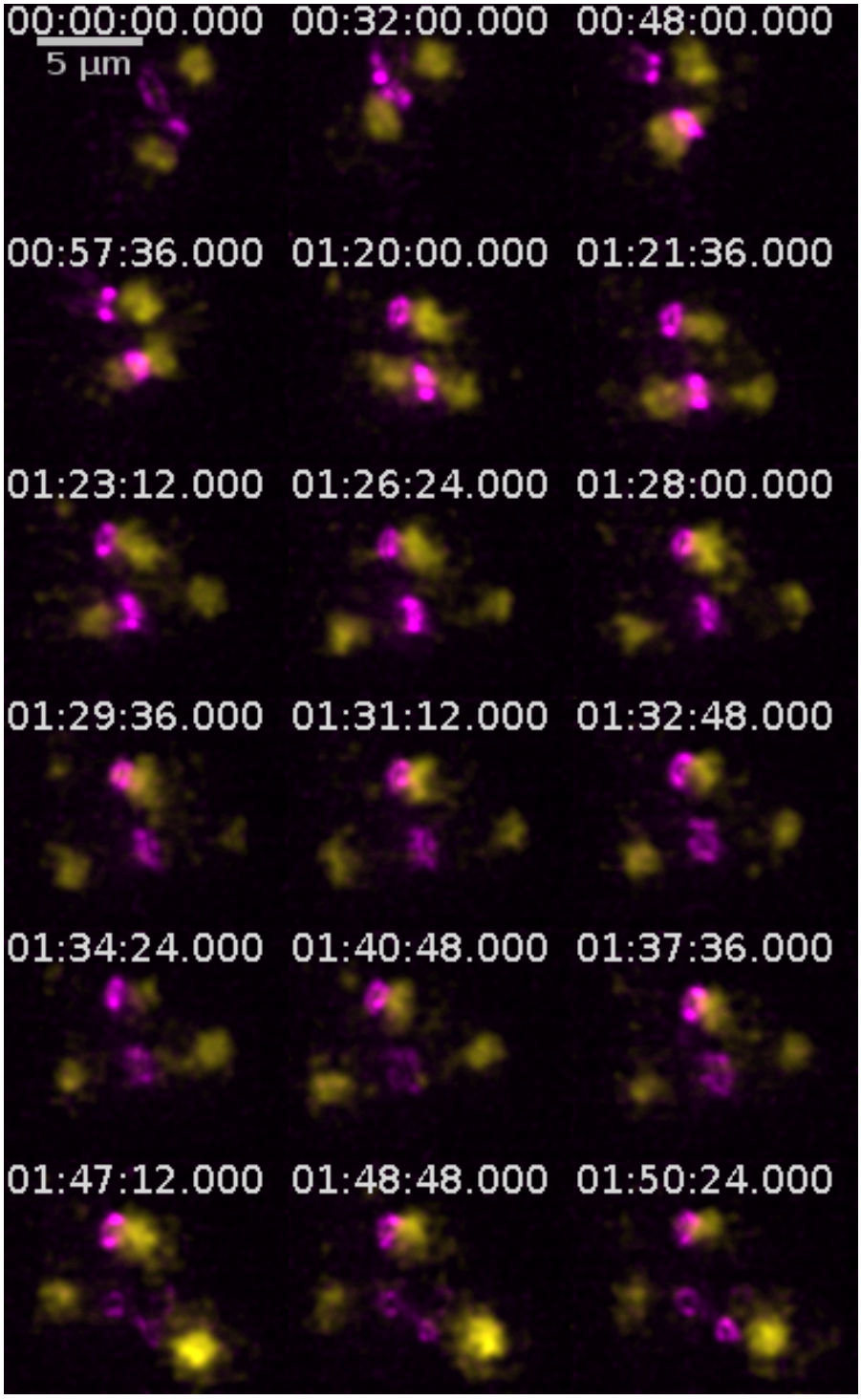

Figure 28: Cell cycle markers in LLSM. Selected time points are shown. Note the emergence of a new bud neck in axial position to the bud scar (next to the previous, fading bud neck) at 1:47 h, suggesting that cell cycle progression is not perturbed by imaging conditions. Bud necks are magenta, nuclei yellow. Scale bar = 5 µm. A video of the complete time series is attached. Filename: CC_markers_LLSM.avi.

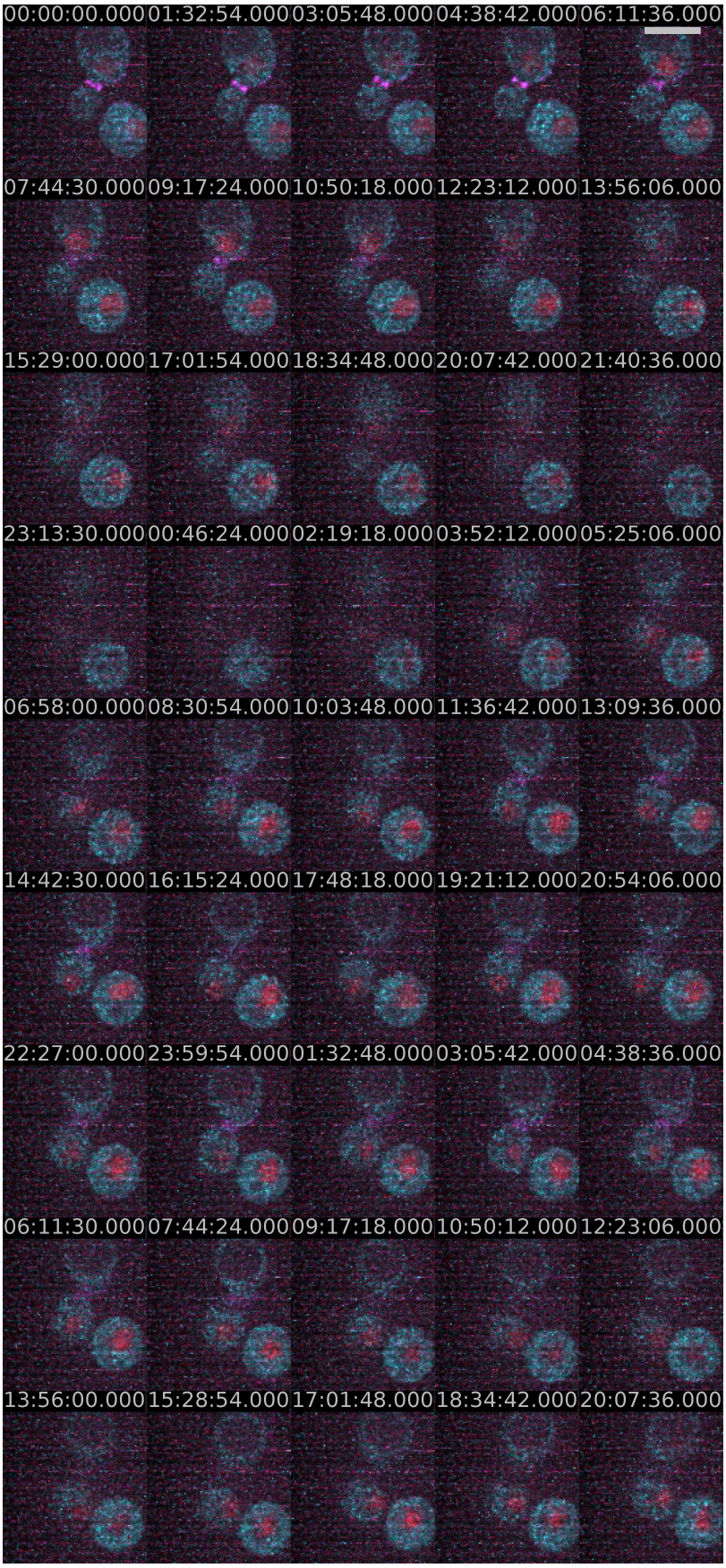

Figure 29: Montage of timelapse LLSM data on negative controls. Depicted are MCP-mNeonGreen (cyan), the dividing nucleus (red) and the bud neck (magenta). Scale bar = 5 µm.

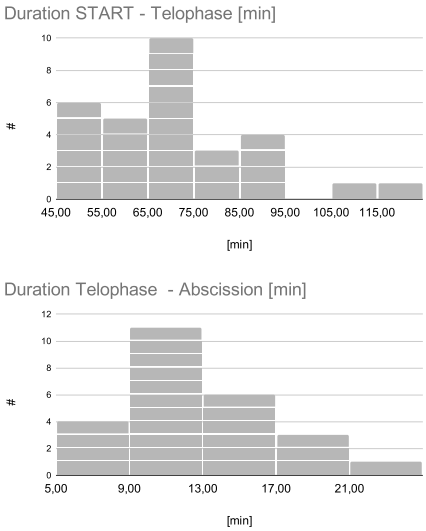

Figure 30: Duration of cell cycle phases was determined manually based on 3D projections and full image stacks of all LLSM time series (N = 168). Data included in the histogram is from cells that were observed at least from t_{START} to $t_{telophase}$, N = 30. Four of these cells were not imaged during cytokinesis; for $t_{telophase}$ to $t_{abscisssion}$ N = 26.

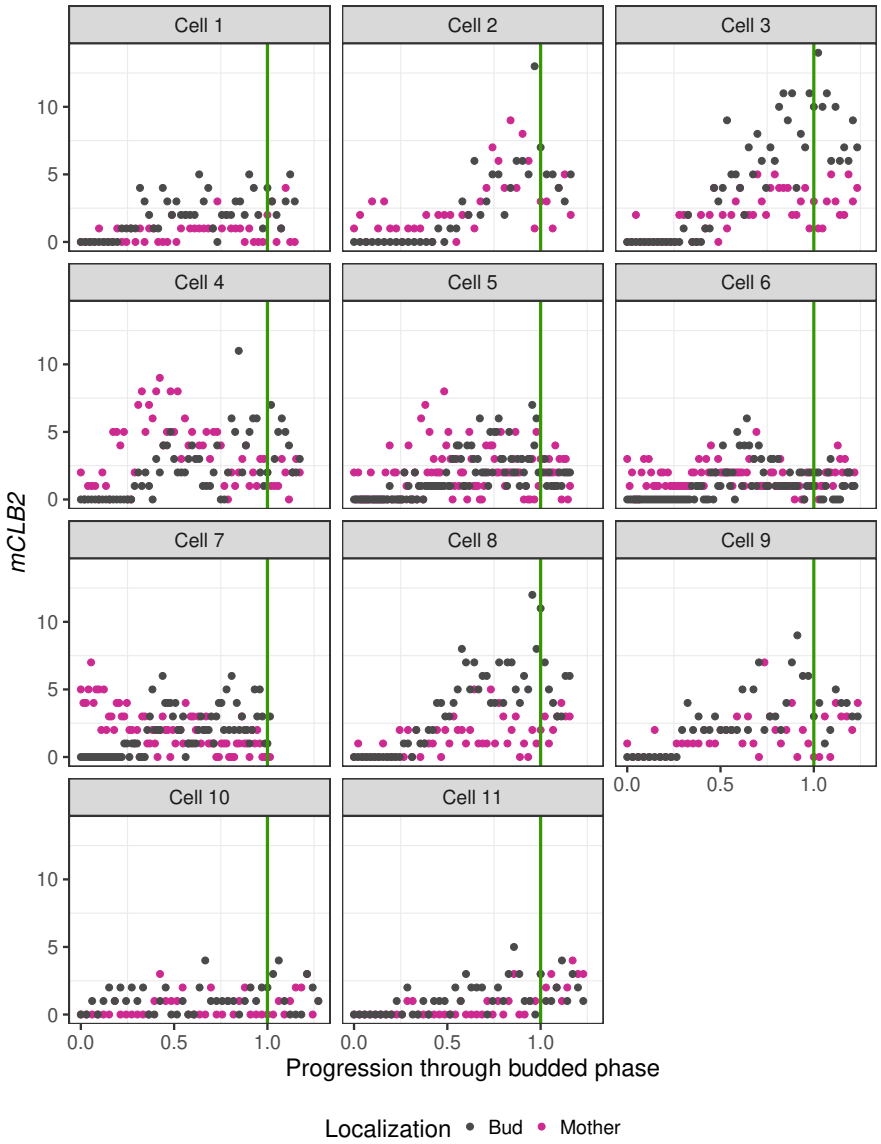

Figure 31: Distribution of *mCLB2* throughout the budded phase of the yeast cell cycle. To lay the focus on possible cell cycle phase specific patterns, time between bud emergence and the end of mitosis ($t_{telophase}$, vertical green line) was normalized to 1. All time series with physical time units are in figure 19.

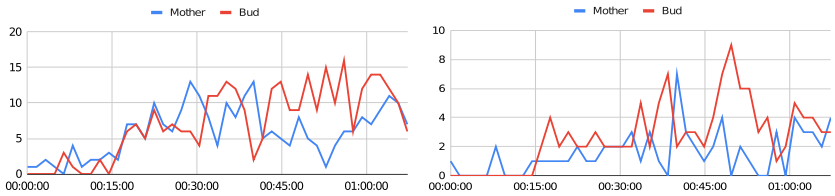

Figure 32: Time course example of LLSM data on *mCLB2* distribution during budded phase. Figure 32a was analyzed in FISH-quant by Dr. Gabriele Schreiber, figure 32b was analyzed in TrackMate. Time is in minutes.

A.3 DISPLACEMENT DISTRIBUTIONS

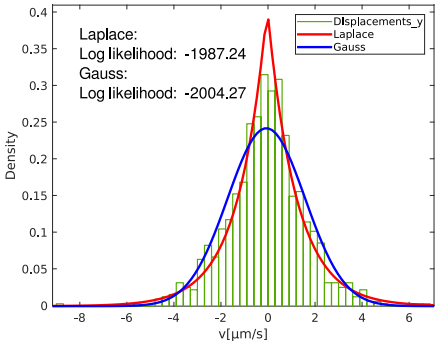

Distribution: Laplace
Log likelihood: -1987.24
Domain: -Inf < y < Inf
Mean: -0.0342602
Variance: 3.02387

Parameter	Estimate	Std. Err.
mu	-0.0342602	0.038019
sigma	1.22961	0.038019

Estimated covariance of parameter estimates:

	mu	sigma
mu	0.00144545	0
sigma	0	0.00144545

Distribution: Normal
Log likelihood: -2004.27
Domain: -Inf < y < Inf
Mean: -0.0689529
Variance: 2.70562

Parameter	Estimate	Std. Err.
mu	-0.0689529	0.050859
sigma	1.64488	0.0359886

Estimated covariance of parameter estimates:

	mu	sigma
mu	0.00258664	-1.17949e-19
sigma	-1.17949e-19	0.00129518
sigma	-4.20073e-21	0.00127669

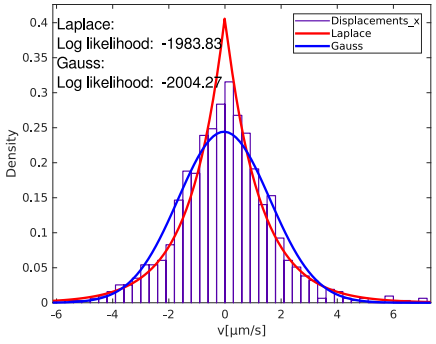

Distribution: Laplace
Log likelihood: -1983.83
Domain: -Inf < y < Inf
Mean: -0.00526364
Variance: 3.00422

Parameter	Estimate	Std. Err.
mu	-0.00526364	0.0378953
sigma	1.22561	0.0378953

Estimated covariance of parameter estimates:

	mu	sigma
mu	0.00143605	0
sigma	0	0.00143605

Distribution: Normal
Log likelihood: -1996.75
Domain: -Inf < y < Inf
Mean: -0.0345863
Variance: 2.667

Parameter	Estimate	Std. Err.
mu	-0.0345863	0.0504947
sigma	1.63309	0.0357308

Estimated covariance of parameter estimates:

	mu	sigma
mu	0.00254971	-4.20073e-21
sigma	-4.20073e-21	0.00127669

Figure 33: Fits for the displacement distribution without pixel level localizations.

A.4 SINGLE MOLECULE FISH

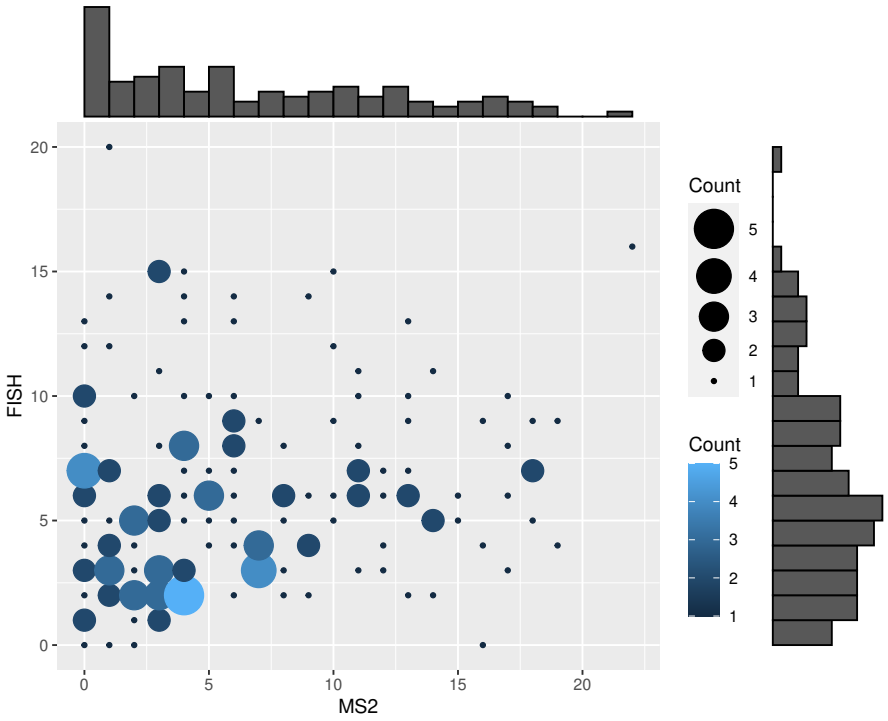

Figure 34: Number of *mCLB2* per cell assessed by MS2 and smFISH. This indicates that more spots are tagged by MS2 than by smFISH. As expected, excess MS2 signal is not observed in these cells that are in G_2 as *mCLB2* is expected to be stable prior to mitosis (Trcek et al., 2011). This comparison is based on an unsynchronized population. Cells that are in G_2 were identified by cell cycle markers. N = 160 cells.

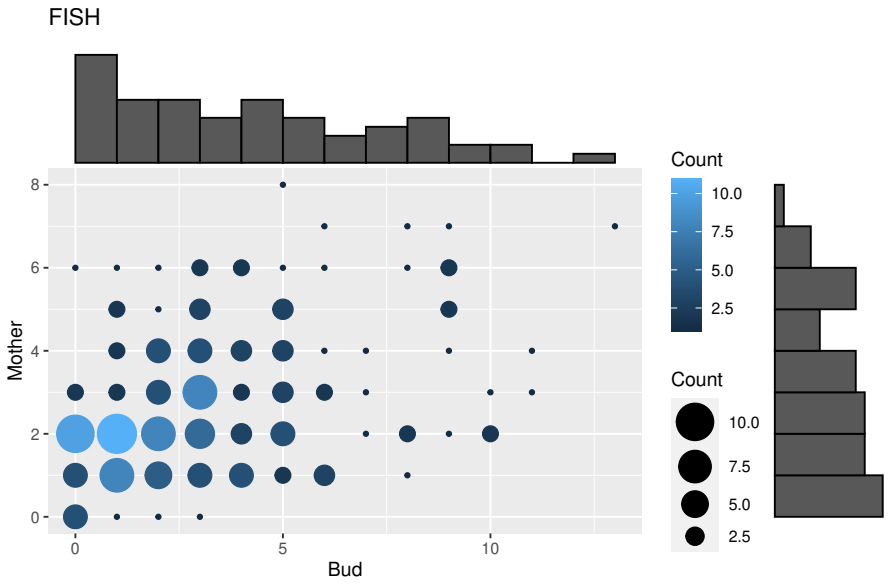

Figure 35: Distribution of MS2 labeled *mCLB2* assessed by smFISH. Of interest is the comparison to figure 36, as these cells are genetically different only with regards to MCP expressed from the HO locus and *CLB2*-MBS. Overall, fewer spots were detected by *CLB2*- smFISH in this strain, carrying the MS2 system. However, the distribution of molecules between mother and bud seems not to be shifted. This comparison is based on cells that were fixed in G_2. N = 160 cells.

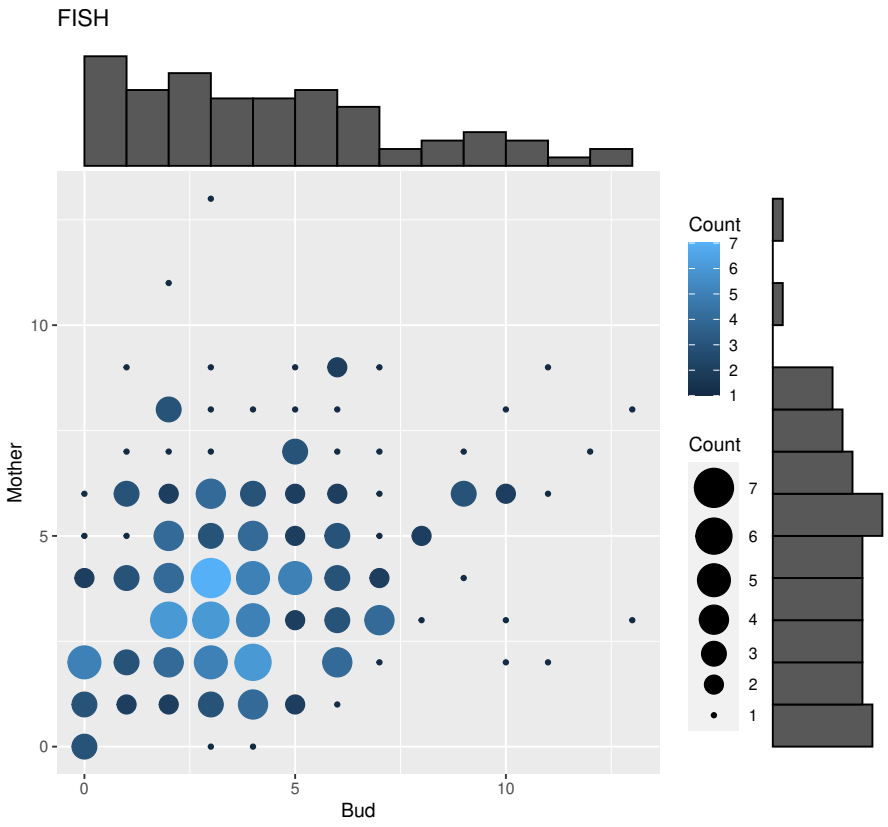

Figure 36: Distribution of *mCLB2* assessed by smFISH in a yeast strain without the MS2 system. Only cells that were fixed in G_2 were analyzed. N = 187 cells.

A.5 HMM-BAYES

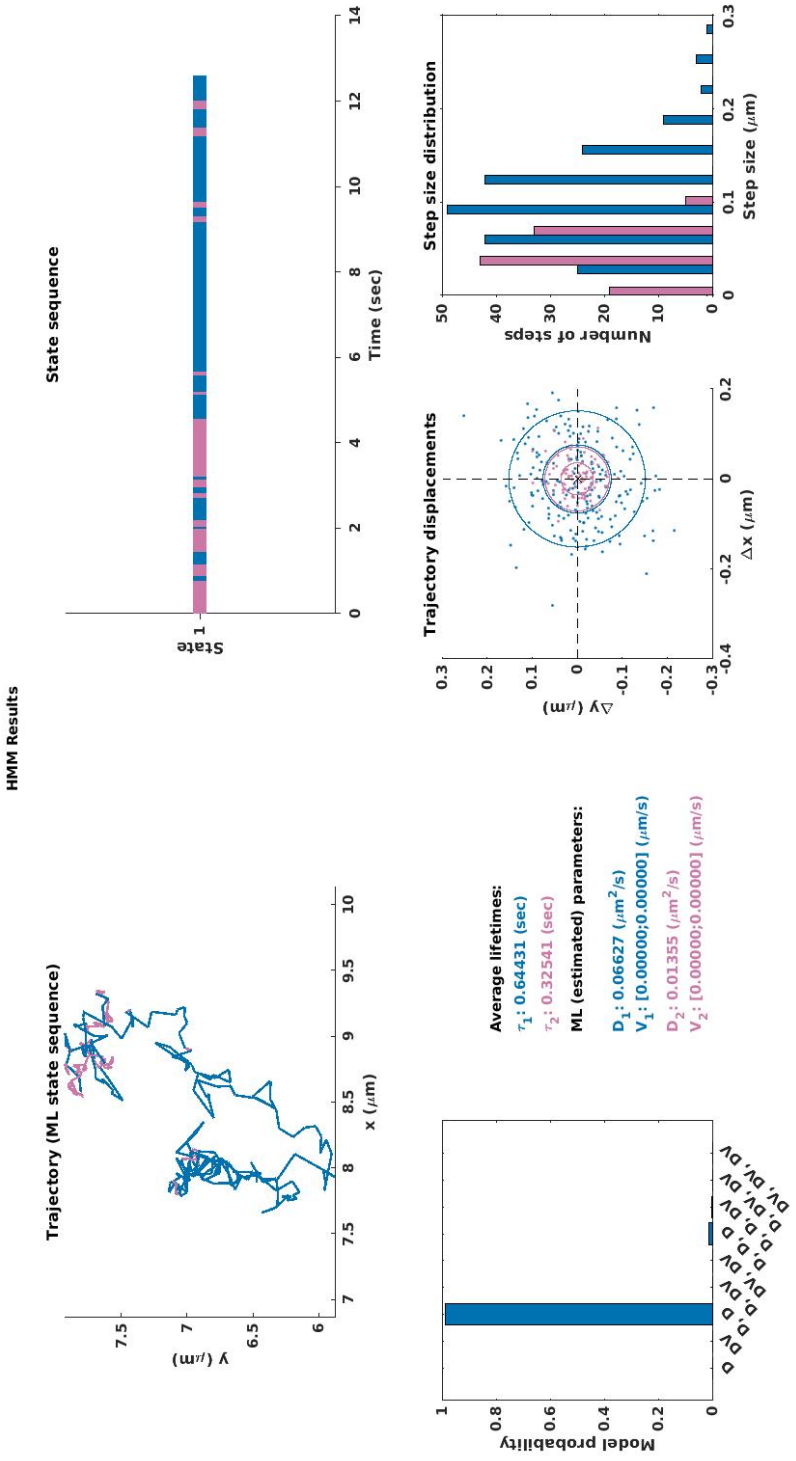

Figure 37: Trajectory analyzed with HMM-Bayes. Diffusive motion states are clearly preferred along the entire trajectory. A maximum of 3 hidden states was tested.

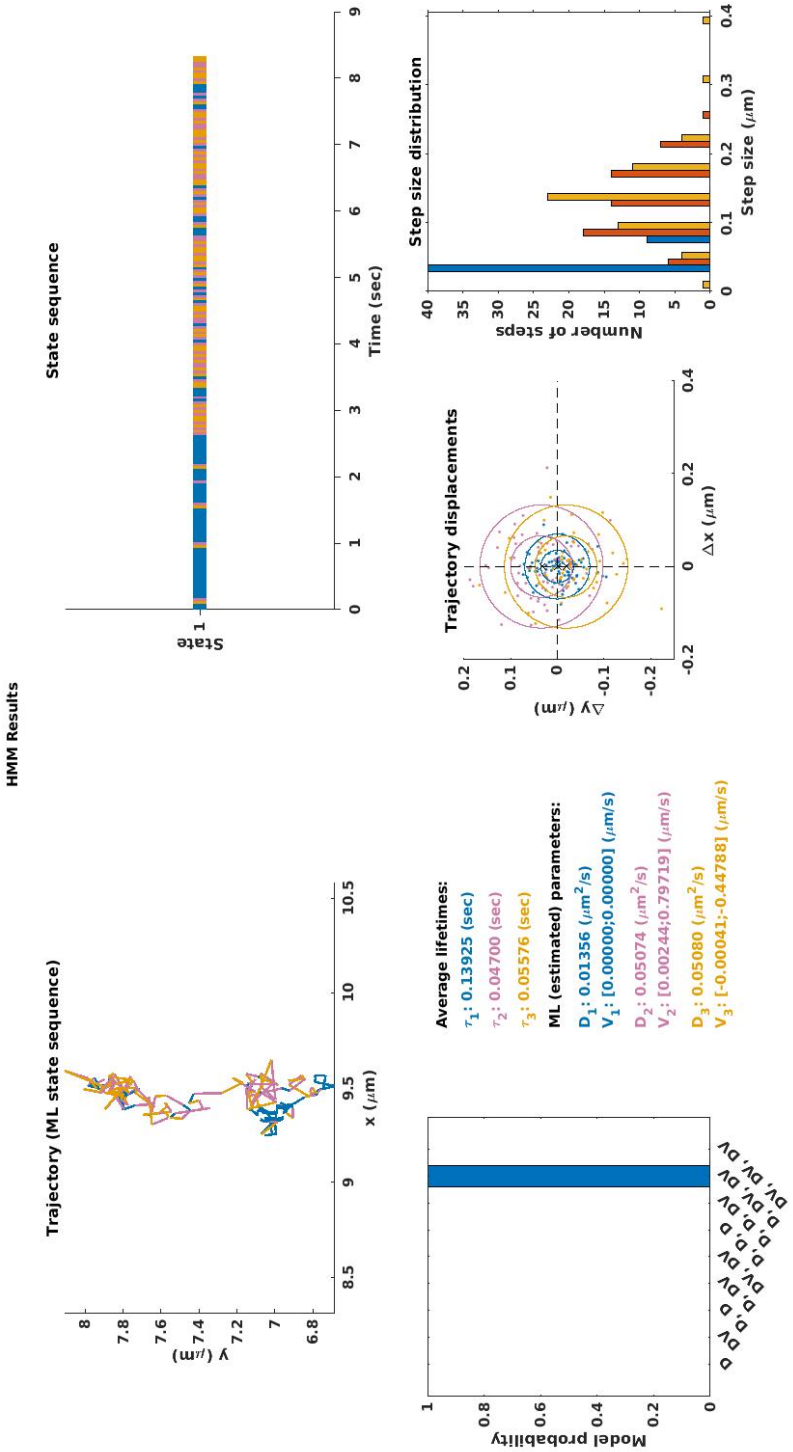

Figure 38: Trajectory analyzed with HMM-Bayes. This trajectory shows *mCLB2* moving from mother to bud.

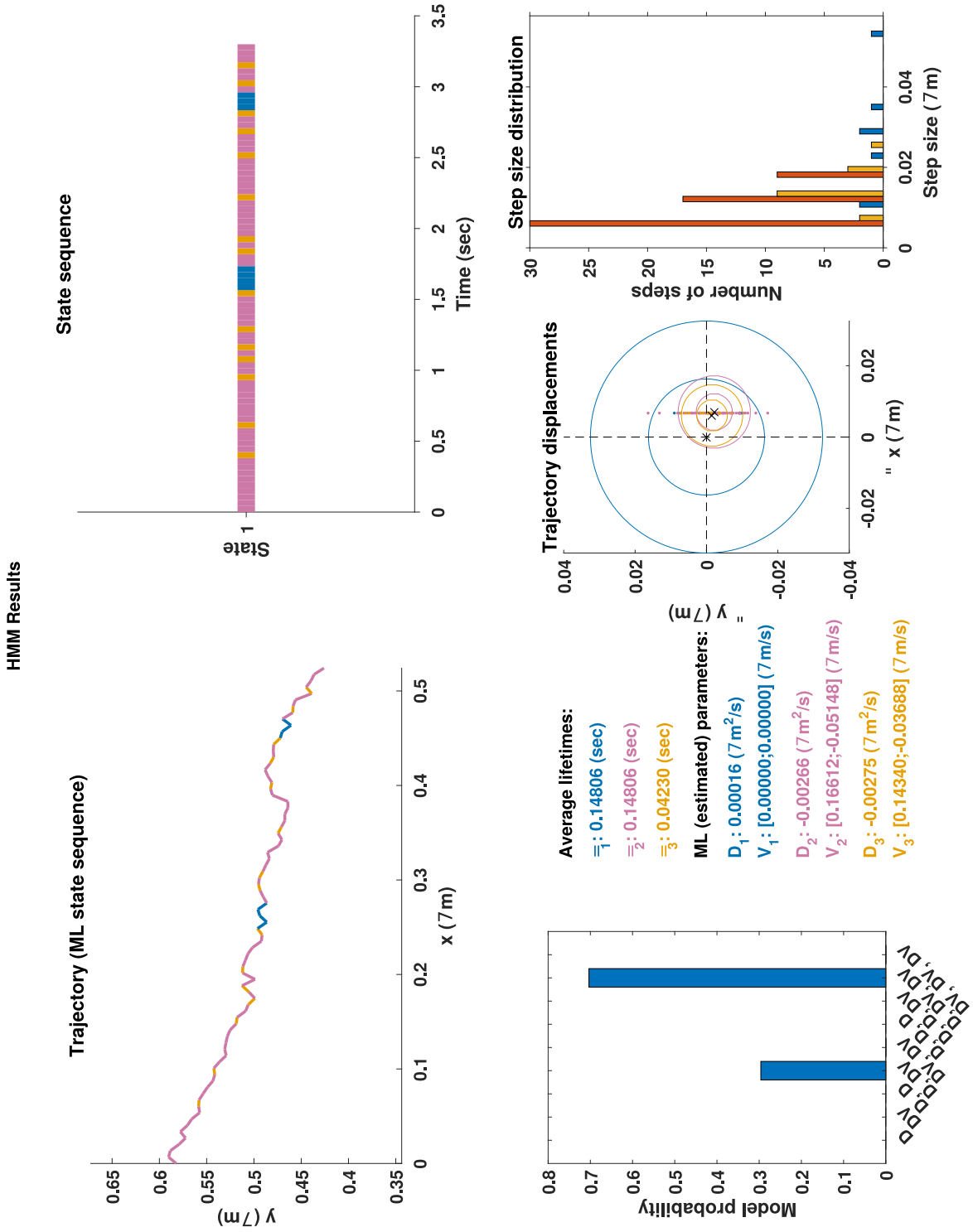

Figure 39: Trajectory analyzed with HMM-Bayes. This trajectory shows motion of *mCLB2* in a budding mother cell along the cell membrane, away from the bud. A maximum of 3 hidden states was tested.

A.6 ELUTRIATION

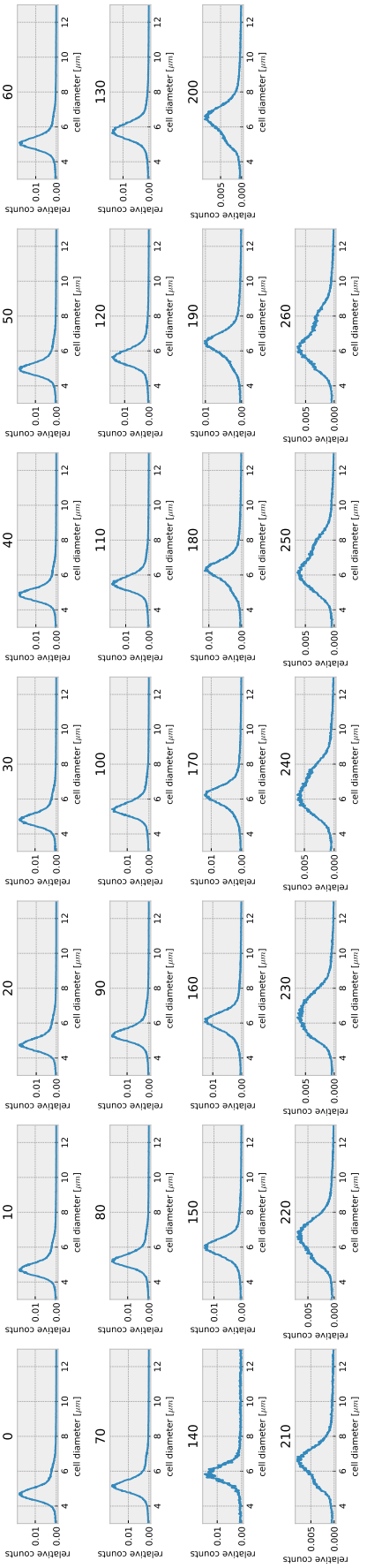

Figure 40: Cells without the MS2 system. Cell size distribution formed a narrow peak directly after elutriation (sample 0). At $\sim$ 200 minutes after elutriation, a distinct shoulder emerges, indicating that cells of the initial culture have budded. Cell size distributions were measured twice per time point for cells synchronized by elutriation.

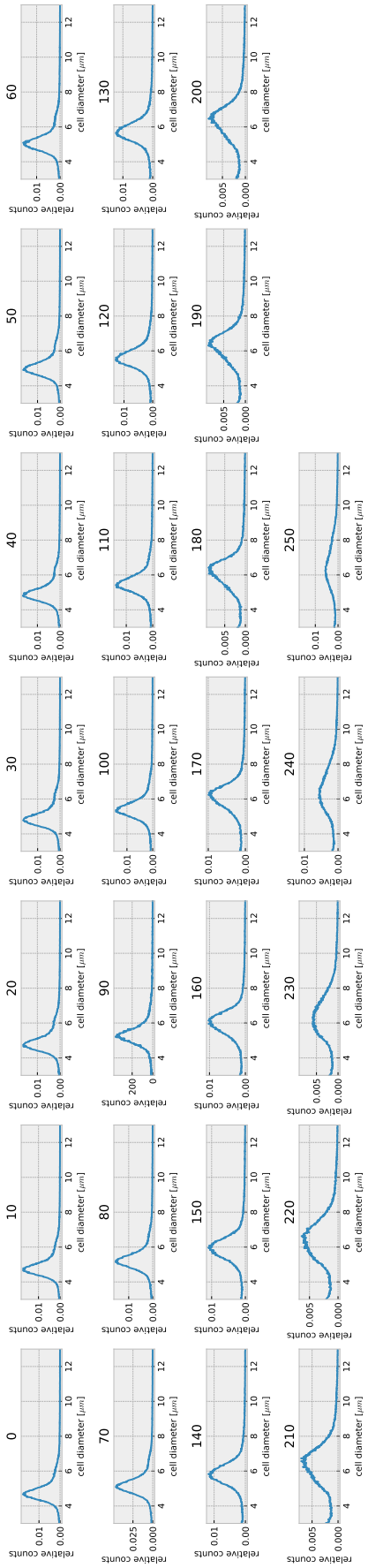

Figure 41: Cells with the MS2 system. Cell size distribution formed a narrow peak directly after elutriation (sample 0). Like in untagged cells (figure 40) a distinct shoulder emerges after $\sim$ 200 minutes. Cell size distributions were measured twice per time point for cells synchronized by elutriation.

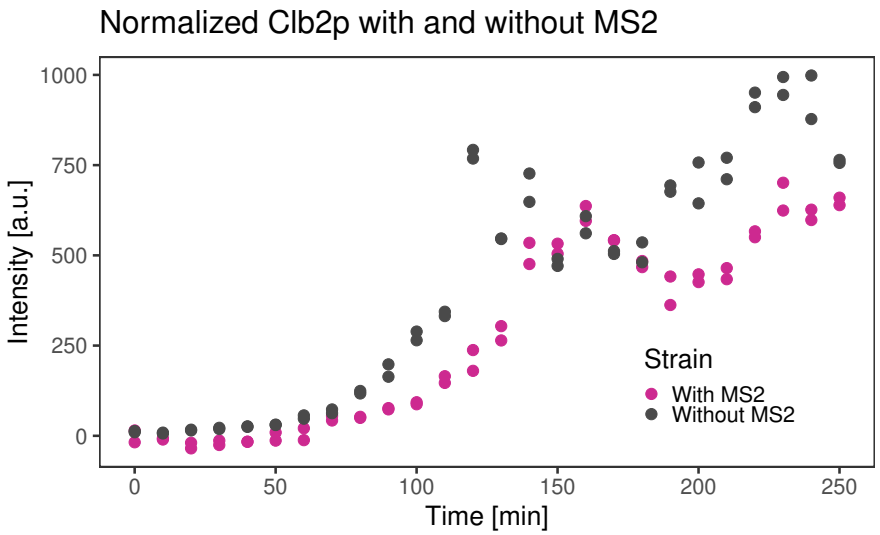

Figure 42: Clb2p was quantified in strains with and without the MS2 system. The oscillatory, cell cycle phase dependent expression of Clb2p was not suppressed by MS2 tagging. Size distributions of the cells used for western blots indicate that both the untagged and tagged strains progressed with similar timing through the cell cycle. Thus, expression levels of Clb2p can be compared between strains for a given time point. Cell size distributions are in appendix A.6.

A.7 GROWTH CURVES

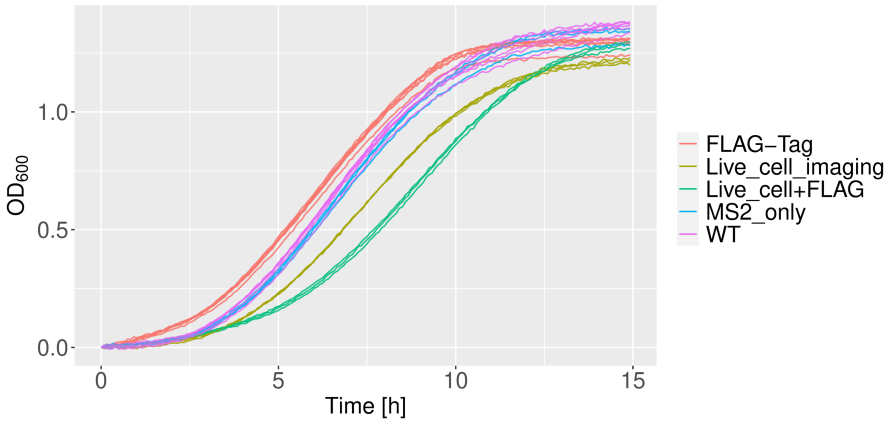

(a)

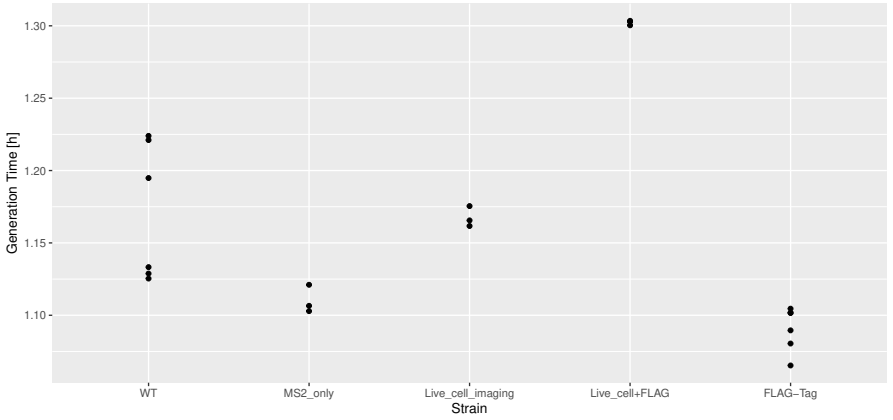

(b)

Figure 43: As the endogenous markers lay an extra metabolic burden on the strains, growth tests were performed. Growth of the yeast cells used for live cell imaging, as well strains carrying only selected markers were included. The growth curves in figure 44 were fitted to a standard logistic equation (for fits see figure 44). Figure 43b: The minimum generation times based on these fits was similar for most strains; only strains carrying additional FLAG-tags grew slower. For all strains at least 3 growth curves were recorded. These were technical replicates, as the cultures were taken from the same clone. However, strains are periodically tested, and growth for the cells used in live cell experiments was normal (data not shown).

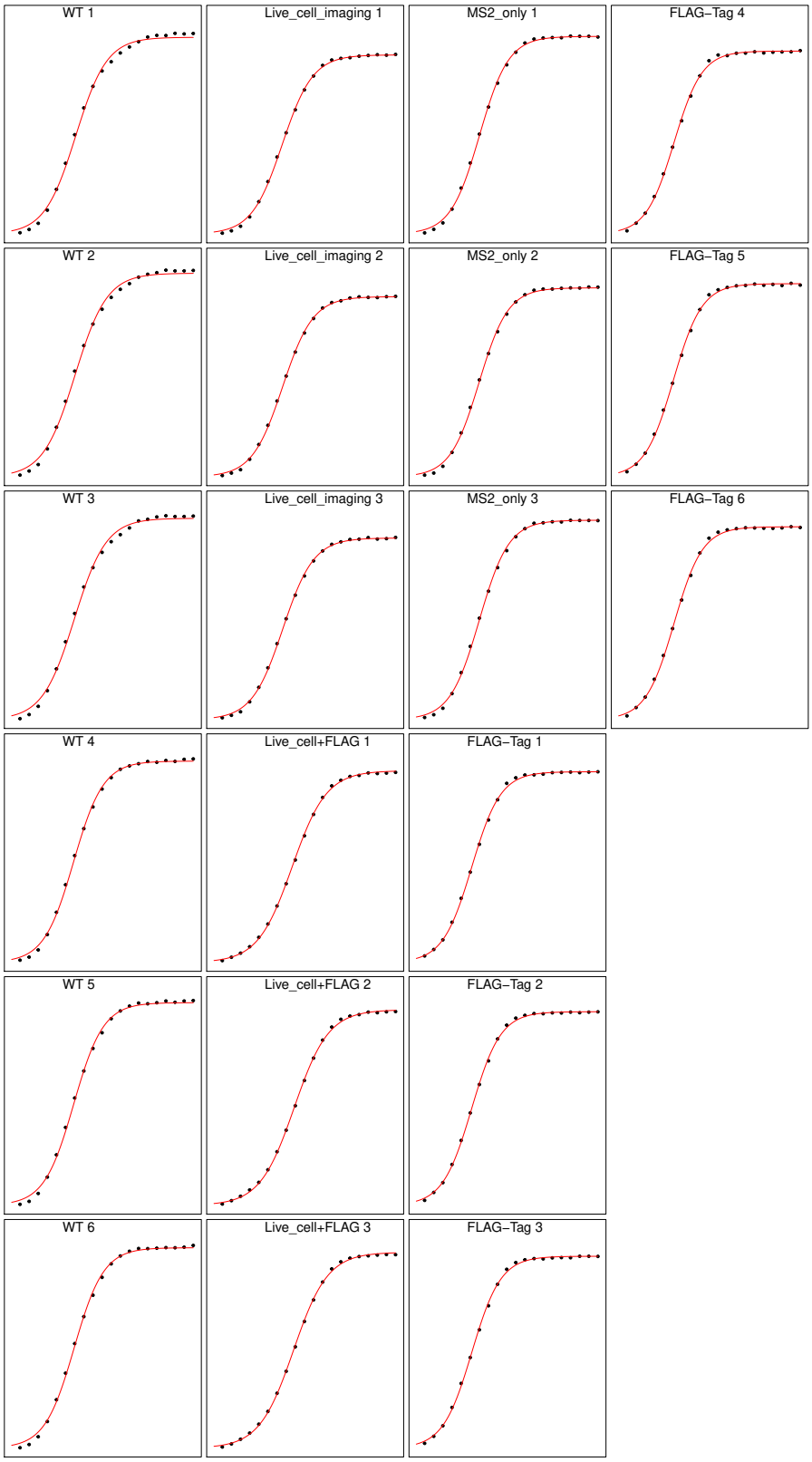

Figure 44: Growth curves are sparsely visualized, plotting only every twentieth measured time point (black dots) so the fit of the logarithmic equation becomes clearer. Scaled versions of the growth curves are shown in figure 43.

B MUTIFOCUS MICROSCOPY IMAGE RECONSTRUCTION

The matlab suite for acMFM image reconstruction was written by Jesse Aaron, Advanced Imaging Center, HHMI Janelia Research Campus. I include relevant parts of the manual with the authors permission. Code is available from me (contact through Theoretical Biophysics Group, Humboldt-Universität zu Berlin) or the Advanced Imaging Center, HHMI Janelia Research Campus.

INTRODUCTION

The aberration-corrected multifocal microscope (acMFM) can acquire fluorescent images of up to 9-focal planes in a sample simultaneously. This technology is particularly well-suited for dynamic imaging of very rapid biological processes in all three dimensions, including 3D single particle tracking (SPT). It can perform this function at high acquisition rates – up to *ca.* thirty 9-plane stacks per second. It can also obtain images of two different colors at this rate simultaneously. See Abrahamsson et al. *Nat. Meth.* **10** 60-63 (2013) for a technical description of this system.

Interpreting acMFM data requires several processing and analysis steps. These algorithms have been implemented in a Matlab-based graphical user interface (GUI) that is freely available to users of the Advanced Imaging Center (AIC). In summary, the major steps are:

1. **Calibration:** images of standard fluorescent beads are taken across a range of focal positions to assess several parameters needed to reconstruct and analyze final images. These parameters include (i) inter-plane spacing, (ii) relative emission intensity distribution across planes, (iii) affine transform matrices for alignment of each plane relative to each other, and (iv) the measured point-spread function (PSF) in each plane. *Calibration images must be taken using the same objective lens and excitation wavelength(s) that will be used for the experiment being performed.*

2. **Image Alignment/Processing:** The parameters calculated in step 1 are used to properly re-construct MFM images such that they can be analyzed. The software allows for batch processing of multiple time-course movies (comprising up to two color channels), but can only process images using a single calibration file for each color channel. Several options are available. The only required step is image alignment – transforming each raw 3D data set into a properly aligned 4D (x/y/z/t) "hyperstack" that can be opened in ImageJ/FIJI. Options also exist to correct for non-uniform intensity distribution across each focal plane, and to perform a background subtraction and Richardson-Lucy deconvolution.

3. **Particle Localization/Tracking:** Once images have been properly aligned and processed, single particle localization and tracking can be performed to assess the transport behavior of particles or single molecules within the cell. The algorithm is based on the Mosaic ImageJ/Fiji plugin to estimate the location of single point-sources within the image to a precision higher than the diffraction limit. These locations can be linked together using a LAP tracker (see Jaquaman, et. al, *Nat. Meth.* 2008). These trajectories can be visualized either as a 2D overlay with the original data, or as a 3D Matlab plot. Trajectories can also be analyzed to calculate individual diffusion constants, either with a Brownian or anomalous diffusion model. An option also exists to calculate a 2D diffusion constant in cases where particles are tightly confined within a 2D structure such as a cell membrane.

SOFTWARE REQUIREMENTS, CONFIGURATION, AND INSTALLATION

Matlab Requirements

The acMFM software is platform independent (Windows, Mac OS, or Linux) but requires installation of Matlab R2014a or later. It also requires the following toolboxes to be installed:

- Curve Fitting
- Image Processing
- Parallel Computing
- Statistics

For users that do not have access to these products, the AIC can provide a stand-alone compiled package, but this has not been tested extensively. We recommend that the software be installed on a high-end workstation with >16GB of RAM and a multi-core processor.

Graphical Processing Unit (GPU) and CUDA Requirements

To take advantage of the software's GPU-accelerated computational capabilities, your system must have a recent CUDA-compatible NVIDIA video card.

To see a list of CUDA-compatible video cards, visit: https://developer.nvidia.com/cuda-gpus.

To download the latest CUDA driver, go to: http://www.nvidia.com/Download/index.aspx.

To ensure that Matlab can communicate with your GPU device, type the following into the Matlab command prompt:

```
>> D = gpuDevice
```

An example output is shown below. Of particular importance is the `ComputeCapability` field. For proper performance, this value should be 1.3 or greater.

```
D =

  CUDADevice with properties:

                      Name: 'GeForce GTX TITAN Black'
                     Index: 1
         ComputeCapability: '3.5'
            SupportsDouble: 1
             DriverVersion: 6.5000
            ToolkitVersion: 5.5000
        MaxThreadsPerBlock: 1024
          MaxShmemPerBlock: 49152
        MaxThreadBlockSize: [1024 1024 64]
               MaxGridSize: [2.1475e+09 65535 65535]
                 SIMDWidth: 32
               TotalMemory: 6.4425e+09
                FreeMemory: 5.8405e+09
      MultiprocessorCount: 15
             ClockRateKHz: 1071500
              ComputeMode: 'Default'
     GPUOverlapsTransfers: 1
   KernelExecutionTimeout: 1
         CanMapHostMemory: 1
          DeviceSupported: 1
           DeviceSelected: 1
```

The MFM software relies on calls to a Java package in order to read Nikon-formatted (.nd2) data files. To avoid memory errors, it is generally necessary to increase the Java Heap Memory allocation in Matlab from its default value. See the following instructions to perform this configuration:

http://www.mathworks.com/matlabcentral/answers/159220-how-i-can-increase-java-heap-memory

In general, the Java Heap Memory should be set to at least 4GB or more if you are working with very large data sets.

The particle tracking feature requires a newer version of Java (v1.8) than what is typically used in the latest Matlab releases (v1.7). You can download the latest version of Java here:

https://www.java.com/en/download/

You then need to tell Matlab to use this latest version. Operating specific Instructions for doing this can be found here:

MAC OS: https://www.mathworks.com/matlabcentral/answers/103056-how-do-i-change-the-java-virtual-machine-jvm-that-matlab-is-using-for-mac-os

Windows: https://www.mathworks.com/matlabcentral/answers/130359-how-do-i-change-the-java-virtual-machine-jvm-that-matlab-is-using-on-windows

Linux: https://www.mathworks.com/matlabcentral/answers/130360-how-do-i-change-the-java-virtual-machine-jvm-that-matlab-is-using-for-linux

To install the MFM GUI, unzip the ***MFM.zip*** file into your Matlab working directory. Add the resulting directory into Matlab's search path. See here for instructions:
http://www.mathworks.com/help/matlab/matlab_env/what-is-the-matlab-search-path.html

ImageJ/Fiji Requirements

Miji

The automated particle tracking aspect of the MFM package uses the MOSAIC ToolSuite. See: http://mosaic.mpi-cbg.de/?q=downloads/imageJ for details on this package. However, the most recent version of MOSAIC is not available as a standalone Matlab code. Thus, we make use of an interface between Matlab and Fiji/ImageJ called Miji. See here for a tutorial:

http://bigwww.epfl.ch/sage/soft/mij/ .

You will need to add the path that contains the Miji.m file to Matlab's search path. Importantly, be sure that this path is below the MFM software path in Matlab's search directory list. You will also need to add the java class path for miji.jar and ij.jar. The above website explains how to do this, and AIC staff can help you.

MOSAIC ToolSuite

The final feature of the acMFM software package allows users to perform particle tracking analysis on their data. This package currently utilizes the Mosaic Particle Tracking software.

See: http://mosaic.mpi-cbg.de/?q=downloads/imageJ . Users will need to make sure the Mosaic plugin suite is installed in ImageJ/Fiji, using the following steps.

Fiji

1. To install in Fiji, click Help → Update Fiji.
2. Click Manage update sites
3. Check "MOSAIC ToolSuite"
4. Click Close
5. Click Apply Changes. You will be prompted to re-start Fiji.

ImageJ

1. Go to http://mosaic.mpi-cbg.de/Downloads/Mosaic_ToolSuite_imagej_new.jar
2. Download into the ImageJ plugins folder.
3. Restart ImageJ if needed.

You should now be ready to start the MFM software.

MAIN GUI WINDOW

To start the MFM software, simply type `MFM` at the Matlab command prompt:

```
>> MFM
```

The following window should appear:

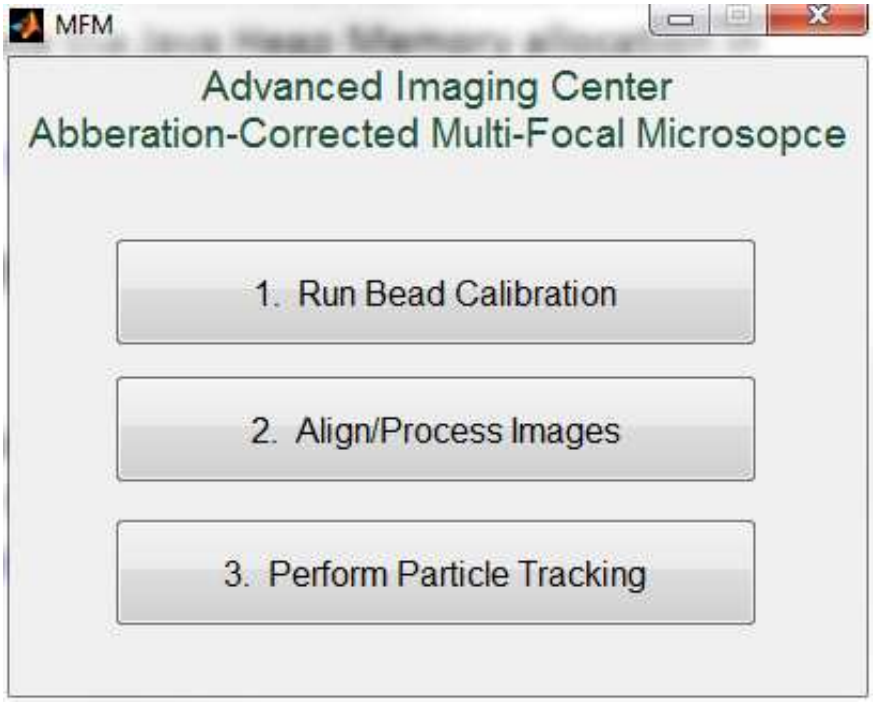

Figure 1. MFM software main window

The three buttons refer to the 3 steps outlined in the introduction section of this manual. In general, they should be performed in the order given.

RUN BEAD CALIBRATION

Press the **Run Bead Calibration** button, and the following window should appear:

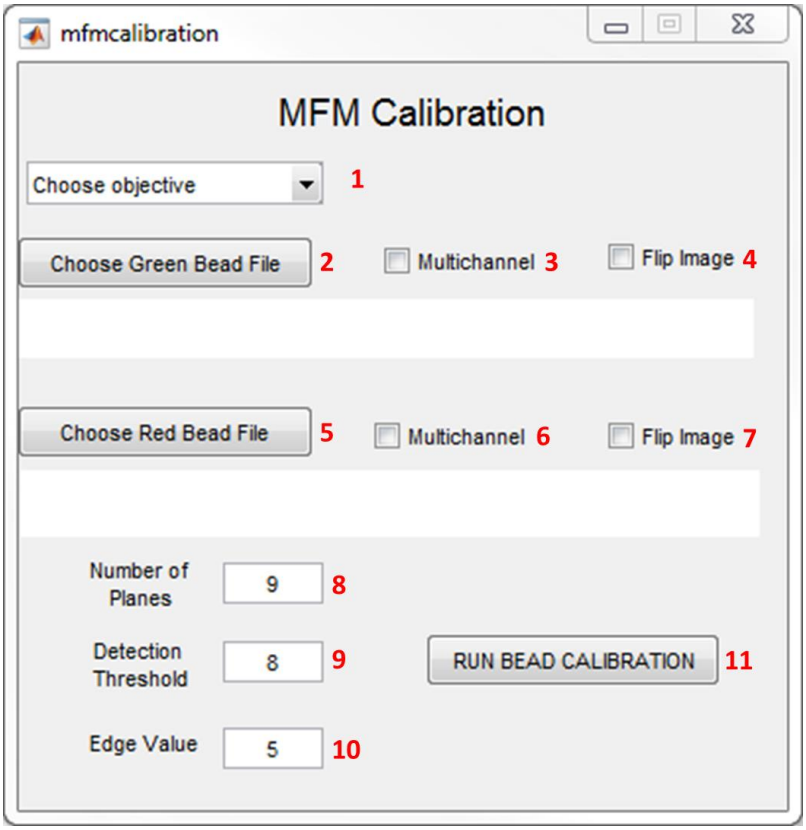

Figure 2. MFM calibration window. Red numbers reference the steps outlined below.

To perform a calibration:

1. Choose the correct objective lens from the drop-down menu at top (this will generally be 100x oil).

2. Click the **Choose Green Bead File** (if applicable), and navigate to the folder containing the .nd2 file corresponding to the green calibration image, and choose the file.

3. If the data contains two color data, check the Multichannel box.

4. If the data needs to be flipped left to right, click the Flip Image box. This is not generally needed for the AIC MFM.

5. Click the **Choose Red Bead File** (if applicable), and navigate to the folder containing the .nd2 file corresponding to the red calibration image, and choose the file. If the calibration data is multicolor, you will choose the same file as in step 2.

6. If the data contains two color data, check the Multichannel box.

7. If the data needs to be flipped left to right, click the Flip Image box. This is not generally needed for the AIC MFM.

8. Ensure that the number of planes is set to 9

9. Set the detection threshold to an appropriate value. Assuming that calibration images were acquired with sufficient signal-to-noise ratio, the value should be 5-40 (typically 8 is sufficient).

10. The Edge Value refers to the number of pixels from the edge of each image to ignore when detecting particles. This may be increased if there are particles very near the image edge, but should not be decreased below 5 in order to accurately measure the PSF.

11. Once all parameters have been specified, click **RUN BEAD CALIBRATION.**

The software will then attempt to read the .nd2 files corresponding to each color channel. It will automatically detect if the calibration is single or multi-color.

Either one (single color calibration) or two (multi-color calibration) Matlab figure Windows should appear. In the case of multi-color calibration, the first window shows the green channel bead image, and the second is the red channel bead image. Each of the 9 planes (in each color channel) will have a number next to each detected bead. Visually inspect all 9 images (across each color channel if applicable) to make sure that (i) each image has the same number of beads and (ii) each number references the same bead in all images. The figure below shows a multi-color calibration where these two conditions are satisfied for both color channels.

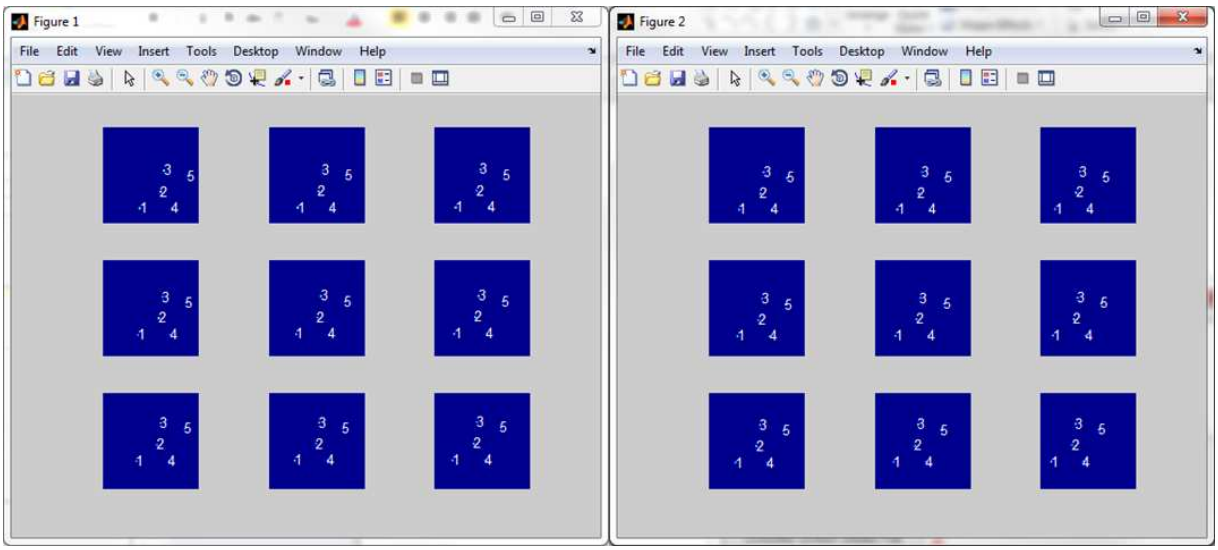

Figure 3. Green (left) and Red (right) channel bead images. In this example, 5 beads are detected in each plane of each color channel. Also, the relative position of each number with respect to the other numbers is consistent in each image/channel.

The software will prompt the user to confirm that all bead images satisfy these two conditions:

```
>>Beads ok? (y/n)
```

Type `y` if this is the case. If the bead images do not satisfy conditions (i) and (ii) above, then there are a few options. First, type `n` at the command prompt. This will exit out of the calibration GUI running mode. If a bead is apparent in the images, but there is no number next to it that indicates it was detected, try increasing or lowering the detection threshold. This is not a particularly sensitive parameter – increasing from 10 to 20 (or vice versa) will generally be necessary to see a difference. Also note if there are beads near the edges of any images. If this is the case, try increasing the Edge value parameter from 5 to 10. Once all parameters have been specified, click the RUN BEAD CALIBRATION button again, and follow the guidelines above. If the calibration procedure continues to fail even after adjustment of the threshold and edge parameters, it may be necessary to repeat the calibration image acquisition.

Once the bead detection has been verified (and you have typed `y` at the command prompt), the algorithm will proceed to calculate the relevant parameters needed for acMFM image processing/analysis. A number of windows will appear to indicate which parameters are being determined. In the case of a single color calibration only one of each of the following windows will appear. In the case of a multi-color calibration, each of the following windows will appear twice (one for each color).

The first window(s) to appear will denote the inter-plane spacing data. This is a plot of focal position vs. plane number. The slope of the red fit curve will correspond to the spacing between each focal plane. Note the R^2 value at top. A good calibration should have $R^2 > 0.98$. Note that the slope of the curve will be either positive or negative, depending on whether data was acquired in ascending or descending z-position. The software will accommodate either situation by taking the absolute value of the slope.

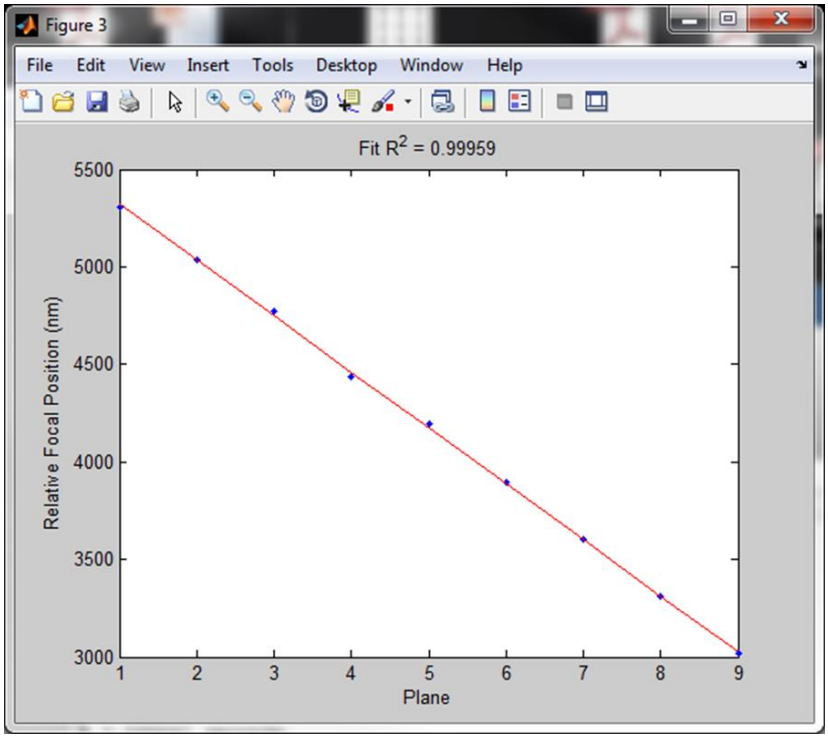

Figure 4. Plot of focal position vs. plane number. The slope of the red fit line is the interplane spacing. The R^2 value should be greater than 0.99.

The algorithm will then attempt to find the sub-pixel location of every bead in every plane, across each color channel (if applicable). The progress of this procedure will be displayed in the Matlab command window, indicating the bead and plane currently being localized.

Once the localization step has completed, the second window(s) to appear will indicate the alignment accuracy computed by the algorithm. In the case of a single color calibration, all images are aligned to the central plane. In the case of a multi-color calibration, all images are aligned to the central green-channel plane. Each image plane is shown as a two-color overlay, with the reference plane in green and the image being aligned in red. Atop each image will be the average alignment error for that plane, given in pixels. A value of *ca.* <0.2 is generally acceptable (corresponding to <25nm with the 100x objective). Figure 5 below shows an example alignment image for the red channel in a multi-color calibration.

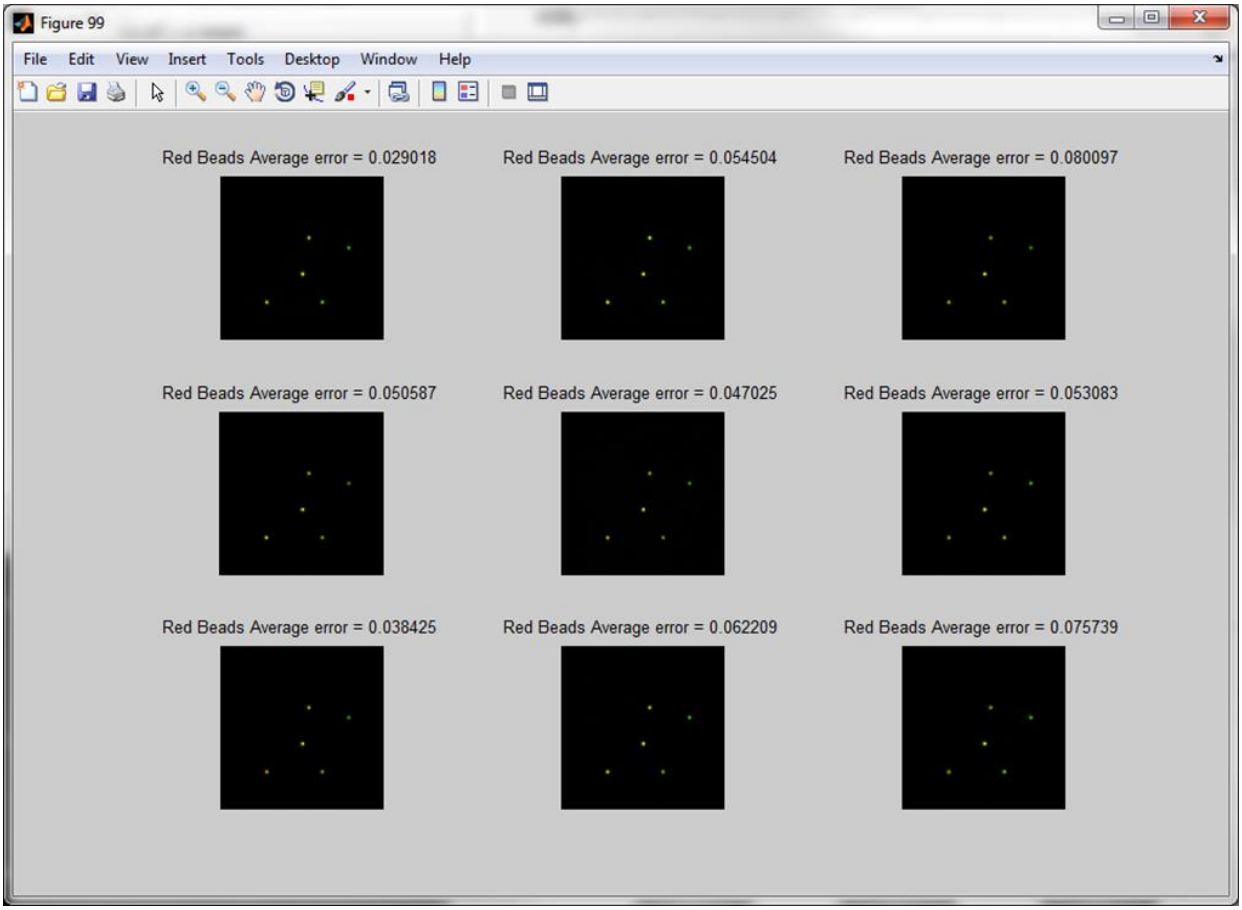

Figure 5. Example alignment image, in this case for the red channel in a multi-color calibration. The average alignment error (in pixels) for each plane is indicated on top of each corresponding image. A value of <0.2 for each plane is acceptable.

Finally, the calibration algorithm will produce three more images (for each color) that display the average point-spread function (PSF) in each acMFM plane. Images denote the xy, xz, and yz projections of the PSF, respectively. While there are no quantities that need to be monitored for this step, it is useful to observe the general shape of the PSF, and noting any large asymmetries or curvatures, particularly with the xz and yz projections. Figure 6 shows an example.

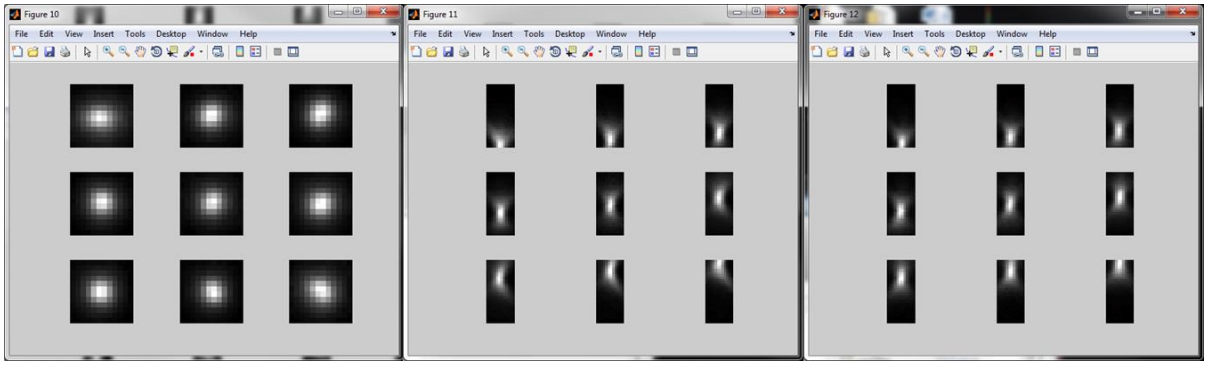

Figure 6. Example images of the point-spread function (PSF) in each of the nine planes. The xy (left), xz (middle) and yz (right) projections are each displayed.

All of the parameters calculated by the calibration algorithm are stored in a .mat file that is saved in the same directory as the raw calibration images. In the case of multi-color calibration, separate values for each color channel are stored. To view the contents, you can open the .mat file in Matlab. Although not necessary for any subsequent processing and analysis, viewing the results of the calibration may help identify potential problems. The following is a summary of the parameters saved in each calibration .mat file. In the case of a multi-color calibration, the names of some of the following variables will have either a ***g*** or an ***r*** appended to the end of their name to indicate whether it is specific for the green or red channel, respectively. You can view these values by simply dragging the calibration .mat file into the Matlab workspace.

- ***d***: the interplane spacing, in nanometers. The result will depend on wavelength and objective. At 515nm and 100x magnification, it should be ca. 350nm.

- ***fitparams***: The Gaussian fit parameters (in the Z-direction) used to estimate the relative focal position and average intensity across each MFM plane. This variable will be in the form of a cell array. Each cell in the array corresponds to each bead in the image. Within each cell, there is a matrix with 9 rows and 3 columns. Each row corresponds to each MFM plane. Each column corresponds to the intensity, focal-position, and z-width (in terms of 2x standard deviation) of the resulting Gaussian fit of the PSF in the z-direction.

- ***intscorrect***: derived from the data in *fitparams*, this variable lists the relative intensity distribution across each plane, normalized to unity. These values can vary widely with wavelength, with some MFM planes only reaching ~0.5 relatively intensity.

- ***objmag:*** The selected objective magnification

- ***psfs:*** a three dimensional matrix that represents the complete psf in each MFM plane. The matrix will be 12 pixels wide by 12x9 pixels tall. It will have a third dimension corresponding to the number of z-steps that contain an image with at least one psf in focus.

- ***tform:*** A nine-member cell array that contains the affine transformation matrices for each MFM plane. Each member of the cell array is stored as a structured array as per requirement for the Matlab *imwarp* function.

- ***zstepsize:*** The step size, in nanometers, used to take the z-series acquisition to acquire the calibration data set.

This completes the acMFM calibration process. To proceed to the next step, click the ***Align/Process Images*** button on the MFM software main window (see figure 1).

ALIGN/PROCESS IMAGES

MFM Image Processing

Once any pre-processing is completed, you can proceed to the Align/Process window described above, and shown in the figure below:

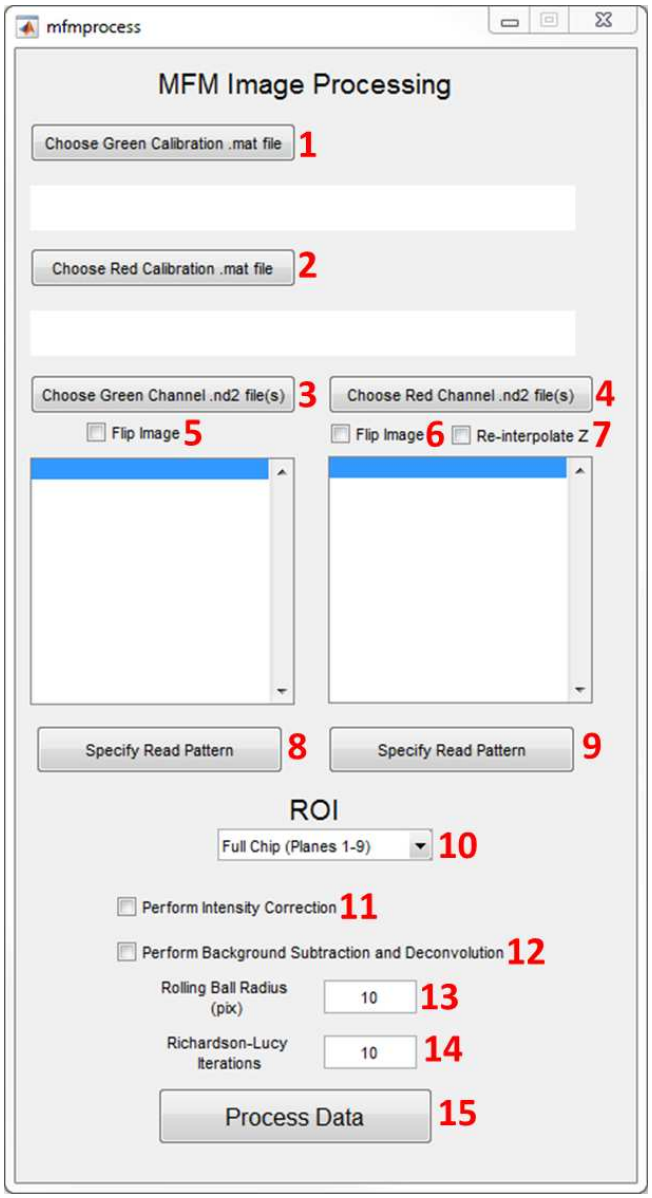

Figure 7. MFM Image Processing window. The red numbers correspond to the detailed steps outlined below.

1. Choose the green channel .mat file (if applicable) that was generated in the Calibration steps above.

2. Choose the red channel .mat file (if applicable) that was generated in the Calibration steps above. In the case of multi-color calibrations, this will be the same file as in step 1.

3. Now, choose the green channel .nd2 files (if applicable) that correspond to the imaging data you acquired. If the data is multicolor, the software will automatically read only the channel 1 images.

4. Then, choose the red channel .nd2 files (if applicable) that correspond to the imaging data you acquired. If the data is multicolor, the software will automatically read only the channel 2 images.

5. If the green data needs to be flipped left to right, click this box. This is not generally necessary for the AIC MFM.

6. If the red data needs to be flipped left to right, click this box. This is not generally necessary for the AIC MFM.

7. In the case of multicolor data, you can choose the re-interpolate the red channel data such that its z-spacing matches the green channel. This is useful for direct overlaying of green/red data. However, because the green data spans a smaller z-depth, doing this will reduce the red channel depth accordingly.

8. If the green channel data has been acquired using an interlaced or other custom illumination mode, then users may want to only process a portion of the total data set. In such cases click the Specify Read Pattern button. A new window will open that prompts users for 3 pieces of information:

    a. The pattern length: This is the total length of the illumination/acquisition pattern, as defined in the custom illumination plugin in the Nikon Elements software. In the case of 2-color interlaced acquisition, the pattern length is simply 2.

    b. The frames to keep within the specified pattern. This is expressed in Matlab vector notation. For example, if a custom illumination pattern is defined over 12 frames, and the data of interest is contained in the odd numbered frames up to the 9^{th} acquisiton, you would type 1:2:9 (start frame 1, increment by 2, end frame 9). In the case of 2-color interlaced acquisition, you can simply type 1 for the odd frames or 2 for the even frames.

    c. You can specify a file suffix to be added to the processed data file name that indicates which “subpopulation” of timepoints that were processed.

9. Same as 8 above, but applied to the red channel data.

10. AIC recommends using the full chip (planes 1-9) in order to maximize the z-depth of imaging. However, in special cases, users may acquire data using only a portion of the EMCCD chip in order to attain higher acquisition speed. In these cases, the user should specify which sub-region (corresponding to which planes) was used for the selected data. There are 3 possible sub-regions

which must be specified prior to acquisition of the data. Ask AIC staff how to set this up prior to image collection.

a. "Top 6" corresponds to a subregion containing pixel columns of 1-512, and pixel rows of 1-340.
b. "Middle 3" corresponds to a subregion containing pixel columns of 1-512, and pixel rows of 171-340.
c. "Bottom 6" corresponds to a subregion containing pixel columns of 1-512, and pixel rows of 171-512.

11. The MFM system does not perfectly distribute light intensity across each plane. To correct for this, check the box entitled "**Perform Intensity Correction**". This should make your images appear more uniform, and is should always be done unless troubleshooting the system.

12. To improve image quality and apparent resolution, you may perform background subtraction and Richardson-Lucy Deconvolution on your data sets by checking the "**Perform Background Subtraction and Deconvolution**" box. This step will improve the sharpness of your images, though will take longer. This will create a new directory within your data folder called **Deconvolution**, and all data will be placed in this new location. Checking this option will forgo saving non-deconvolved data.

13. Choose the rolling-ball background subtraction radius. This value should be just larger than the largest features of interest in your image, but generally smaller than the size of your cells.

14. Choose the number of Richardson-Lucy iterations. Larger number of iterations will increase the resolution of your images. However, more iterations on relatively low SNR images will begin to look "grainy" as the algorithm attempts to deconvolve noise spikes. Also, more iterations will increase processing time. Typical values are between 5 and 15.

15. Once all files and options have been chosen, click the **Process Data** button. This will initiate the MFM image alignment/processing algorithm. Depending on your computer's speed this can take some time (up to several hours in the case of many Gigabytes of data). A progress bar will denote the frames being processed for the current data file.

All processed data will be saved as a high-density format v5 file (.h5). This format is open source, and plugins exist in ImageJ and FIJI to view this data (explained below). A metadata file is also included in .csv format that contains the x, y, and z position of the image, as well as the time stamp for each time point in the image. Do not modify the .csv file, as it will be necessary for computation of diffusion coefficients in later steps (if applicable).

BIBLIOGRAPHY

Abrahamsson, Sara et al. (2013). "Fast multicolor 3D imaging using aberration-corrected multifocus microscopy." In: *Nature methods* 10.1, pp. 60–3. ISSN: 1548-7105. DOI: 10.1038/nmeth.2277. URL: http://www.ncbi.nlm.nih.gov/pubmed/23223154 (cit. on pp. 26, 33, 43).

Abrahamsson, Sara, Molly McQuilken, Shalin B Mehta, Amitabh Verma, Johannes Larsch, Rob Ilic, Rainer Heintzmann, Cornelia I Bargmann, Amy S Gladfelter, and Rudolf Oldenbourg (2015). "MultiFocus Polarization Microscope (MF-PolScope) for 3D polarization imaging of up to 25 focal planes simultaneously." In: *Optics Express* 23.6, p. 7734. ISSN: 1094-4087. DOI: 10.1364/oe.23.007734. URL: www.openpolscope.org. (cit. on p. 27).

Abrahamsson, Sara et al. (2016). "Multifocus microscopy with precise color multi-phase diffractive optics applied in functional neuronal imaging." In: *Biomedical Optics Express* 7.3, p. 855. ISSN: 2156-7085. DOI: 10.1364/boe.7.000855. URL: http://dx.doi.org/10.6084/m9.figshare.2062047 (cit. on pp. 26, 29).

Adams, A E and J R Pringle (1984). "Relationship of actin and tubulin distribution to bud growth in wild-type and morphogenetic-mutant Saccharomyces cerevisiae." In: *The Journal of Cell Biology* 98.3, pp. 934–945. ISSN: 0021-9525. DOI: 10.1083/JCB.98.3.934. URL: http://www.ncbi.nlm.nih.gov/pubmed/6365931http://www.pubmedcentral.nih.gov/articlerender.fcgi?artid=PMC2113156 (cit. on p. 16).

Allain, Frédéric H.T., Peter W.A. Howe, David Neuhaus, and Gabriele Varani (1997). "Structural basis of the RNA-binding specificity of human U1A protein." In: *EMBO Journal*. ISSN: 02614189. DOI: 10.1093/emboj/16.18.5764 (cit. on p. 19).

Altenburg, Tom, Björn Goldenbogen, Jannis Uhlendorf, and Edda Klipp (2019). "Osmolyte homeostasis controls single-cell growth rate and maximum cell size of Saccharomyces cerevisiae." In: *npj Systems Biology and Applications* 5.1. ISSN: 20567189. DOI: 10.1038/s41540-019-0111-6 (cit. on p. 7).

Amberg, David C. (1998). *Three-dimensional imaging of the yeast actin cytoskeleton through the budding cell cycle*. DOI: 10.1091/mbc.9.12.3259 (cit. on p. 16).

Amon, Angelika (1996). "Mother and daughter are doing fine: Asymmetric cell division in yeast." In: *Cell* 84.5. ISSN: 00928674. DOI: 10.1016/S0092-8674(00)81041-7 (cit. on p. 16).

Amon, Angelika, Mike Tyers, Bruce Futcher, and Kim Nasmyth (1993). "Mechanisms that help the yeast cell cycle clock tick: G2 cyclins transcriptionally activate G2 cyclins and repress G1 cyclins." In: *Cell*

74.6, pp. 993–1007. ISSN: 00928674. DOI: 10.1016/0092-8674(93)90722-3 (cit. on pp. 9–11).

Amoussouvi, Aouefa, Lotte Teufel, Matthias Reis, Martin Seeger, Julia Katharina Schlichting, Gabriele Schreiber, Andreas Herrmann, and Edda Klipp (2018). "Transcriptional timing and noise of yeast cell cycle regulators—a single cell and single molecule approach." In: *npj Systems Biology and Applications*. ISSN: 20567189. DOI: 10.1038/s41540-018-0053-4 (cit. on pp. 32, 42).

Anastasia, Steph D., Duy Linh Nguyen, Vu Thai, Melissa Meloy, Tracy MacDonough, and Douglas R. Kellogg (2012). "A link between mitotic entry and membrane growth suggests a novel model for cell size control." In: *Journal of Cell Biology*. ISSN: 00219525. DOI: 10.1083/jcb.201108108 (cit. on p. 9).

Anderluh, Andreas, Enrico Klotzsch, Jonas Ries, Alexander W.A.F. Reismann, Stefan Weber, Martin Fölser, Florian Koban, Michael Freissmuth, Harald H. Sitte, and Gerhard J. Schütz (2014). "Tracking single serotonin transporter molecules at the endoplasmic reticulum and plasma membrane." In: *Biophysical Journal* 106.9, pp. L33–L35. ISSN: 15420086. DOI: 10.1016/j.bpj.2014.03.019 (cit. on pp. 13, 22).

Andor (Oxford Instruments). *Andor*. URL: https://andor.oxinst.com/learning/view/article/emccd-vs-scmos-cameras-for-spinning-disk-confocal-microscopy (visited on 07/24/2020) (cit. on pp. 21, 22).

Arava, Yoav, Yulei Wang, John D. Storey, Chih Long Liu, Patrick O. Brown, and Daniel Herschlag (2003). "Genome-wide analysis of mRNA translation profiles in Saccharomyces cerevisiae." In: *Proceedings of the National Academy of Sciences of the United States of America* 100.7, pp. 3889–3894. ISSN: 00278424. DOI: 10.1073/pnas.0635171100. URL: www.pnas.orgcgidoi10.1073pnas.0635171100 (cit. on pp. 10, 11, 86).

Aravind, L., Hidemi Watanabe, David J. Lipman, and Eugene V. Koonin (2000). "Lineage-specific loss and divergence of functionally linked genes in eukaryotes." In: *Proceedings of the National Academy of Sciences of the United States of America* 97.21, pp. 11319–11324. ISSN: 00278424. DOI: 10.1073/pnas.200346997. URL: www.pnas.org (cit. on p. 3).

Archambault, Vincent, Emmanuel J. Chang, Benjamin J. Drapkin, Frederick R. Cross, Brian T. Chait, and Michael P. Rout (2004). "Targeted proteomic study of the cyclin-Cdk module." In: *Molecular Cell*. ISSN: 10972765. DOI: 10.1016/j.molcel.2004.05.025 (cit. on p. 11).

Archambault, Vincent, Nicolas E. Buchler, Gwendolyn M. Wilmes, Matthew D. Jacobson, and Frederick R. Cross (2005). "Two-faced cyclins with eyes on the targets." In: *Cell Cycle* 4.1, pp. 125–130. ISSN: 15514005. DOI: 10.4161/cc.4.1.1402. URL: http://www.

landesbioscience.com/journals/cc/abstract.php?id=1402 (cit. on p. 3).

Baddeley, David, Mark B. Cannell, and Christian Soeller (2011). "Three-dimensional sub-100 nm super-resolution imaging of biological samples using a phase ramp in the objective pupil." In: *Nano Research* 4.6, pp. 589–598. ISSN: 19980000. DOI: 10.1007/s12274-011-0115-z. URL: https://link.springer.com/article/10.1007/s12274-011-0115-z (cit. on p. 28).

Badieirostami, Majid, Matthew D. Lew, Michael A. Thompson, and W. E. Moerner (2010). "Three-dimensional localization precision of the double-helix point spread function versus astigmatism and biplane." In: *Applied Physics Letters* 97.16, p. 161103. ISSN: 00036951. DOI: 10.1063/1.3499652. URL: http://aip.scitation.org/doi/10.1063/1.3499652 (cit. on p. 28).

Bähler, Jürg (2005). *Cell-cycle control of gene expression in budding and fission yeast*. DOI: 10.1146/annurev.genet.39.110304.095808 (cit. on p. 10).

Bailly, Eric, Sandrine Cabantous, Delphine Sondaz, Alain Bernadac, and Marie-Noelle Simon (2003). "Differential cellular localization among mitotic cyclins from Saccharomyces cerevisiae: a new role for the axial budding protein Bud3 in targeting Clb2 to the mother-bud neck." In: *Journal of cell science* 116.Pt 20, pp. 4119–30. ISSN: 0021-9533. DOI: 10.1242/jcs.00706. URL: http://www.ncbi.nlm.nih.gov/pubmed/11171327http://www.ncbi.nlm.nih.gov/pubmed/12972503 (cit. on p. 11).

Baker Brachmann, Carrie, Adrian Davies, Gregory J. Cost, Emerita Caputo, Joachim Li, Philip Hieter, and Jef D. Boeke (1998). "Designer deletion strains derived from Saccharomyces cerevisiae." In: *Yeast*. ISSN: 0749503X. DOI: 10.1002/(SICI)1097-0061(19980130)14:2<115::AID-YEA204>3.0.CO;2-2 (cit. on p. 31).

Baker, J. E., E. B. Krementsova, G. G. Kennedy, A. Armstrong, K. M. Trybus, and D. M. Warshaw (2004). "Myosin V processivity: Multiple kinetic pathways for head-to-head coordination." In: *Proceedings of the National Academy of Sciences* 101.15, pp. 5542–5546. ISSN: 0027-8424. DOI: 10.1073/pnas.0307247101 (cit. on pp. 48, 59, 82, 85).

Bakshi, Somenath, Albert Siryaporn, Mark Goulian, and James C. Weisshaar (2012). "Superresolution imaging of ribosomes and RNA polymerase in live Escherichia coli cells." In: *Molecular Microbiology*. ISSN: 0950382X. DOI: 10.1111/j.1365-2958.2012.08081.x (cit. on p. 12).

Ball, David A., Gunjan D. Mehta, Ronit Salomon-Kent, Davide Mazza, Tatsuya Morisaki, Florian Mueller, James G. McNally, and Tatiana S. Karpova (2016). "Single molecule tracking of Ace1p in Saccharomyces cerevisiae defines a characteristic residence time for non-specific interactions of transcription factors with chromatin." In: *Nucleic Acids Research* 44.21, gkw744. ISSN: 0305-1048. DOI: 10.1093/nar/

gkw744. URL: https://academic.oup.com/nar/article-lookup/doi/10.1093/nar/gkw744 (cit. on p. 19).

Bar-Shavit, Z and R. Goldman (1976). "Concanavalin A-mediated attachment and ingestion of yeast cells by macrophages." In: *Experimental Cell Research* 99.2, pp. 221–236. ISSN: 00144827. DOI: 10.1016/0014-4827(76)90578-4. URL: https://www.sciencedirect.com/science/article/pii/0014482776905784 (cit. on p. 43).

Barford, J. P. and R. J. Hall (1976). "Estimation of the length of cell cycle phases from asynchronous cultures of Saccharomyces cerevisiae." In: *Experimental Cell Research*. ISSN: 00144827. DOI: 10.1016/0014-4827(76)90043-4 (cit. on p. 8).

Barnett, James A. (2007). "A history of research on yeasts 10: foundations of yeast genetics1." In: *Yeast* 24.10, pp. 799–845. ISSN: 0749503X. DOI: 10.1002/yea.1513. URL: http://doi.wiley.com/10.1002/yea.1513 (cit. on p. 2).

Barral, Yves, Valerie Mermall, Mark S. Mooseker, and Michael Snyder (2000). "Compartmentalization of the cell cortex by septins is required for maintenance of cell polarity in yeast." In: *Molecular Cell*. ISSN: 10972765. DOI: 10.1016/S1097-2765(00)80324-X (cit. on p. 9).

Beach, Dale L., E.D. Salmon, and Kerry Bloom (1999). "Localization and anchoring of mRNA in budding yeast." In: *Current Biology* 9.11, 569–S1. ISSN: 09609822. DOI: 10.1016/S0960-9822(99)80260-7. URL: http://www.sciencedirect.com/science/article/pii/S0960982299802607 (cit. on pp. 15, 80).

Bertalanffy, Ludwig von (1949). "Zu einer allgemeinen Systemlehre." In: *Biologia Generalis* 19.1, pp. 114–129 (cit. on p. 1).

Bertrand, Edouard, Pascal Chartrand, Matthias Schaefer, Shailesh M Shenoy, Robert H Singer, and Roy M Long (1998). "Localization of ASH1 mRNA Particles in Living Yeast." In: *Molecular Cell* 2, pp. 437–445 (cit. on pp. 18, 29, 41, 80, 81).

Bhavsar-Jog, Yogini P. and Erfei Bi (2017). *Mechanics and regulation of cytokinesis in budding yeast*. DOI: 10.1016/j.semcdb.2016.12.010 (cit. on p. 72).

Bier, Karl-Heinz (1963). "Synthese, interzellulärer Transport, und Abbau von Ribonukleinsäuren im Ovar der Stubenfliege Musca domesitica." In: *The Journal of Cell Biology* 16, pp. 436–440. ISSN: 1819-4036. DOI: 10.36718/1819-4036-2020-4-97-101 (cit. on p. 15).

Bloom, Joanna and Frederick R. Cross (2007). *Multiple levels of cyclin specificity in cell-cycle control*. DOI: 10.1038/nrm2105 (cit. on pp. 7, 10).

Boehm, Manfred and Elizabeth G. Nabel (2003). *The cell cycle and cardiovascular diseases.* URL: https://europepmc.org/article/med/14593697 (cit. on p. 7).

Boersma, S., Deepak Khuperkar, Bram M.P. Verhagen, S. Sonneveld, Jonathan B. Grimm, Luke D. Lavis, and Marvin E. Tanenbaum (2019). "Multi-Color Single-Molecule Imaging Uncovers Extensive

Heterogeneity in mRNA Decoding." In: *Cell* 178.2, 458–472.e19. ISSN: 10974172. DOI: 10.1016/j.cell.2019.05.001. URL: https://pubmed.ncbi.nlm.nih.gov/31178119/ (cit. on p. 86).

Boersma, Sanne, Deepak Khuperkar, Bram M.P. Verhagen, Stijn Sonneveld, Jonathan B. Grimm, Luke D. Lavis, and Marvin E. Tanenbaum (2018). "Multi-color single molecule imaging uncovers extensive heterogeneity in mRNA decoding." In: *bioRxiv*, p. 477661. DOI: 10.1101/477661. URL: https://www.biorxiv.org/content/early/2018/11/24/477661 (cit. on p. 86).

Born, M. and E. Wolf (1999). *Principles of Optics 7th edition*. ISBN: 0521642221. arXiv: arXiv:1011.1669v3 (cit. on p. 25).

Borodavka, Alexander, Surendra W. Singaram, Peter G. Stockley, William M. Gelbart, Avinoam Ben-Shaul, and Roman Tuma (2016). "Sizes of Long RNA Molecules Are Determined by the Branching Patterns of Their Secondary Structures." In: *Biophysical Journal* 111.10, pp. 2077–2085. ISSN: 15420086. DOI: 10.1016/j.bpj.2016.10.014. URL: /pmc/articles/PMC5113152/?report=abstracthttps://www.ncbi.nlm.nih.gov/pmc/articles/PMC5113152/ (cit. on p. 82).

Brodsky, Alexander S. and Pamela A. Silver (2002). "Identifying proteins that affect mRNA localization in living cells." In: *Methods* 26.2, pp. 151–155. ISSN: 10462023. DOI: 10.1016/S1046-2023(02)00017-8 (cit. on p. 18).

Brouk, Igor, Amikam Nemirovsky, Kamal Alameh, and Yael Nemirovsky (2010). "Analysis of noise in CMOS image sensor based on a unified time-dependent approach." In: *Solid-State Electronics*. ISSN: 00381101. DOI: 10.1016/j.sse.2009.09.003 (cit. on p. 21).

Cai, En et al. (2014). "Stable small quantum dots for synaptic receptor tracking on live neurons." In: *Angewandte Chemie - International Edition*. ISSN: 15213773. DOI: 10.1002/anie.201405735 (cit. on p. 84).

Cai, Ti, Jason Aulds, Tina Gill, Michael Cerio, and Mark E. Schmitt (2002). "The Saccharomyces cerevisiae RNase mitochondrial RNA processing is critical for cell cycle progression at the end of mitosis." In: *Genetics* 161.3, pp. 1029–1042. ISSN: 00166731 (cit. on p. 11).

Carlton, Peter M. et al. (2010). "Fast live simultaneous multiwavelength four-dimensional optical microscopy." In: *Proceedings of the National Academy of Sciences of the United States of America*. ISSN: 10916490. DOI: 10.1073/pnas.1004037107 (cit. on p. 72).

Casolari, Jason M, Michael a Thompson, Julia Salzman, Lowry M Champion, W E Moerner, and Patrick O Brown (2012). "Widespread mRNA association with cytoskeletal motor proteins and identification and dynamics of myosin-associated mRNAs in S. cerevisiae." In: *PloS one* 7.2, e31912. ISSN: 1932-6203. DOI: 10.1371/journal.pone.0031912. URL: http://www.pubmedcentral.nih.gov/articlerender.fcgi?artid=3281097{\&}tool=pmcentrez{\&}rendertype=abstract (cit. on pp. 10, 28, 29, 57, 82).

Cawte, Adam D., Peter J. Unrau, and David S. Rueda (2020). "Live cell imaging of single RNA molecules with fluorogenic Mango II arrays." In: *Nature Communications*. ISSN: 20411723. DOI: 10.1038/s41467-020-14932-7 (cit. on p. 19).

Chan, Leon Y., Christopher F. Mugler, Stephanie Heinrich, Pascal Vallotton, and Karsten Weis (2018). "Non-invasive measurement of mRNA decay reveals translation initiation as the major determinant of mRNA stability." In: *eLife*. ISSN: 2050084X. DOI: 10.7554/eLife.32536 (cit. on p. 20).

Chan, Yee Hung M. and Wallace F. Marshall (2010). *Scaling properties of cell and organelle size*. DOI: 10.4161/org.6.2.11464 (cit. on p. 7).

Chao, Jeffrey A., Yury Patskovsky, Steven C. Almo, and Robert H. Singer (2008). "Structural basis for the coevolution of a viral RNA-protein complex." In: *Nature Structural and Molecular Biology*. ISSN: 15459993. DOI: 10.1038/nsmb1327 (cit. on p. 18).

Chen, Hsin, Audrey S Howell, Alex Robeson, and Daniel J Lew (2011). "Dynamics of septin ring and collar formation in Saccharomyces cerevisiae." In: *Biological Chemistry*. Vol. 392. 8-9, pp. 689–697. DOI: 10.1515/BC.2011.075 (cit. on p. 72).

Chen, Jiji et al. (2014). "Single-molecule dynamics of enhanceosome assembly in embryonic stem cells." In: *Cell* 156.6, pp. 1274–1285. ISSN: 10974172. DOI: 10.1016/j.cell.2014.01.062 (cit. on pp. 23, 27, 38, 45, 72, 74).

Chen, Piaopiao, Dandan Wang, Han Chen, Zhenzhen Zhou, and Xionglei He (2016). "The nonessentiality of essential genes in yeast provides therapeutic insights into a human disease." In: *Genome Research* 26.10, pp. 1355–1362. ISSN: 15495469. DOI: 10.1101/gr.205955.116. URL: /pmc/articles/PMC5052060/?report=abstracthttps://www.ncbi.nlm.nih.gov/pmc/articles/PMC5052060/ (cit. on p. 12).

Chenouard, Nicolas et al. (2014). *SI for Objective comparison of particle tracking methods*. DOI: 10.1038/nmeth.2808. URL: http://www.ncbi.nlm.nih.gov/pubmed/24441936 (cit. on p. 47).

Chidley, Christopher, Hirohito Haruki, Miriam GrØnlund Pedersen, Evelyne Muller, and Kai Johnsson (2011). "A yeast-based screen reveals that sulfasalazine inhibits tetrahydrobiopterin biosynthesis." In: *Nature Chemical Biology* 7.6, pp. 375–383. ISSN: 15524469. DOI: 10.1038/nchembio.557. URL: www.nature.com/naturechemicalbiology (cit. on p. 19).

Cho, Chun Yi, Christina M. Kelliher, and Steven B. Haase (2019). "The cell-cycle transcriptional network generates and transmits a pulse of transcription once each cell cycle." In: *Cell Cycle*. ISSN: 15514005. DOI: 10.1080/15384101.2019.1570655 (cit. on p. 6).

Clemen, Anabel E.M., Mojca Vilfan, Johann Jaud, Junshan Zhang, Michael Bärmann, and Matthias Rief (2005). "Force-dependent stepping kinetics of myosin-V." In: *Biophysical Journal* 88.6, pp. 4402–

4410. ISSN: 00063495. DOI: 10.1529/biophysj.104.053504 (cit. on pp. 48, 59, 82).

Coelho, C. M. and S. J. Leevers (2000). "Do growth and cell division rates determine cell size in multicellular organisms?" In: *Journal of Cell Science*. ISSN: 00219533 (cit. on p. 7).

Condeelis, John and Robert H. Singer (2005). "How and why does β-actin mRNA target?" In: *Biology of the Cell* 97.1, pp. 97–110. ISSN: 02484900. DOI: 10.1042/BC20040063. URL: http://doi.wiley.com/10.1042/BC20040063 (cit. on p. 9).

Crofts, Andrew J., Haruhiko Washida, Thomas W. Okita, Masahiro Ogawa, Toshihiro Kumamaru, and Hikaru Satoh (2004). *Targeting of proteins to endoplasmic reticulum-derived compartments in plants. The importance of RNA localization*. DOI: 10.1104/pp.104.048934 (cit. on p. 18).

Cross, Frederick R. and Matthew D. Jacobson (2000). "Conservation and Function of a Potential Substrate-Binding Domain in the Yeast Clb5 B-Type Cyclin." In: *Molecular and Cellular Biology*. ISSN: 0270-7306. DOI: 10.1128/mcb.20.13.4782-4790.2000 (cit. on p. 11).

Cross, Frederick R. and Arthur H. Tinkelenberg (1991). "A potential positive feedback loop controlling CLN1 and CLN2 gene expression at the start of the yeast cell cycle." In: *Cell*. ISSN: 00928674. DOI: 10.1016/0092-8674(91)90394-E (cit. on p. 6).

Cross, Frederick R. and James G. Umen (2015). "The Chlamydomonas cell cycle." In: *Plant Journal* 82.3, pp. 370–392. ISSN: 1365313X. DOI: 10.1111/tpj.12795. URL: https://onlinelibrary.wiley.com/doi/full/10.1111/tpj.12795https://onlinelibrary.wiley.com/doi/abs/10.1111/tpj.12795https://onlinelibrary.wiley.com/doi/10.1111/tpj.12795 (cit. on p. 3).

Cross, Frederick R., Nicolas E. Buchler, and Jan M. Skotheim (2011). "Evolution of Crpss and sequences in eukaryotic cell cycle control." In: *Philosophical Transactions of the Royal Society B: Biological Sciences* 366.1584, pp. 3532–3544. ISSN: 14712970. DOI: 10.1098/rstb.2011.0078. URL: /pmc/articles/PMC3203458/?report=abstracthttps://www.ncbi.nlm.nih.gov/pmc/articles/PMC3203458/ (cit. on p. 4).

Currais, Antonio, Tibor Hortobágyi, and Salvador Soriano (2009). *The neuronal cell cycle as a mechanism of pathogenesis in Alzheimer's disease.* DOI: 10.18632/aging.100045 (cit. on p. 7).

Cvijovic, Marija et al. (2014). *Bridging the gaps in systems biology.* DOI: 10.1007/s00438-014-0843-3 (cit. on p. 1).

David, Lior, Wolfgang Huber, Marina Granovskaia, Joern Toedling, Curtis J. Palm, Lee Bofkin, Ted Jones, Ronald W. Davis, and Lars M. Steinmetz (2006). "A high-resolution map of transcription in the yeast genome." In: *Proceedings of the National Academy of Sciences of the United States of America*. ISSN: 00278424. DOI: 10.1073/pnas.0601091103 (cit. on p. 82).

Deng, Yingfeng, Robert H. Singer, and Wei Gu (2008). "Translation of ASH1 mRNA is repressed by Puf6p-Fun12p/eIF5B interaction and released by CK2 phosphorylation." In: *Genes and Development*. ISSN: 08909369. DOI: 10.1101/gad.1611308 (cit. on p. 10).

Denk, Winfried, James H. Strickler, and Watt W. Webb (1990). "Two-photon laser scanning fluorescence microscopy." In: *Science*. ISSN: 00368075. DOI: 10.1126/science.2321027 (cit. on p. 23).

Deshaies, Raymond J. (1997). "Phosphorylation and proteolysis: Partners in the regulation of cell division in budding yeast." In: *Current Opinion in Genetics and Development*. ISSN: 0959437X. DOI: 10.1016/S0959-437X(97)80103-7 (cit. on p. 11).

Deshler, James O., Martin I. Highett, and Bruce J. Schnapp (1997). "Localization of Xenopus Vg1 mRNA by Vera protein and the endoplasmic reticulum." In: *Science*. ISSN: 00368075. DOI: 10.1126/science.276.5315.1128 (cit. on p. 18).

Diezmann, Alex von, Yoav Shechtman, and W. E. Moerner (2017). "Three-Dimensional Localization of Single Molecules for Super-Resolution Imaging and Single-Particle Tracking." In: *Chemical Reviews* 117.11, pp. 7244–7275. ISSN: 15206890. DOI: 10.1021/acs.chemrev.6b00629 (cit. on pp. 22, 26, 28).

Dolgosheina, Elena V., Sunny C.Y. Jeng, Shanker Shyam S. Panchapakesan, Razvan Cojocaru, Patrick S.K. Chen, Peter D. Wilson, Nancy Hawkins, Paul A. Wiggins, and Peter J. Unrau (2014). "RNA Mango aptamer-fluorophore: A bright, high-affinity complex for RNA labeling and tracking." In: *ACS Chemical Biology* 9.10, pp. 2412–2420. ISSN: 15548937. DOI: 10.1021/cb500499x. URL: https://pubs.acs.org/doi/abs/10.1021/cb500499x (cit. on p. 19).

Douzery, Emmanuel J.P., Elizabeth A. Snell, Eric Bapteste, Frédéric Delsuc, and Hervé Philippe (2004). "The timing of eukaryotic evolution: Does a relaxed molecular clock reconcile proteins and fossils?" In: *Proceedings of the National Academy of Sciences of the United States of America*. ISSN: 00278424. DOI: 10.1073/pnas.0403984101 (cit. on p. 2).

Du, Tung-Gia, Maria Schmid, and Ralf-Peter Jansen (2007). "Why cells move messages: the biological functions of mRNA localization." In: *Seminars in cell & developmental biology* 18.2, pp. 171–7. ISSN: 1084-9521. DOI: 10.1016/j.semcdb.2007.01.010. URL: http://www.sciencedirect.com/science/article/pii/S1084952107000341 (cit. on p. 9).

Du, Tung-Gia, Stephan Jellbauer, Marisa Müller, Maria Schmid, Dierk Niessing, and Ralf-Peter Jansen (2008). "Nuclear transit of the RNA-binding protein She2 is required for translational control of localized ASH1 mRNA." In: *EMBO reports* 9.8, pp. 781–787. ISSN: 1469-221X. DOI: 10.1038/embor.2008.112. URL: http://www.ncbi.nlm.nih.gov/pubmed/15459746http://www.pubmedcentral.nih.gov/

articlerender.fcgi?artid=PMC1299151http://embor.embopress.org/cgi/doi/10.1038/embor.2008.112 (cit. on p. 16).

Dupres, Vincent, Yves F. Dufreêne, and Jürgen J. Heinisch (2010). "Measuring cell wall thickness in living yeast cells using single molecular rulers." In: *ACS Nano*. ISSN: 19360851. DOI: 10.1021/nn101598v (cit. on p. 22).

Edelmann, Franziska Theresia (2017). "Structural and functional characterization of the ASH1-mRNP transport-complex from budding yeast." PhD thesis. Technical University of Munich, Germany, p. 185 (cit. on pp. 10, 15).

Edelmann, Franziska Theresia et al. (2017). "Molecular architecture and dynamics of ASH1 mRNA recognition by its mRNA-transport complex." In: *Nature Structural and Molecular Biology* 24.2, pp. 152–161. ISSN: 15459985. DOI: 10.1038/nsmb.3351. URL: https://pubmed.ncbi.nlm.nih.gov/28092367/ (cit. on p. 17).

Eglinger, Jan (2017). *Add Max Quality Spot Analyzer by imagejan · Pull Request #1 · fmi-faim/fmi-trackmate-addons*. URL: https://github.com/fmi-faim/fmi-trackmate-addons/pull/1/files{\#}diff-c32bf09ac9637bc049d44fa86d13b6ee (visited on 02/15/2021) (cit. on p. 85).

Einstein, A. (1906). "Zur Theorie der Brownschen Bewegung." In: *Annalen der Physik* 324.2, pp. 371–381. ISSN: 00033804. DOI: 10.1002/andp.19063240208. URL: http://doi.wiley.com/10.1002/andp.19063240208 (cit. on p. 13).

– (1907). "Theoretische Bemerkungen Über die Brownsche Bewegung." In: *Zeitschrift für Elektrochemie und angewandte physikalische Chemie* 13.6, pp. 41–42. ISSN: 03728323. DOI: 10.1002/bbpc.19070130602 (cit. on p. 47).

Elf, Johan and Irmeli Barkefors (2018). "Single-Molecule Kinetics in Living Cells." In: *Annual Review of Biochemistry* 88.1, pp. 1–25. ISSN: 0066-4154. DOI: 10.1146/annurev-biochem-013118-110801 (cit. on pp. 22, 25, 68).

Eliscovich, Carolina and Robert H Singer (2017). "RNP transport in cell biology: the long and winding road." In: *Current opinion in cell biology* 45, pp. 38–46. ISSN: 1879-0410. DOI: 10.1016/j.ceb.2017.02.008. URL: http://www.ncbi.nlm.nih.gov/pubmed/28258033http://www.pubmedcentral.nih.gov/articlerender.fcgi?artid=PMC5482755 (cit. on p. 9).

Elowitz, Michael B., Michael G. Surette, Pierre Etienne Wolf, Jeff Stock, and Stanislas Leibler (1997). "Photoactivation turns green fluorescent protein red." In: *Current Biology*. ISSN: 09609822. DOI: 10.1016/S0960-9822(06)00342-3 (cit. on p. 15).

Elowitz, Michael B., Michael G. Surette, Pierre Etienne Wolf, Jeffry B. Stock, and Stanislas Leibler (1999). "Protein mobility in the cytoplasm of Escherichia coli." In: *Journal of Bacteriology*. ISSN: 00219193. DOI: 10.1128/jb.181.1.197-203.1999 (cit. on pp. 13, 15).

English, Brian P., Vasili Hauryliuk, Arash Sanamrad, Stoyan Tankov, Nynke H. Dekker, and Johan Elf (2011). "Single-molecule investigations of the stringent response machinery in living bacterial cells." In: *Proceedings of the National Academy of Sciences of the United States of America*. ISSN: 00278424. DOI: 10.1073/pnas.1102255108 (cit. on p. 12).

Enserink, Jorrit M and Richard D Kolodner (2010). "An overview of Cdk1-controlled targets and processes." In: *Cell division* 5, p. 11. ISSN: 1747-1028. DOI: 10.1186/1747-1028-5-11. URL: http://www.pubmedcentral.nih.gov/articlerender.fcgi?artid=2876151{\&}tool=pmcentrez{\&}rendertype=abstract (cit. on p. 6).

Epstein, C. B. and F. R. Cross (1992). "CLB5: A novel B cyclin from budding yeast with a role in S phase." In: *Genes and Development*. ISSN: 08909369. DOI: 10.1101/gad.6.9.1695 (cit. on p. 11).

Erickson, Harold P (2009). "Size and shape of protein molecules at the nanometer level determined by sedimentation, gel filtration, and electron microscopy." In: *Biological procedures online* 11.1, pp. 32–51. ISSN: 1480-9222. DOI: 10.1007/s12575-009-9008-x. URL: http://www.pubmedcentral.nih.gov/articlerender.fcgi?artid=3055910{\%}7B{\&}{\%}7Dtool=pmcentrez{\%}7B{\&}{\%}7Drendertype=abstracthttp://www.pubmedcentral.nih.gov/articlerender.fcgi?artid=3055910{\%}7B{\%}7B{\%}7D{\%}7B{\&}{\%}7D{\%}7B{\%}7D{\%}7Dtool=pmcentrez{\%}7B{\%}7B{\%}7D{\%}7B{\&}{\%}7D{\%}7B{\%}7D{\%}7Drendertype=abstracthttp://www.pubmedcentral.nih.gov/ (cit. on p. 82).

Evans, Tom, Eric T. Rosenthal, Jim Youngblom, Dan Distel, and Tim Hunt (1983). "Cyclin: A protein specified by maternal mRNA in sea urchin eggs that is destroyed at each cleavage division." In: *Cell*. ISSN: 00928674. DOI: 10.1016/0092-8674(83)90420-8 (cit. on p. 2).

Ewald, Jennifer C. (2018). *How yeast coordinates metabolism, growth and division*. DOI: 10.1016/j.mib.2017.12.012 (cit. on p. 6).

Fahrbach, Florian O., Philipp Simon, and Alexander Rohrbach (2010). "Microscopy with self-reconstructing beams." In: *Nature Photonics* 4.11, pp. 780–785. ISSN: 1749-4885. DOI: 10.1038/nphoton.2010.204. URL: http://dx.doi.org/10.1038/nphoton.2010.204 (cit. on pp. 23, 45).

Filonov, Grigory S., Jared D. Moon, Nina Svensen, and Samie R. Jaffrey (2014). "Broccoli: Rapid selection of an RNA mimic of green fluorescent protein by fluorescence-based selection and directed evolution." In: *Journal of the American Chemical Society* 136.46, pp. 16299–16308. ISSN: 15205126. DOI: 10.1021/ja508478x. URL: https://pubs.acs.org/sharingguidelines (cit. on p. 19).

Findley, David F. and Emanuel Parzen (1995). "A conversation with Hirotugu akaike." In: *Statistical Science*. ISSN: 08834237. DOI: 10.1214/ss/1177010133 (cit. on p. 65).

Fitch, I., C. Dahmann, U. Surana, A. Amon, K. Nasmyth, L. Goetsch, B. Byers, and B. Futcher (1992). "Characterization of four B-type cyclin genes of the budding yeast Saccharomyces cerevisiae." In: *Molecular Biology of the Cell*. ISSN: 10591524. DOI: 10.1091/mbc.3.7.805 (cit. on pp. 10, 11).

Forney, G. David (1972). "Maximum-Likelihood Sequence Estimation of Digital Sequences in the Presence of Intersymbol Interference." In: *IEEE Transactions on Information Theory*. ISSN: 15579654. DOI: 10.1109/TIT.1972.1054829 (cit. on pp. 47, 84).

Forsburg, S. L. and P. Nurse (1991). *Cell cycle regulation in the yeasts Saccharomyces cerevisiae and Schizosaccharomyces pombe*. DOI: 10.1146/annurev.cb.07.110191.001303 (cit. on p. 5).

Fossum, Eric R. (1993). "Active Pixel Sensors: Are CCD's Dinosaurs?" In: *Charge-Coupled Devices and Solid State Optical Sensors III* 1900, pp. 2–14. DOI: 10.1117/12.148585 (cit. on p. 22).

Fullerton, Stephanie, Keith Bennett, Eiji Toda, and Teruo Takahashi (2012). "Whitepaper." URL: http://www.hamamatsu.com/resources/pdf/sys/e{_}flash4{_}whitepaper.pdf?{_}ga=2.219683545.1754567246.1595583868-1974504271.1595583868 (cit. on p. 22).

Fundakowski, Julia, Orit Hermesh, and Ralf Peter Jansen (2012). "Localization of a subset of yeast mRNAs depends on inheritance of endoplasmic reticulum." In: *Traffic*. ISSN: 13989219. DOI: 10.1111/tra.12011 (cit. on pp. 18, 29).

Füreder-Kitzmüller, Erwin, Jan Hesse, Andreas Ebner, Hermann J. Gruber, and Gerhard J. Schütz (2005). "Non-exponential bleaching of single bioconjugated Cy5 molecules." In: *Chemical Physics Letters* 404.1-3, pp. 13–18. ISSN: 00092614. DOI: 10.1016/j.cplett.2005.01.053 (cit. on p. 44).

Fusco, Dahlene, Nathalie Accornero, Brigitte Lavoie, Shailesh M. Shenoy, Jean-Marie Blanchard, Robert H. Singer, and Edouard Bertrand (2003). "Single mRNA Molecules Demonstrate Probabilistic Movement in Living Mammalian Cells." In: *Current Biology* 13.2, pp. 161–167. ISSN: 09609822. DOI: 10.1016/S0960-9822(02)01436-7. URL: https://linkinghub.elsevier.com/retrieve/pii/S0960982202014367 (cit. on p. 12).

Futcher, Bruce (1999). "Cell cycle synchronization." In: *Methods in Cell Science*. ISSN: 13815741. DOI: 10.1023/A:1009872403440 (cit. on pp. 54, 57).

Gabaldón, Toni and Eugene V. Koonin (2013). *Functional and evolutionary implications of gene orthology*. DOI: 10.1038/nrg3456 (cit. on p. 2).

Gao, Liang, Lin Shao, Bi-Chang Chen, and Eric Betzig (2014). "3D live fluorescence imaging of cellular dynamics using Bessel beam plane illumination microscopy." In: *Nature Protocols* 9.5, pp. 1083–1101. ISSN: 1754-2189. DOI: 10.1038/nprot.2014.087. URL: http:

//www.nature.com/doifinder/10.1038/nprot.2014.087 (cit. on p. 23).

Garcia, Jennifer F. and Roy Parker (2015). "MS2 coat proteins bound to yeast mRNAs block 5 to 3 degradation and trap mRNA decay products: Implications for the localization of mRNAs by MS2-MCP system." In: *RNA*. ISSN: 14699001. DOI: 10.1261/rna.051797.115 (cit. on pp. 19, 20, 57).

– (2016). "Ubiquitous accumulation of 3 mRNA decay fragments in Saccharomyces cerevisiae mRNAs with chromosomally integrated MS2 arrays." In: *RNA*. ISSN: 14699001. DOI: 10.1261/rna.056325.116 (cit. on pp. 19, 20, 57).

Ghiara, Jayant B., Helena E. Richardson, Katsunori Sugimoto, Martha Henze, Daniel J. Lew, Curt Wittenberg, and Steven I. Reed (1991). "A cyclin B homolog in S. cerevisiae: Chronic activation of the Cdc28 protein kinase by cyclin prevents exit from mitosis." In: *Cell*. ISSN: 00928674. DOI: 10.1016/0092-8674(91)90417-W (cit. on p. 10).

Giaever, Guri et al. (2002). "Functional profiling of the Saccharomyces cerevisiae genome." In: *Nature*. ISSN: 00280836. DOI: 10.1038/nature00935 (cit. on p. 2).

Gill, Tina, Ti Cai, Jason Aulds, Sara Wierzbicki, and Mark E. Schmitt (2004). "RNase MRP Cleaves the CLB2 mRNA To Promote Cell Cycle Progression: Novel Method of mRNA Degradation." In: *Molecular and Cellular Biology*. ISSN: 0270-7306. DOI: 10.1128/mcb.24.3.945-953.2004 (cit. on pp. 11, 82).

Ginzberg, Miriam B., Ran Kafri, and Marc Kirschner (2015). *On being the right (cell) size*. DOI: 10.1126/science.1245075 (cit. on p. 8).

Godinez, W. J., M. Lampe, S Wörz, B Müller, R. Eils, and K. Rohr (2009). "Deterministic and probabilistic approaches for tracking virus particles in time-lapse fluorescence microscopy image sequences." In: *Medical image analysis* 13.2, pp. 325–342. ISSN: 1361-8423. DOI: 10.1016/j.media.2008.12.004. URL: http://www.ncbi.nlm.nih.gov/pubmed/19223219 (cit. on p. 84).

Goffeau, A. et al. (1996). "Life with 6000 genes." In: *Science*. ISSN: 00368075. DOI: 10.1126/science.274.5287.546 (cit. on p. 3).

Golding, Ido and Edward C. Cox (2004). "RNA dynamics in live Escherichia coli cells." In: *Proceedings of the National Academy of Sciences of the United States of America*. ISSN: 00278424. DOI: 10.1073/pnas.0404443101 (cit. on p. 19).

Gonsalvez, Graydon B, Carl R Urbinati, and Roy M Long (2005). "RNA localization in yeast: moving towards a mechanism." In: *Biology of the cell / under the auspices of the European Cell Biology Organization* 97.1, pp. 75–86. ISSN: 0248-4900. DOI: 10.1042/BC20040066. URL: http://www.ncbi.nlm.nih.gov/pubmed/15601259 (cit. on p. 17).

Gonzalez, Isabel, Sara B.C. Buonomo, Kim Nasmyth, and Uwe Von Ahsen (1999). "ASH1 mRNA localization in yeast involves multiple secondary structural elements and ASH1 protein translation." In:

Current Biology. ISSN: 09609822. DOI: 10.1016/S0960-9822(99)80145-6 (cit. on p. 17).

Gopal, Ajaykumar, Z. Hong Zhou, Charles M. Knobler, and William M. Gelbart (2012). "Visualizing large RNA molecules in solution." In: *RNA* 18.2, pp. 284–299. ISSN: 13558382. DOI: 10.1261/rna.027557.111 (cit. on p. 82).

Gopinath, S., Q. Wen, N. Thakoor, K. Luby-Phelps, and J. X. Gao (2008). "A statistical approach for intensity loss compensation of confocal microscopy images." In: *Journal of Microscopy*. ISSN: 00222720. DOI: 10.1111/j.1365-2818.2008.01964.x (cit. on p. 44).

Grandin, N and S I Reed (1993). "Differential function and expression of Saccharomyces cerevisiae B-type cyclins in mitosis and meiosis." In: *Molecular and Cellular Biology*. ISSN: 0270-7306. DOI: 10.1128/mcb.13.4.2113 (cit. on p. 10).

Grünwald, David and Robert H Singer (2010). "SI -In vivo imaging of labelled endogenous β-actin mRNA during nucleocytoplasmic transport." In: *Nature* 467.7315, pp. 604–607. ISSN: 1476-4687. DOI: 10.1038/nature09438. URL: http://www.pubmedcentral.nih.gov/articlerender.fcgi?artid=3005609{\%}7B{\%}7B{\%}7D{\%}7B{\&}{\%}7D{\%}7B{\%}7D{\%}7Dtool=pmcentrez{\%}7B{\%}7B{\%}5E{\%}7D{\%}7B{\&}{\%}7D{\%}7B{\%}7D{\%}7Drendertype=abstracthttp://www.pubmedcentral.nih.gov/articlerender.fcgi?artid=3005609{\%}7B{\&}{\%}7Dtool=pmcentrez{\%}7B{\&}{\%}7Drendertype (cit. on pp. 12, 59).

Gu, Wei, Yingfeng Deng, Daniel Zenklusen, and Robert H. Singer (2004). "A new yeast PUF family protein, Puf6p, represses ASH1 mRNA translation and is required for its localization." In: *Genes and Development*. ISSN: 08909369. DOI: 10.1101/gad.1189004 (cit. on p. 10).

Gueldener, U., J. Heinisch, G. J. Koehler, D. Voss, and J. H. Hegemann (2002). "A second set of loxP marker cassettes for Cre-mediated multiple gene knockouts in budding yeast." In: *Nucleic acids research*. ISSN: 13624962. DOI: 10.1093/nar/30.6.e23 (cit. on p. 42).

Guigas, Gernot and Matthias Weiss (2008). "Sampling the cell with anomalous diffusion - The discovery of slowness." In: *Biophysical Journal* 94.1, pp. 90–94. ISSN: 00063495. DOI: 10.1529/biophysj.107.117044. URL: /pmc/articles/PMC2134854/?report=abstracthttps://www.ncbi.nlm.nih.gov/pmc/articles/PMC2134854/ (cit. on p. 14).

Gustavsson, Anna Karin, Petar N. Petrov, Maurice Y. Lee, Yoav Shechtman, and W. E. Moerner (2018). "3D single-molecule super-resolution microscopy with a tilted light sheet." In: *Nature Communications*. ISSN: 20411723. DOI: 10.1038/s41467-017-02563-4 (cit. on p. 29).

Haarer, B K and J R Pringle (1987). "Immunofluorescence localization of the Saccharomyces cerevisiae CDC12 gene product to the vicinity of the 10-nm filaments in the mother-bud neck." In: *Molecular and*

Cellular Biology. ISSN: 0270-7306. DOI: 10.1128/mcb.7.10.3678 (cit. on p. 72).

Haase, Steven B. and Steven I. Reed (1999). "Evidence that a free-running oscillator drives G1 events in the budding yeast cell cycle." In: *Nature* 401.6751, pp. 394–397. ISSN: 0028-0836. DOI: 10.1038/43927. URL: http://www.nature.com/doifinder/10.1038/43927 (cit. on p. 6).

Haase, Steven B and Curt Wittenberg (2014). "Topology and control of the cell-cycle-regulated transcriptional circuitry." In: *Genetics* 196.1, pp. 65–90. ISSN: 1943-2631. DOI: 10.1534/genetics.113.152595. URL: http://www.genetics.org/content/196/1/65.abstract (cit. on p. 4).

Haber, James E. (2012). "Mating-type genes and MAT switching in Saccharomyces cerevisiae." In: *Genetics*. ISSN: 00166731. DOI: 10.1534/genetics.111.134577 (cit. on p. 6).

Haim-Vilmovsky, Liora and Jeffrey E. Gerst (2009). "m-TAG: A PCR-based genomic integration method to visualize the localization of specific endogenous mRNAs in vivo in yeast." In: *Nature Protocols*. ISSN: 17542189. DOI: 10.1038/nprot.2009.115 (cit. on p. 41).

Haim, Liora, Gadi Zipor, Stella Aronov, and Jeffrey E. Gerst (2007). "A genomic integration method to visualize localization of endogenous mRNAs in living yeast." In: *Nature Methods*. ISSN: 15487091. DOI: 10.1038/nmeth1040 (cit. on p. 41).

Haimovich, Gal, Mordechai Choder, Robert H Singer, and Tatjana Trcek (2013). "The fate of the messenger is pre-determined: a new model for regulation of gene expression." In: *Biochimica et biophysica acta* 1829.6-7, pp. 643–53. ISSN: 0006-3002. DOI: 10.1016/j.bbagrm.2013.01.004. URL: http://www.ncbi.nlm.nih.gov/pubmed/23337853http://www.pubmedcentral.nih.gov/articlerender.fcgi?artid=PMC3891481 (cit. on p. 11).

Haimovich, Gal, Dmitry Zabezhinsky, Brian Haas, Boris Slobodin, Pravinkumar Purushothaman, Lin Fan, Joshua Z. Levin, Chad Nusbaum, and Jeffrey E. Gerst (2016). "Use of the MS2 aptamer and coat protein for RNA localization in yeast: A response to "MS2 coat proteins bound to yeast mRNAs block 5 to 3 degradation and trap mRNA decay products: Implications for the localization of mRNAs by MS2-MCP system"." In: *RNA*. ISSN: 14699001. DOI: 10.1261/rna.055095.115 (cit. on pp. 19, 20).

Hain, Rainer, Christian J. Kähler, and Cam Tropea (2007). "Comparison of CCD, CMOS and intensified cameras." In: *Experiments in Fluids*. ISSN: 07234864. DOI: 10.1007/s00348-006-0247-1 (cit. on pp. 21, 22).

Halatek, J. and E. Frey (2018). "Rethinking pattern formation in reaction-diffusion systems." In: *Nature Physics*. ISSN: 17452481. DOI: 10.1038/s41567-017-0040-5 (cit. on p. 16).

Halstead, James M., Timothée Lionnet, Johannes H. Wilbertz, Frank Wippich, Anne Ephrussi, Robert H. Singer, and Jeffrey A. Chao (2015). "An RNA biosensor for imaging the first round of translation from single cells to living animals." In: *Science* 347.6228, pp. 1367–1671. ISSN: 0036-8075. DOI: 10.1126/science.aaa3380. URL: http://www.ncbi.nlm.nih.gov/pubmed/25792328{\%}5Cnhttp://www.pubmedcentral.nih.gov/articlerender.fcgi?artid=PMC4451088{\%}5Cnhttp://www.sciencemag.org/cgi/doi/10.1126/science.aaa3380http://www.sciencemag.org/content/347/6228/1367.abstract (cit. on p. 87).

Hansen, Anders S., Maxime Woringer, Jonathan B. Grimm, Luke D. Lavis, Robert Tjian, and Xavier Darzacq (2018). "Robust model-based analysis of single-particle tracking experiments with spot-on." In: *eLife* 7, pp. 1–33. ISSN: 2050084X. DOI: 10.7554/eLife.33125 (cit. on p. 81).

Harashima, Hirofumi, Nico Dissmeyer, and Arp Schnittger (2013). *Cell cycle control across the eukaryotic kingdom*. DOI: 10.1016/j.tcb.2013.03.002 (cit. on p. 3).

Hartwell, L. H., J. Culotti, and B. Reid (1970). "Genetic control of the cell-division cycle in yeast. I. Detection of mutants." In: *Proceedings of the National Academy of Sciences of the United States of America*. ISSN: 00278424. DOI: 10.1073/pnas.66.2.352 (cit. on pp. 2, 3).

Hartwell, L. H., R. K. Mortimer, J. Culotti, and M. Culotti (1973). "Genetic control of the cell division cycle in yeast: V. Genetic analysis of cdc mutants." In: *Genetics* 74.2, pp. 267–286. ISSN: 00166731 (cit. on p. 2).

Hartwell, Leland H. and Ted A. Weinert (1989). "Checkpoints: Controls that ensure the order of cell cycle events." In: *Science*. ISSN: 00368075. DOI: 10.1126/science.2683079 (cit. on p. 6).

Harvey, Stacy L. and Douglas R. Kellogg (2003). "Conservation of mechanisms controlling entry into mitosis: Budding yeast wee1 delays entry into mitosis and is required for cell size control." In: *Current Biology*. ISSN: 09609822. DOI: 10.1016/S0960-9822(03)00049-6 (cit. on pp. 8, 9).

Hasnain, Sabeeha, Christopher L. McClendon, Monica T. Hsu, Matthew P. Jacobson, and Pradipta Bandyopadhyay (2014). "A new coarse-grained model for E. coli cytoplasm: Accurate calculation of the diffusion coefficient of proteins and observation of anomalous diffusion." In: *PLoS ONE*. ISSN: 19326203. DOI: 10.1371/journal.pone.0106466 (cit. on p. 13).

Hazelrigg, Tulle (1998). "The destinies and destinations of RNAs." In: *Cell* 95.4, pp. 451–460. ISSN: 00928674. DOI: 10.1016/S0092-8674(00)81613-X (cit. on p. 15).

He, Xionglei and Jianzhi Zhang (2009). "On the Growth of Scientific Knowledge: Yeast Biology as a Case Study." In: *PLoS Computational Biology* 5.3. Ed. by Andrey Rzhetsky, e1000320. ISSN: 1553-7358. DOI:

10.1371/journal.pcbi.1000320. URL: https://dx.plos.org/10.1371/journal.pcbi.1000320 (cit. on p. 3).

Heinrich, Stephanie, Corinne L. Sidler, Claus M. Azzalin, and Karsten Weis (2017). "Stem-loop RNA labeling can affect nuclear and cytoplasmic mRNA processing." In: *RNA*. ISSN: 14699001. DOI: 10.1261/rna.057786.116 (cit. on pp. 19, 20).

Herskowitz, I. (1988). *Life cycle of the budding yeast Saccharomyces cerevisiae*. DOI: 10.1128/mmbr.52.4.536-553.1988 (cit. on p. 16).

Herskowitz, Ira (1985). *Cell biology: Yeast as the universal cell*. DOI: 10.1038/316678a0. URL: https://www.nature.com/articles/316678a0 (cit. on p. 3).

Heym, Roland Gerhard and Dierk Niessing (2012). "Principles of mRNA transport in yeast." In: *Cellular and molecular life sciences : CMLS* 69.11, pp. 1843–53. ISSN: 1420-9071. DOI: 10.1007/s00018-011-0902-4. URL: http://www.ncbi.nlm.nih.gov/pubmed/22159587http://www.pubmedcentral.nih.gov/articlerender.fcgi?artid=PMC3350770 (cit. on pp. 10, 15, 17, 85).

Hocine, Sami, Pascal Raymond, Daniel Zenklusen, Jeffrey A Chao, and Robert H Singer (2013). "Single-molecule analysis of gene expression using two-color RNA labeling in live yeast." en. In: *Nature methods* 10.2, pp. 119–21. ISSN: 1548-7105. DOI: 10.1038/nmeth.2305. URL: http://www.nature.com/nmeth/journal/v10/n2/abs/nmeth.2305.html{\#}affil-auth (cit. on pp. 19, 20).

Hoffman, Charles S., Valerie Wood, and Peter A. Fantes (2015). "An ancient yeast for young geneticists: A primer on the Schizosaccharomyces pombe model system." In: *Genetics* 201.2, pp. 403–423. ISSN: 19432631. DOI: 10.1534/genetics.115.181503. URL: www.genetics.org/lookup/suppl/doi:10.1534/genetics.115.181503/-/DC1 (cit. on p. 3).

Holtzer, Laurent, Tobias Meckel, and Thomas Schmidt (2007). "Nanometric three-dimensional tracking of individual quantum dots in cells." In: *Applied Physics Letters*. ISSN: 00036951. DOI: 10.1063/1.2437066 (cit. on p. 27).

Holyst, Robert et al. (2009). "Scaling form of viscosity at all length-scales in poly(ethylene glycol) solutions studied by fluorescence correlation spectroscopy and capillary electrophoresis." In: *Physical Chemistry Chemical Physics* 11.40, pp. 9025–9032. ISSN: 14639076. DOI: 10.1039/b908386c. URL: https://pubmed.ncbi.nlm.nih.gov/19812821/ (cit. on p. 13).

Hood, JK K, WW W Hwang, and PA A Silver (2001). "The Saccharomyces cerevisiae cyclin Clb2p is targeted to multiple subcellular locations by cis- and trans-acting determinants." In: *J. Cell Sci.* 114.3, pp. 589–597. URL: http://jcs.biologists.org/content/114/3/589.short (cit. on p. 11).

Hosny, Neveen A. et al. (2020). "Planar Airy beam light-sheet for two-photon microscopy." In: *Biomedical Optics Express* 11.7, pp. 3927–

3935. ISSN: 23318422. DOI: 10.1364/boe.395547. arXiv: 2001.06829 (cit. on p. 23).

Huang, Bo, Wenqin Wang, Mark Bates, and Xiaowei Zhuang (2008). "Three-dimensional super-resolution imaging by stochastic optical reconstruction microscopy." In: *Science*. ISSN: 00368075. DOI: 10.1126/science.1153529 (cit. on p. 27).

Huisken, Jan, Jim Swoger, Filippo Del Bene, Joachim Wittbrodt, and Ernst H.K. Stelzer (2004). "Optical sectioning deep inside live embryos by selective plane illumination microscopy." In: *Science*. ISSN: 00368075. DOI: 10.1126/science.1100035 (cit. on p. 23).

Irie, Kenji, Tomofumi Tadauchi, and Peter A. Takizawa (2002). "The Khd1 protein, which has three KH RNA-binding motifs, is required for proper localization of ASH1 mRNA in yeast." In: *EMBO Journal*. ISSN: 02614189. DOI: 10.1093/emboj/21.5.1158 (cit. on p. 10).

Ivanova, Tsvetomira, Michael Maier, Alsu Missarova, Céline Ziegler-Birling, Monica Dam, Mercè Gomar-Alba, Lucas B. Carey, and Manuel Mendoza (2020). "Budding yeast complete DNA synthesis after chromosome segregation begins." In: *Nature Communications* 11.1, pp. 1–13. ISSN: 20411723. DOI: 10.1038/s41467-020-16100-3. URL: https://doi.org/10.1038/s41467-020-16100-3 (cit. on p. 5).

Izeddin, I., J. Boulanger, V. Racine, C.G. Specht, A. Kechkar, D. Nair, A. Triller, D. Choquet, M. Dahan, and J.B. Sibarita (2012). "Wavelet analysis for single molecule localization microscopy." In: *Optics Express*. ISSN: 1094-4087. DOI: 10.1364/oe.20.002081 (cit. on p. 84).

Jambor, Helena, Vineeth Surendranath, Alex T. Kalinka, Pavel Mejstrik, Stephan Saalfeld, and Pavel Tomancak (2015). "Systematic imaging reveals features and changing localization of mRNAs in Drosophila development." In: *eLife*. ISSN: 2050084X. DOI: 10.7554/eLife.05003 (cit. on p. 15).

Janesick, James R. (2001). "Noise Sources." In: *Scientific Charge-Coupled Devices*. Ed. by SPIE. Spie Press. Bellingham, WA, USA, pp. 605–720. DOI: https://doi.org/10.1117/3.374903 (cit. on p. 21).

Jansen, Ralf Peter, Celia Dowzer, Christine Michaelis, Marta Galova, and Kim Nasmyth (1996). "Mother cell-specific HO expression in budding yeast depends on the unconventional myosin Myo4p and other cytoplasmic proteins." In: *Cell*. ISSN: 00928674. DOI: 10.1016/S0092-8674(00)81047-8 (cit. on p. 16).

Jaqaman, Khuloud, Dinah Loerke, Marcel Mettlen, Hirotaka Kuwata, Sergio Grinstein, Sandra L. Schmid, and Gaudenz Danuser (2008). "Robust single-particle tracking in live-cell time-lapse sequences." In: *Nature Methods*. ISSN: 15487091. DOI: 10.1038/nmeth.1237 (cit. on p. 47).

Jaqaman, Khuloud, Hirotaka Kuwata, Nicolas Touret, Richard Collins, William S. Trimble, Gaudenz Danuser, and Sergio Grinstein (2011). "Cytoskeletal control of CD36 diffusion promotes its receptor and

signaling function." In: *Cell*. ISSN: 00928674. DOI: 10.1016/j.cell.2011.06.049 (cit. on p. 51).

Jensen, R., G. F. Sprague, and I. Herskowitz (1983). "Regulation of yeast mating-type interconversion: feedback control of HO gene expression by the mating-type locus." In: *Proceedings of the National Academy of Sciences of the United States of America* 80.10, pp. 3035–3039. ISSN: 00278424. DOI: 10.1073/pnas.80.10.3035 (cit. on p. 5).

Jeon, Jae Hyung and Ralf Metzler (2010). "Fractional Brownian motion and motion governed by the fractional Langevin equation in confined geometries." In: *Physical Review E - Statistical, Nonlinear, and Soft Matter Physics* 81.2. ISSN: 15393755. DOI: 10.1103/PhysRevE.81.021103 (cit. on p. 14).

Jeon, Jae Hyung, Vincent Tejedor, Stas Burov, Eli Barkai, Christine Selhuber-Unkel, Kirstine Berg-Sørensen, Lene Oddershede, and Ralf Metzler (2011). "In vivo anomalous diffusion and weak ergodicity breaking of lipid granules." In: *Physical Review Letters* 106.4, p. 048103. ISSN: 00319007. DOI: 10.1103/PhysRevLett.106.048103. arXiv: 1010.0347. URL: https://journals.aps.org/prl/abstract/10.1103/PhysRevLett.106.048103 (cit. on p. 14).

Jia, Shu, Joshua C. Vaughan, and Xiaowei Zhuang (2013). "Isotropic 3D super-resolution imaging with a self-bending point spread function." In: *Optics InfoBase Conference Papers*. ISBN: 9781557529879. DOI: 10.1364/fio.2013.ftu2f.2 (cit. on p. 28).

– (2014). "Isotropic three-dimensional super-resolution imaging with a self-bending point spread function." In: *Nature Photonics*. ISSN: 17494893. DOI: 10.1038/nphoton.2014.13 (cit. on p. 28).

Johnson, Amy and Jan M. Skotheim (2013). *Start and the restriction point*. DOI: 10.1016/j.ceb.2013.07.010. URL: /pmc/articles/PMC3836907/?report=abstracthttps://www.ncbi.nlm.nih.gov/pmc/articles/PMC3836907/ (cit. on p. 7).

Joubert, James R. and Deepak K. Sharma (2011). "EMCCD vs. SCMOS for microscopic imaging." In: *Photonics Spectra*. ISSN: 07311230 (cit. on p. 22).

Joyner, Ryan P., Jeffrey H. Tang, Jonne Helenius, Elisa Dultz, Christiane Brune, Liam J. Holt, Sebastien Huet, Daniel J. Müller, and Karsten Weis (2016). "A glucose-starvation response regulates the diffusion of macromolecules." In: *eLife* 5.MARCH2016. ISSN: 2050084X. DOI: 10.7554/eLife.09376 (cit. on p. 13).

Juette, Manuel F., Travis J. Gould, Mark D. Lessard, Michael J. Mlodzianoski, Bhupendra S. Nagpure, Brian T. Bennett, Samuel T. Hess, and Joerg Bewersdorf (2008). "Three-dimensional sub-100 nm resolution fluorescence microscopy of thick samples." In: *Nature Methods*. ISSN: 15487091. DOI: 10.1038/nmeth.1211 (cit. on p. 84).

Jun, Suckjoon and Sattar Taheri-Araghi (2015). *Cell-size maintenance: Universal strategy revealed*. DOI: 10.1016/j.tim.2014.12.001. arXiv: arXiv:1504.00043v1 (cit. on p. 7).

Kachroo, Aashiq H., Jon M. Laurent, Christopher M. Yellman, Austin G. Meyer, Claus O. Wilke, and Edward M. Marcotte (2015). "Systematic humanization of yeast genes reveals conserved functions and genetic modularity." In: *Science* 348.6237, pp. 921–925. ISSN: 10959203. DOI: 10.1126/science.aaa0769. URL: /pmc/articles/PMC4718922/?report=abstracthttps://www.ncbi.nlm.nih.gov/pmc/articles/PMC4718922/ (cit. on p. 2).

Kaeberlein, Matt, Kathryn T. Kirkland, Stanley Fields, and Brian K. Kennedy (2005). "Genes determining yeast replicative life span in a long-lived genetic background." In: *Mechanisms of Ageing and Development* 126.4, pp. 491–504. ISSN: 00476374. DOI: 10.1016/j.mad.2004.10.007 (cit. on p. 5).

Kao, H. P. and A. S. Verkman (1994). "Tracking of single fluorescent particles in three dimensions: use of cylindrical optics to encode particle position." In: *Biophysical Journal*. ISSN: 00063495. DOI: 10.1016/S0006-3495(94)80601-0 (cit. on p. 27).

Katz, Zachary B, Brian P English, Timothée Lionnet, Young J Yoon, Nilah Monnier, Ben Ovryn, Mark Bathe, and Robert H Singer (2016). "Mapping translation 'hot-spots' in live cells by tracking single molecules of mRNA and ribosomes." In: *eLife* 5, e10415. ISSN: 2050-084X. DOI: 10.7554/eLife.10415. URL: http://elifesciences.org/content/early/2016/01/13/eLife.10415.abstract (cit. on pp. 12, 68).

Kay, Steven M. (1993). "Cramer-Rao Lower Bound." In: *Fundamentals of Statistical Signal Processing Estimation Theory*. Upper Saddle River, NJ: Prentice Hall, pp. 27–82 (cit. on pp. 21, 28).

Kejiou, Nevraj S. and Alexander F. Palazzo (2017). *mRNA localization as a rheostat to regulate subcellular gene expression*. DOI: 10.1002/wrna.1416 (cit. on p. 17).

Keller, Philipp J. and Misha B. Ahrens (2015). *Visualizing whole-brain activity and development at the single-cell level using light-sheet microscopy*. DOI: 10.1016/j.neuron.2014.12.039 (cit. on p. 23).

Kiernan, John A. (2000). "Formaldehyde, Formalin, Paraformaldehyde And Glutaraldehyde: What They Are And What They Do." In: *Microscopy Today*. ISSN: 1551-9295. DOI: 10.1017/s1551929500057060 (cit. on p. 52).

Kilmartin, J. V. and A. E.M. Adams (1984). "Structural rearrangements of tubulin and actin during the cell cycle of the yeast Saccharomyces." In: *Journal of Cell Biology*. ISSN: 00219525. DOI: 10.1083/jcb.98.3.922 (cit. on p. 16).

Kim, Songhee H., Melissa Vieira, Hye Jin Kim, Mahipal Singh Kesawat, and Hye Yoon Park (2019). "MS2 Labeling of Endogenous Beta-Actin mRNA Does Not Result in Stabilization of Degradation Intermediates." In: *Molecules and cells*. ISSN: 02191032. DOI: 10.14348/molcells.2019.2398 (cit. on p. 20).

Kinkhabwala, Ali, Anton Khmelinskii, and Michael Knop (2014). "Analytical model for macromolecular partitioning during yeast cell division." In: *BMC Biophysics* 7.1, pp. 1–10. ISSN: 2046-1682. DOI: 10.1186/s13628-014-0010-6. URL: http://www.biomedcentral.com/2046-1682/7/10 (cit. on p. 83).

Kitano, Hiroaki (2002). *Systems biology: A brief overview*. DOI: 10.1126/science.1069492 (cit. on p. 1).

Klipp, Edda (2007). "Modelling dynamic processes in yeast." In: *Yeast (Chichester, England)* 24.11, pp. 943–959. ISSN: 0749-503X. DOI: 10.1002/yea.1544. URL: http://apps.webofknowledge.com/full{_}record.do?product=WOS{\&}search{_}mode=Refine{\&}qid=6{\&}SID=W1mje1Xp9JK4BtA53OO{\&}page=6{\&}doc=59{\&}cacheurlFromRightClick=no (cit. on p. 4).

Klipp, Edda, Bodil Nordlander, Roland Krüger, Peter Gennemark, and Stefan Hohmann (2005). "Integrative model of the response of yeast to osmotic shock." In: *Nature Biotechnology*. ISSN: 10870156. DOI: 10.1038/nbt1114 (cit. on p. 1).

Koff, Andrew, Fred Cross, Alfred Fisher, Jill Schumacher, Katherine Leguellec, Michel Philippe, and James M. Roberts (1991). "Human cyclin E, a new cyclin that interacts with two members of the CDC2 gene family." In: *Cell* 66.6, pp. 1217–1228. ISSN: 00928674. DOI: 10.1016/0092-8674(91)90044-Y. URL: http://www.cell.com/article/009286749190044Y/fulltexthttp://www.cell.com/article/009286749190044Y/abstracthttps://www.cell.com/cell/abstract/0092-8674(91)90044-Y (cit. on p. 4).

Kolaczkowski, Marcin, Anna Kolaczkowska, Jacek Luczynski, Stanislaw Witek, and Andre Goffeau (1998). "In vivo characterization of the drug resistance profile of the major ABC transporters and other components of the yeast pleiotropic drug resistance network." In: *Microbial Drug Resistance* 4.3, pp. 143–158. ISSN: 10766294. DOI: 10.1089/mdr.1998.4.143. URL: https://pubmed.ncbi.nlm.nih.gov/9818966/ (cit. on p. 19).

Kong, Hui, Hatice Cinar Akakin, and Sanjay E. Sarma (2013). "A generalized laplacian of gaussian filter for blob detection and its applications." In: *IEEE Transactions on Cybernetics*. ISSN: 21682267. DOI: 10.1109/TSMCB.2012.2228639 (cit. on p. 85).

Koshland, Daniel E. (2002). *The seven pillars of life*. DOI: 10.1126/science.1068489 (cit. on p. 4).

Kostriken, R, J N Strathern, A J Klar, J B Hicks, and F Heffron (1983). "A site-specific endonuclease essential for mating-type switching in Saccharomyces cerevisiae." In: *Cell* 35.1, pp. 167–74. ISSN: 0092-8674. DOI: 10.1016/0092-8674(83)90219-2. URL: http://www.ncbi.nlm.nih.gov/pubmed/6313222 (cit. on p. 5).

Kraut-Cohen, Judith, Evgenia Afanasieva, Liora Haim-Vilmovsky, Boris Slobodin, Ido Yosef, Eitan Bibi, and Jeffrey E. Gerst (2013). "Translation- and SRP-independent mRNA targeting to the endoplas-

mic reticulum in the yeast Saccharomyces cerevisiae." In: *Molecular Biology of the Cell*. ISSN: 10591524. DOI: 10.1091/mbc.E13-01-0038 (cit. on p. 20).

Kukhtevich, I. V., N. Lohrberg, F. Padovani, R. Schneider, and K. M. Schmoller (2020). "Cell size sets the diameter of the budding yeast contractile ring." In: *Nature Communications*. ISSN: 20411723. DOI: 10.1038/s41467-020-16764-x (cit. on p. 72).

Lampo, Thomas J., Stella Stylianidou, Mikael P. Backlund, Paul A. Wiggins, and Andrew J. Spakowitz (2017). "Cytoplasmic RNA-Protein Particles Exhibit Non-Gaussian Subdiffusive Behavior." In: *Biophysical Journal* 112.3, pp. 532–542. ISSN: 15420086. DOI: 10.1016/j.bpj.2016.11.3208. URL: https://pubmed.ncbi.nlm.nih.gov/28088300/ (cit. on pp. 12–15, 28, 29, 48, 60, 82, 83, 85).

Landry, B. D., C. E. Mapa, H. E. Arsenault, K. E. Poti, and J. A. Benanti (2014). "Regulation of a transcription factor network by Cdk1 coordinates late cell cycle gene expression." In: *The EMBO Journal* 33.9, pp. 1044–1060. ISSN: 0261-4189. DOI: 10.1002/embj.201386877. URL: http://emboj.embopress.org/cgi/doi/10.1002/embj.201386877 (cit. on pp. 6, 10).

Lange, Susanne, Yoshihiko Katayama, Maria Schmid, Ondrej Burkacky, Christoph Brauchle, Don C. Lamb, and Ralf Peter Jansen (2008). "Simultaneous transport of different localized mRNA species revealed by live-cell imaging." In: *Traffic* 9.8, pp. 1256–1267. ISSN: 13989219. DOI: 10.1111/j.1600-0854.2008.00763.x (cit. on pp. 17, 18).

Langmuir, Irving (1918). "The adsorption of gases on plane surfaces of glass, mica and platinum." In: *Journal of the American Chemical Society* 40.9, pp. 1361–1403. ISSN: 15205126. DOI: 10.1021/ja02242a004. URL: https://zenodo.org/record/1429050 (cit. on p. 12).

Laplace, Pierre-Simon de (1812). *Théorie analytique des probabilitiés*. Paris: Courcier, p. 411 (cit. on p. 12).

Lasko, Paul (2012). *mRNA localization and translational control in Drosophila oogenesis*. DOI: 10.1101/cshperspect.a012294 (cit. on p. 9).

Laughery, Marian F., Tierra Hunter, Alexander Brown, James Hoopes, Travis Ostbye, Taven Shumaker, and John J. Wyrick (2015). "New vectors for simple and streamlined CRISPR-Cas9 genome editing in Saccharomyces cerevisiae." In: *Yeast* 32.12, pp. 711–720. ISSN: 0749503X. DOI: 10.1002/yea.3098. URL: http://doi.wiley.com/10.1002/yea.3098 (cit. on p. 42).

Laurent, Jon M., Jonathan H. Young, Aashiq H. Kachroo, and Edward M. Marcotte (2016). "Efforts to make and apply humanized yeast." In: *Briefings in Functional Genomics*. ISSN: 20412657. DOI: 10.1093/bfgp/elv041 (cit. on p. 2).

Lawrence, Jeanne Bentley and Robert H. Singer (1986). "Intracellular localization of messenger RNAs for cytoskeletal proteins." In: *Cell* 45.3, pp. 407–415. ISSN: 00928674. DOI: 10.1016/0092-8674(86)90326-0 (cit. on p. 15).

Lee, Melanie G. and Paul Nurse (1987). "Complementation used to clone a human homologue of the fission yeast cell cycle control gene cdc2." In: *Nature* 327.6117, pp. 31–35. ISSN: 00280836. DOI: 10.1038/327031a0. URL: https://www.nature.com/articles/327031a0 (cit. on pp. 3, 4).

Léopold, Pierre and Patrick H O'farrell (1991). *An Evolutionarily Conserved Cyclin Homolog from Drosophila Rescues Yeast Deficient in G1 Cyclins*. Tech. rep. 6, p. 1207. URL: /pmc/articles/PMC2753436/?report=abstracthttps://www.ncbi.nlm.nih.gov/pmc/articles/PMC2753436/ (cit. on p. 4).

Lew, Daniel J. and Steven I. Reed (1995). "Cell cycle control of morphogenesis in budding yeast." In: *Current Opinion in Genetics and Development*. ISSN: 0959437X. DOI: 10.1016/S0959-437X(95)90048-9 (cit. on p. 8).

Lew, Daniel J., Vjekoslav Dulić, and Steven I. Reed (1991). "Isolation of three novel human cyclins by rescue of G1 cyclin (cln) function in yeast." In: *Cell*. ISSN: 00928674. DOI: 10.1016/0092-8674(91)90042-W (cit. on p. 4).

Lew, Matthew D., Steven F. Lee, Majid Badieirostami, and W. E. Moerner (2011). "Corkscrew point spread function for far-field three-dimensional nanoscale localization of pointlike objects." In: *Optics Letters* 36.2, p. 202. ISSN: 0146-9592. DOI: 10.1364/ol.36.000202. URL: https://www.osapublishing.org/viewmedia.cfm?uri=ol-36-2-202{\&}seq=0{\&}html=truehttps://www.osapublishing.org/abstract.cfm?uri=ol-36-2-202https://www.osapublishing.org/ol/abstract.cfm?uri=ol-36-2-202 (cit. on p. 28).

Li, Tongcang, Simon Kheifets, David Medellin, and Mark G. Raizen (2010). "Measurement of the Instantaneous Velocity of a Brownian Particle." In: *Science* 328.5986, pp. 1673–1675. ISSN: 0036-8075. DOI: 10.1126/SCIENCE.1189403. URL: https://science.sciencemag.org/content/328/5986/1673https://science.sciencemag.org/content/328/5986/1673.abstract (cit. on p. 47).

Linke, Christian et al. (2017). "A Clb/Cdk1-mediated regulation of Fkh2 synchronizes CLB expression in the budding yeast cell cycle." In: *npj Systems Biology and Applications* 3.1, p. 7. ISSN: 2056-7189. DOI: 10.1038/s41540-017-0008-1. URL: http://www.nature.com/articles/s41540-017-0008-1 (cit. on pp. 6, 10, 57, 79).

Lit, John W.Y. and Real Tremblay (1973). "FOCAL DEPTH OF A TRANSMITTING AXICON." In: *J Opt Soc Am*. ISSN: 0030-3941. DOI: 10.1364/JOSA.63.000445 (cit. on p. 45).

Long, R. M., D. U. Elliott, F. Stutz, M. Rosbash, and R. H. Singer (1995). "Spatial consequences of defective processing of specific yeast mRNAs revealed by fluorescent in situ hybridization." In: *RNA*. ISSN: 13558382 (cit. on p. 81).

Long, Roy M., Robert H. Singer, Xiuhua Meng, Isabel Gonzalez, Kim Nasmyth, and Ralf Peter Jansen (1997). "Mating type switching in

yeast controlled by asymmetric localization of ASH1 mRNA." In: *Science*. ISSN: 00368075. DOI: 10.1126/science.277.5324.383 (cit. on p. 15).

Lovrics, Anna, Attila Csikász-Nagy, István Gy Zsély, Judit Zádor, Tamás Turányi, and Béla Novák (2006). "Time scale and dimension analysis of a budding yeast cell cycle model." In: *BMC Bioinformatics* 7, p. 494. ISSN: 14712105. DOI: 10.1186/1471-2105-7-494. URL: /pmc/articles/PMC1660553/?report=abstracthttps://www.ncbi.nlm.nih.gov/pmc/articles/PMC1660553/ (cit. on p. 5).

Lowe, David G. (1999). "Object recognition from local scale-invariant features." In: *Proceedings of the IEEE International Conference on Computer Vision*. DOI: 10.1109/iccv.1999.790410 (cit. on p. 47).

– (2004). "Distinctive image features from scale-invariant keypoints." In: *International Journal of Computer Vision*. ISSN: 09205691. DOI: 10.1023/B:VISI.0000029664.99615.94 (cit. on p. 47).

Loy, Gareth and Alexander Zelinsky (2003). "Fast radial symmetry for detecting points of interest." In: *IEEE Transactions on Pattern Analysis and Machine Intelligence*. ISSN: 01628828. DOI: 10.1109/TPAMI.2003.1217601 (cit. on p. 85).

Lu, Ying and Frederick R. Cross (2010). "Periodic cyclin-cdk activity entrains an autonomous cdc14 release oscillator." In: *Cell*. ISSN: 00928674. DOI: 10.1016/j.cell.2010.03.021 (cit. on p. 6).

Lucy, L. B. (1974). "An iterative technique for the rectification of observed distributions." In: *The Astronomical Journal* 79.6, p. 745. ISSN: 00046256. DOI: 10.1086/111605. URL: https://ui.adsabs.harvard.edu/abs/1974AJ.....79..745L/abstract (cit. on p. 44).

Ma, Jiabo, Sibo Liu, Shenghua Cheng, Xiuli Liu, Li Chen, and Shaoqun Zeng (2020). "Reconstruct high-resolution multi-focal plane images from a single 2D wide field image." In: *arXiv* XX.Xx, pp. 1–9. ISSN: 23318422. arXiv: 2009.09574 (cit. on p. 87).

Maioli, Vincent, Antoine Boniface, Pierre Mahou, Júlia Ferrer Ortas, Lamiae Abdeladim, Emmanuel Beaurepaire, and Willy Supatto (2020). "Fast in vivo multiphoton light-sheet microscopy with optimal pulse frequency." In: *Biomedical Optics Express*. ISSN: 2156-7085. DOI: 10.1364/boe.400113 (cit. on p. 23).

Major, Michael L., Rita Lepe, and Robert H. Costa (2004). "Forkhead Box M1B Transcriptional Activity Requires Binding of Cdk-Cyclin Complexes for Phosphorylation-Dependent Recruitment of p300/CBP Coactivators." In: *Molecular and Cellular Biology* 24.7, pp. 2649–2661. ISSN: 0270-7306. DOI: 10.1128/mcb.24.7.2649-2661.2004. URL: http://mcb.asm.org/ (cit. on p. 10).

Mandracchia, Biagio, Xuanwen Hua, Changliang Guo, Jeonghwan Son, Tara Urner, and Shu Jia (2020). "Fast and accurate sCMOS noise correction for fluorescence microscopy." In: *Nature Communications* 11.1, pp. 1–12. ISSN: 20411723. DOI: 10.1038/s41467-019-13841-8.

URL: http://dx.doi.org/10.1038/s41467-019-13841-8 (cit. on pp. 21, 22).

Margolin, William and Rolf Bernander (2004). *How do prokaryotic cells cycle?* DOI: 10.1016/j.cub.2004.09.017 (cit. on p. 4).

Marr, D. and E. Hildreth (1980). "Theory of edge detection." In: *Proceedings of the Royal Society of London - Biological Sciences*. ISSN: 09628452. DOI: 10.1098/rspb.1980.0020 (cit. on p. 84).

Mathuranyanon, R., T. Tsukamoto, a. Takeuchi, Y. Ishiwata-Kimata, Y. Tsuchiya, K. Kohno, and Y. Kimata (2015). "Tight regulation of the unfolded protein sensor Ire1 by its intramolecularly antagonizing subdomain." In: *Journal of Cell Science* 128.9, pp. 1762–1772. ISSN: 0021-9533. DOI: 10.1242/jcs.164111. URL: http://jcs.biologists.org/cgi/doi/10.1242/jcs.164111 (cit. on p. 42).

McMillan, John N., Rey A.L. Sia, and Daniel J. Lew (1998). "A morphogenesis checkpoint monitors the actin cytoskeleton in yeast." In: *Journal of Cell Biology*. ISSN: 00219525. DOI: 10.1083/jcb.142.6.1487 (cit. on p. 8).

Medioni, C., K. Mowry, and F. Besse (2012). "Principles and roles of mRNA localization in animal development." In: *Development* 139.18, pp. 3263–3276. ISSN: 0950-1991. DOI: 10.1242/dev.078626. URL: http://dev.biologists.org/cgi/doi/10.1242/dev.078626 (cit. on p. 15).

Mendel, Gregor (1866). "Versuche über Plflanzenhybriden. Verhandlungen des naturforschenden Vereines in Brünn." In: *Abhandlungen* (cit. on p. 2).

Mendenhall, M D and a E Hodge (1998). "Regulation of Cdc28 cyclin-dependent protein kinase activity during the cell cycle of the yeast Saccharomyces cerevisiae." In: *Microbiology and molecular biology reviews : MMBR* 62.4, pp. 1191–1243. ISSN: 1092-2172 (cit. on pp. 6, 9, 10).

Metzler, Ralf, Jae-Hyung Jeon, Andrey G Cherstvy, and Eli Barkai (2014). "Anomalous diffusion models and their properties: non-stationarity, non-ergodicity, and ageing at the centenary of single particle tracking." In: *Physical chemistry chemical physics : PCCP* 16.44, pp. 24128–64. ISSN: 1463-9084. DOI: 10.1039/c4cp03465a. URL: http://www.ncbi.nlm.nih.gov/pubmed/25297814 (cit. on pp. 13, 14, 81).

Michalet, Xavier (2010). "Mean square displacement analysis of single-particle trajectories with localization error: Brownian motion in an isotropic medium." In: *Physical review. E, Statistical, nonlinear, and soft matter physics* 82.4 Pt 1, p. 041914. ISSN: 1550-2376. DOI: 10.1103/PhysRevE.82.041914. URL: http://www.ncbi.nlm.nih.gov/pubmed/21230320http://www.pubmedcentral.nih.gov/articlerender.fcgi?artid=PMC3055791 (cit. on pp. 49, 64).

Middendorff, Claas v., Alexander Egner, Claudia Geisler, Stefan W. Hell, and Andreas Schönle (2008). "Isotropic 3D Nanoscopy based on single emitter switching." In: *Optics Express* 16.25, p. 20774.

ISSN: 1094-4087. DOI: 10.1364/oe.16.020774. URL: http://www.nanoscopy.de (cit. on p. 26).

Middleton, Sarah A., James Eberwine, and Junhyong Kim (2019). "Comprehensive catalog of dendritically localized mRNA isoforms from sub-cellular sequencing of single mouse neurons." In: *BMC Biology* 17.1, p. 5. ISSN: 17417007. DOI: 10.1186/s12915-019-0630-z. URL: https://bmcbiol.biomedcentral.com/articles/10.1186/s12915-019-0630-z (cit. on p. 15).

Miller, Christian et al. (2011). "Dynamic transcriptome analysis measures rates of mRNA synthesis and decay in yeast." In: *Molecular Systems Biology* 7.458. ISSN: 17444292. DOI: 10.1038/msb.2010.112 (cit. on p. 20).

Mishra, Mithilesh, Junqi Huang, and Mohan K. Balasubramanian (2014). "The yeast actin cytoskeleton." In: *FEMS Microbiology Reviews* 38.2, pp. 213–227. ISSN: 1574-6976. DOI: 10.1111/1574-6976.12064. URL: https://academic.oup.com/femsre/article-lookup/doi/10.1111/1574-6976.12064 (cit. on p. 16).

Miura, Kota (2020). "Bleach correction ImageJ plugin for compensating the photobleaching of time-lapse sequences." In: *F1000Research* 9, p. 1494. DOI: 10.12688/f1000research.27171.1. URL: https://doi.org/10.12688/f1000research.27171.1 (cit. on p. 44).

Moerner, W. E. (2007). *New directions in single-molecule imaging and analysis*. DOI: 10.1073/pnas.0610081104 (cit. on p. 25).

Moerner, W. E., Yoav Shechtman, and Quan Wang (2015). "Single-molecule spectroscopy and imaging over the decades." In: *Faraday Discussions* 184.0, pp. 9–36. ISSN: 13645498. DOI: 10.1039/c5fd00149h. URL: https://pubs.rsc.org/en/content/articlehtml/2015/fd/c5fd00149hhttps://pubs.rsc.org/en/content/articlelanding/2015/fd/c5fd00149h (cit. on p. 28).

Moivre, Abraham De (1733). "Approximatio ad summam terminorum binomii (a+b)^n in seriem expansi." In: *self published* (cit. on p. 12).

Monnier, Nilah, Syuan Ming Guo, Masashi Mori, Jun He, Péter Lénárt, and Mark Bathe (2012). "Bayesian approach to MSD-based analysis of particle motion in live cells." In: *Biophysical Journal*. ISSN: 00063495. DOI: 10.1016/j.bpj.2012.06.029 (cit. on pp. 50, 51).

Monnier, Nilah et al. (2015). "Inferring transient particle transport dynamics in live cells." In: *Nature Methods* 12.9, pp. 838–840. ISSN: 1548-7091. DOI: 10.1038/nmeth.3483. URL: http://www.nature.com/doifinder/10.1038/nmeth.3483 (cit. on pp. 18, 40, 51, 68, 81).

Monod, Jacques (1995). *The statue within: An autobiography*. Plainview, NY: Cold Spring Harbor Laboratory Press (cit. on p. 2).

Montgomery, Douglas C. and George Runger (2010). *Applied Statistics and probability for Engineers*. John Wiley & Sons, Ltd. DOI: 10.2307/1269738 (cit. on p. 12).

Montiel, D., H. Cang, and H. Yang (2006). " Quantitative Characterization of Changes in Dynamical Behavior for Single-Particle Tracking

Studies †." In: *The Journal of Physical Chemistry B*. ISSN: 1520-6106. DOI: 10.1021/jp062024j (cit. on pp. 49, 64).

Mori, Yoichiro, Alexandra Jilkine, and Leah Edelstein-Keshet (2008). "Wave-pinning and cell polarity from a bistable reaction-diffusion system." In: *Biophysical Journal*. ISSN: 15420086. DOI: 10.1529/biophysj.107.120824 (cit. on p. 16).

Morisaki, Tatsuya et al. (2016). "Real-time quantification of single RNA translation dynamics in living cells." In: *Science* 0899.May, aaf0899. ISSN: 0036-8075, 1095-9203. DOI: 10.1126/science.aaf0899. URL: http://science.sciencemag.org/content/early/2016/05/04/science.aaf0899{\%}5Cnhttp://files/104/Morisakietal.-2016-Real-timequantificationofsingleRNAtranslation.pdf{\%}5Cnhttp://files/105/science.html (cit. on p. 86).

Mortimer, Robert K. and John R. Johnston (1959). "Life span of individual yeast cells." In: *Nature*. ISSN: 00280836. DOI: 10.1038/1831751a0 (cit. on p. 5).

Mueller, Florian, Adrien Senecal, Katjana Tantale, Hervé Marie-Nelly, Nathalie Ly, Olivier Collin, Eugenia Basyuk, Edouard Bertrand, Xavier Darzacq, and Christophe Zimmer (2013). *FISH-quant: Automatic counting of transcripts in 3D FISH images*. DOI: 10.1038/nmeth.2406 (cit. on p. 46).

Mulholland, Jon, Daphne Preuss, Anne Moon, Amie Wong, David Drubin, and David Botstein (1994). "Ultrastructure of the yeast actin cytoskeleton and its association with the plasma membrane." In: *Journal of Cell Biology*. ISSN: 00219525. DOI: 10.1083/jcb.125.2.381 (cit. on p. 16).

Müller, Marisa, Roland Gerhard Heym, Andreas Mayer, Katharina Kramer, Maria Schmid, Patrick Cramer, Henning Urlaub, Ralf Peter Jansen, and Dierk Niessing (2011). "A cytoplasmic complex mediates specific mrna recognition and localization in yeast." In: *PLoS Biology*. ISSN: 15449173. DOI: 10.1371/journal.pbio.1000611 (cit. on p. 17).

Munchel, Sarah E., Ryan K. Shultzaberger, Naoki Takizawa, and Karsten Weis (2011). "Dynamic profiling of mRNA turnover reveals gene-specific and system-wide regulation of mRNA decay." In: *Molecular Biology of the Cell* 22.15, pp. 2787–2795. ISSN: 10591524. DOI: 10.1091/mbc.E11-01-0028. URL: http://www.molbiolcell.org/cgi/ (cit. on p. 20).

Murray, Andrew W. (2004). *Recycling the Cell Cycle: Cyclins Revisited*. DOI: 10.1016/S0092-8674(03)01080-8 (cit. on p. 6).

Nasmyth, Kim (1993). "Control of the yeast cell cycle by the Cdc28 protein kinase." In: *Current Opinion in Cell Biology* 5.2, pp. 166–179. ISSN: 09550674. DOI: 10.1016/0955-0674(93)90099-C (cit. on p. 57).

– (1996). *At the heart of the budding yeast cell cycle*. DOI: 10.1016/0168-9525(96)10041-X (cit. on pp. 5, 6).

Neiman, Aaron M. (2011). "Sporulation in the budding yeast Saccharomyces cerevisiae." In: *Genetics*. ISSN: 00166731. DOI: 10.1534/genetics.111.127126 (cit. on p. 6).

Neufeld, Thomas P. and Bruce A. Edgar (1998). "Connections between growth and the cell cycle." In: *Current Opinion in Cell Biology*. ISSN: 09550674. DOI: 10.1016/S0955-0674(98)80122-1 (cit. on p. 7).

Neurohr, Gabriel E., Rachel L. Terry, Arzu Sandikci, Ke Zou, Hao Li, and Angelika Amon (2018). "Deregulation of the G1/S-phase transition is the proximal cause of mortality in old yeast mother cells." In: *Genes and Development* 32.15-16, pp. 1075–1084. ISSN: 15495477. DOI: 10.1101/gad.312140.118. URL: http://www.genesdev.org/cgi/doi/10.1101/gad.312140.118. (cit. on pp. 19, 87).

Nurse, Paul (2000). *A long twentieth century of the cell cycle and beyond*. DOI: 10.1016/S0092-8674(00)81684-0 (cit. on p. 4).

Nurse, Paul, Pierre Thuriaux, and Kim Nasmyth (1976). "Genetic control of the cell division cycle in the fission yeast Schizosaccharomyces pombe." In: *MGG Molecular & General Genetics*. ISSN: 00268925. DOI: 10.1007/BF00268085 (cit. on p. 2).

O'Brien, Kevin P., Maido Remm, and Erik L.L. Sonnhammer (2005). "Inparanoid: A comprehensive database of eukaryotic orthologs." In: *Nucleic Acids Research*. ISSN: 03051048. DOI: 10.1093/nar/gki107 (cit. on p. 2).

Ober, Raimund J., Sripad Ram, and E. Sally Ward (2004). "Localization Accuracy in Single-Molecule Microscopy." In: *Biophysical Journal* 86.2, pp. 1185–1200. ISSN: 00063495. DOI: 10.1016/S0006-3495(04)74193-4. URL: http://dx.doi.org/10.1016/S0006-3495(04)74193-4 (cit. on p. 21).

Oeffinger, Marlene and Daniel Zenklusen (2012). *To the pore and through the pore: A story of mRNA export kinetics*. DOI: 10.1016/j.bbagrm.2012.02.011 (cit. on pp. 15, 59).

Oeffinger, Marlene, Karen E Wei, Richard Rogers, Jeffrey A DeGrasse, Brian T Chait, John D Aitchison, and Michael P Rout (2007). "Comprehensive analysis of diverse ribonucleoprotein complexes." In: *Nature Methods* 4.11, pp. 951–956. ISSN: 15487091. DOI: 10.1038/nmeth1101. URL: http://www.nature.com/doifinder/10.1038/nmeth1101 (cit. on p. 17).

Okada, Satoshi, Marcin Leda, Julia Hanna, Natasha S. Savage, Erfei Bi, and Andrew B. Goryachev (2013). "Daughter Cell Identity Emerges from the Interplay of Cdc42, Septins, and Exocytosis." In: *Developmental Cell*. ISSN: 15345807. DOI: 10.1016/j.devcel.2013.06.015 (cit. on p. 72).

Olivo-Marin, Jean Christophe (2002). "Extraction of spots in biological images using multiscale products." In: *Pattern Recognition*. ISSN: 00313203. DOI: 10.1016/S0031-3203(01)00127-3 (cit. on p. 85).

Onishi, Masayuki, Ko Nolan, Ryuichi Nishihama, and John R. Pringle (2013). "Distinct roles of Rho1, Cdc42, and Cyk3 in septum formation

and abscission during yeast cytokinesis." In: *Journal of Cell Biology*. ISSN: 00219525. DOI: 10.1083/jcb.201302001 (cit. on p. 72).

Orlando, David A, Charles Y Lin, Allister Bernard, Jean Y Wang, Joshua E S Socolar, Edwin S Iversen, Alexander J Hartemink, and Steven B Haase (2008). "Global control of cell-cycle transcription by coupled CDK and network oscillators." In: *Nature* 453.7197, pp. 944–7. ISSN: 1476-4687. DOI: 10.1038/nature06955. URL: http://dx.doi.org/10.1038/nature06955 (cit. on p. 6).

Özsezen, Serdar, Alexandros Papagiannakis, Haoqi Chen, Bastian Niebel, Andreas Milias-Argeitis, and Matthias Heinemann (2019). "Inference of the High-Level Interaction Topology between the Metabolic and Cell-Cycle Oscillators from Single-Cell Dynamics." In: *Cell Systems* 9.4, 354–365.e6. ISSN: 24054720. DOI: 10.1016/j.cels.2019.09.003 (cit. on p. 6).

Paige, Jeremy S, Karen Y Wu, and Samie R Jaffrey (2011). "RNA mimics of green fluorescent protein." In: *Science (New York, N.Y.)* 333.6042, pp. 642–6. ISSN: 1095-9203. DOI: 10.1126/science.1207339. URL: http://www.pubmedcentral.nih.gov/articlerender.fcgi?artid=3314379{\&}tool=pmcentrez{\&}rendertype=abstract (cit. on p. 19).

Palenik, Brian et al. (2007). "The tiny eukaryote Ostreococcus provides genomic insights into the paradox of plankton speciation." In: *Proceedings of the National Academy of Sciences of the United States of America*. ISSN: 00278424. DOI: 10.1073/pnas.0611046104 (cit. on p. 7).

Papagiannakis, Alexandros, Bastian Niebel, Ernst C. Wit, and Matthias Heinemann (2017). "Autonomous Metabolic Oscillations Robustly Gate the Early and Late Cell Cycle." In: *Molecular Cell* 65.2, pp. 285–295. ISSN: 10974164. DOI: 10.1016/j.molcel.2016.11.018 (cit. on p. 6).

Paquin, Nicolas, Marie Ménade, Guillaume Poirier, Damiane Donato, Emmanuel Drouet, and Pascal Chartrand (2007). "Local Activation of Yeast ASH1 mRNA Translation through Phosphorylation of Khd1p by the Casein Kinase Yck1p." In: *Molecular Cell*. ISSN: 10972765. DOI: 10.1016/j.molcel.2007.05.016 (cit. on p. 10).

Pardee, A. B. (1974). "A restriction point for control of normal animal cell proliferation." In: *Proceedings of the National Academy of Sciences of the United States of America*. ISSN: 00278424. DOI: 10.1073/pnas.71.4.1286 (cit. on p. 7).

Park, Hye Yoon, Hyungsik Lim, Young J Yoon, Antonia Follenzi, Chiso Nwokafor, Melissa Lopez-Jones, Xiuhua Meng, and Robert H Singer (2014). "Visualization of dynamics of single endogenous mRNA labeled in live mouse." en. In: *Science (New York, N.Y.)* 343.6169, pp. 422–4. ISSN: 1095-9203. DOI: 10.1126/science.1239200. URL: http://science.sciencemag.org/content/343/6169/422.abstract (cit. on pp. 12, 18).

Pavani, Sri Rama Prasanna and Rafael Piestun (2008). "Three dimensional tracking of fluorescent microparticles using a photon-limited double-helix response system." In: *Optics Express* 16.26, p. 22048. ISSN: 1094-4087. DOI: 10.1364/oe.16.022048. URL: https://www.osapublishing.org/viewmedia.cfm?uri=oe-16-26-22048{\&}seq=0{\&}html=truehttps://www.osapublishing.org/abstract.cfm?uri=oe-16-26-22048https://www.osapublishing.org/oe/abstract.cfm?uri=oe-16-26-22048 (cit. on p. 28).

Pavani, Sri Rama Prasanna, Michael A. Thompson, Julie S. Biteen, Samuel J. Lord, Na Liu, Robert J. Twieg, Rafael Piestun, and W. E. Moerner (2009). "Three-dimensional, single-molecule fluorescence imaging beyond the diffraction limit by using a double-helix point spread function." In: *Proceedings of the National Academy of Sciences of the United States of America*. ISSN: 00278424. DOI: 10.1073/pnas.0900245106 (cit. on pp. 28, 29).

Pentland, Alex P. (1984). "Fractal-Based Description of Natural Scenes." In: *IEEE Transactions on Pattern Analysis and Machine Intelligence*. ISSN: 01628828. DOI: 10.1109/TPAMI.1984.4767591 (cit. on p. 84).

Perrin, J (1909). "Mouvement brownien et réalité moléculaire." In: *Ann. Chim. Phys.* ISSN: 0368-3893 (cit. on pp. 12, 13).

Persson, Fredrik, Martin Lindén, Cecilia Unoson, and Johan Elf (2013). "Extracting intracellular diffusive states and transition rates from single-molecule tracking data." In: *Nature Methods* 10.3, pp. 265–269. ISSN: 1548-7091. DOI: 10.1038/nmeth.2367. arXiv: arXiv:1503.03891v1. URL: http://www.nature.com/doifinder/10.1038/nmeth.2367 (cit. on pp. 12, 25, 51, 68).

Pichon, Xavier, Amandine Bastide, Adham Safieddine, Racha Chouaib, Aubin Samacoits, Eugenia Basyuk, Marion Peter, Florian Mueller, and Edouard Bertrand (2016). "Visualization of single polysomes reveals translation dynamics in living human cells." In: *Journal of Cell Biology* 214.6, pp. 769–781. ISSN: 0021-9525. DOI: 10.1083/jcb.201605024 (cit. on pp. 24, 84).

Pierobon, Paolo, Sarra Achouri, Sébastien Courty, Alexander R. Dunn, James A. Spudich, Maxime Dahan, and Giovanni Cappello (2009). "Velocity, processivity, and individual steps of single myosin V molecules in live cells." In: *Biophysical Journal* 96.10, pp. 4268–4275. ISSN: 15420086. DOI: 10.1016/j.bpj.2009.02.045. URL: /pmc/articles/PMC2712235/?report=abstracthttps://www.ncbi.nlm.nih.gov/pmc/articles/PMC2712235/ (cit. on pp. 48, 59, 82, 85).

Piestun, Rafael, Yoav Y. Schechner, and Joseph Shamir (2000). "Propagation-invariant wave fields with finite energy." In: *Journal of the Optical Society of America A* 17.2, p. 294. ISSN: 1084-7529. DOI: 10.1364/josaa.17.000294. URL: https://www.osapublishing.org/viewmedia.cfm?uri=josaa-17-2-294{\&}seq=0{\&}html=truehttps://www.osapublishing.org/abstract.cfm?uri=josaa-17-2-294https:

//www.osapublishing.org/josaa/abstract.cfm?uri=josaa-17-2-294 (cit. on p. 28).

Pietzsch, Tobias, Stephan Preibisch, Pavel Tomančák, and Stephan Saalfeld (2012). "ImgLib2—generic image processing in Java." In: *Bioinformatics* 28.22, pp. 3009–3011. ISSN: 1460-2059. DOI: 10.1093/bioinformatics/bts543. URL: https://academic.oup.com/bioinformatics/article-lookup/doi/10.1093/bioinformatics/bts543 (cit. on p. 40).

Planchon, Thomas A, Liang Gao, Daniel E Milkie, Michael W Davidson, James A Galbraith, Catherine G Galbraith, and Eric Betzig (2011). "Rapid three-dimensional isotropic imaging of living cells using Bessel beam plane illumination." In: *Nature methods* 8.5, pp. 417–423. ISSN: 1548-7105. DOI: 10.1038/nmeth.1586. URL: http://www.pubmedcentral.nih.gov/articlerender.fcgi?artid=3626440{\&}tool=pmcentrez{\&}rendertype=abstract (cit. on pp. 23, 45, 74).

Politz, Joan C.Ritland, Richard A. Tuft, and Thoru Pederson (2003). "Diffusion-based Transport of Nascent Ribosomes in the Nucleus." In: *Molecular Biology of the Cell*. ISSN: 10591524. DOI: 10.1091/mbc.E03-06-0395 (cit. on p. 83).

Pollard, Thomas D. and Gary G. Borisy (2003). *Cellular motility driven by assembly and disassembly of actin filaments*. DOI: 10.1016/S0092-8674(03)00120-X (cit. on p. 16).

Pollard, Thomas D. and John A. Cooper (2009). *Actin, a central player in cell shape and movement*. DOI: 10.1126/science.1175862 (cit. on p. 16).

Pollard, Thomas D., Laurent Blanchoin, and R. Dyche Mullins (2000). *Molecular mechanisms controlling actin filament dynamics in nonmuscle cells*. DOI: 10.1146/annurev.biophys.29.1.545 (cit. on p. 16).

Polymenis, Michael and Emmett V. Schmidt (1999). "Coordination of cell growth with cell division." In: *Current Opinion in Genetics and Development*. ISSN: 0959437X. DOI: 10.1016/S0959-437X(99)80011-2 (cit. on p. 7).

Powell, Chris D., David E. Quain, and Katherine A. Smart (2003). "Chitin scar breaks in aged Saccharomyces cerevisiae." In: *Microbiology*. ISSN: 13500872. DOI: 10.1099/mic.0.25940-0 (cit. on p. 5).

Prabhat, Prashant, Sripad Ram, E. Sally Ward, and Raimund J. Ober (2004). "Simultaneous imaging of different focal planes in fluorescence microscopy for the study of cellular dynamics in three dimensions." In: *IEEE Transactions on Nanobioscience* 3.4, pp. 237–242. ISSN: 15361241. DOI: 10.1109/TNB.2004.837899. arXiv: NIHMS150003 (cit. on p. 26).

Prabhat, Prashant, Zhuo Gan, Jerry Chao, Sripad Ram, Carlos Vaccaro, Steven Gibbons, Raimund J. Ober, and E. Sally Ward (2007). "Elucidation of intracellular recycling pathways leading to exocytosis of the Fc receptor, FcRn, by using multifocal plane microscopy." In: *Proceedings of the National Academy of Sciences of the United States*

of America. ISSN: 00278424. DOI: 10.1073/pnas.0700337104 (cit. on p. 26).

Pringle, J.R. and L.H. Hartwell (1981). "The Saccharomyces cerevisiae cell cycle." In: *The Molecular Biology of the Yeast Saccharomyces*. Ed. by J.D. Strathern, E.W. Jones, and J.R. Broach. Cold Spring Harbor, NY: Cold Spring Harbor Laboratory Press, pp. 97–142 (cit. on p. 8).

Pruyne, David and Anthony Bretscher (2000). *Polarization of cell growth in yeast. 1. Establishment and maintenance of polarity states* (cit. on p. 11).

Rahi, Sahand Jamal, Kresti Pecani, Andrej Ondracka, Catherine Oikonomou, and Frederick R. Cross (2016). "The CDK-APC/C Oscillator Predominantly Entrains Periodic Cell-Cycle Transcription." In: *Cell* 165.2, pp. 475–487. ISSN: 10974172. DOI: 10.1016/j.cell.2016.02.060. URL: http://dx.doi.org/10.1016/j.cell.2016.02.060 (cit. on p. 6).

Ram, Sripad, Prashant Prabhat, Jerry Chao, E Sally Ward, and Raimund J Ober (2008). "High accuracy 3D quantum dot tracking with multifocal plane microscopy for the study of fast intracellular dynamics in live cells." In: *Biophysical journal* 95.12, pp. 6025–6043. ISSN: 00063495. DOI: 10.1529/biophysj.108.140392. URL: http://dx.doi.org/10.1529/biophysj.108.140392 (cit. on p. 26).

Ram, Sripad, Dongyoung Kim, Raimund J. Ober, and E. Sally Ward (2012). "3D single molecule tracking with multifocal plane microscopy reveals rapid intercellular transferrin transport at epithelial cell barriers." In: *Biophysical Journal*. ISSN: 00063495. DOI: 10.1016/j.bpj.2012.08.054 (cit. on p. 26).

Rao, Calyampudi Radhakrishna (1965). *Linear Statistical Inference and Its Applications*. Hoboken, NJ: John Wiley & Sons Inc, p. 522. ISBN: 978-0471708223 (cit. on p. 21).

Rapoport, Anatol (1986). *General System Theory: Essential Concepts and Applications*. Harwood Academic. ISBN: 978-0856261725 (cit. on p. 1).

Reynolds, David, Bu Jun Shi, Cameron McLean, Frosa Katsis, Bruce Kemp, and Stephen Dalton (2003). "Recruitment of Thr 319-phosphorylated Ndd1p to the FHA domain of Fkh2p requires C1b kinase activity: A mechanism for CLB cluster gene activation." In: *Genes and Development* 17.14, pp. 1789–1802. ISSN: 08909369. DOI: 10.1101/gad.1074103. URL: http://www.genesdev.org/cgi/doi/10.1101/ (cit. on p. 10).

Rhind, N. and P. Russell (2000). "Chk1 and Cds1: Linchpins of the DNA damage and replication checkpoint pathways." In: *Journal of Cell Science* 113.22, pp. 3889–3896. ISSN: 00219533 (cit. on p. 4).

Richardson, William Hadley (1972). "Bayesian-Based Iterative Method of Image Restoration." In: *Journal of the Optical Society of America* 62.1. ISSN: 0030-3941. DOI: 10.1364/josa.62.000055 (cit. on p. 44).

Richman, Tamara J., Mathew M. Sawyer, and Douglas I. Johnson (1999). "The Cdc42p GTPase is involved in a G2/M morphogenetic

checkpoint regulating the apical-isotropic switch and nuclear division in yeast." In: *Journal of Biological Chemistry*. ISSN: 00219258. DOI: 10.1074/jbc.274.24.16861 (cit. on p. 11).

Rivin, Carol J. and Walton L. Fangman (1980). "Cell cycle phase expansion in nitrogen-limited cultures of Saccharomyces Cerevisiae." In: *Journal of Cell Biology*. ISSN: 15408140. DOI: 10.1083/jcb.85.1.96 (cit. on p. 8).

Rogozin, Igor B., Malay Kumar Basu, Miklós Csürös, and Eugene V. Koonin (2009). "Analysis of Rare Genomic Changes Does Not Support the Unikont–Bikont Phylogeny and Suggests Cyanobacterial Symbiosis as the Point of Primary Radiation of Eukaryotes." In: *Genome Biology and Evolution*. ISSN: 1759-6653. DOI: 10.1093/gbe/evp011 (cit. on p. 3).

Ross, W. D (1924). *Aristotle's Metaphysics: A revised text with introduction and commentary*. Oxford: Clarendon Press. URL: https://www.documentacatholicaomnia.eu/03d/-384{_}-322,{_}Aristoteles,{_}13{_}Metaphysics,{_}EN.pdf (cit. on p. 1).

Rueden, Curtis T., Johannes Schindelin, Mark C. Hiner, Barry E. DeZonia, Alison E. Walter, Ellen T. Arena, and Kevin W. Eliceiri (2017). "ImageJ2: ImageJ for the next generation of scientific image data." In: *BMC Bioinformatics*. ISSN: 14712105. DOI: 10.1186/s12859-017-1934-z (cit. on p. 40).

Rupeš, Ivan (2002). "Checking cell size in yeast." In: *TRENDS in Genetics* 18.9. URL: http://tig.trends.com0168-9525/02/{\$}-seefrontmatter (cit. on pp. 7, 8).

SE-scholar (2019). *Who said "The whole is greater than the sum of the parts"?* URL: http://se-scholar.com/se-blog/2017/6/23/who-said-the-whole-is-greater-than-the-sum-of-the-parts (cit. on p. 1).

Sage, Daniel, Franck R. Neumann, Florence Hediger, Susan M. Gasser, and Michael Unser (2005). "Automatic tracking of individual fluorescence particles: Application to the study of chromosome dynamics." In: *IEEE Transactions on Image Processing* 14.9, pp. 1372–1383. ISSN: 10577149. DOI: 10.1109/TIP.2005.852787 (cit. on pp. 47, 84).

Sanderson, Richard J., Karyn E. Bird, Nigel F. Palmer, and Jeff Brenman (1976). "Design principles for a counterflow centrifugation cell separation chamber." In: *Analytical Biochemistry*. ISSN: 10960309. DOI: 10.1016/S0003-2697(76)80036-X (cit. on p. 53).

Saroufim, Mark-Albert, Pierre Bensidoun, Pascal Raymond, Samir Rahman, Matthew R Krause, Marlene Oeffinger, and Daniel Zenklusen (2015). "The nuclear basket mediates perinuclear mRNA scanning in budding yeast." In: *The Journal of cell biology* 211.6, pp. 1131–40. ISSN: 1540-8140. DOI: 10.1083/jcb.201503070. URL: http://www.ncbi.nlm.nih.gov/pubmed/26694838http://www.pubmedcentral.nih.gov/articlerender.fcgi?artid=PMC4687876 (cit. on pp. 12, 18, 19, 22, 23, 59, 68).

Savin, Thierry and Patrick S. Doyle (2005). "Static and dynamic errors in particle tracking microrheology." In: *Biophysical Journal* 88.1, pp. 623–638. ISSN: 00063495. DOI: 10.1529/biophysj.104.042457. URL: http://www.cell.com/article/S0006349505731362/fulltexthttp://www.cell.com/article/S0006349505731362/abstracthttps://www.cell.com/biophysj/abstract/S0006-3495(05)73136-2 (cit. on pp. 49, 64).

Saxton, Michael J. and Ken Jacobson (1997). *Single-particle tracking: Applications to membrane dynamics*. DOI: 10.1146/annurev.biophys.26.1.373 (cit. on pp. 13, 51).

Schaechter, M., J. P. Williamson, J. R. Hood, and KOCHAL (1962). "Growth, cell and nuclear divisions in some bacteria." In: *Journal of general microbiology* 29.3, pp. 421–434. ISSN: 00221287. DOI: 10.1099/00221287-29-3-421. URL: https://www.microbiologyresearch.org/content/journal/micro/10.1099/00221287-29-3-421 (cit. on p. 7).

Schindelin, Johannes et al. (2012). "Fiji: an open-source platform for biological-image analysis." In: *Nature methods* 9.7, pp. 676–82. ISSN: 1548-7105. DOI: 10.1038/nmeth.2019. URL: http://dx.doi.org/10.1038/nmeth.2019 (cit. on p. 40).

Schlichting, Julia Katharina (2019). "Modeling synchronization effects in the yeast cell cycle Dissertation Zum Erlangung des akademischen Grades." PhD thesis. URL: https://edoc.hu-berlin.de/handle/18452/20633 (cit. on pp. 54, 57).

Schmoller, Kurt M., J. J. Turner, M. Kõivomägi, and Jan M. Skotheim (2015). "Dilution of the cell cycle inhibitor Whi5 controls budding-yeast cell size." In: *Nature* 526.7572, pp. 268–272. ISSN: 0028-0836. DOI: 10.1038/nature14908. URL: http://www.nature.com/articles/nature14908 (cit. on pp. 7, 8).

Schneider, Caroline A, Wayne S Rasband, and Kevin W Eliceiri (2012). *NIH Image to ImageJ: 25 years of Image Analysis HHS Public Access*. Tech. rep. (cit. on p. 40).

Schnyder, Tim, Angelo Castello, Christoph Feest, Naomi E. Harwood, Thomas Oellerich, Henning Urlaub, Michael Engelke, Jürgen Wienands, Andreas Bruckbauer, and Facundo D. Batista (2011). "B Cell Receptor-Mediated Antigen Gathering Requires Ubiquitin Ligase Cbl and Adaptors Grb2 and Dok-3 to Recruit Dynein to the Signaling Microcluster." In: *Immunity* 34.6, pp. 905–918. ISSN: 10747613. DOI: 10.1016/j.immuni.2011.06.001 (cit. on p. 22).

Schrödinger, Erwin (1944). *What is Life? The Physical Aspect of the Living Cell*. Cambridge University Press. DOI: 10.1086/281292 (cit. on p. 4).

Schuss, Z., A. Singer, and D. Holcman (2007). "The narrow escape problem for diffusion in cellular microdomains." In: *Proceedings of the National Academy of Sciences of the United States of America*. ISSN: 00278424. DOI: 10.1073/pnas.0706599104 (cit. on p. 83).

Schwab, Michael, Annegret Schulze Lutum, and Wolfgang Seufert (1997). "Yeast Hct1 is a regulator of Cib2 cyclin proteolysis." In: *Cell* 90.4, pp. 683–693. ISSN: 00928674. DOI: 10.1016/S0092-8674(00)80529-2 (cit. on p. 11).

Semplice, Matteo, Andrea Veglio, Giovanni Naldi, Guido Serini, and Andrea Gamba (2012). "A bistable model of cell polarity." In: *PLoS ONE*. ISSN: 19326203. DOI: 10.1371/journal.pone.0030977 (cit. on p. 16).

Seufert, Wolfgang, Bruce Futcher, and Stefan Jentsch (1995). *Role of a ubiquitin-conjugating enzyme in degradation of S- and M-phase cyclins*. DOI: 10.1038/373078a0 (cit. on p. 11).

Shaner, Nathan C et al. (2013). "A bright monomeric green fluorescent protein derived from Branchiostoma lanceolatum." In: *Nature Methods* 10.5, pp. 407–409. ISSN: 1548-7091. DOI: 10.1038/nmeth.2413. URL: http://www.nature.com/doifinder/10.1038/nmeth.2413 (cit. on pp. 19, 31, 42, 88).

Sharova, Lioudmila V., Alexei A. Sharov, Timur Nedorezov, Yulan Piao, Nabeebi Shaik, and Minoru S.H. Ko (2009). "Database for mRNA half-life of 19 977 genes obtained by DNA microarray analysis of pluripotent and differentiating mouse embryonic stem cells." In: *DNA Research* 16.1, pp. 45–58. ISSN: 13402838. DOI: 10.1093/dnares/dsn030 (cit. on p. 20).

Shav-Tal, Y. (2004). "Dynamics of Single mRNPs in Nuclei of Living Cells." In: *Science* 304.5678, pp. 1797–1800. ISSN: 0036-8075. DOI: 10.1126/science.1099754. URL: http://www.sciencemag.org/cgi/doi/10.1126/science.1099754 (cit. on pp. 12, 15).

Shechtman, Yoav, Steffen J. Sahl, Adam S. Backer, and W. E. Moerner (2014). "Optimal point spread function design for 3D imaging." In: *Physical Review Letters* 113.3, p. 133902. ISSN: 10797114. DOI: 10.1103/PhysRevLett.113.133902. URL: https://journals.aps.org/prl/abstract/10.1103/PhysRevLett.113.133902 (cit. on p. 28).

Shechtman, Yoav, Lucien E. Weiss, Adam S. Backer, Steffen J. Sahl, and W. E. Moerner (2015). "Precise Three-Dimensional Scan-Free Multiple-Particle Tracking over Large Axial Ranges with Tetrapod Point Spread Functions." In: *Nano Letters* 15.6, pp. 4194–4199. ISSN: 15306992. DOI: 10.1021/acs.nanolett.5b01396. URL: https://pubs.acs.org/sharingguidelines (cit. on p. 28).

Shepard, K A, A P Gerber, A Jambhekar, P A Takizawa, P O Brown, D Herschlag, J L DeRisi, and R D Vale (2003). "Widespread cytoplasmic mRNA transport in yeast: identification of 22 bud-localized transcripts using DNA microarray analysis." In: *Proceedings of the National Academy of Sciences of the United States of America* 100.20, pp. 11429–34. ISSN: 0027-8424. DOI: 10.1073/pnas.2033246100. URL: http://www.pnas.org/content/100/20/11429.full (cit. on pp. 9, 10, 17, 18, 29, 57, 59, 79, 82, 85).

Sheppard, C. J.R. (2004). "Microscopy: Overview." In: *Encyclopedia of Modern Optics, Five-Volume Set*. Elsevier Inc., pp. 61–69. ISBN: 9780123693952. DOI: 10.1016/B0-12-369395-0/00823-X (cit. on p. 44).

Shtengel, Gleb et al. (2009). "Interferometric fluorescent super-resolution microscopy resolves 3D cellular ultrastructure." In: *Proceedings of the National Academy of Sciences of the United States of America* 106.9, pp. 3125–3130. ISSN: 00278424. DOI: 10.1073/pnas.0813131106. URL: www.pnas.org/cgi/content/full/ (cit. on p. 26).

Sia, R. A., H. A. Herald, and D. J. Lew (1996). "Cdc28 tyrosine phosphorylation and the morphogenesis checkpoint in budding yeast." In: *Molecular Biology of the Cell*. ISSN: 1059-1524. DOI: 10.1091/mbc.7.11.1657 (cit. on p. 8).

Siedentopf, H. and R. Zsigmondy (1903). "Über Sichtbarmachung und Grössenbestimmung ultramikroskopischer Teilchen." In: *Annalen der Physik* 315, pp. 1–39 (cit. on p. 23).

Sil, Anita and Ira Herskowitz (1996). "Identification of an asymmetrically localized determinant, Ash1p, required for lineage-specific transcription of the yeast HO gene." In: *Cell*. ISSN: 00928674. DOI: 10.1016/S0092-8674(00)81049-1 (cit. on p. 16).

Simmons Kovacs, Laura A., David A. Orlando, and Steven B. Haase (2008). *Transcription networks and cyclin/CDKs: The yin and yang of cell cycle oscillators*. DOI: 10.4161/cc.7.17.6515 (cit. on p. 6).

Simmons Kovacs, Laura A., Michael B. Mayhew, David A. Orlando, Yuanjie Jin, Qingyun Li, Chenchen Huang, Steven I. Reed, Sayan Mukherjee, and Steven B. Haase (2012). "Cyclin-Dependent Kinases Are Regulators and Effectors of Oscillations Driven by a Transcription Factor Network." In: *Molecular Cell* 45.5, pp. 669–679. ISSN: 10972765. DOI: 10.1016/j.molcel.2011.12.033. URL: http://dx.doi.org/10.1016/j.molcel.2011.12.033 (cit. on p. 6).

Skotheim, Jan M., Stefano Di Talia, Eric D. Siggia, and Frederick R. Cross (2008). "Positive feedback of G1 cyclins ensures coherent cell cycle entry." In: *Nature*. ISSN: 14764687. DOI: 10.1038/nature07118 (cit. on p. 6).

Smith, C. S., S. Preibisch, A. Joseph, S. Abrahamsson, B. Rieger, E. Myers, R. H. Singer, and D. Grunwald (2015). "Nuclear accessibility of beta-actin mRNA is measured by 3D single-molecule real-time tracking." In: *The Journal of Cell Biology* 209.4, pp. 609–619. ISSN: 0021-9525. DOI: 10.1083/jcb.201411032. URL: http://www.jcb.org/cgi/doi/10.1083/jcb.201411032 (cit. on pp. 27, 43, 85).

Smith, Carlas S., Nikolai Joseph, Bernd Rieger, and Keith A. Lidke (2010). "Fast, single-molecule localization that achieves theoretically minimum uncertainty." In: *Nature Methods* 7.5, pp. 373–375. ISSN: 15487091. DOI: 10.1038/nmeth.1449 (cit. on p. 84).

Smoluchowski, M. V. (1916). "Über Brownsche Molekularbewegung unter Einwirkung äußerer Kräfte und deren Zusammenhang mit

der verallgemeinerten Diffusionsgleichung." In: *Annalen der Physik* 353.24, pp. 1103–1112. ISSN: 00033804. DOI: 10.1002/andp.19163532408. URL: http://doi.wiley.com/10.1002/andp.19163532408 (cit. on pp. 12, 13).

Song, Minho S., Hyungseok C. Moon, Jae Hyung Jeon, and Hye Yoon Park (2018). "Neuronal messenger ribonucleoprotein transport follows an aging Lévy walk." In: *Nature Communications* 9.1, pp. 1–8. ISSN: 20411723. DOI: 10.1038/s41467-017-02700-z. URL: http://dx.doi.org/10.1038/s41467-017-02700-z (cit. on p. 81).

Spellman, Paul T., Gavin Sherlock, Michael Q. Zhang, Vishwanath R. Iyer, Kirk Anders, Michael B. Eisen, Patrick O. Brown, David Botstein, and Bruce Futcher (1998). "Comprehensive identification of cell cycle-regulated genes of the yeast Saccharomyces cerevisiae by microarray hybridization." In: *Molecular Biology of the Cell*. ISSN: 10591524. DOI: 10.1091/mbc.9.12.3273 (cit. on pp. 6, 9).

Spiesser, Thomas W., Christiane Müller, Gabriele Schreiber, Marcus Krantz, and Edda Klipp (2012). "Size homeostasis can be intrinsic to growing cell populations and explained without size sensing or signalling." In: *FEBS Journal* 279.22, pp. 4213–4230. ISSN: 1742464X. DOI: 10.1111/febs.12014. URL: http://doi.wiley.com/10.1111/febs.12014 (cit. on pp. 7, 8, 17).

Spiesser, Thomas W., Clemens Kühn, Marcus Krantz, and Edda Klipp (2015). "Bud-Localization of CLB2 mRNA Can Constitute a Growth Rate Dependent Daughter Sizer." In: *PLOS Computational Biology* 11.4, e1004223. ISSN: 1553-7358. DOI: 10.1371/journal.pcbi.1004223. URL: http://dx.plos.org/10.1371/journal.pcbi.1004223 (cit. on pp. 9, 74, 87).

Spring, Kenneth R., John C. Long, and Michael W. Davidson. *Depth of Field and Depth of Focus*. URL: https://www.microscopyu.com/microscopy-basics/depth-of-field-and-depth-of-focus (visited on 01/12/2021) (cit. on p. 24).

Sprouffske, Kathleen and Andreas Wagner (2016). "Growthcurver: An R package for obtaining interpretable metrics from microbial growth curves." In: *BMC Bioinformatics*. ISSN: 14712105. DOI: 10.1186/s12859-016-1016-7 (cit. on p. 55).

Srinorakutara, Teerapatr (1998). "Determination of yeast cell wall thickness and cell diameter using new methods." In: *Journal of Fermentation and Bioengineering* 86.3, pp. 253–260. ISSN: 0922338X. DOI: 10.1016/S0922-338X(98)80002-0 (cit. on p. 22).

Steinmetzger, Christian, Navaneethan Palanisamy, Kiran R. Gore, and Claudia Höbartner (2019). "A Multicolor Large Stokes Shift Fluorogen-Activating RNA Aptamer with Cationic Chromophores." In: *Chemistry – A European Journal* 25.8, pp. 1931–1935. ISSN: 0947-6539. DOI: 10.1002/chem.201805882. URL: https://onlinelibrary.wiley.com/doi/abs/10.1002/chem.201805882 (cit. on p. 19).

Stylianidou, Stella, Nathan J. Kuwada, and Paul A. Wiggins (2015). "Cytoplasmic dynamics reveals two modes of nucleoid-dependent mobility." In: *Biophysical Journal*. ISSN: 15420086. DOI: 10.1016/j.bpj.2014.10.030 (cit. on p. 13).

Sun, Mai, Björn Schwalb, Daniel Schulz, Nicole Pirkl, Stefanie Etzold, Laurent Larivière, Kerstin C. Maier, Martin Seizl, Achim Tresch, and Patrick Cramer (2012). "Comparative dynamic transcriptome analysis (cDTA) reveals mutual feedback between mRNA synthesis and degradation." In: *Genome Research*. ISSN: 10889051. DOI: 10.1101/gr.130161.111 (cit. on p. 20).

Surana, Uttam, Helmut Robitsch, Clive Price, Tillman Schuster, Ian Fitch, A.Bruce Futcher, and Kim Nasmyth (1991). "The role of CDC28 and cyclins during mitosis in the budding yeast S. cerevisiae." In: *Cell* 65.1, pp. 145–161. ISSN: 00928674. DOI: 10.1016/0092-8674(91)90416-V (cit. on pp. 6, 10).

Sutherland, William (1905). "LXXV. A dynamical theory of diffusion for non-electrolytes and the molecular mass of albumin." In: *The London, Edinburgh, and Dublin Philosophical Magazine and Journal of Science* IX.6, pp. 781–785. ISSN: 1941-5982. DOI: 10.1080/14786440509463331. URL: http://www.physik.uni-augsburg.de/theo1/hanggi/History/BM-History.html (cit. on p. 13).

Sveiczer, A., B. Novak, and J. M. Mitchison (1996). "The size control of fission yeast revisited." In: *Journal of Cell Science*. ISSN: 00219533 (cit. on p. 8).

Szymański, Jedrzej, Adam Patkowski, Agnieszka Wilk, Piotr Garstecki, and Robert Holyst (2006). "Diffusion and viscosity in a crowded environment: From nano- to macroscale." In: *Journal of Physical Chemistry B* 110.51, pp. 25593–25597. ISSN: 15206106. DOI: 10.1021/jp0666784. URL: https://pubs.acs.org/doi/full/10.1021/jp0666784 (cit. on pp. 13, 82).

Taheri-Araghi, Sattar, Serena Bradde, John T. Sauls, Norbert S. Hill, Petra Anne Levin, Johan Paulsson, Massimo Vergassola, and Suckjoon Jun (2015). "Cell-size control and homeostasis in bacteria." In: *Current Biology* 25.3, pp. 385–391. ISSN: 09609822. DOI: 10.1016/j.cub.2014.12.009 (cit. on p. 4).

Takizawa, P a and R D Vale (2000). "The myosin motor, Myo4p, binds Ash1 mRNA via the adapter protein, She3p." In: *Proceedings of the National Academy of Sciences of the United States of America* 97.10, pp. 5273–8. ISSN: 0027-8424. DOI: 10.1073/pnas.080585897. URL: http://www.pubmedcentral.nih.gov/articlerender.fcgi?artid=25818{\&}tool=pmcentrez{\&}rendertype=abstract (cit. on pp. 9, 80).

Takizawa, Peter A., Anita Sil, Jason R. Swedlow, Ira Herskowitz, and Ronald D. Vale (1997). "Actin-dependent localization of an RNA encoding a cell-fate determinant in the yeast." In: *Nature*. ISSN: 00280836. DOI: 10.1038/38015 (cit. on p. 17).

Tanenbaum, Marvin E., Luke A. Gilbert, Lei S. Qi, Jonathan S. Weissman, and Ronald D. Vale (2014). "A protein-tagging system for signal amplification in gene expression and fluorescence imaging." In: *Cell* 159.3, pp. 635–646. ISSN: 10974172. DOI: 10.1016/j.cell.2014.09.039. URL: http://dx.doi.org/10.1016/j.cell.2014.09.039 (cit. on p. 86).

Tang, Yunqing, Johnny Hendriks, Thomas Gensch, Luru Dai, and Junbai Li (2016). "Automatic Bayesian single molecule identification for localization microscopy." In: *Scientific Reports* 6.1, pp. 1–11. ISSN: 20452322. DOI: 10.1038/srep33521. URL: www.nature.com/scientificreports (cit. on p. 85).

Tarantino, Nadine, Jean Yves Tinevez, Elizabeth Faris Crowell, Bertrand Boisson, Ricardo Henriques, Musa Mhlanga, Fabrice Agou, Alain Israël, and Emmanuel Laplantine (2014). "Tnf and il-1 exhibit distinct ubiquitin requirements for inducing NEMO-IKK supramolecular structures." In: *Journal of Cell Biology*. ISSN: 00219525. DOI: 10.1083/jcb.201307172 (cit. on pp. 40, 50, 68).

Tessera, Marc (2011). "Origin of evolution versus origin of life: A shift of paradigm." In: *International Journal of Molecular Sciences* 12.6, pp. 3445–3458. ISSN: 14220067. DOI: 10.3390/ijms12063445. URL: /pmc/articles/PMC3131571/?report=abstracthttps://www.ncbi.nlm.nih.gov/pmc/articles/PMC3131571/ (cit. on p. 4).

Thompson, Michael A., Jason M. Casolarib, Majid Badieirostami, Patrick O. Brown, and W. E. Moernera (2010). "Three-dimensional tracking of single mRNA particles in Saccharomyces cerevisiae using a double-helix point spread function." In: *Proceedings of the National Academy of Sciences of the United States of America*. ISSN: 00278424. DOI: 10.1073/pnas.1012868107 (cit. on pp. 14, 25, 28, 29, 48).

Tinevez, Jean-Yves (2016). "TrackMate documentation." URL: https://imagej.net/{_}images/8/85/TrackMate-manual.pdf (cit. on p. 47).

Tinevez, Jean Yves, Nick Perry, Johannes Schindelin, Genevieve M. Hoopes, Gregory D. Reynolds, Emmanuel Laplantine, Sebastian Y. Bednarek, Spencer L. Shorte, and Kevin W. Eliceiri (2017). "TrackMate: An open and extensible platform for single-particle tracking." In: *Methods* 115, pp. 80–90. ISSN: 10959130. DOI: 10.1016/j.ymeth.2016.09.016. URL: http://creativecommons.org/licenses/by/4.0/ (cit. on pp. 40, 46, 84).

Tokunaga, Makio, Naoko Imamoto, and Kumiko Sakata-Sogawa (2008). "Highly inclined thin illumination enables clear single-molecule imaging in cells." In: *Nature Methods*. ISSN: 15487091. DOI: 10.1038/nmeth1171 (cit. on p. 22).

Trcek, Tatjana, Daniel R Larson, Alberto Moldón, Charles C Query, and Robert H Singer (2011). "Single-molecule mRNA decay measurements reveal promoter- regulated mRNA stability in yeast." In: *Cell* 147.7, pp. 1484–97. ISSN: 1097-4172. DOI: 10.1016/j.cell.2011.

11.051. URL: http://www.pubmedcentral.nih.gov/articlerender.fcgi?artid=3286490{\%}7B{\&}{\%}7Dtool=pmcentrez{\%}7B{\&}{\%}7Drendertype=abstracthttp://www.pubmedcentral.nih.gov/articlerender.fcgi?artid=3286490{\&}tool=pmcentrez{\&}rendertype=abstract (cit. on pp. 9, 11, 29, 57, 74, 79, 80, 101).

Trcek, Tatjana, Jeffrey A. Chao, Daniel R. Larson, Hye Yoon Park, Daniel Zenklusen, Shailesh M. Shenoy, and Robert H. Singer (2012). "Single-mRNA counting using fluorescent in situ hybridization in budding yeast." In: *Nature Protocols*. ISSN: 17542189. DOI: 10.1038/nprot.2011.451 (cit. on p. 20).

Truong, Thai V., Willy Supatto, David S. Koos, John M. Choi, and Scott E. Fraser (2011). "Deep and fast live imaging with two-photon scanned light-sheet microscopy." In: *Nature Methods*. ISSN: 15487091. DOI: 10.1038/nmeth.1652 (cit. on p. 23).

Tsanov, Nikolay et al. (2016). "SmiFISH and FISH-quant - A flexible single RNA detection approach with super-resolution capability." In: *Nucleic Acids Research* 44.22. ISSN: 13624962. DOI: 10.1093/nar/gkw784 (cit. on pp. 52, 84).

Tsokolov, Serhiy A. (2009). "Why is the definition of life so elusive? Epistemological considerations." In: *Astrobiology*. ISSN: 15311074. DOI: 10.1089/ast.2007.0201 (cit. on p. 4).

Turner-Bridger, Benita, Cinzia Caterino, and Jean Michel Cioni (2020). "Molecular mechanisms behind mRNA localization in axons: Axonal mRNA Localisation." In: *Open Biology* 10.9. ISSN: 20462441. DOI: 10.1098/rsob.200177. URL: https://royalsocietypublishing.org/doi/abs/10.1098/rsob.200177 (cit. on p. 15).

Tutucci, Evelina, Maria Vera, and Robert H. Singer (2018). "Single-mRNA detection in living S. cerevisiae using a re-engineered MS2 system." In: *Nature Protocols* 13.10, pp. 2268–2296. ISSN: 17502799. DOI: 10.1038/s41596-018-0037-2 (cit. on pp. 19, 20, 57, 81).

Verkman, Alan S. (2002). *Solute and macromolecule diffusion in cellular aqueous compartments*. DOI: 10.1016/S0968-0004(01)02003-5 (cit. on pp. 82, 83).

Vettenburg, Tom, Heather I.C. Dalgarno, Jonathan Nylk, Clara Coll-Lladó, David E.K. Ferrier, Tomáš Čižmár, Frank J. Gunn-Moore, and Kishan Dholakia (2014). "Light-sheet microscopy using an Airy beam." In: *Nature Methods*. ISSN: 15487105. DOI: 10.1038/nmeth.2922 (cit. on p. 23).

Viswanathan, Sarada et al. (2015). "High-performance probes for light and electron microscopy." In: *Nature Methods* 12.6, pp. 568–576. ISSN: 15487105. DOI: 10.1038/nmeth.3365. URL: /pmc/articles/PMC4573404//pmc/articles/PMC4573404/?report=abstracthttps://www.ncbi.nlm.nih.gov/pmc/articles/PMC4573404/ (cit. on p. 86).

Vliet, Lj Van, Damir Sudar, and It Young (1998). "Digital fluorescence imaging using cooled charge-coupled device array cameras." In:

Cell Biology III.Castleman 1996, pp. 109–120. ISSN: 0263-6484. URL: http://qi.tnw.tudelft.nl/fileadmin/Faculteit/TNW/Over{_}de{_}faculteit/Afdelingen/Imaging{_}Science{_}and{_}Technology/Research/Research{_}Groups/Quantitative{_}Imaging/Publications/List{_}Publications/doc/AP98LVDSTY.pdf (cit. on p. 21).

Wan, Yinan, Katie McDole, and Philipp J. Keller (2019). *Light-sheet microscopy and its potential for understanding developmental processes*. DOI: 10.1146/annurev-cellbio-100818-125311 (cit. on p. 23).

Wang, Chong, Boran Han, Ruobo Zhou, and Xiaowei Zhuang (2016). "Real-Time Imaging of Translation on Single mRNA Transcripts in Live Cells." In: *Cell* 165.4, pp. 990–1001. ISSN: 10974172. DOI: 10.1016/j.cell.2016.04.040. arXiv: 15334406. URL: http://dx.doi.org/10.1016/j.cell.2016.04.040 (cit. on pp. 24, 72, 86).

Wang, Jingyu et al. (2020). "Implementation of a 4Pi-SMS super-resolution microscope." In: *Nature Protocols*, pp. 1–51. ISSN: 17502799. DOI: 10.1038/s41596-020-00428-7. URL: https://doi.org/10.1038/s41596-020-00428-7 (cit. on p. 26).

Wang, Yulei, Chih Long Liu, John D. Storey, Robert J. Tibshirani, Daniel Herschlag, and Patrick O. Brown (2002). "Precision and functional specificity in mRNA decay." In: *Proceedings of the National Academy of Sciences of the United States of America* 99.9, pp. 5860–5865. ISSN: 00278424. DOI: 10.1073/pnas.092538799 (cit. on p. 20).

Warner, Katherine Deigan, Michael C. Chen, Wenjiao Song, Rita L. Strack, Andrea Thorn, Samie R. Jaffrey, and Adrian R. Ferré-D'Amaré (2014). "Structural basis for activity of highly efficient RNA mimics of green fluorescent protein." In: *Nature Structural and Molecular Biology*. ISSN: 15459985. DOI: 10.1038/nsmb.2865 (cit. on p. 19).

Warner, Katherine Deigan, Ljiljana Sjekloa, Wenjiao Song, Grigory S. Filonov, Samie R. Jaffrey, and Adrian R. Ferré-D'Amaré (2017). "A homodimer interface without base pairs in an RNA mimic of red fluorescent protein." In: *Nature Chemical Biology*. ISSN: 15524469. DOI: 10.1038/nchembio.2475 (cit. on p. 19).

Wäsch, Ralph and Frederick R. Cross (2002). "APC-dependent proteolysis of the mitotic cyclin Clb2 is essential for mitotic exit." In: *Nature*. ISSN: 00280836. DOI: 10.1038/nature00856 (cit. on p. 11).

Weiss, Matthias (2013). "Single-particle tracking data reveal anticorrelated fractional Brownian motion in crowded fluids." In: *Physical Review E - Statistical, Nonlinear, and Soft Matter Physics*. ISSN: 15393755. DOI: 10.1103/PhysRevE.88.010101 (cit. on p. 13).

Welford, W. T. (1960). "Use of Annular Apertures to Increase Focal Depth." In: *Journal of the Optical Society of America*. ISSN: 0030-3941. DOI: 10.1364/josa.50.000749 (cit. on p. 45).

Wiener, Norbert (1948). *Cybernetics or control and communication in the animal and the machine*. Technology Press (cit. on p. 1).

Williams, N. (1996). *Yeast genome sequence ferments new research*. DOI: 10.1126/science.272.5261.481. URL: http://science.sciencemag.org/content/272/5261/481 (cit. on p. 3).

Winge, Øjvind and Otto Laustsen (1937). "On two types of spore germination, and on genetic segregations in Saccharomyces , demonstrated through single-spore cultures." In: *Comptes Rendus des Travaux du Laboratoire Carlsberg, Série Physiologique* 22, pp. 99–117 (cit. on p. 2).

– (1938). "Artificial species hybridization in yeasttle." In: *Comptes Rendus des Travaux du Laboratoire Carlsberg, Série Physiologique* 22, pp. 235–245 (cit. on p. 2).

– (1939). "On 14 new yeast types, produced by hybridization." In: *Comptes Rendus des Travaux du Laboratoire Carlsberg, Série Physiologique* 22, pp. 337–353 (cit. on p. 2).

Winston, Fred, Catherine Dollard, and Stephanie L. Ricupero-Hovasse (1995). "Construction of a set of convenient saccharomyces cerevisiae strains that are isogenic to S288C." In: *Yeast*. ISSN: 10970061. DOI: 10.1002/yea.320110107 (cit. on p. 31).

Winzeler, Elizabeth A. et al. (1999). "Functional characterization of the S. cerevisiae genome by gene deletion and parallel analysis." In: *Science*. ISSN: 00368075. DOI: 10.1126/science.285.5429.901 (cit. on p. 2).

Wirth, Regina, Peng Gao, G. Ulrich Nienhaus, Murat Sunbul, and Andres Jäschke (2019). "SiRA: A Silicon Rhodamine-Binding Aptamer for Live-Cell Super-Resolution RNA Imaging." In: *Journal of the American Chemical Society* 141.18, pp. 7562–7571. ISSN: 15205126. DOI: 10.1021/jacs.9b02697. URL: https://pubs.acs.org/doi/abs/10.1021/jacs.9b02697 (cit. on p. 19).

Wittenberg, Curt and Steven I. Reed (2005). *Cell cycle-dependent transcription in yeast: Promoters, transcription factors, and transcriptomes*. DOI: 10.1038/sj.onc.1208606 (cit. on p. 9).

Wood, Valerie (2006). "How to get the most from fission yeast genome data: a report from the 2006 European Fission Yeast Meeting computing workshop." In: *Yeast* 23.13, pp. 905–912. ISSN: 0749503X. DOI: 10.1002/yea.1419. URL: http://doi.wiley.com/10.1002/yea.1419 (cit. on p. 3).

Worn, A., A. Auf der Maur, D. Escher, A. Honegger, A. Barberis, and A. Pluckthun (2000). "Correlation between in Vitro Stability and in Vivo Performance of Anti-GCN4 Intrabodies as Cytoplasmic Inhibitors." In: *Journal of Biological Chemistry* 275.4, pp. 2795–2803. ISSN: 0021-9258. DOI: 10.1074/jbc.275.4.2795. URL: http://www.jbc.org/cgi/doi/10.1074/jbc.275.4.2795 (cit. on p. 86).

Wu, Bin, Carolina Eliscovich, Young J Yoon, and Robert H Singer (2016). "Translation dynamics of single mRNAs in live cells and neurons." In: *Science*, aaf1084. ISSN: 0036-8075, 1095-9203. DOI: 10.1126/science.aaf1084. arXiv: 15334406. URL: http://science.

sciencemag.org/content/early/2016/05/04/science.aaf1084{\%}5Cnhttp://files/98/Wuetal.-2016-TranslationdynamicsofsinglemRNAsinlivecells pdf{\%}5Cnhttp://files/101/science.html (cit. on pp. 24, 86).

Wu, Yichen, Yair Rivenson, Hongda Wang, Yilin Luo, Eyal Ben-David, Laurent A. Bentolila, Christian Pritz, and Aydogan Ozcan (2019). "Three-dimensional virtual refocusing of fluorescence microscopy images using deep learning." In: *Nature Methods* 16.12, pp. 1323–1331. ISSN: 15487105. DOI: 10.1038/s41592-019-0622-5. URL: https://doi.org/10.1038/s41592-019-0622-5 (cit. on p. 87).

Wu, Yicong et al. (2013). "Spatially isotropic four-dimensional imaging with dual-view plane illumination microscopy." In: *Nature biotechnology* 31.11, pp. 1032–8. ISSN: 1546-1696. DOI: 10.1038/nbt.2713. URL: http://dx.doi.org/10.1038/nbt.2713 (cit. on p. 23).

Yamagishi, Mai, Yoshitaka Shirasaki, and Takashi Funatsu (2009). "Size-dependent accumulation of mRNA at the leading edge of chicken embryo fibroblasts." In: *Biochemical and Biophysical Research Communications* 390.3, pp. 750–754. ISSN: 0006291X. DOI: 10.1016/j.bbrc.2009.10.043. URL: https://linkinghub.elsevier.com/retrieve/pii/S0006291X0902021X (cit. on p. 13).

Yan, Xiaowei, Tim A. Hoek, Ronald D. Vale, and Marvin E. Tanenbaum (2016). "Dynamics of Translation of Single mRNA Molecules in Vivo." In: *Cell* 165.4, pp. 976–989. ISSN: 10974172. DOI: 10.1016/j.cell.2016.04.034 (cit. on pp. 23, 86).

Yang, Edward, Erik van Nimwegen, Mihaela Zavolan, Nikolaus Rajewsky, Mark Schroeder, Marcelo Magnasco, and James E. Darnell (2003). "Decay rates of human mRNAs: Correlation with functional characteristics and sequence attributes." In: *Genome Research* 13.8, pp. 1863–1872. ISSN: 10889051. DOI: 10.1101/gr.1272403. URL: https://pubmed.ncbi.nlm.nih.gov/12902380/ (cit. on p. 20).

Yeh, Elaine, Robert V. Skibbens, Judy W. Cheng, E. D. Salmon, and Kerry Bloom (1995). "Spindle dynamics and cell cycle regulation of dynein in the budding yeast, Saccharomyces cerevisiae." In: *Journal of Cell Biology*. ISSN: 00219525. DOI: 10.1083/jcb.130.3.687 (cit. on p. 72).

Young, I T, R Zagers, L J Van Vliet, J Mullikin, F Boddeke, and H Netten (1993). "Depth-of-Focus in microscopy." In: *8th Scandinavian Conference on Image Analysis*, pp. 493–498. URL: http://citeseerx.ist.psu.edu/viewdoc/download?doi=10.1.1.218.8128{\&}rep=rep1{\&}type=pdf (cit. on p. 24).

Zacks, Shelemyahu (1971). *The Theory of Statistical Inference*. Wiley series in probability and mathematical statistics. John Wiley, p. 609. ISBN: 9780608169422. URL: https://books.google.de/books?id=zHV3uAAACAAJ (cit. on p. 21).

Zadrag-Tecza, Renata, Magdalena Kwolek-Mirek, Grzegorz Bartosz, and Tomasz Bilinski (2009). "Cell volume as a factor limiting the replicative lifespan of the yeast Saccharomyces cerevisiae." In: *Biogeron-*

tology 10.4, pp. 481–488. ISSN: 13895729. DOI: 10.1007/s10522-008-9192-0. URL: https://pubmed.ncbi.nlm.nih.gov/18985429/https://pubmed.ncbi.nlm.nih.gov/18985429/?dopt=Abstract (cit. on p. 83).

Zeng, Qingyi and Kathleen B. Hall (1997). "Contribution of the C-terminal tail of U1A RBD1 to RNA recognition and protein stability." In: *RNA*. ISSN: 13558382 (cit. on p. 19).

Zhao, Ning, Kouta Kamijo, Philip D. Fox, Haruka Oda, Tatsuya Morisaki, Yuko Sato, Hiroshi Kimura, and Timothy J. Stasevich (2018). "A genetically encoded probe for imaging HA-tagged protein translation, localization, and dynamics in living cells and animals." In: *bioRxiv*, p. 474668. DOI: 10.1101/474668. URL: https://www.biorxiv.org/content/10.1101/474668v1 (cit. on p. 86).

– (2019). "A genetically encoded probe for imaging nascent and mature HA-tagged proteins in vivo." In: *Nature Communications* 10.1, p. 2947. ISSN: 2041-1723. DOI: 10.1038/s41467-019-10846-1. URL: http://www.nature.com/articles/s41467-019-10846-1 (cit. on p. 86).

Zhivotovsky, B. and S. Orrenius (2010). "Cell cycle and cell death in disease: Past, present and future." In: *Journal of Internal Medicine*. DOI: 10.1111/j.1365-2796.2010.02282.x (cit. on p. 7).

Zhu, Gefeng, Paul T. Spellman, Tom Volpe, Patrick O. Brown, David Botstein, Trisha N. Davis, and Bruce Futcher (2000). "Two yeast forkhead genes regulate the cell cycle and pseudohyphal growth." In: *Nature*. ISSN: 00280836. DOI: 10.1038/35017581 (cit. on p. 9).

ACKNOWLEDGMENTS

I want to thank my supervisor Edda Klipp for providing me with an opportunity to work in a stimulating environment, where I could learn to approach the life sciences from a systems perspective. I appreciate the continued support and the lessons I learned from looking at a biological system with a physicists eyes. She supported me by enabling my participation in numerous conferences, scientific meetings, training courses; both in Berlin and internationally. I also appreciated her openness for my repeated excursions to Janelia. Andreas Herrmann generously gave me access to his laboratory, let me take part of his own and his group's experience in seminars, and gave me helpful feedback and ideas regarding experiments and data analysis. Life on his floor was a great complement to the input I received in the Theoretical Biophysics group.

The experiments at the core of my thesis were performed at Janelia; and I must acknowledge the invaluable help with experimentation and data analysis I received there from Jesse Aaron, both during my stay and afterwards. I want to thank John Heddleston for his thorough introduction to the lattice light sheet microscope, and his help with data reconstruction. Further, I want to thank Teng-Leong Chew, director of the Janelia Advanced Imaging Center, for helpful discussions on image science - and granting me an extra week of experimentation, when a snow storm had cut off Janelia from the outside world and crushed my original timeline. Satya Khoun expertly handled my yeast cells upon arrival at Janelia and made sure I could start image acquisition without delay.

I am very grateful for the input I received from experts in their respective fields: I want to thank Robert H. Singer (Albert Einstein College of Medicine, New York) for discussing live cell single mRNA imaging and sharing his unpublished results on mRNA localization in yeast so openly. Relatedly, I want to thank Evelina Tutucci (now at Vrije Universiteit Amsterdam), who performed the experiments in question while in Rober Singer's group, and with whom I had a fruitful discussion. I had inspiring discussions on particle detection and the MS2 system with Carlas Smith, who also helped me to relate my particle detection method to the state of the art (Technische Universiteit Delft). Brian P. English (Janelia), who discussed my images with me and gave me helpful input on image analysis methods. Stephan Preibisch pointed me at the opportunity to use the acMFM and was available for helpful discussions. I want to thank Tatsuya Morisaki (Colorado State University, Fort Collins, USA) for demonstrating his translation imaging setup and pointing me at helpful imaging methods.

I also want to thank my late father in law, Bengt Kasemo (Chalmers University of Technology, Gothenburg) for helpful discussions about diffusion and related phenomena.

There are many colleagues in the Theoretical Biophysics group that helped me during the years. I greatly benefited from the practical help and discussions I had with Gabriele Schreiber regarding virtually all the aspects of my work. She helped me to overcome experimental hassle, to stay focused on the aim of my project and to wrap it up when the time had come. Jorin Diemer's model on sperm motion served as a catalyst for our fecund exchange on directionality in RNA motion; I am very grateful for his help with analysis code and useful discussion of methods. Roman Rainer, a great colleague and friend, helped me to convert my ideas for data analysis into computational methods - any time of the day or night. Martin Seeger, thank you for being my compass in all things mathematical - and for purchasing Gloomhaven. It was a valuable experience to co-supervise the graduate work of Lars Knopf, who made a spatial computational model of yeast RNA translocation. Similarly, I am grateful for the smFISH experiments Wiebk Schmidt performed under my-supervision, which I could use as reference for my own image data. I want to thank Katja Tummler who helped me to find a convincing strategy for the preparation of my thesis and helped with data shuffling. Jens Hahn for help with cell counting data and increased throughput of my image analysis workflow. Judith Wodke provided very helpful comments on my thesis, both drawing on her scientific experience and her (usually well hidden) pedantic side. Jannis Uhlendorf, Max Schelker and Max Flöttmann gave me valuable input for image reconstruction scripts. I am grateful to Aouefa Amoussouvi and Lotte Teufel who, as trailblazers for single RNA studies in the Biophysics groups at the Humboldt-Universität, established fixed cell methods and most likely spared me a great many mistakes by making them before I started (I had a fair share, anyway). I also appreciate Björn Goldenbogen's input on experimental procedures, his help with elutriation methods and discussions regarding data analysis. I also want to acknowledge Marcus Krantz, whose vast knowledge of yeast biology made him a valuable discussion partner. I also want to acknowledge Aviv Korman for discussions on image reconstruction. I am grateful for discussions I had with all the smart people making up the Theoretical Biophysics group, from the day of my job interview until today (hopefully tomorrow, too.) I want to thank Christiane Müller and Lisa Mallis for all their help in the lab, Ivo Maintz for his help with IT infrastructure, Thomas Korte for his help with microscopy and Sabine Wagnitz for her help with administrative issues.

My research was funded by the Einstein Foundation, through their program 'Single molecule RNA biology - dynamics and function of RNA from transcription to degradation' and the Deutsche

Forschungsgemeinschaft, via the Collaborative Research Centre 740 'From Molecules to Modules: Organisation and Dynamics of Functional Units in Cells'. Research at Janelia was financed by the Gordon and Betty Moore Foundation and Howard Hughes Medical Institution (hhmi) through the Janelia Advanced Imaging Center.

I am indebted to my family: My parents Maria and Jürgen Ehret for their unwavering support, particularly during pandemic times when penning and parenting were hard to reconcile. My children Mira and Espen who learn so much faster than me, forcing me to try harder by appealing to my competitive instinct. Lastly, my loved Totta, thank you for challenging me, discussing and improving my project with me, and supporting me.

DECLARATION

I hereby declare that I completed the doctoral thesis independently based on the stated resources and aids. I have not applied for a doctoral degree elsewhere and do not have a corresponding doctoral degree. I have not submitted the doctoral thesis, or parts of it, to another academic institution and the thesis has not been accepted or rejected. I declare that I have acknowledged the Doctoral Degree Regulations which underlie the procedure of the Faculty of Mathematics and Natural Sciences of Humboldt-Universität zu Berlin, as amended on June 27, 2012. Furthermore, I declare that no collaboration with commercial doctoral degree supervisors took place, and that the principles of Humboldt-Universität zu Berlin for ensuring good academic practice were abided by.

Berlin, 02.03.2021

Severin Ehret